

UNIVERSIDADE DE SANTIAGO DE COMPOSTELA

Departamento de Física de Partículas

# New physics implications and searches at LHCb

Miriam Lucio Martínez

## Tese de Doutoramento



Programa de Doutoramento  
en Física Nuclear e de Partículas



# Contents

|          |  |           |
|----------|--|-----------|
| <b>1</b> | <b>Introduction</b>                                      | <b>1</b>  |
| 1.1      | Higgs Mechanism . . . . .                                | 1         |
| 1.1.1    | Coupling to fermions . . . . .                           | 3         |
| 1.1.2    | Coupling to photons and gluons . . . . .                 | 3         |
| 1.2      | Particle Content . . . . .                               | 3         |
| 1.3      | CKM Matrix . . . . .                                     | 5         |
| 1.4      | Need for New Physics . . . . .                           | 5         |
| 1.4.1    | Matter-antimatter imbalance . . . . .                    | 5         |
| 1.4.2    | Dark matter and dark energy . . . . .                    | 6         |
| 1.4.3    | Unification of forces . . . . .                          | 6         |
| <b>2</b> | <b>Supersymmetry</b>                                     | <b>10</b> |
| 2.1      | Introduction . . . . .                                   | 10        |
| 2.2      | Points addressed by SUSY . . . . .                       | 11        |
| 2.3      | Supersymmetry breaking . . . . .                         | 11        |
| 2.4      | Minimal Supersymmetrical Standard Model (MSSM) . . . . . | 12        |
| 2.4.1    | Dark Matter in the MSSM . . . . .                        | 12        |
| 2.4.2    | MSSM Lagrangian . . . . .                                | 13        |
| 2.4.3    | CMSSM . . . . .  | 15        |
| 2.4.4    | AMSB . . . . .   | 16        |
| 2.4.4.1  | mAMSB . . . . .  | 16        |
| 2.4.5    | Renormalization Group equations . . . . .                | 18        |
| 2.5      | RPV Models . . . . .                                     | 20        |
| 2.5.1    | Consequences of RPV . . . . .                            | 21        |
| 2.6      | Experimental searches . . . . .                          | 22        |
| <b>3</b> | <b>Low E in SUSY (MFV)</b>                               | <b>24</b> |
| 3.1      | Motivation for MFV . . . . .                             | 24        |
| 3.2      | MFV EFT . . . . .  | 24        |
| 3.3      | MFV SUSY . . . . .                                       | 25        |
| 3.4      | MFV R-parity . . . . .                                   | 26        |
| 3.5      | Characteristics . . . . .                                | 27        |
| 3.6      | CMFV . . . . .   | 27        |

|          |  |           |
|----------|--|-----------|
| 3.7      | Experimental bounds . . . . .                | 27        |
| 3.8      | Unitarity Triangle . . . . .                 | 28        |
| <b>4</b> | <b>LHCb</b>                                  | <b>30</b> |
| 4.1      | LHC . . . . .                                | 30        |
| 4.2      | LHCb . . . . .                               | 31        |
| 4.2.1    | Beam pipe, vacuum chamber and BCM . . . . .  | 32        |
| 4.2.2    | Magnet . . . . .                             | 32        |
| 4.2.3    | Tracking . . . . .                           | 33        |
| 4.2.3.1  | VELO . . . . .                               | 34        |
| 4.2.3.2  | ST . . . . .                                 | 34        |
| 4.2.3.3  | OT . . . . .                                 | 35        |
| 4.2.4    | PID . . . . .                                | 36        |
| 4.2.4.1  | RICH . . . . .                               | 36        |
| 4.2.4.2  | Calorimeters . . . . .                       | 37        |
| 4.2.4.3  | Muon System . . . . .                        | 38        |
| 4.2.5    | Trigger . . . . .                            | 39        |
| 4.2.5.1  | L0 . . . . .                                 | 39        |
| 4.2.5.2  | HLT . . . . .                                | 40        |
| 4.2.5.3  | HLT1 . . . . .                               | 41        |
| 4.2.5.4  | HLT2 . . . . .                               | 42        |
| 4.2.6    | Tracking and Vertexing performance . . . . . | 42        |
| 4.2.7    | PID performance . . . . .                    | 45        |
| 4.2.8    | Trigger performance . . . . .                | 48        |
| 4.2.8.1  | L0 hardware trigger . . . . .                | 48        |
| 4.2.8.2  | High Level Trigger . . . . .                 | 50        |
| 4.2.9    | The LHCb Upgrade . . . . .                   | 51        |
| 4.2.9.1  | Trigger Upgrade . . . . .                    | 51        |
| 4.2.9.2  | VELO Upgrade . . . . .                       | 52        |
| 4.2.9.3  | PID Upgrade . . . . .                        | 52        |
| 4.2.9.4  | Tracking Upgrade . . . . .                   | 53        |
| 4.2.10   | Analysis workflow . . . . .                  | 54        |
| <b>5</b> | <b><math>\Delta F=2</math></b>               | <b>56</b> |
| 5.1      | Introduction . . . . .                       | 56        |
| 5.2      | $\phi_s$ experimental . . . . .              | 57        |
| 5.2.1    | Phenomenology . . . . .                      | 58        |
| 5.2.2    | Samples and event selection . . . . .        | 58        |
| 5.2.2.1  | Data sample . . . . .                        | 59        |
| 5.2.2.2  | Simulation samples . . . . .                 | 59        |
| 5.2.2.3  | Stripping selection . . . . .                | 60        |
| 5.2.2.4  | Trigger selection . . . . .                  | 60        |
| 5.2.2.5  | Corrections . . . . .                        | 61        |

|          |   |           |
|----------|---|-----------|
| 5.2.3    | Mass fit and computation of signal sWeights . . . . .                   | 62        |
| 5.2.4    | $C_{\text{SP}}$ factors . . . . .                                       | 64        |
| 5.2.5    | Decay time resolution . . . . .   | 66        |
| 5.2.6    | Angular acceptance . . . . .  | 66        |
| 5.2.7    | Decay time acceptance . . . . .   | 67        |
| 5.2.7.1  | Measurement of $\tau(B^0)$ . . . . .                                    | 69        |
| 5.2.8    | Flavour tagging . . . . .   | 70        |
| 5.2.9    | Data fitting . . . . .  | 72        |
| 5.2.10   | Baseline fit . . . . .  | 72        |
| 5.2.11   | Coverage of the uncertainty with the sFit . . . . .                     | 73        |
| 5.2.11.1 | Simulation . . . . .  | 73        |
| 5.2.11.2 | Signal and background simulation . . . . .                              | 74        |
| 5.2.11.3 | Data . . . . .  | 75        |
| 5.3      | $\phi_s$ pheno . . . . .  | 76        |
| 5.3.1    | Observables . . . . .   | 76        |
| 5.4      | $\phi_s$ MultiNest . . . . .  | 76        |
| 5.4.1    | MultiNest . . . . .   | 84        |
| 5.4.1.1  | Bayesian inference . . . . .  | 84        |
| 5.4.1.2  | Nested sampling . . . . .   | 85        |
| 5.4.1.3  | Ellipsoidal nested sampling . . . . .                                   | 86        |
| 5.4.1.4  | The MultiNest algorithm . . . . .                                       | 86        |
| <b>6</b> | <b>Kaon Physics</b> . . . . .   | <b>87</b> |
| 6.1      | Introduction . . . . .  | 87        |
| 6.2      | $K_s^0 \rightarrow \pi^0 \mu^+ \mu^-$ Sensitivity study . . . . .       | 88        |
| 6.2.1    | Analysis strategy . . . . .   | 89        |
| 6.2.2    | Reconstruction and selection . . . . .                                  | 90        |
| 6.2.3    | Background sources . . . . .  | 92        |
| 6.2.4    | Fit model . . . . .   | 93        |
| 6.2.5    | Expected sensitivity . . . . .  | 93        |
| 6.2.6    | Conclusions . . . . .   | 94        |
| 6.3      | Probing SUSY effects in $K_s^0 \rightarrow \mu^+ \mu^-$ . . . . .       | 96        |
| 6.3.1    | Formalism . . . . .   | 96        |
| 6.3.1.1  | Observables . . . . .   | 97        |
| 6.3.1.2  | $K_s^0 \rightarrow \mu^+ \mu^-$ . . . . .                               | 98        |
| 6.3.1.3  | $\varepsilon'_K/\varepsilon_K$ . . . . .                                | 104       |
| 6.3.1.4  | $\varepsilon_K$ and $\Delta M_K$ . . . . .                              | 106       |
| 6.3.2    | Parameter scan . . . . .  | 108       |
| 6.3.3    | Results . . . . .   | 109       |
| 6.3.3.1  | Effects from $\left(\delta_d^{LL(RR)}\right)_{12}$ separately . . . . . | 110       |
| 6.3.3.2  | Floating <i>LL</i> and <i>RR</i> MIs simultaneously . . . . .           | 110       |
| 6.3.3.3  | Non degenerate Higgs masses . . . . .                                   | 113       |
| 6.3.4    | Conclusions . . . . .   | 114       |

|   |            |
|---|------------|
| <b>7 CMSSM</b>                                      | <b>121</b> |
| 7.1 MasterCode framework . . . . .                  | 121        |
| 7.2 Sampling algorithm . . . . .                    | 122        |
| 7.3 Scan Ranges . . . . .                           | 122        |
| 7.4 Method . . . . .                                | 122        |
| 7.4.1 Gaussian Constraints . . . . .                | 123        |
| 7.4.2 Non-Gaussian Constraints . . . . .            | 124        |
| <b>Appendices</b>                                   | <b>126</b> |
| <b>A MasterCode observables</b>                     | <b>127</b> |
| A.1 Mass Spectrum . . . . .                         | 127        |
| A.2 Dark Matter Relic Density . . . . .             | 128        |
| A.3 Neutralino Scattering off Nuclei . . . . .      | 129        |
| A.3.1 Spin-Independent Term . . . . .               | 129        |
| A.3.2 Spin-Dependent Term . . . . .                 | 130        |
| A.4 Anomalous Magnetic Moment of the Muon . . . . . | 130        |
| A.5 Electroweak Precision Observables . . . . .     | 131        |
| A.6 Flavour Physics Observables . . . . .           | 132        |
| <b>B Coverage of the uncertainty with the sFit</b>  | <b>133</b> |
| <b>Bibliography</b>                                 | <b>138</b> |



# <sup>1</sup> Chapter 1

## <sup>2</sup> Introduction

<sup>3</sup> The Standard Model (hereafter SM) of Particle Physics, mainly formulated in the [1970s](#),  
<sup>4</sup> is the quantum field theory that describes the strong and electroweak interactions. It is  
<sup>5</sup> represented in Group Theory by [\[1\]](#):

$$SU(3)_C \bigotimes SU(2)_T \bigotimes U(1)_Y \quad (1.1)$$

<sup>6</sup> Where the strong interaction, described by Quantum Chromodynamics (QCD), is con-  
<sup>7</sup> tained in the  $SU(3)_C$  group (a symmetry group of *color*, C), and  $SU(2)_T \bigotimes U(1)_Y$ , where  
<sup>8</sup> T and Y stand for weak isospin and hypercharge respectively, relates to the electroweak  
<sup>9</sup> interaction (EW). The SM fermions (described in [1.2](#)) consist of three families with two  
<sup>10</sup>  $SU(2)_L$  doublets ( $Q_L$  and  $L_L$ ) and three  $SU(2)_L$  singlets ( $U_R$ ,  $D_R$  and  $E_R$ ). In order  
<sup>11</sup> to preserve the electroweak gauge invariance (and so, keep the SM renormalizable), the  
<sup>12</sup> particles predicted by this lagrangian have to be massless. This leads to the necessity of a  
<sup>13</sup> spontaneously breaking of the symmetry into  $SU(3)_C \bigotimes U(1)_{EM}$ . Such breaking is done  
<sup>14</sup> by the vacuum expectation value (VEV) of a scalar isospin doublet, with hypercharge  
<sup>15</sup> 1/2, called *Higgs* [\[2\]](#). More details on this mechanism are given in [1.1](#).

$$G_{SM} \xrightarrow{Higgs(1,2)_{1/2}} SU(3)_C \bigotimes U(1)_{EM} \quad (1.2)$$

### <sup>16</sup> 1.1 Higgs Mechanism

<sup>17</sup> Similarly to what happens in the Ginzburg-Landau theory for superconductivity, the  
<sup>18</sup> Higgs mechanism arises from the need of EWSB, together with the requirement that  
<sup>19</sup> gauge invariance is preserved in  $\mathcal{L}_{SM}$ . The Higgs field interacts with the particles corre-  
<sup>20</sup> sponding to the elementary field, including gauge bosons. Resulting of this interaction,  
<sup>21</sup> these particleless acquire mass. As for the others, the Higgs field has associated at least one  
<sup>22</sup> particle in the SM, the Higgs boson, a scalar particle with spin zero. Within the SM, it  
<sup>23</sup> is not possible to make a prediction of its mass (other than setting loose upper and lower  
<sup>24</sup> limits), since it depends on a parameter that needs to be determined experimentally.

<sup>25</sup> The term in the SM lagrangian that accounts for the self-interaction of the Higgs field  
<sup>26</sup> is the following:

$$\mathcal{L}_{Higgs} = \mu^2 \phi^\dagger \phi - \lambda (\phi^\dagger \phi)^2, \quad \mu^2 < 0, \lambda > 0 \quad (1.3)$$

<sup>27</sup> Where  $\phi$  denotes the (complex) Higgs Field :

$$\phi = \begin{pmatrix} \phi^+ \\ \phi^0 \end{pmatrix} \quad (1.4)$$

<sup>28</sup> A scalar isospin doublet with hypercharge  $+1/2$ . The initial symmetry of the system is  
<sup>29</sup> broken for a non-zero value of this field:

$$\phi = \frac{1}{\sqrt{2}} \begin{pmatrix} 0 \\ v \end{pmatrix}, \quad v = \frac{\mu}{\sqrt{\lambda}} \quad (1.5)$$

<sup>30</sup> Leading to the Higgs particle, with mass  $\sqrt{2\lambda v^2}$ , neutral charge and hypercharge 1. It  
<sup>31</sup> was discovered in 2012 by 2 detectors at LHC, ATLAS [3] and CMS [4]. Its mass was  
<sup>32</sup> measured to be  $125.09 \pm 0.24$  GeV.

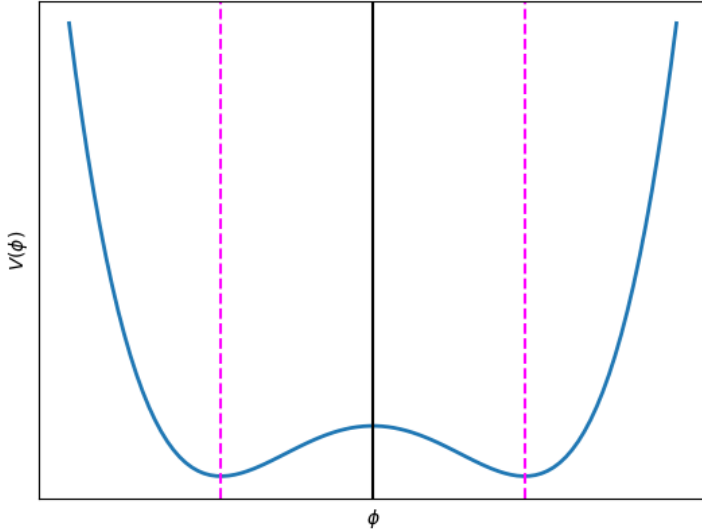


Figure 1.1: Higgs mechanism. The dashed-magenta vertical line indicate the two vacuum states. The black vertical line is located at the origin. The minimum is not at 0, and therefore the potential has a VEV.

<sup>33</sup> The gauge fields  $W^\pm$  and Z acquire mass through their interaction with the Higgs  
<sup>34</sup> boson. Thus:

$$W^\pm = \frac{1}{\sqrt{2}} (W^{(1)} \mp W^{(2)}), \quad Z = \frac{1}{\sqrt{g_I^2 + g_Y^2}} (g_I W^{(3)} - g_Y B) \quad (1.6)$$

<sup>35</sup> Where  $Z$  and  $W^\pm$  are linear combinations of the weak and hypercharge bosons (3 and 1,  
<sup>36</sup> respectively). Then:

$$m_{W^\pm} = \frac{vg_I}{\sqrt{2}}, m_Z = v\sqrt{\frac{g_I^2 + g_Y^2}{2}} \quad (1.7)$$

<sup>37</sup> Notice that the relation between both masses is given by the so-called *weak-mixing angle*,  
<sup>38</sup>  $\theta_W$

$$\frac{m_W^\pm}{m_Z} = \frac{g_I}{\sqrt{(g_I + g_Y)}} = \cos \theta_W \quad (1.8)$$

<sup>39</sup> Measured experimentally to be  $\theta_W \sim 0.50$  rad [1].

### <sup>40</sup> 1.1.1 Coupling to fermions

<sup>41</sup> The lagrangian term corresponding to the Higgs ( $H$ )-fermions ( $f$ ) interaction can be  
<sup>42</sup> written as follows:

$$\mathcal{L}_{H\{f\}} = -\lambda_e \bar{E}_L \phi E_R - \lambda_d \bar{Q}_L \phi D_R - \lambda_u \varepsilon^{ab} \phi_b^\dagger U_R + \text{h.c.} \quad (1.9)$$

<sup>43</sup> Where  $\lambda_e$ ,  $\lambda_d$  and  $\lambda_u$  are the respective coupling constants (*Yukawa couplings*), different  
<sup>44</sup> for each fermion. Substituting in this expression the Higgs field with the result obtained  
<sup>45</sup> before:

$$m_e = \frac{v\lambda_e}{\sqrt{2}}, m_u = \frac{v\lambda_u}{\sqrt{2}}, m_d = \frac{v\lambda_d}{\sqrt{2}} \quad (1.10)$$

<sup>46</sup> The fermion masses are therefore proportional to the Yukawa couplings.

### <sup>47</sup> 1.1.2 Coupling to photons and gluons

<sup>48</sup> Both gluons and photons are gauge bosons of the strong and electromagnetic interactions,  
<sup>49</sup> respectively. They have zero mass and spin 1. For the gluons, given that the color  
<sup>50</sup> symmetry  $SU(3)$  is not modified by the Higgs mechanism, they don't directly interact  
<sup>51</sup> with the Higgs boson. The only way this interaction can happen is via quark loops.  
<sup>52</sup> Contrary to what happens with the gluons, the photons can interact directly with the  
<sup>53</sup> Higgs field. Nevertheless, they don't acquire mass as a result of this interaction,  $m_\gamma = 0$ .

## <sup>54</sup> 1.2 Particle Content

<sup>55</sup> The particle content of the SM is categorized as a function of the intrinsic angular mo-  
<sup>56</sup> mentum of each particle, or *spin*. Particles with half-integer spin are called *fermions*,  
<sup>57</sup> while those with an integer value for the spin are *bosons*. The latter ones are the carriers  
<sup>58</sup> of the different interactions that enter the SM lagrangian:

$$\mathcal{L} = \mathcal{L}_{kin} + \mathcal{L}_{Higgs} + \mathcal{L}_{Yuk} \quad (1.11)$$

59 Where the first term accounts for the kinetic part of the interaction, and the two others  
 60 describe the Higgs mechanism (described in 1.1) and its interaction with the fermions.  
 61 Regarding the fermions, a further classification can be made depending on whether they  
 62 are affected (*quarks*) or not (*leptons*) by the strong interaction. If affected, a quantum  
 63 number, color, further characterizes the particle. Note that the electroweak interaction  
 64 affects all the particles.

65 An additional quantum number, *flavour*, is used to label the different elementary  
 66 particles. There are three flavour families of quarks and leptons in the SM, represented in  
 67 1.2. Each lepton (electron,  $i$ , muon,  $\mu$ , tauon,  $\tau$ ) has associated a neutral particle, called  
 68 the *neutrino*:  $\nu_e$ ,  $\nu_\mu$ ,  $\nu_{\text{tau}}$ . Even though they are predicted to be massless within the SM  
 69 (so that there are not right-handed neutrinos in the SM and, equivalently, there are not  
 70 left-handed antineutrinos), they are known to have mass [5].

71 The elementary particles of the SM are represented in 1.2. For each of this particles,  
 72 there exists another one with the same mass but opposite physical charges. Those are  
 73 called *antiparticles*. Notice that some particles (e.g. the photon) are their own antiparticle.

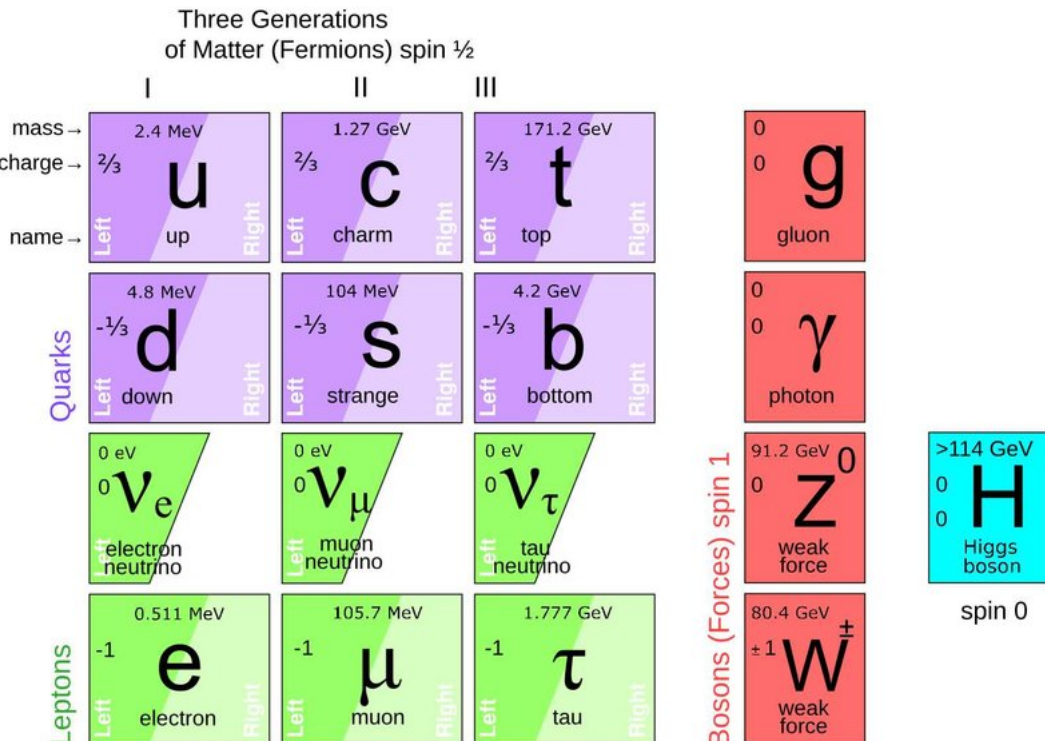


Figure 1.2: The SM particle content [6].

74 Quarks form bound states named *hadrons* that have a quantum number associated  
 75 called the baryonic number,  $\mathcal{B}$ . They are composed either by a quark and an antiquark  
 76 (forming *mesons*, with  $\mathcal{B} = 0$ ) or by three quarks (*baryons*, with  $\mathcal{B} = 1$ ). Given the spin

77 that results of the *sum* of the quarks, baryons are fermions and mesons are bosons.

## 78 1.3 CKM Matrix

79 The Yukawa couplings, seen in 1.1, generate off-diagonal terms that allow for the quarks  
80 to *mix* between the three generations. Diagonalizing the quark mass matrices, 4 unitary  
81 matrices are obtained,  $V_{L,R}^{u,d}$ , that determine the coupling of the  $W^\pm$  bosons to the different  
82 quarks.

83 This diagonalization can be seen as the rotation from one basis ( $q$ ) to another, hereafter  
84 called *mass basis* or *physical basis*,  $q'$ . These are related by the aforementioned matrices  
85 [7]:

$$\small{86} \quad u_L^i = V_u^{ij} u_L'^j \quad d_L^i = V_d^{ij} d_L'^j \quad (1.12)$$

87 With this, the weak current transforms from  $\bar{u}_L^i \gamma^\mu d_L^i$  to  $\bar{u}_L'^i \gamma^\mu (V_u^\dagger V_d)_{ij} d_L'^j \equiv$   
88  $\bar{u}_L'^i \gamma^\mu V_{\text{CKM}} d_L'^i$ , where  $V_{\text{CKM}}$  is a non-diagonal, unitary matrix called the *Cabibbo-Kobayashi-*  
89 *Maskawa* (CKM) matrix. The most up-to-date measured values of its elements can be  
90 found in [1].

$$\small{91} \quad V^{\text{CKM}} = \begin{pmatrix} V_{ud} & V_{us} & V_{ub} \\ V_{cd} & V_{cs} & V_{cb} \\ V_{td} & V_{ts} & V_{tb} \end{pmatrix} \quad (1.13)$$

92 This matrix is the responsible for the transitions between different quark generations,  
93 that allow for processes in which there is change in the quark flavour but not in the electric  
94 charge to happen. These are known as Flavour Changing Neutral Currents (FCNC). Most  
95 of the rare decays are of this type. It also causes CP violation, that will be discussed in  
96 the following sections. It is worth noticing that this matrix is not necessarily restricted  
97 to being 3x3, thus extra quark generations (not discovered yet) can exist [7].

## 98 1.4 Need for New Physics

99 Even though the SM has shown to be a very successful theory, it lacks explanation for  
100 several phenomena present in nature.

### 101 1.4.1 Matter-antimatter imbalance

102 In order to have an excess of matter over antimatter in the early universe (process known  
103 as *baryogenesis* [8], three requirements have to be fulfilled. These are known as the  
104 *Sakharov conditions* [8], and include a large CP-violation. The SM predicts a rate of the  
105 CP-violation smaller than the one needed, thus, a new source is required.

## 106 1.4.2 Dark matter and dark energy

107 Several experimental evidences, such as the rotational speed of spiral galaxies, gravitational  
 108 lensing, or observed fluctuations in the Cosmic Microwave Background radiation  
 109 (see for example [9], [10]) have lead to discovery of dark matter and dark energy, that  
 110 take up the vast majority of the Universe composition and don't interact with light. The  
 111 possible baryonic (MACHOs, MAssive Compact Halo Objects, such as black holes, and  
 112 RAMBOs, Robust Association of Massive Baryonic Objects) percentage of dark matter is small.  
 113 The rest cannot be explained within the SM, it is *non baryonic cold dark matter*, where cold refers to its non-relativistic nature, or neutrinos. Possible candidates  
 114 for cold dark matter entail weakly interacting sub-eV particles (WISPs), such as axions([11], [12], [13]), primordial black holes ref and weakly interacting massive particles  
 115 (WIMPs).  
 116

## 118 1.4.3 Unification of forces

119 The behavior of the three coupling constants at the order of TeV, *naturalness* ,(figure1.3,  
 120 left) suggests the existence of a *primary* interaction, represented by a higher symmetry  
 121 group (e.g. SU(5) or SO(10)). Spontaneous symmetry breaking of this interaction would  
 122 lead to the existence of the electromagnetic, weak, and strong interactions at lower energy  
 123 scales. Nevertheless, in order for this to happen, there should be a matching of these  
 124 coupling constants for such high energies, which is not perfectly achieved in the SM. This  
 125 hints the existence of new symmetries or fields (figure1.3, right). Some of these suggestions  
 126 will be discussed in the following chapter.

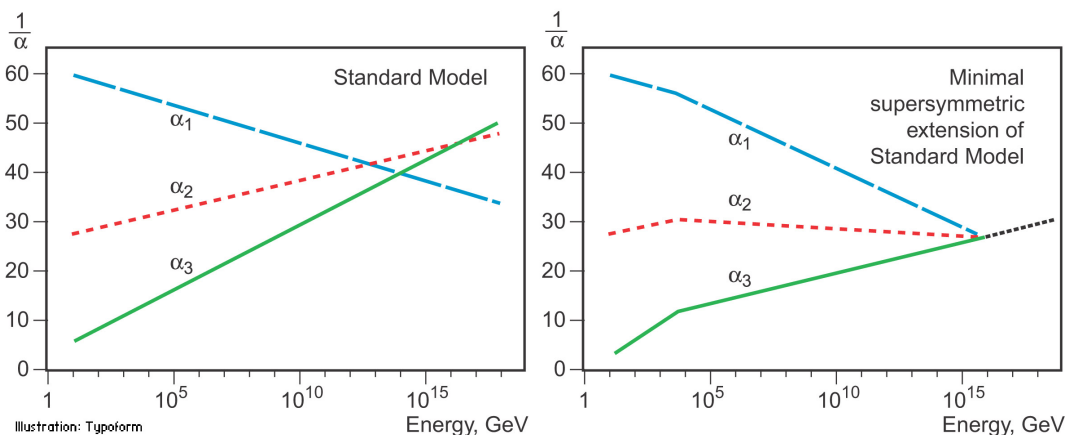


Figure 1.3: Running coupling constants as a function of the energy scale, for the SM (left) and in the context of supersymmetry (right) [14]

- 127 • The number of fermion families. As mentioned earlier, the number of fermion families  
 128 is not an observable, but rather an input for the theory. More generations could in principle be accommodated as part of the SM particle content.

- The gauge hierarchy problem. This is intrinsically related to the mass of the Higgs boson. Apart from the fact that it is not predicted by the theory, it requires fine-tuning in order not to diverge, leading to the enlargement of the EW scale. Also, it is very small compared to the gravity scale, given by the Planck mass:  $M_{Pl} = \sqrt{\hbar c/G_N} = 1.2 \times 10^{19}$  GeV, which is not fully understood.
- Inclusion of gravity. The SM fails to include gravity as one of the interactions, as there is no quantum theory for it.
- Neutrino masses. As it was already mentioned before, neutrinos are massless within the SM model. Nevertheless, experimental observations such as the oscillations of solar neutrinos [5] prove this prediction wrong. Thus, a Beyond the SM (BSM) mechanism to give neutrinos mass is required. There are several proposals for this, such as the seesaw mechanism or the Majorana theory [15].
- Charge quantisation. The fact that the electron charge and the proton charge are of the same magnitude but opposite sign has no explanation in the SM.
- Fermion masses and mixing angles. Similarly to what happened with the number of fermion families, these quantities are not predicted by the SM. Moreover, the mass of the top quark, much bigger than the other quark masses, is an intriguing fact not explained by this theory.
- The magnetic dipole moment of the muon, whose experimental measurement [16] deviates more than  $3\sigma$  from the SM predictions.

In addition to this, several results provided by the LHCb collaboration refs on flavour anomalies and lepton flavour universality studies contribute to the motivation of the search for BSM physics.

Several theories have been proposed to cope with the SM problems, that make this model look more like an effective low energy theory than a model itself. Among these, Supersymmetry and Minimal Flavour Violation (MFV) are of special importance and will be discussed in the following chapters. However, there are other alternatives, some of which are briefly discussed below.

- **Majorana neutrinos:** in the SM, neutrinos are supposed to be massless *Dirac* particles. However it's been suggested that they are instead its own antiparticle, *Majorana neutrinos*. Within this theory, they are allowed to acquire mass. Several experiments search for a neutrinoless double beta decay that would prove this [17], [18].
- **Axions:** axions are hypothetical particles that compose DM, including the Peccei-Quinn mechanism [11] to solve the **strong CP problem** [19]. They would have been massively produced soon after the Big Bang. The couplings and masses axions can cover several orders of magnitudes.

- 167 • **Two Higgs Doublet Models (THDM):** in this scenario, there are two Higgs  
 168 fields populating the vacuum instead of one.

$$\langle \phi_a \rangle_0 = \begin{pmatrix} 0 \\ \frac{v_1}{\sqrt{2}} \end{pmatrix}, \quad \langle \phi_b \rangle_0 = \begin{pmatrix} 0 \\ \frac{v_2}{\sqrt{2}} \end{pmatrix} \quad (1.14)$$

169 Where  $v_1$  and  $v_2$  follow the relation:

$$v \equiv (v_1^2 + v_2^2)^{1/2} \quad (1.15)$$

170 The ratio between these two VEVs,  $\tan \beta \equiv \frac{v_2}{v_1}$  is the most important parameter  
 171 in this model. It describes the diagonalization of the mass-squared matrices of the  
 172 charged scalars and of the pseudoscalars, resulting in 4 fields

$$\begin{aligned} \phi_1 &= \sin \beta \phi_b + \cos \beta \phi_a & \phi_2 &= -\sin \beta \phi_a + \cos \beta \phi_b \\ \langle \phi_1 \rangle_0 &= \begin{pmatrix} 0 \\ \frac{v_{SM}}{\sqrt{2}} \end{pmatrix}, \quad \langle \phi_2 \rangle_0 = \begin{pmatrix} 0 \\ 0 \end{pmatrix} \end{aligned} \quad (1.16)$$

173 The spontaneous symmetry breaking leads in this case to 5 physical Higgs particles:  
 174 two neutral scalars linear combinations of  $Re(\phi_1^0)$  and  $Re(\phi_2^0)$ ,  $H^0$  and  $h^0$ ; a neutral  
 175 pseudoscalar,  $A^0 \propto Im(\phi_2^0)$  and two charged scalars  $H^\pm = \phi_2^\pm$ .

- 176 • **Models with extra dimensions:** models with extra dimensions (apart from the  
 177 usual 4 from the observed spacetime) are motivated by the attempts made to unify  
 178 electromagnetism and gravity within the Kaluza-Klein theory [20], [21]. There are  
 179 several proposals, such as *string theory* or the *Randall-Sundrum model* [22], that  
 180 gives explanation to hierarchy using 5 dimensions and predicts the existence of the  
 181 *graviton*.
- 182 • **SM with fourth generation (SM4):** adding a fourth generation of fermions  
 183 requires the corresponding neutrino to be heavy,  $m_{\nu_4} > M_Z/2$ , to match the current  
 184 experimental constraints [23].
- 185 • **Little Higgs Models:** in these models, the Higgs is realised as a light pseudo-  
 186 Nambu Goldstone boson of a broken global symmetry. They attempt to solve the  
 187 gauge hierarchy problem. The minimal version of such models include 4 new heavy  
 188 vector bosons,  $(W'^\pm, Z', B')$ , coupled to SM fermions, mixed with the SM  $W^\pm$   
 189 and  $Z$ ; light Higgs doublet(s), with possibility of extra light scalar multiplets; heavy  
 190 Higgs multiplets, coupled to Higgs/Goldstone pairs, decoupled from fermions, mixed  
 191 with light Higgses, and heavy up-type quark(s),  $t'$ . An example spectrum can be  
 192 seen in 1.4. Updated constraints in this model can be found in [24].

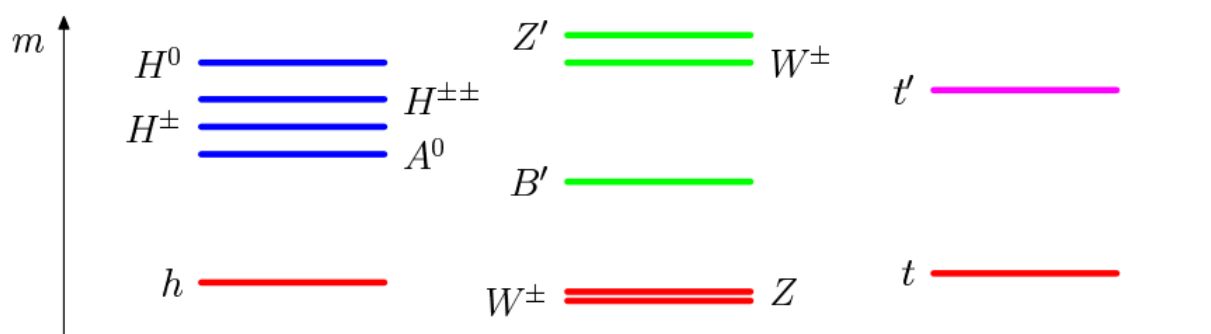


Figure 1.4: Example spectrum for LHM [ref?](#)

193 **Chapter 2**

194 **Supersymmetry**

195 **2.1 Introduction**

196 Supersymmetry (henceforth SUSY) is a framework that constitutes one of the main alter-  
197 natives for BSM Physics. Postulated in the 70s as a graded Lie algebra (with commutators  
198 and anticommutators), allowed by the Coleman-Mandula theorem [25], possess a unique  
199 mathematical nature that allows for the solution of several of the SM caveats that were  
200 discussed in the chapter before. It is being searched for in several experiments, and not  
201 yet discovered. Lower limits are set in the scale of SUSY breaking, the so-called scale of  
202 new physics. current bounds?

203 SUSY can be seen as a generalization of space-time symmetries in QFT, establishing  
204 an invariance under the transformations of fermions to bosons, requiring their number  
205 to be the same in nature. Hence, for each boson (fermion) there is a superpartner of  
206 fermionic (bosonic) nature. If SUSY wasn't broken, the symmetry would be exact and  
207 the masses of the particles would coincide with those of their respective superpartners,  
208 which is not observed in nature. Moreover, none of the particles known to date fulfills  
209 the quality to be a superpartner, which leads to the conclusion that for Supersymmetry  
210 to exist there must be more particles than those seen so far (the double, in the simplest  
211 supersymmetric extension of the SM).

212 A new quantity number can be introduced within SUSY, R-parity, defined as:

$$R = (-1)^{3B+L+2S} \tag{2.1}$$

213 Where B is the baryon number, L the lepton number (both quantities conserved in the  
214 SM) and S the spin. Particles with R = 1 are SM particles, while their superpartners  
215 have R = -1. Models where R-Parity is conserved (hence, B-L invariance) predict the  
216 production of superparticle in pairs, and at least one stable supersymmetric particle, the  
217 Lightest Supersymmetric Particle (LSP), thus providing a good candidate for dark matter.  
218 There are also SUSY models where R-parity is violated, allowing the LSP to decay to SM  
219 particles. An example of a RPV model is the bilinear RPV CMSSM [26].

## 220 2.2 Points addressed by SUSY

221 As mentioned earlier, the success of SUSY lies in the coverage of SM most important  
222 **pitfalls**. A summary of this is discussed in this section.

- 223 • **Unification of forces:** as explained in the 2.1, gravity is not included in the SM.  
224 Nevertheless, given that SUSY algebra is a generalization of Poincaré algebra, it is  
225 therefore invariant under general coordinate transformation if it is local. With this,  
226 a theory including gravity (*supergravity*) can be obtained from SUSY.
- 227 • **Gauge hierarchy problem:** Supersymmetry (and supersymmetric partners) lead  
228 to the cancellation of quadratic mass terms causing divergences up to the SUSY  
229 breaking scale,  $M_{SUSY}$ , given the relation

$$\sum_{bosons} m^2 - \sum_{fermions} m^2 = M_{SUSY}^2 \quad (2.2)$$

230 The origin of EWSB can also be explained from radiative electroweak symmetry  
231 breaking within SUSY, also explaining the difference between the scales ( $M_{SUSY}$   
232 and the Higgs mass).

- 233 • **Unification of forces:** as mentioned earlier, the behavior of the coupling constants  
234 at high energies hints a *great unification* of forces. This match, while not perfect in  
235 the SM, is obtained in a supersymmetric scenario, as it can be seen in figure 1.3,  
236 thanks to the change in the parameters of the renormalization group equations.
- 237 • **Matter-antimatter imbalance:** leptogenesis (a scenario in which there is an  
238 asymmetry between leptons and antileptons in the early universe) can happen in  
239 RPV models, being able to accommodate the total matter-antimatter imbalance.
- 240 • **Dark matter and dark energy:** as pointed out in 1.4.2, most of the origin of  
241 dark matter and dark energy remains unexplained in the SM. Supersymmetry can  
242 provide several candidates for this, provided R-parity is conserved. More details on  
243 the possibilities are discussed in [ref](#).

## 244 2.3 Supersymmetry breaking

245 Supersymmetry breaking is inferred from experimental observation. Without it, the abundance  
246 and mass of partners and superpartners would be equal, as said in 2.1. Moreover,  
247 experimental constraints can help reducing the arbitrariness of the MSSM parameters.

248 All global continuous symmetries can be broken with an *extra* component of the Lagrangian  
249 that breaks the symmetry of the larger part (Heisenberg-Wigner mode), with  
250 spontaneous symmetry breaking and the resulting appearance of Goldstone particles, or  
251 with a combination of these two methods. The Minimal Supersymmetric Standard Model  
252 is an example of the former, and will be discussed in more detail in the following section.

253 **2.4 Minimal Supersymmetrical Standard Model**  
 254 **(MSSM)**

255 The Minimal Supersymmetrical Standard Model is the simplest supersymmetric extension  
 256 of the SM, containing some general features that do not depend on the choice of model.  
 257 Among said features is the fact that for each SM partner there is a *superpartner* (*gauginos*  
 258 for bosons and *sfermions* for fermions), with spin differing 1/2. The particle content is  
 259 summarized in 2.1.

Table 2.1: Particle content of the MSSM

| SM                            | MSSM   | Spin |
|-------------------------------|--|------|
| gluon ( $g$ )                 | gluino $\tilde{g}$   | 1/2  |
| Hypercharge & Weak bosons     | $\tilde{W}^0, \tilde{W}^\pm, \tilde{B}^0$                                      | 1/2  |
| leptons ( $(\nu, l)_L, e_R$ ) | sleptons ( $(\tilde{\nu}, \tilde{l})_L, \tilde{e}_R$ )                         | 0    |
| quarks ( $q$ )                | squarks ( $\tilde{q}$ )  | 0    |
| Higgs field                   | Higgsinos ( $\tilde{H}_u^\pm, \tilde{H}_d^\pm, \tilde{H}_u^0, \tilde{H}_d^0$ ) | 1/2  |

260 Notice that in the MSSM, as in any supersymmetric scenario, it is required the presence  
 261 of 2 Higgs bosons in the SM with hypercharge -1 and 1, compatible with FCNC constraints,  
 262 as it fulfills the Glashow-Weinberg/Paschos condition( [?], [?]). Gauginos have spin zero  
 263 in order to be matter scalars and not gauge bosons. As for the sfermions, the only  
 264 consistent interacting field theory of spin 3/2 has to include gravity [27], hence they have  
 265 spin 1/2. This theory, known as *supergravity*, includes the superpartner of the *graviton*,  
 266 known as *gravitino*. It is also worth mentioning that the MSSM, like the SM, fails to  
 267 explain the number of fermion families.

268 The MSSM has some interesting features, such as the improvement in the unification  
 269 of gauge coupling constants at some high energy scale,  $\Lambda$ , still undetermined but known  
 270 to be in the order of  $2 \times 10^{16}$  GeV. This unification is kept if SUSY is broken at a scale  
 271  $M_S \leq \mathcal{O}(1\text{TeV})$ . Even if gravity is included, its coupling constant seems to roughly point  
 272 to the same value at the same  $\Lambda$ .

273 The soft-explicit breaking of the MSSM (or the electroweak symmetry breaking itself)  
 274 allows for mixing between different sparticles with the same charge and color to happen.  
 275 This leads to the existence of *charginos* ( $\tilde{\chi}_{1,2}^\pm$ ) and *neutralinos* ( $\tilde{\chi}_{1,2,3,4}^0$ ), as a combination  
 276 of gauginos and higgsinos for the former and neutral gauginos for the latter. Sfermion  
 277 mixing can also happen. The mixing patterns and mass values of sparticle mass eigenstates  
 278 depend crucially on the manner of supersymmetry breaking.

279 **2.4.1 Dark Matter in the MSSM**

280 As said before, within the SUSY framework there are several candidates to constitute  
 281 DM. A common feature they share is their stability. These candidates are:

- 282     ● Sneutrino: ruled out in the MSSM because of the current limits on the interaction  
 283       cross section of dark matter particles with ordinary matter as measured by direct  
 284       detection experiments
- 285     ● Lightest neutralino: the LSP for models conserving R-parity. Depending on its  
 286       composition it can be of different natures. Said composition comes determined by a  
 287       unitary 4x4 matrix that diagonalize the neutralino mass matrix,  $N$ , as seen in 2.3.  
 288       2.4.
- 289       1. Bino-like: when the term  $N_{11}$  dominates the neutralino diagonalization matrix,  
 290        $N$ , fulfilled for  $M_1 < \mu$
- 291       2. Higgsino-like: when the off-diagonal elements in the mixing matrix ( $N_{13}^2 + N_{14}^2$ )  
 292       dominate, for  $\mu < M_1$
- 293       3. Wino-like: when the term  $N_{12}$  dominates the neutralino diagonalization matrix,  
 294        $N$ , fulfilled for  $\mu, M_{1,3} < M_2$
- 295       4. Mixed states of the above

- 296     ● Gravitino

$$\begin{pmatrix} N_{11} & N_{12} & N_{13} & N_{14} \\ N_{21} & N_{22} & N_{23} & N_{24} \\ N_{31} & N_{32} & N_{33} & N_{34} \\ N_{41} & N_{42} & N_{43} & N_{44} \end{pmatrix} \quad (2.3)$$

$$\chi_1^0 = N_{11}\tilde{B} + N_{12}\tilde{W} + N_{13}\tilde{H}_d^0 + N_{14}\tilde{H}_u^0 \quad (2.4)$$

## 2.4.2 MSSM Lagrangian

The MSSM lagrangian consists of two parts:

$$\mathcal{L}_{\text{MSSM}} = \mathcal{L}_{\text{SUSY}} + \mathcal{L}_{\text{SOFT}} \quad (2.5)$$

Where the first part is just a generalization of the SM lagrangian, and the second part contains the supersymmetry breaking mechanism. The corresponding *superpotential* used in  $\mathcal{L}_{\text{rmSUSY}}$  is of the form:

$$W = \epsilon_{ij}(y_{ab}^U Q_a^j U_b^c H_2^i + y_{ab}^D Q_a^j D_b^c H_1^i + y_{ab}^L L_a^j E_b^c H_1^i + \mu H_1^i H_2^j) \quad (2.6)$$

Where  $Q$ ,  $U$  and  $D$  represent the squark superfields,  $L$  and  $E$  the **slepton** ones,  $y^{U,D,L}$  are the Yukawa couplings and  $H_{1,2}$  the Higgs superfields. The only qualitative difference with respect to  $\mathcal{L}_{\text{SM}}$  is the last term, that accounts for the Higgs mixing. Additional lepton violating leptonic or baryonic number can be added to this superpotential in RPV models.

311      Because of gauge invariance, supersymmetry breaking in the MSSM cannot happen  
 312      spontaneously. Thus, an explicit term accounting for this breaking appears in the la-  
 313      grangian,  $\mathcal{L}_{\text{SOFT}}$ , where *soft* refers to the dimension 2 and 3 of the operators. This  
 314      breaking is the responsible for the SM particles not to be degenerate with their respective  
 315      superpartners, as mentioned earlier, having these larger masses. **Nonetheless this SUSY**  
 316      **breaking, some properties from it remain.**

317      A possible alternative to the soft-explicit supersymmetry breaking explained before  
 318      consists in spontaneous symmetry breaking for a given scale,  $\Lambda_s$ , with a sector of fields  
 319      that belong to a *hidden* sector and communicates with the *observable* sector with the  
 320      exchange of fields known as *messengers*, as represented schematically in 2.1. This type of  
 321      supersymmetry has been extensively searched for in several experiments, with negative  
 322      results so far REFERENCES.

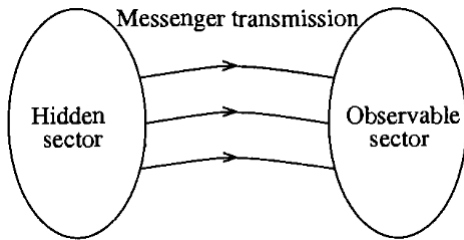


Figure 2.1: Schematic view of the hidden sector

323      The MSSM has 124 free parameters, namely:

- 324      • 18 SM parameters
- 325      • 1 Higgs sector parameter, analogue to the SM Higgs mass
- 326      • 5 real and 3 CP violating phases in the gaugino/higgsino sector
- 327      • 21 squark and slepton masses
- 328      • 36 real mixing angles for squark and slepton mass eigenstates
- 329      • real mixing angles for squark and slepton mass eigenstates

330      The complex phases are usually considered small. Some experiments are capable  
 331      of measuring some of these parameters individually. Nevertheless, in general this large  
 332      amount of degrees of freedom spoil the predictive power of the model. In order to reduce  
 333      it, *mass universality* is imposed to some particular cases that will be further discussed  
 334      in the next section. This implies that all spin 0 (1/2) sparticle masses are equal to  
 335      a universal value  $m_0$  ( $m_{1/2}$ ). Another way of reducing the number of parameters is  
 336      specifying the mechanism that breaks the symmetry, either with gauge fields (Gauge  
 337      Mediated Supersymmetry Breaking, GMSB)[40] or as a consequence of a dominating  
 338      super-Weyl anomaly (Anomaly Mediated Supersymmetry Breaking, AMSB). Some of  
 339      this models will be explained in more detail later.

### 340 2.4.3 CMSSM

341 The *constrained* MSSM (hereafter CMSSM) is one of the most popular subversions of  
 342 the MSSM. In this model, the concept introduced earlier of mass universality is imposed,  
 343 meaning that for a given GUT scale  $\Lambda \sim 2 \times 10^{16}$ GeV:

- 344 • All scalar masses are set to  $m_0$

$$345 M_l^2(\Lambda) = M_{\tilde{q}}^2(\Lambda) \equiv m_0^2 I_3 \quad (2.7)$$

$$345 M_{\tilde{u}}^2(\Lambda) = M_{\tilde{e}}^2(\Lambda) = M_{\tilde{d}}^2(\Lambda) \equiv m_0^2 I_3 \quad (2.8)$$

$$346 m_{H_u}^2 = m_{H_d}^2 = m_0^2 \quad (2.9)$$

347 Where  $I_3$  represents the 3x3 identity matrix

- 348 • All gaugino masses are set to  $m_{1/2}$

$$m_{\tilde{B}}(\Lambda) = m_{\tilde{W}}(\Lambda) = m_{\tilde{g}}(\Lambda) \equiv m_{1/2} \quad (2.10)$$

- 349 • The trilinear couplings are set to  $A_0$

$$A_{\tilde{u}}(\Lambda) = A_{\tilde{e}}(\Lambda) = A_{\tilde{d}}(\Lambda) \equiv A_0 I_3 \quad (2.11)$$

350 These requirements lead to the following relation between the gaugino masses at the TeV  
 351 scale:

$$M_1 = \frac{\alpha_s}{\alpha} \sin \theta_W^2 M_2 = \frac{3}{5} \cos \theta_W^2 M_1 \quad (2.12)$$

352 Which translates into the ratios:

$$M_1 : M_2 : M_3 \approx 1 : 2 : 6 \quad (2.13)$$

353 With these conditions, the CMSSM ends up with a set of 5 free parameters:  $(m_0,$   
 354  $m_{1/2}, A_0, \tan \beta = \frac{v_1}{v_2}, \text{sign}(\mu))$ . The last one refers to the sign of the Higgs self-coupling  
 355 in the superpotential, while  $\tan \beta = \frac{v_u}{v_d}$  is the ratio of the vevs from the Higgs doublet.  
 356 Since gaugino masses run in the same way as the gauge couplings, within the CMSSM  
 357 the LSP is generally the lightest neutralino. The status of CMSSM in light of current  
 358 experimental constraints will be reviewed in chapter 2.4.3.

359 A more restrictive version of CMSSM exists, mSUGRA, where supersymmetry breaking  
 360 is gravity-mediated. Within this model, the gravitino mass is equal to the scalar  
 361 mass,  $m_{3/2} = m_0$ , thus adding a new constraint on the parameters. On the contrary,  
 362 there are models with more relaxed conditions. An example of these is when the univer-  
 363 sality condition on the Higgs masses is not applied, hence having Non Universal Higgs  
 364 Masses (NUHM1 and NUHM2 [28]). This adds two extra free parameters,  $M_A$ , the mass  
 365 of the CP-odd neutral higgs,  $A^0$ , and  $\mu$ , the Higgs self-coupling.

### 366 2.4.4 AMSB

367 In the Anomaly Mediated SUSY Breaking (AMSB), the supersymmetry breaking occurs  
 368 mainly via a loop-induced super-Weyl anomaly. In some scenarios, such breaking is  
 369 assumed to take place in a different *brane* from respect to the *observable* sector, within  
 370 the context of *Extra Dimensions*. The anomaly-mediated SUSY breaking parameters are  
 371 RG-invariant, being the corresponding masses given as functions of the gauge and Yukawa  
 372 coupling constants. This helps avoiding a SUSY flavor problem.

373 To generate the weak scale masses of the sparticles, the gravitino mass,  $m_{3/2}$  must be  
 374 fairly heavy (of the order of tens of TeV). Ths, it's not affected by Big-Bang nucleosyn-  
 375 thesis bounds. The gaugino masses  $M_{1,2,3}$  are suppressed by loop factors relative to this  
 376 gravitino mass, and the wino-like states are lighter than the bino-like ones. The following  
 377 approximate ratios hold:

$$|M_1| : |M_2| : |M_3| \approx 2.8 : 1 : 7.1 \quad (2.14)$$

378 Within this model, the soft supersymmetry breaking terms can be computed from the  
 379 gravitino mass, and the soft terms are real and both flavor and renormalization group  
 380 invariant. Despite its many advantages, AMSB has a strong drawback: renormalization  
 381 leads to negative squared masses for sleptons. There are several proposals to cope with  
 382 this, like the *minimal* AMSB (mAMSB), that will be discussed further in 2.4.4.1.

#### 383 2.4.4.1 mAMSB

384 In mAMSB, with the purpose of avoiding *tachyonic* sleptons in AMSB models, a constant  
 385 contribution ( $m_0^2$ ) is added to all squared scalar masses at the grand unified theory (GUT)  
 386 scale,  $\Lambda_{GUT} \sim 2^{16}\text{GeV}$ . This addition can be mostly related to the presence of extra  
 387 field(s)in the bulk [29], and destroys the aforementioned RG invariance, desirable in order  
 388 to fulfill the **Flavour-Changing-Neutrl-Current (FCNC)** constraint. Nevertheless some  
 389 characteristics are inherited.

390 Both the  $\mu$  term and the to match soft bilinear Higgs coupling,  $B_\mu$  are parameters of  
 391 this model too. Given that they determine the Higgs potential:

$$G_F = [2\sqrt{2}(v_2^2 + v_1^1)]^{-1} \simeq 1.7 \times 10^{-5}\text{GeV}^{-2} \quad (2.15)$$

392 The minimization of 2.15 leads to the determination of such paramaters as a function  
 393 of  $\tan\beta$ . Therefore, the mAMSB model has 3 continuous free parameters,  $(m_0, m_{3/2},$   
 394  $\tan\beta)$ . In addition, the sign of the Higgsino mixing parameter,  $\mu$ , is also free. The  
 395 trilinear soft SUSY-breaking mass terms, like the gaugino masses, are determined by  
 396 anomalies, therefore they are proportional to the gravitino mass.

397 This model has some interesting features, such as:

- 398 • The left and right sleptons are nearly degenerate ( $m_{\tilde{l}_R} \approx m_{\tilde{l}_L}$ ), being stau the  
 399 lightest slepton. As a consequence, the third and second generation *L-R* mixing  
 400 angles become significantly larger, reaching the maximal limit at large  $\tan\beta$ .

- The lightest chargino and neutralino are also almost degenerate ( $m_{\tilde{\chi}_1^\pm} \approx m_{\tilde{\chi}_1^0}$ ). This induces to a relatively long-lived  $\tilde{\chi}_1^\pm$ , that decays to a soft charged pion.
- Sfermion masses increase linearly with  $m_0$ , but also depend on the precise value of  $m_{3/2}$ .
- The mass hierarchy between sleptons and gauginos depends on the input parameters.
- The squark masses are typically very heavy, as they grow with  $g_3^4 m_{3/2}^2$ .
- The stop masses are relatively high, because of the Higgs mass and the relatively low values of the trilinear couplings.
- The LSP (lightest neutralino) can be wino-, Higgsino-like or mixed-

The most up-to-date likelihood analysis of this model in light of current constraints can be found in [30]. A complete spectra at the best-fit points for the two signs of  $\mu$  are shown in Fig. 2.2 in the wino-LSP case, where branching ratios exceeding 20% are indicated by dashed lines. As it can be seen, a relatively heavy spectrum is favoured in the global fit.

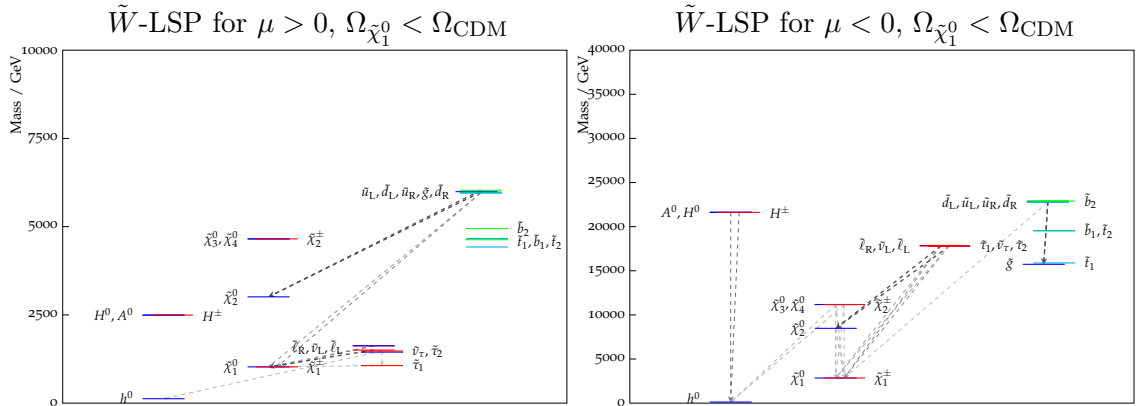


Figure 2.2: The spectra of the best-fit points for  $\mu > 0$ , allowing the LSP to contribute only part of the cold dark matter density. The wino-like LSP (lower) best-fit point is shown, indicating all the decay modes with branching ratios (BRs) above 20%, with darker shading for larger BRs, and the colours of the horizontal bars reflect particles' electric charges.

The preferred regions of the  $(m_0, m_{3/2})$  planes for  $\mu > 0$  (left panel) and  $\mu < 0$  (right panel) are shown in the upper panels of Fig 2.3<sup>1</sup>. It is seen that the wino region allowed at the 95% CL extends to smaller  $m_{3/2}$  for both signs of  $\mu$ , and also to larger  $m_0$  at  $m_{3/2} \gtrsim 300$  TeV when  $\mu < 0$ . The 68% CL region extends to much larger  $m_0$  and  $m_{3/2}$

<sup>1</sup>The sharp boundaries at low  $m_0$  in the upper panels of Fig 2.3 are due to the stau becoming the LSP, and the narrow separation between the near-horizontal portions of the 68 and 95% CL contours in the upper right panel of Fig. 2.3 is due to the sharp upper limit on the CDM density.

419 when  $\mu < 0$ , and the best-fit point also moves to larger masses than for  $\mu > 0$ , though  
420 with smaller  $\tan \beta$ .

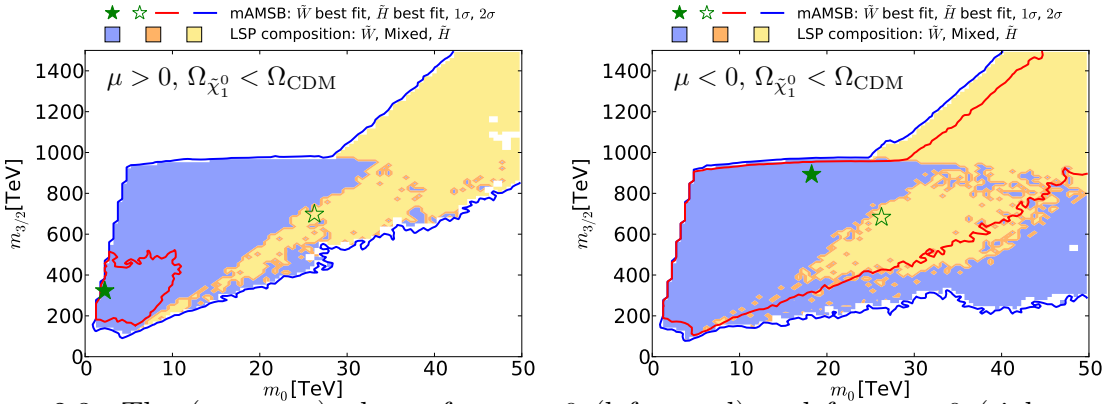


Figure 2.3: The  $(m_0, m_{3/2})$  planes for  $\mu > 0$  (left panel) and for  $\mu < 0$  (right panel), allowing the  $\tilde{\chi}_1^0$  to contribute only part of the CDM density. The best-fit points for the two signs of  $\mu$  are indicated by green stars, closed in the wino-like region and open in the Higgsino-like region.

421 Fig 2.4 displays the cross section for spin-independent scattering on a proton,  $\sigma_p^{\text{SI}}$  ,  
422 versus the neutralino mass, for the case in which the LSP is allowed to contribute only  
423 a fraction of the CDM density. As previously, the left plane is for  $\mu > 0$ , the right plane  
424 is for  $\mu < 0$ , the 1 and  $2\sigma$  CL contours are shown as red and blue lines, and the wino-  
425 and Higgsino-LSP regions are shaded in pale blue and yellow. The pale-green-shaded  
426 region represents the range of  $\sigma_p^{\text{SI}}$ ) excluded at the 95% CL by a combination of the latest  
427 PandaX and LUX results [?, ?], while the purple and blue lines show the prospective  
428 sensitivities of the LUX-Zeplin (LZ), XENON1T and XENONnT experiments [?, ?]. Also  
429 shown, as a dashed orange line, is the neutrino ‘floor’, below which astrophysical neutrino  
430 backgrounds would dominate any DM signal [?] (grey region). The plot shows good  
431 prospects for future DM direct detection experiments when  $\mu > 0$ , with only a small  
432 fraction of the parameter space lying below the neutrino ‘floor’. However, when  $\mu < 0$   
433  $\sigma_p^{\text{SI}}$ ) may fall considerably below the ‘floor’, because of cancellations [?] in the scattering  
434 matrix element.

#### 435 2.4.5 Renormalization Group equations

436 The renormalization group equations(RGE) are applied within the MSSM to describe the  
437 evolution of gauge couplings, superpotential parameters and soft terms from a given *input*  
438 scale up to near the *electroweak* scale. The method used in the SM (dimensional regu-  
439 larization, DREG) cannot be used within SUSY, as it introduces a spurious violation of  
440 this symmetry. The most common method for it is the dimensional reduction, DRED,  
441 with modified minimal subtraction ( $\overline{\text{DR}}$ ), as opposed to DREG with modified minimal  
442 subtraction ( $\overline{\text{MS}}$ ). Figure 2.5 compares the RG evolution of the coupling constants both

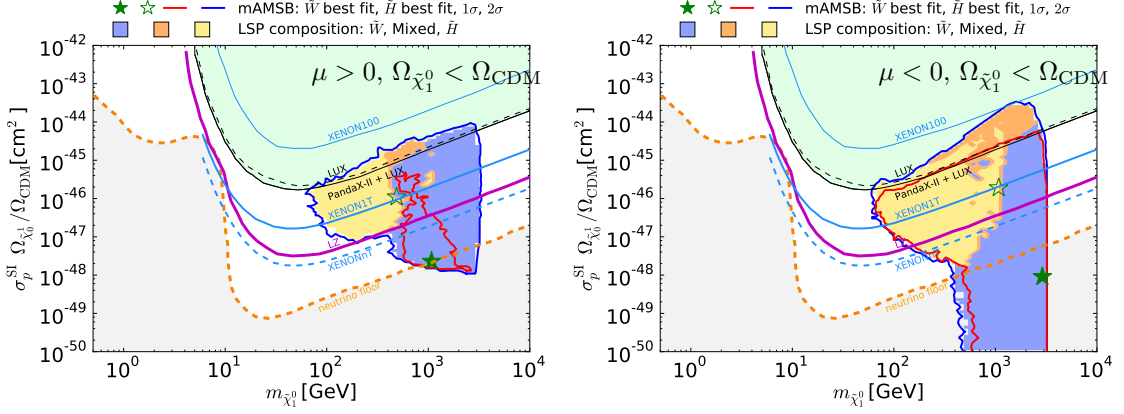


Figure 2.4: The  $(m_{\tilde{\chi}_1^0}, \sigma_p^{SI})$  planes in the mAMSB for  $\mu > 0$  (left) and  $\mu < 0$  (right) in the case when the LSP only accounts for a fraction of the CDM density. The best-fit points for the two signs of  $\mu$  are indicated by green stars, closed in the wino-like region and open in the Higgsino-like region.

in the SM and in the MSSM. As it can be seen, a better match at the electroweak scale is achieved within the MSSM, as discussed in 2.1.

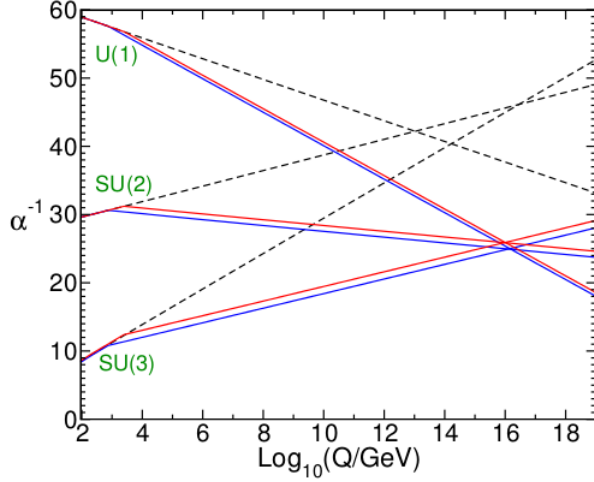


Figure 2.5: Two-loop renormalization group evolution of the inverse gauge couplings  $\alpha_a^{-1}(Q)$  in the SM (dashed lines) and the MSSM (solid lines). In the MSSM case, the sparticle masses are treated as a common threshold varied between 750 GeV and 2.5 TeV, and  $\alpha_3(m_Z)$  is varied between 0.117 and 0.120 [31].

The RGE are derived using what is known as the *supersymmetric non-renormalization theorem*, that implies that the logarithmically divergent contribution to a particular pro-

cess can always be written in terms of wave-function renormalizations [31]. One consequence derived from this is that for a given value of  $\mu$  at tree-level, RG corrections to it will be proportional to the parameter itself and some combinations of dimensionless couplings, thus avoiding very large radiative corrections that could greatly enhance  $\mu$ .

Within this framework, it is assumed that gauge couplings unify at a given scale,  $\Lambda$ . Hence, gaugino masses are considered to be unified near that scale as well (which come naturally in GUT models):

$$\frac{M_1}{g_1^2} = \frac{M_2}{g_2^2} = \frac{M_3}{g_3^2} = \frac{m_{1/2}}{g_\Lambda^2} \quad (2.16)$$

where  $g_\Lambda$  is the unified gauge coupling at  $\Lambda$ , and  $m_{1/2}$  the unification value for the gaugino masses.

Some more consequences of the RGE are listed below.

1. Because they are not protected by the supersymmetric non-renormalization theorem, the soft parameters that describe the Yukawa couplings don't vanish at the electroweak scale, even if they are zero at the input scale.
2. The scalar squared masses will be almost diagonal, with the second family squarks and sleptons very nearly degenerate. The third-family squarks and sleptons will get normalized differently
3. The scalar squared-mass parameters grow as they are RG-evolved, due to the gaugino masses effect on the RGE. Therefore, large masses can be obtained at the electroweak scale even if these are small or even zero at the weak scale.
4. Because of the contributions they receive from the RGE, the Higgs squared masses generally decrease at the electroweak scale with respect to the input scale. This can lead to a negative value of  $m_{H_u}^2$ , with the consequence of a non-zero Higgs vev. This effect increases as the top Yukawa coupling does.
5. If the gaugino mass parameters  $M_1$ ,  $M_2$  and  $M_3$  have non-zero values for a given input scale, all the soft terms will be generated via RGE. Otherwise, gauginos would be extremely light, causing the model to be inviable due to experimental measurements.

## 2.5 RPV Models

R-parity (or matter parity) conservation can be justified in terms of a grand unified theory or as a consequence of a residual symmetry of a superstring vacuum. However, it is not necessarily the existing scenario. Additional terms can be added to the superpotential in 2.6 that violate baryon number (B) or lepton number (L), namely: **check consistency with other equation**

$$W_{\Delta L=1} = \frac{1}{2} \lambda^{ijk} L_i L_j \bar{e}_k + \lambda'^{ijk} L_i Q_j \bar{d}_k + \mu'^i L_i H_u \quad (2.17)$$

480

$$W_{\Delta B=1} = \frac{1}{2} \lambda''^{ijk} \bar{u}_i \bar{d}_j \bar{d}_k \quad (2.18)$$

481 Where  $i = 1, 2, 3$ , depending on the fermionic family. Terms in 2.17 (??) violate lepton  
 482 (baryon) number by 1 unit. If both terms accompanying  $\lambda'$  and  $\lambda''$  were to exist (without  
 483 suppression), proton decays to final products such as  $e^+ \pi^0$  would be feasible. Nevertheless,  
 484 the lifetime for the proton is known to be  $> 10^{34}$  years [32]. This, together with more  
 485 experimental evidence , leads to the conclusion that one of these couplings must be zero or  
 486 very small, being RPV models either B-violating or L-violating, with experimental upper  
 487 bounds existing for both couplings.

488 One example of such type of RPV model is a scenario where R-parity is replaced by  
 489 a *baryon triality*, defined in 2.19.

$$Z_3^B = \exp 2\pi i[B - 2Y]/3 \quad (2.19)$$

490 The corresponding symmetry establishes that the product of the baryon trialities of the  
 491 particles in any term in the superpotential must be 1. With this, proton decay and  
 492 neutron-antineutron oscillation are forbidden processes, as they would violate triality.  
 493 This symmetry does allow the LSP to decay.

494 Another alternative is the spontaneous R-parity symmetry breaking by particles, like  
 495 sneutrinos in the context of MSSM( [33], [34]). Strong experimental bounds exist on  
 496 this ref?. Either way, RPV scenarios greatly change the SUSY signatures in colliders,  
 497 allowing processes like single sfermion production or exchange of sfermions to happen.

### 498 2.5.1 Consequences of RPV

499 Numerous consequences can be derived in the different possible RPV models. Some of  
 500 them are briefly addressed below.

- 501 1. Within some of these models, there can be *leptogenesis* (asymmetry between leptons and antileptons in the early Universe), that would lead to the current matter-  
 502 antimatter asymmetry discussed in 2.1.
- 503 2. The LSP can have color/charge, while fulfilling current constraints, and no longer  
 504 needs to be stable.
- 505 3. Some RPV models include a seesaw mechanism that provides neutrinos with mass,  
 506 while including sterile neutrinos [35].
- 507 4. A possible candidate for DM is the heavy gravitino, superpartner of the graviton.  
 508 Even though it is unstable, its decay is heavily suppressed by the gravitational  
 509 coupling, resulting in a lifetime bigger than the age of the Universe.

## 511 2.6 Experimental searches

512 Many experimental efforts have been done in the search for supersymmetry, both via direct  
 513 searches of supersymmetric particles and by looking for indirect effects. A summary of  
 514 the former is represented in figures 2.6 and 2.7, where bounds on the masses are set for  
 515 different models, with data from ATLAS and CMS experiments, described in chapter 4.

516 With these experimental constraints, together with other experimental measurements,  
 517 such as DM direct detection results ?? global fits can be made for different SUSY mod-  
 518 els. A specific case will be discussed in chapter 7. More of these fits can be found  
 519 in [36], [37], [38], [39], [30], [40], [41].

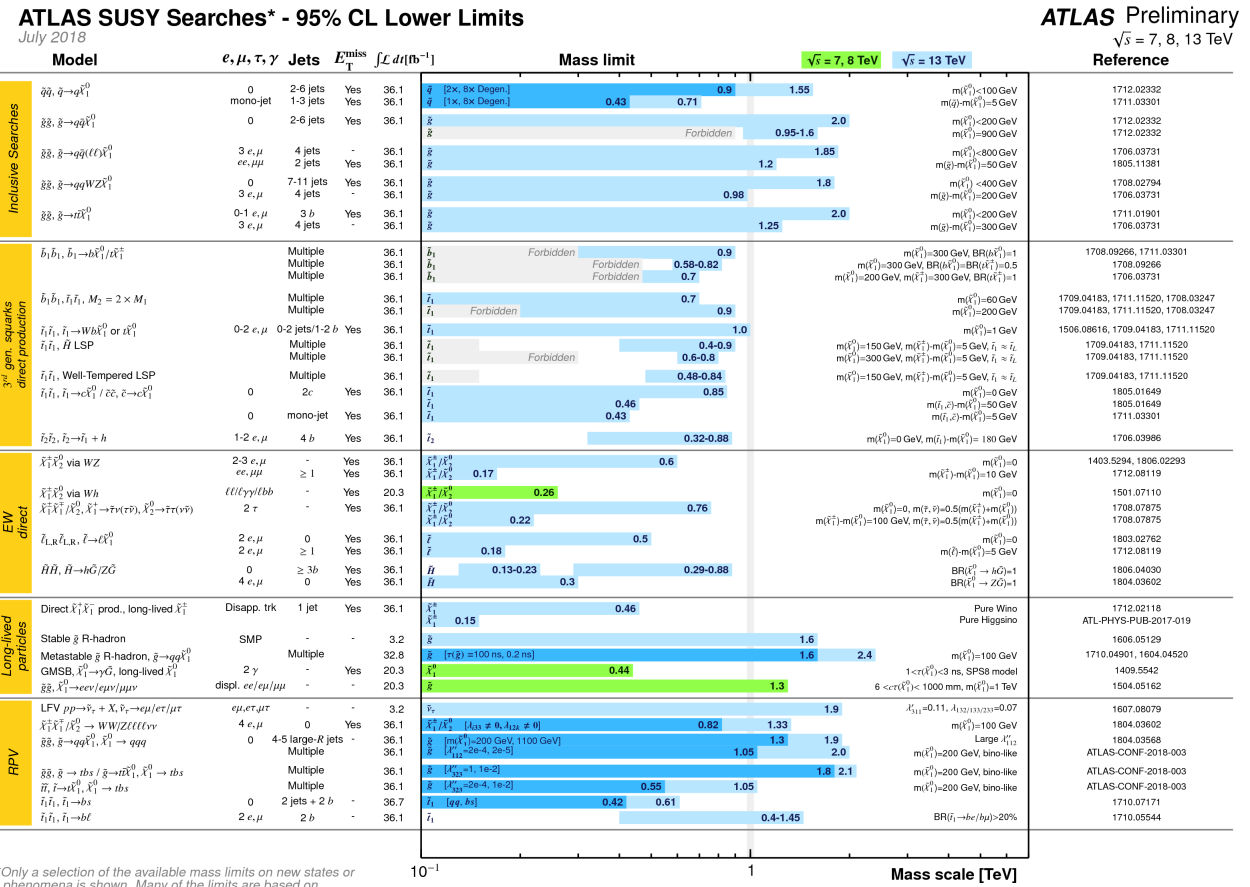


Figure 2.6: Experimental status of SUSY searches in ATLAS ref

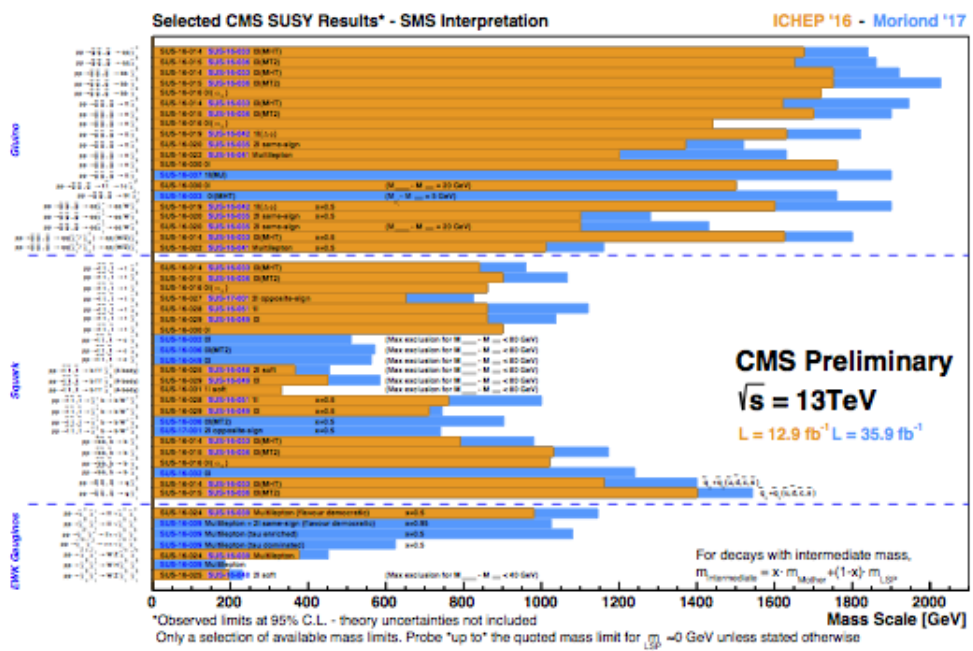


Figure 2.7: Experimental status of SUSY searches at CMS [ref](#)

# 520 Chapter 3

## 521 Low E in SUSY (MFV)

### 522 3.1 Motivation for MFV

523 The success of the SM in predicting flavour and CP violation effects leads to thinking  
524 that NP has to follow its pattern. Otherwise, experimental evidence of additional flavour  
525 violating structures should have appeared by now. Additionally, the hierarchy problem  
526 suggests  $\Lambda < \text{TeV}$ , while in the case in which flavour violation is generated generically in  
527 SUSY,  $\Lambda \sim \mathcal{O}(\text{TeV})$  [42]. An effective field theory (henceforth, EFT) becomes necessary in  
528 order to address the favour problem in SUSY, where the flavour violation predictions can  
529 largely exceed the experimental constraints and are *a priori* unrelated to the SM sources  
530 [43]. Minimal Flavour Violation (hereafter MFV) requires all flavour and CP-violating  
531 interactions to be governed by the known structure of the SM Yukawa couplings [44]  
532 in the low-energy regime. Hence, in any SM extension the amount of FCNC and CP  
533 violating process should be ruled by these. As for supersymmetry, MFV holds under  
534 the assumption of *mass universality*, and if the trilinear soft terms are proportional to  
535 the Yukawa couplings at the GUT scale. This MFV can be seen as the remnant of an  
536 underlying favor symmetry at the  $\Lambda$  scale [42].

### 537 3.2 MFV EFT

538 Minimal Flavour Violation (hereafter MFV) is constructed as a low-energy EFT [44],  
539 within which the SM is contained. Its main feature is that the only source of  $SU(3)^5$   
540 flavour symmetry breaking are the background values of fields transforming under the  
541 flavour group like the ordinary Yukawa couplings [44]. In the SM, the  $U(3)^5$  flavour  
542 symmetry is the largest group of unitary field transformations that commutes with the  
543 gauge group. This can be decomposed [44] as:  $U(3)^5 = [SU(3)]^5 \otimes U(1)_E$ , more details

(3.1)

544 Notice that the baryon, lepton and hypercharge numbers are not modified by Yukawa in-  
545 teractions. The  $U(3)^5 = [SU(3) \otimes U(1)]^5$  check group is broken by Yukawa interactions.

546 Flavour invariance is recovered introducing dimensionless auxiliary fields,  $Y_U$ ,  $Y_D$  and  $Y_E$   
 547 transforming under  $SU(3)_q^3 \otimes SU(3)_l^3$  promoting to **spurion** fields in order for flavour  
 548 violation to appear [43], thus leading to the Yukawa interaction terms of the SM lagrangian  
 549 as discussed in 2.1, consistent with flavour symmetry. These term can be rotated such  
 550 that:

551

$$Y_d = \hat{Y}_d, Y_e = \hat{Y}_e, Y_u = V^\dagger \hat{Y}_u \quad (3.2)$$

552 denoting  $\hat{Y}$  diagonal matrices, and  $V$  being the CKM matrix. The notation in [44] is  
 553 followed.

554 In MFV all higher-dimensional operators are constructed from SM and  $Y$  fields, and  
 555 are invariant under CP and the flavour group  $G_F$ . Therefore, they can be rewritten  
 556 in terms of the SM Yukawa couplings [43]. Given that the top Yukawa coupling is  
 557 considerably large with respect to the others, the only relevant non-diagonal structure in  
 558 the low  $\tan\beta$  regime is obtained contracting two  $Y_u$ , hence having:

$$(\lambda_{FC})_{ij} = \begin{cases} (Y_u Y_u^\dagger)_{ij} \approx \lambda_t^2 V_{3i}^* V_{3j} & i \neq h \\ 0 & i = j \end{cases} \quad (3.3)$$

559 where  $\lambda_t = (\hat{Y}_u)_{33}$  and subleading effects on the r.h.s of 3.3 are suppressed by powers of  
 560  $m_c/m_t$  [43] as the effective coupling ruling all FCNC processes with external down-type  
 561 quarks. Such processes are governed by  $\Delta F = 2$  and  $\Delta F = 1$  (Higgs field, gauge fields  
 562 and four-fermion) operators. Further details on this operators can be found in [44].

### 563 3.3 MFV SUSY

564 Consider the MSSM (where R-parity is conserved) as a low-energy EFT. Differently to  
 565 what happens in other non-supersymmetric MFV scenarios, there are renormalizable  
 566 terms with non-trivial flavour structure, besides the ordinary Yukawa couplings. Within  
 567 MFV, the off-diagonal entries in the soft terms (the genuinely new sources of flavour  
 568 violation in the MSSM) are CKM-like [43].

569 The squark mass matrices after the electroweak breaking and using the soft terms, 3.9  
 570 and 3.10 have the form

571

$$\tilde{M}_U^2 = \begin{pmatrix} \tilde{m}_{Q_L}^2 + Y_u Y_u^\dagger v_u^2 + (1/2 - 2/3 \sin \theta_W^2) M_Z^2 \cos 2\beta & (A_u - \mu Y_u \cot \beta) v_u \\ (A_u - \mu Y_u \cot \beta)^\dagger v_u & \tilde{m}_{U_R}^2 + Y_U^\dagger Y_u v_u^2 + 2/3 \sin \theta_W^2 M_Z^2 \cos 2\beta \end{pmatrix} \quad (3.4)$$

572

$$\tilde{M}_D^2 = \begin{pmatrix} \tilde{m}_{Q_L}^2 + Y_d Y_d^\dagger v_d^2 + (1/2 - 1/3 \sin \theta_W^2) M_Z^2 \cos 2\beta & (A_d - \mu Y_d \tan \beta) v_d \\ (A_d - \mu Y_d \tan \beta)^\dagger v_d & \tilde{m}_{D_R}^2 + Y_D^\dagger Y_d v_d^2 - 1/3 \sin \theta_W^2 M_Z^2 \cos 2\beta \end{pmatrix} \quad (3.5)$$

573 According to MFV, the squark masses and trilinear couplings in 3.4,3.5 can be written  
 574 as follows [44]:

$$\tilde{m}_{Q_L}^2 = \tilde{m}^2(a_1\mathbb{I} + b_1Y_uY_u^\dagger + b_2Y_dY_d^\dagger + b_3Y_dY_d^\dagger Y_uY_u^\dagger + b_4Y_uY_u^\dagger Y_dY_d^\dagger) \quad (3.6)$$

$$\tilde{m}_{U_R}^2 = \tilde{m}^2(a_2\mathbb{I} + b_5Y_uY_u^\dagger) \quad (3.7)$$

$$\tilde{m}_{D_R}^2 = \tilde{m}^2(a_3\mathbb{I} + b_6Y_dY_d^\dagger) \quad (3.8)$$

$$A_U = A(a_4\mathbb{I} + b_7Y_dY_d^\dagger)Y_u \quad (3.9)$$

$$A_D = A(a_5\mathbb{I} + b_8Y_uY_u^\dagger)Y_d \quad (3.10)$$

579 Where  $\tilde{m}$  and  $A$  set the mass scale of the soft terms,  $a_i$  and  $b_i$  are numerical coefficients  
 580 and  $\mathbb{I}$  is the 3x3 identity matrix. Quadratic terms of the first two families of Yukawas  
 581 have been neglected. In the limit of low  $\tan\beta$  the terms quadratic in  $Y_d$  can be dropped  
 582 too.

583 Under the assumption of mass universality and proportionality of trilinear terms, the  
 584  $b_i$  coefficients are zero at the GUT scale  $\Lambda$  and generated via RGE.

585 It is worth noticing from 3.4, 3.5 the physical squark masses are not degenerate under  
 586 the MFV assumption, but the mass splitting is severely constrained.

587 The mass matrices in 3.5 and 3.4 are then diagonalized using the expansions in  
 588 3.6,3.7,3.8,3.9 and 3.10. Analogously to the SM case, it is possible to change to a *super-*  
 589 *CKM* basis, where:

$$\hat{m}_u = \frac{v_d}{\sqrt{2}}\hat{Y}_u, \quad \hat{m}_d = -\frac{v_u}{\sqrt{2}}\hat{Y}_d \quad (3.11)$$

591 Notice that in this basis the Yukawa matrices are diagonal, but the trilinear couplings  
 592 and the mass-matrices are still non-diagonal. Unitary matrices  $Z_U$  and  $Z_D$  are needed in  
 593 order to change to a mass eigenstate basis. In the MFV scenario the off-diagonal entries  
 594 of this matrices are not zero, but CKM-like [43].

595 equation?, MIA?

## 596 3.4 MFV R-parity

597 MFV can be used instead of the R-parity conservation assumption [45]. Under this  
 598 scenario the baryon number can be violated, while the lepton number violation is strongly  
 599 suppressed and only possible with massive neutrinos. This is strongly discouraged by the  
 600 proton lifetime, and bounds from  $n - \bar{n}$  oscillation and dinucleon decay. In some specific  
 601 models, extra suppression from the neutrino sector can help further alleviate this bounds.  
 602 Under this models R-parity is obtained as an approximate symmetry as a side effect. The  
 603 LSP decays fast and is not necessarily neutral, it can be a stop or sbottom (decaying to 2  
 604 bodies), a neutralino or chargino (decaying to 3 bodies) or a slepton (with the subsequent  
 605 4 body decay). A possible DM candidate is the gravitino.

606 **3.5 Characteristics**

607 Given that the top Yukawa coupling is much larger than the others, in MFV all flavour-  
608 changing effective operators are proportional to the same non-diagonal structure. This  
609 greatly affects the **predictability** of this model, as will be discussed in 3.7. Within this  
610 approach, the squark masses in the physical eigenbasis are not degenerate, but the induced  
611 flavour violation is described in terms of the usual CKM parameters [44].

612 Strong assumptions need to be made in order to maintain MFV within different SUSY  
613 scenarios, such as supergravity. Other models with different susy-breaking mechanism  
614 (such as AMSB) can alleviate this **conundrum** [44].

615 As will be discussed in 3.8, the Universal Unitarity Triangle does not necessarily hold  
616 within the MFV scenario.

617 Within MFV, both the gaugino masses  $M_{1,2}$  and the Higgs mixing parameter  $\mu$ . Otherwise,  
618 given that they appear in the neutralino and chargino mixing matrices, they would  
619 induce new sources of CP violation, thus violating MFV. An **alternative** approach [46]  
620 consists in assuming the soft SUSY breaking sector to be CP conserving only in the limit  
621 of flavour blindness, while allowing CP violation to happen by the MFV-compatible terms.  
622 In this scenario,  $\mu$  and the gaugino masses are real at low energies and the trilinear cou-  
623 pings (**the only sources of CP-violation**) are strongly hierarchical, being the EDMs **explain**  
624 the most **important** experimental constraints [42]. Nevertheless, in the case in which this  
625 *ansatz* holds not at the low scale, but at the GUT scale (determined by  $\Lambda$ ), complex  
626 parameters can be generated via RGE [42], [46].

627 **3.6 CMFV**

628 The *constrained* MFV (cMFV) is a phenomenological definition of MFV, that uses the  
629 CKM matrix (instead of the Yukawa couplings) as the only source of flavour violation and  
630 restricts the set of relevant operators in the low-energy effective Hamiltonian to the SM  
631 ones [43] ( $\mathcal{Q}_1$ ). Contrarily to the more general definition of MFV proposed in [44], it is  
632 not model-independent. In the limit in which  $b_i \rightarrow 0$  in 3.6-3.10, the cMFV is recovered  
633 from the general MFV. Nevertheless, it is worth mentioning that not all the scenarios are  
634  $\mathcal{Q}_1$ -dominated, as it is assumed in cMFV. Indeed, in the limit of low  $\tan \beta$  it is not always  
635 the case [43].

636 **3.7 Experimental bounds**

637 Generic flavour-violating interactions at  $\Lambda \simeq$  TeV are known to be experimentally ex-  
638 cluded. Within a MFV scenario, it is possible to **relate** various flavour-changing neutral  
639 current (FCNC) processes, such as rare  $B$  and  $K$  decays. Furthermore, CP-violation in  
640 the  $B_s$  system provide an excellent probe where to look for non-CKM sources of flavour  
641 and CP-violation [43]. Besides, this constraint in the soft sector helps further reduce the

642 number of parameters of the MSSM, discussed in [ref](#), thus improving its predictivity.  
 643 Experimental bounds to the generic MFV approach come mainly from:

- 644 •  $\Delta F = 2$  processes that help further improve the precision for CKM matrix elements
- 645 • The inclusive rare decay  $B \rightarrow X_s \gamma$  to constraint the scale of the FCNC operators  
 646 check
- 647 • Rare FCNC decays into a lepton pair, e.g.  $K_L(B) \rightarrow l^+l^-$ ,  $K^+ \rightarrow \pi^+\nu\bar{\nu}$ , that  
 648 provide constraints on several Wilson coefficients
- 649 • Non-leptonic decays, provided electroweak contributions can be properly disentangled  
 650 from the dominant effects coming from tree-level and gluon-penguin amplitudes

## 651 3.8 Unitarity Triangle

652 The *universal unitarity triangle* [47] (henceforth, UUT) represented in [3.1](#) is characterized  
 653 by not having any new operators beyond those present in the SM, hence only valid for  
 654 cMFV models [3.6](#). Depending on the mass regime and the value of  $\tan \beta$ , variations up to  
 655 the percent level can be found in a general MFV scenario [43]. In this triangle, no phases  
 656 are beyond the CKM phase, hence they are not polluted by new physics contributions  
 657 (since the quantities only depend on the CKM parameters). A virtue of the universal  
 658 triangle is that it allows to separate the determination of the CKM parameters from the  
 659 determination of new parameters present in the extensions of the SM, since new physics  
 660 could contribute to the values. As an example, new phases could affect  $\alpha$ ,  $\beta$  and  $\gamma$ .

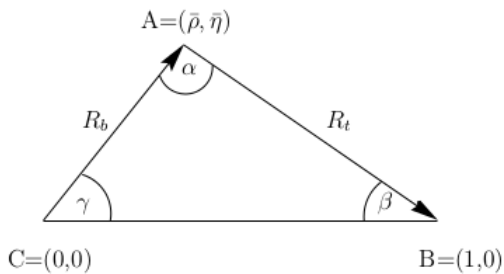


Figure 3.1: Unitarity Triangle, using the Wolfenstein parametrization [ref](#), [PDG](#)

661 Experimental measurements help determining the different values for the elements  
 662 that define the triangle in [3.1](#). Some of these measurements are  $(\Delta M)_d/(\Delta M)_s$  (for  $R_t$ ),  
 663  $\sin 2\beta$ ,  $B_d^0 \rightarrow \phi K_S^0$  (for  $\beta$ ) and tree-level decays (for  $\gamma$ ). As said before, NP contributions  
 664 can affect these values, hence hinting the existence of BSM Physics.

665 In order for this triangle to be *universal* to any SM extension, the requirement that  
 666 new operators don't exist has to be fulfilled. Also, FCNC transitions should be ruled  
 667 by the CKM elements. Hence, only the values of the functions describing top-mediated

668 contributions to box and penguin diagrams can be modified by this new physics [47].  
 669 Under these conditions, the CKM matrix can be determined without further assumption  
 670 on the unknown BSM parameters, with the possibility of disentangling SM contributions  
 671 from NP ones, looking for inconsistencies in the universal triangle or disagreements of the  
 672 data with respect to the predictions made based on the UUT. As an extra feature, these  
 673 parameters are not affected by hadronic uncertainties [47].

The most up-to-date determination of the elements of the UUT can be found in 3.2.

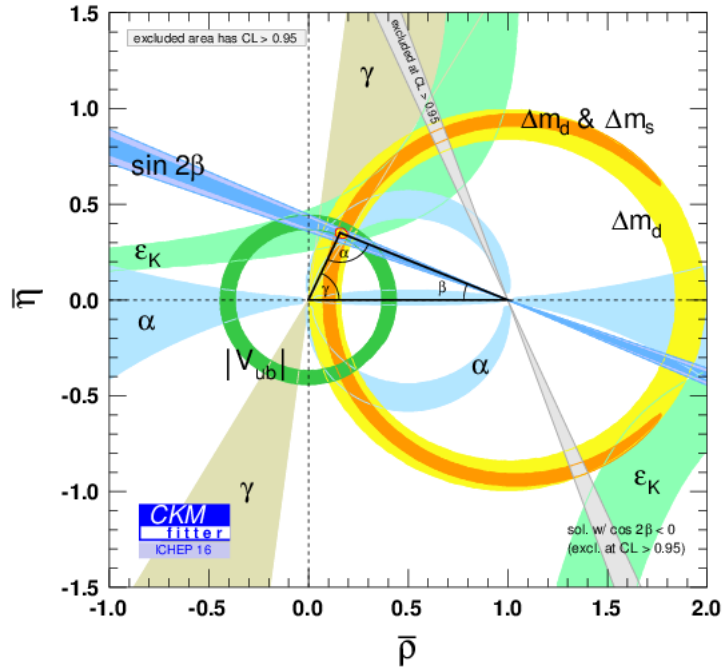


Figure 3.2: Experimental constraints on the UUT, using the Wolfenstein parametrization [48]

674 [?]  
 675

676

# Chapter 4

677

## LHCb

678

### 4.1 LHC

679 The Large Hadron Collider (LHC) is the world's largest and most powerful particle ac-  
 680 celerator. Located at CERN (*European Organization for Nuclear Research*), it consists of  
 681 a 27 km ring of superconducting magnets with a number of accelerating structures, that  
 682 boost the energy of the particles along the way.

683 Two proton beams travelling in opposite directions collide at different points of the  
 684 ring. These are extracted from ion sources, and accelerated in a chain of preaccelerators,  
 685 being the lat stage of such chain the Super Proton Synchrotron (SPS) (see Fig. 4.1). They  
 686 are accelearted to produce collisions at energy in the center of mass ( $\sqrt{s}$ ) of the order of  
 687 the TeV, in order to test the Standard Model and look for New Physics. One of its main  
 688 achievements has been the discovery of the Higgs boson, introduced in [refs](#), the last piece  
 689 of the Standard Model puzzle. Protons are sent on bunches containing up to  $1.5 \times 10^{11}$   
 690 particles, and corssing with a rate of 40 MHz. [check](#) Special runs with heavy ions (e.g.  
 lead) are also made periodically.

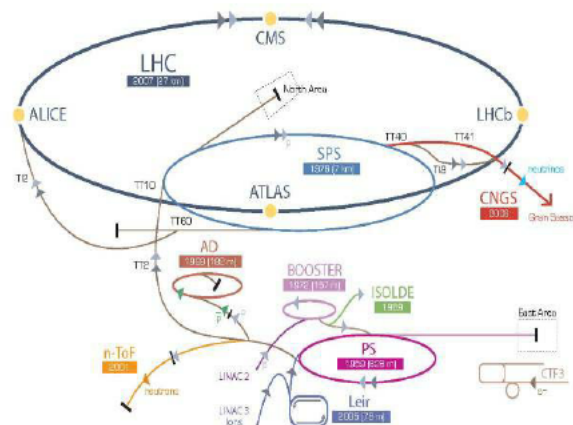


Figure 4.1: The LHC injection complex.

691 Since it first started operating in 2008, it has recorded data with different center of  
692 mass energies, corresponding to 2 data-taking periods: Run 1 (2009-2013,  $\sqrt{s} = 7, 8$  TeV),  
693 and Run 2 (2013-present,  $\sqrt{s} = 13, 14$  TeV). An upgrade of the detectors was made in  
694 between the runs. [check](#)

695 There are four interaction points within the LHC ring, corresponding to the four main  
696 experiments. In these points, the beams cross over to the other beam pipe and collide  
697 under a small angle. These four experiments are: [refs](#)

- 698 • **ATLAS** (*A Toroidal LHC ApparatuS*): a general-purpose  $4\pi$  detector, focused  
699 mainly in the search of New Physics via direct searches and responsible of the  
700 Higgs boson discovery.
- 701 • **CMS** (*Compact Muon Solenoid*): also a general-purpose detector, with a physics  
702 program similar to ATLAS and a more compact layout.
- 703 • **ALICE** (*A Large Ion Collider Experiment*): the smallest of the four detector, it  
704 focuses in heavy-ion studies.
- 705 • **LHCb** (*Large Hadron Collider beauty*): a single-arm forward spectrometer, initially  
706 designed for the study of particles containing  $b$  or  $c$  quarks, now converted into a  
707 general-purpose detector. It is described in more detail in the following section.

## 708 4.2 LHCb

709 The LHCb detector [?, 49] is a single-arm forward spectrometer covering the  
710 pseudorapidity range  $2 < \eta < 5$ , designed for the study of particles containing  $b$  or  $c$   
711 quarks. The detector includes a high-precision tracking system consisting of a silicon-  
712 strip vertex detector surrounding the  $pp$  interaction region [?]\*, a large-area silicon-strip  
713 detector located upstream of a dipole magnet with a bending power of about 4 Tm, and  
714 three stations of silicon-strip detectors and straw drift tubes [?]\* placed downstream  
715 of the magnet. The tracking system provides a measurement of the momentum,  $p$ , of  
716 charged particles with a relative uncertainty that varies from 0.5% at low momentum  
717 to 1.0% at  $200\text{ GeV}/c$ . The minimum distance of a track to a primary vertex (PV), the  
718 impact parameter (IP), is measured with a resolution of  $(15 + 29/p_T)\mu\text{m}$ , where  $p_T$  is  
719 the component of the momentum transverse to the beam, in  $\text{GeV}/c$ . Different types of  
720 charged hadrons are distinguished using information from two ring-imaging Cherenkov  
721 detectors [?]\*. Photons, electrons and hadrons are identified by a calorimeter system  
722 consisting of scintillating-pad and preshower detectors, an electromagnetic calorimeter  
723 and a hadronic calorimeter. Muons are identified by a system composed of alternating  
724 layers of iron and multiwire proportional chambers [?]\*. The online event selection is  
725 performed by a trigger [?]\*, which consists of a hardware stage, based on information  
726 from the calorimeter and muon systems, followed by a software stage, which applies a full  
727 event reconstruction.

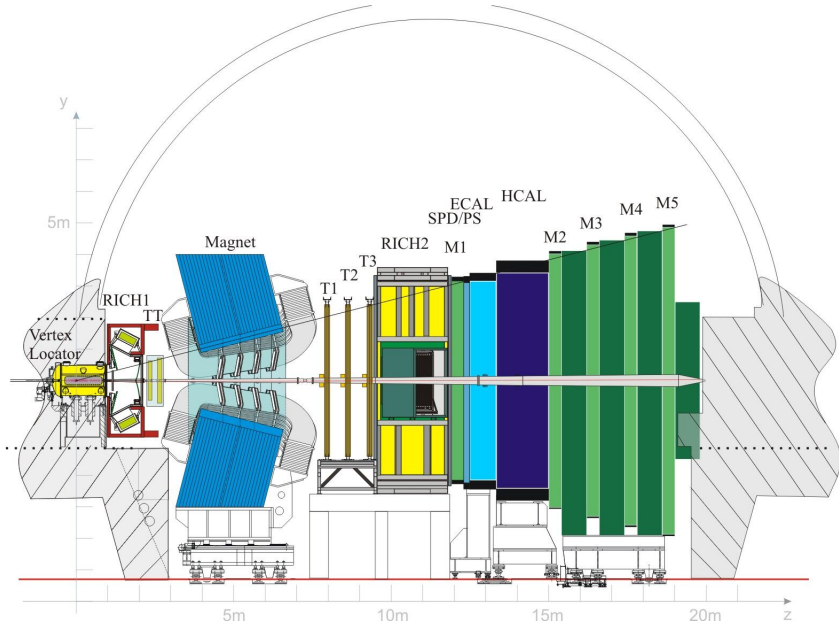


Figure 4.2: LHCb detector

#### **4.2.1 Beam pipe, vacuum chamber and BCM**

The design of the beampipe (4.3) is especially delicate, given the **pseudorapidity** region at which LHCb operates, where there is a high particle density. It is of 19m long and includes the forward window of the VELO and four main conical sectors. The three closer to the interaction point are made of beryllium, as it is highly transparent to particles resulting from collisions. The one left is made of stainless steel because of its good mechanical and vacuum properties. The beampipe support system consists of one fixed and one movable support, in order to reduce the background as much as possible. Two sector valves located at the cavern entrances isolate the experiment beam vacuum from the LHC.

The Beam Conditions Monitor (BCM) takes care of possible problems with the LHC beam conditions, requesting a beam dump if necessary. It monitors the particle flux at two locations close to the vacuum chamber (so as to protect the sensitive LHCb tracking devices). It is connected to the LHCb experiment control system and to the beam interlock controller of the LHC. The two stations consist of eight diamond sensors, with the same dimensions as those of ATLAS and CMS.

#### **4.2.2 Magnet**

LHCb contains a dipole magnet that bends charged particles in order to measure their momenta. The measurement covers the forward acceptance of  $\pm 250\text{mrad}$  vertically and of  $\pm 300\text{mrad}$  horizontally. Two identical conical saddle-shaped coils surround an iron yoke, producing a magnetic field of 4 Tm for tracks of 10 m length (notice that difference parts

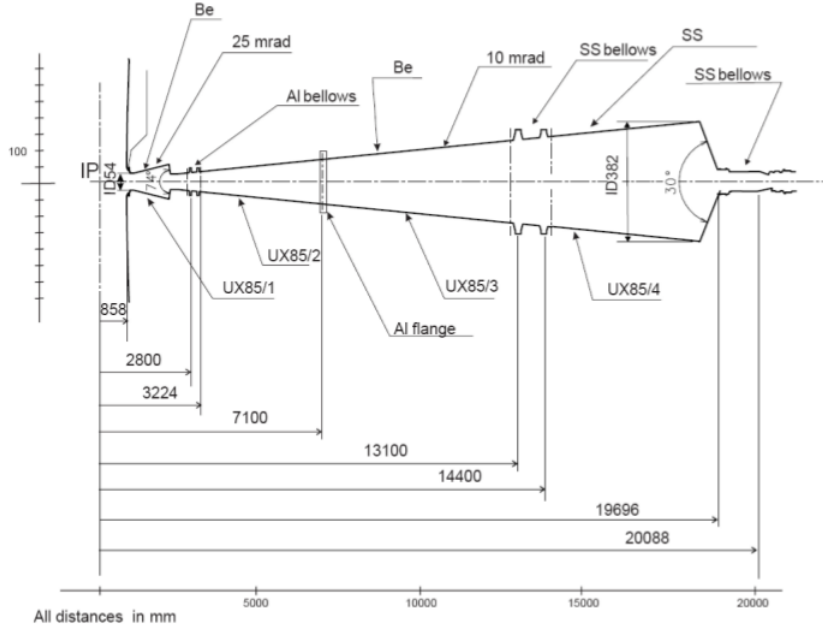


Figure 4.3: LHCb beam pipe

748 of the detector need for different values of the magnetic field). These coils are made of  
 749 pure Al-99.7.

750 The magnet is operated using a Magnet Control System, a well as a Magnet Safety  
 751 System, that takes care of the security of the magnet performance.

752 The precision with which the magnetic field of the magnet is measured needs to be  
 753 of the order of  $10^{-4}$  so as to properly measure the momentum resolution of the charged  
 754 particles. In order to ensure this, field mapping campaigns in the tracking volume were  
 755 made and obtained a value of about  $4 \times 10^{-4}$  (4.4). In order to reduce the systematic  
 756 effects of the detector, especially for  $CP$  studies, the polarity of the magnetic field needs  
 757 to be changed periodically.

### 758 4.2.3 Tracking

759 The tracking system of LHCb consists of two parts: the vertex locator (VELO) and  
 760 four tracking stations: the *Tracker Turicensis* (TT) upstream of the magnet, and T1-T3  
 761 downstream of the magnet. The latter are composed by an Inner Tracker (IT) and an  
 762 Outer Tracker (OT). Both IT and TT belong to a common project, the *Silicon Tracker*  
 763 (ST).

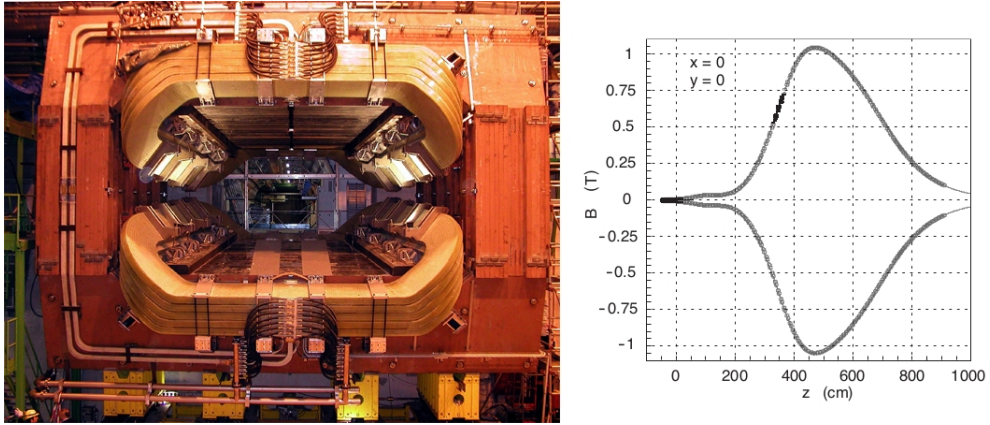


Figure 4.4: LHCb magnet (left) and magnetic field along the  $z$  axis (right)

#### 764 4.2.3.1 VELO

765 The ability to reconstruct vertices with a high precision is a key feature of the LHCb  
 766 detector. It is **vastly** used to accurately measure the decay lifetimes, the impact parameter  
 767 and the flavour of the particles that are produced. Besides, detached vertices are of crucial  
 768 importance for the High Level Trigger (4.2.5).

769 Such reconstruction is done in the VErtex LOcator (VELO), that provides measure-  
 770 ments of the track coordinates close to the interaction region. It consists of 20 semicircular  
 771 silicon modules located along the beam direction, each one providing measurement of  
 772 cylindrical coordinates  $(r, \phi)$  using microstrips, together with two planes perpendicular  
 773 to the beam line, the *pile-up veto system*, as it can be seen in 4.5, that are then used to  
 774 get rid of high multiplicity events. The minimum pitch at the innermost radius is  $38\mu\text{m}$ ,  
 775 increasing linearly to  $101.6\mu\text{m}$  at the outer radius of  $41.9\text{mm}$ . These sensors must be  
 776 retractable, as the distance from them to the beam is smaller than the one required from  
 777 LHC during the injection phase. Vacuum inside the VELO is separated from the machine  
 778 vacuum by corrugated aluminum foils, *RF-foils*.

779 The VELO was designed in order to fulfill the signal to noise ratio, efficiency, reso-  
 780 lution and geometrical requirements. Polar coordinates are used in order to ensure fast  
 781 reconstruction of tracks and vertices in the LHCb trigger [49].

#### 782 4.2.3.2 ST

783 As said before, the Silicon Tracker (ST) refers to two different detectors: the Tracker  
 784 Turicensis (formerly known as *Trigger Tracker* (TT) and the Inner Tracker (IT) (see 4.6).  
 785 Both use silicon microstrip sensors with a strip pitch of about  $200\ \mu\text{m}$ . The TT is a  
 786  $150 \times 130\ \text{cm}^2$  high planar tracking station (covering the full LHCb acceptance), located  
 787 upstream of the LHCb dipole magnet. The IT covers a  $120 \times 40\ \text{cm}^2$  high cross shaped  
 788 region in the centre of the three tracking stations downstream of the magnet.

789 The TT and each of the three IT stations have four detection, organized in an  $(x-u-v)$ -

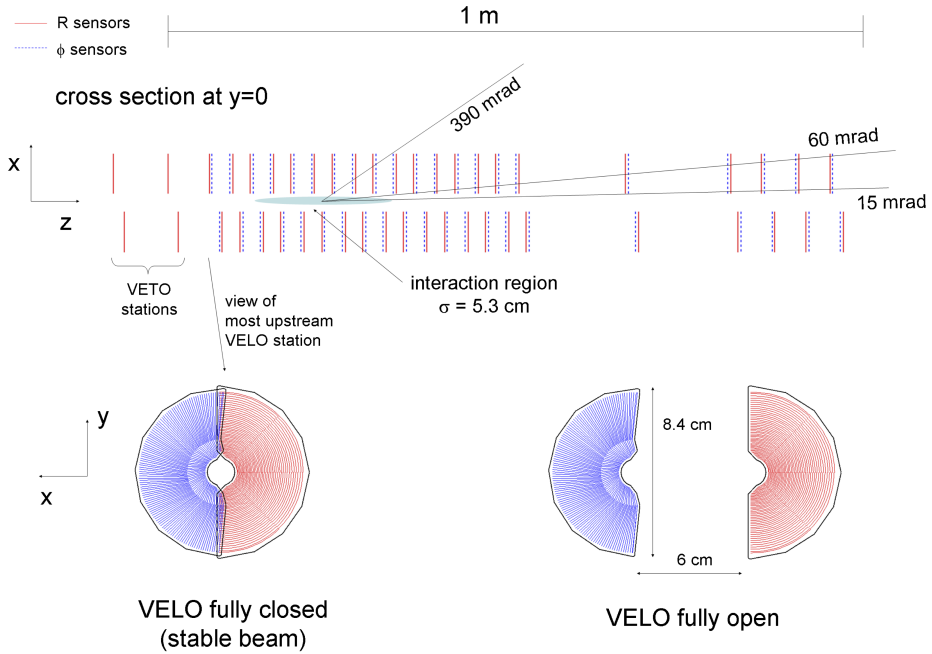


Figure 4.5: Cross section in the  $(x,z)$  plane of the VELO silicon sensors, at  $y = 0$ , with the detector in the fully closed position. The front face of the first modules is also illustrated in both the closed and open positions [49].

790  $x$ ) configuration, with vertical strips in the first and the last layer. Strips in the second  
 791 and third layer are rotated by a stereo angle of  $-5^\circ$  and  $5^\circ$  respectively (so as to get 3D  
 792 reconstruction). The pitch is about  $200\mu\text{m}$  which gives a single hit resolution of  $50\mu\text{m}$ .  
 793 Momentum resolution is then dominated by multiple scattering. The active area is of  
 794 about  $8.4\text{m}^2$  for the TT and of  $4.0\text{m}^2$  for the IT. A temperature below  $5^\circ\text{C}$  is maintained  
 795 in both cases.

#### 796 4.2.3.3 OT

797 The OT detector is designed for the tracking of charged particles, and the measurement of  
 798 their momentum. Excellent momentum resolution and high tracking efficiency are needed  
 799 for LHCb analyses. It consists in a drift-time detector, composed of an array of gas-tight  
 800 straw-tube modules. For the gas, a mixture of Argon (70%) and  $CO_2$  (30%) is used. This  
 801 ensures a fast drift time, as well as a sufficient drift-coordinate resolution.

802 The modules are arranged in three stations, each one consisting of four layers. The  
 803 stations are further splitted in two halves, with two independently retractable units of  
 804 two half layers (C-frames). Such arrangement can be seen in 4.7.

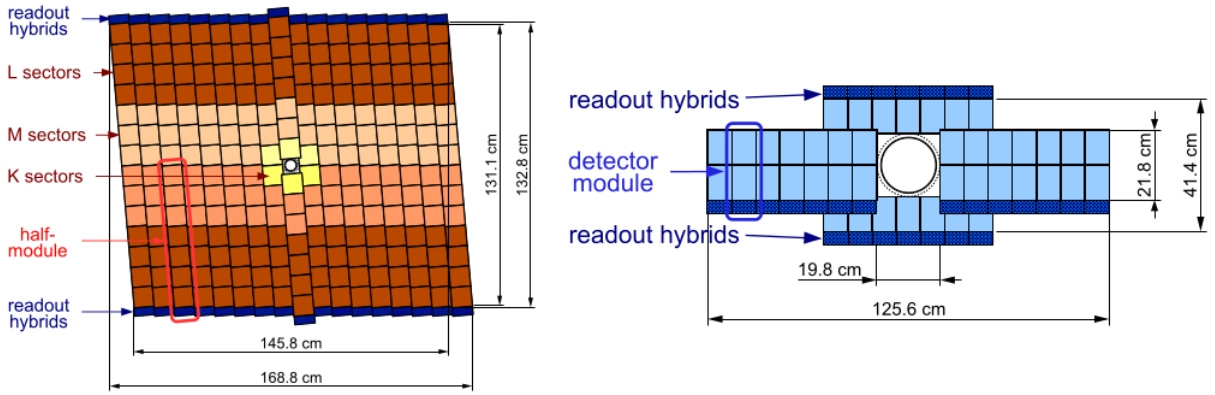


Figure 4.6: Layout of the third TT detection layer (left) and layout of an x detection layer in the second IT station (right) [49].

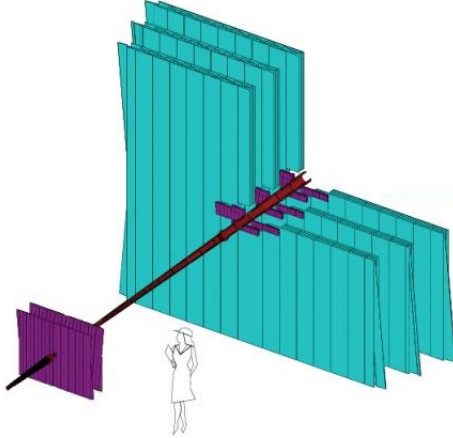


Figure 4.7: Arrangement of OT straw-tube modules in layer and stations [49].

#### 805 4.2.4 PID

806 Particle identification (PID) at LHCb is crucial in order to properly distinguish the dif-  
 807 ferent types of particles that are detected. Particularly, it is important to further reduce  
 808 backgrounds from different decays, as well as at the trigger level (4.2.5). Three different  
 809 subdetectors, described below, are used for PID.

##### 810 4.2.4.1 RICH

811 There are two *Ring Imaging Cherenkov detectors* at LHCb, designed to cover the full  
 812 momentum range. RICH1 (4.8 left) covers the low momentum charged particle range  
 813 ( $\sim 1 - 60\text{GeV}$ ), while RICH2 (4.8 right) covers the high momentum charged particle  
 814 range ( $\sim 15\text{GeV}$  up to and beyond  $\sim 100\text{GeV}$ ). In order to do this, RICH1 (located

815 upstream, between the VELO and the Trigger Tracker) uses aerogel and  $\text{C}_4\text{F}_{10}$  radiators,  
 816 while the downstream detector, RICH2, uses a  $\text{CF}_4$  radiator.

817 While RICH1 covers the full LHCb acceptance, from  $\pm 25\text{rad}$  to  $\pm 300\text{rad}$  horizontal  
 818 and  $\pm 250\text{rad}$  vertical, RICH2 has a more limited angular acceptance (where the high  
 819 momentum particles are produced), of  $\sim \pm 15\text{rad}$  to  $\pm 120\text{rad}$  horizontal and  $\pm 100\text{rad}$ .

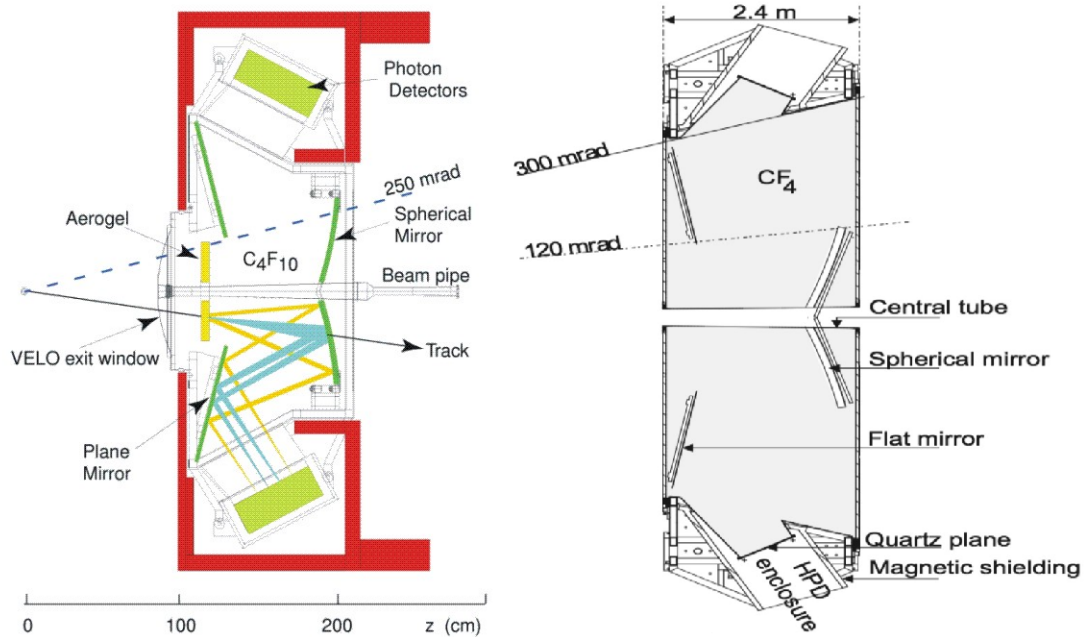


Figure 4.8: Schematic view of RICH1 (left) and RICH2 (right) detectors [49].

820 Both detector use spherical and flat mirrors to focus the Cherenkov light. The optical  
 821 layout is vertical for RICH1 and horizontal for RICH2. Cherenkov photons in the wave-  
 822 length range 200-600 nm are detected by Hybrid Photon Detectors (HPDs), which are  
 823 outside the LHCb acceptance. These are surrounded by external iron shields that shield  
 824 them from the fringe, marginal? field of the LHCb dipole.

#### 825 4.2.4.2 Calorimeters

826 The transverse energy of hadrons, electrons and photons is measured and selected in the  
 827 calorimeter for the L0 trigger (4.2.5). The energy and position is also measured for these  
 828 particles, which are identified in this subdetector, while avoiding the pass of those particles  
 829 to the muon system. The proper identification of hadrons, electrons and photons is also  
 830 of great importance for correctly identifying the flavour of the original meson in the decay  
 831 (*flavour tagging*). This is done taking into account that these particles deposit the energy  
 832 in the different parts of the calorimeter in a different manner.

833 It consists of two separate parts: an electromagnetic calorimeter (ECAL) followed by  
 834 a hadron calorimeter (HCAL), to identify electromagnetic and hadronic showers, respec-

tively. A preshower detector (PS) is located before the ECAL, in order to eliminate a large background of charged pions that could be misidentified as electrons. In front of the PS, a scintillator pad detector (SPD), used to select charged particles, is located. For all these parts a variable lateral segmentation is adopted, given that the hit density varies by two orders of magnitude over the calorimeter surface [49]. Because of the dimensions of the hadronic showers, the HCAL is segmented into two zones with larger cell sizes.

In all cases, the same principle of scintillation light transmitted to a Photo-Multiplier (PMT) (that turn this light into an electric signal) by wavelength-shifting (WLS) fibres is adopted. To have a constant transverse energy scale the gain in the ECAL and HCAL phototubes is set in proportion to their distance to the beampipe.

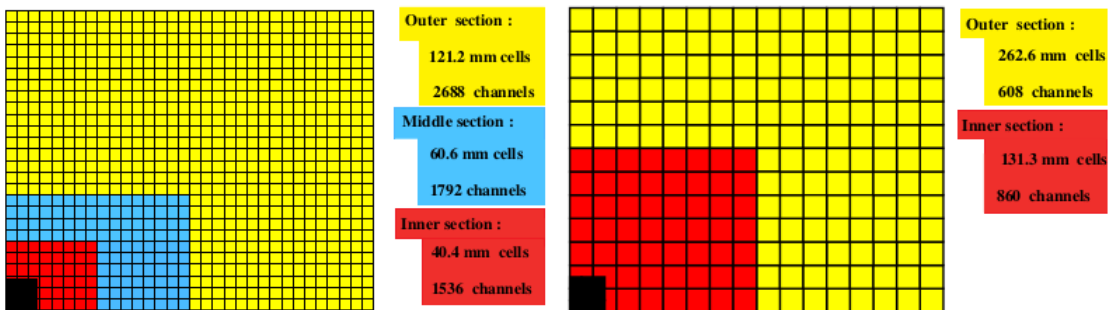


Figure 4.9: Lateral segmentation of the SPD/PS and ECAL (left) and the HCAL (right). One quarter of the detector front face is shown [49].

dimensions?

#### 4.2.4.3 Muon System

The muon system provides fast information for the high- $p_T$  muon trigger at the earliest level (L0) and muon identification for the high-level trigger (HLT) and offline analysis [49]. Given that muons are present in final states of the most relevant channels for LHCb, this is of crucial importance.

It is composed of five rectangular stations (M1-M5), located along the beam axis, with a total of 1380 chambers and  $435\text{m}^2$  of coverage. The inner and outer angular acceptances are 20(16) mrad and 306(258) mrad in the bending (non-bending) plane respectively [49]. All the stations are divided into 4 regions, R1-R4, with increasing distance from the beam axis. Their dimensions (scaling a factor two from one region to the next) and their geometry provide the same flux and channel occupancy for all of them. Multi-wire proportional chambers (MWPC) are used for all regions except the inner region of station M1, where triple-GEM detectors (consisting of three gas electron multipliers) are used.

Stations M2 to M5 are placed downstream the calorimeters, interleaved with three iron filters. They have a threshold of  $\sim 6\text{GeV}/c$  for a muon to cross the five stations. Stations M1-M3 are used to define the track direction and to calculate the  $p_T$  of the candidate muon, due to their high spatial resolution along the bending plane. On the

863 **other hand**, stations M4 and M5 are focused on identifying penetrating particles. Station  
 864 M1 is located in front of the calorimeters. Its function is to improve the  $p_T$  measurement  
 865 in the trigger. The geometry of all the stations is such that all their transverse dimensions  
 866 scale with the distance from the interaction point.

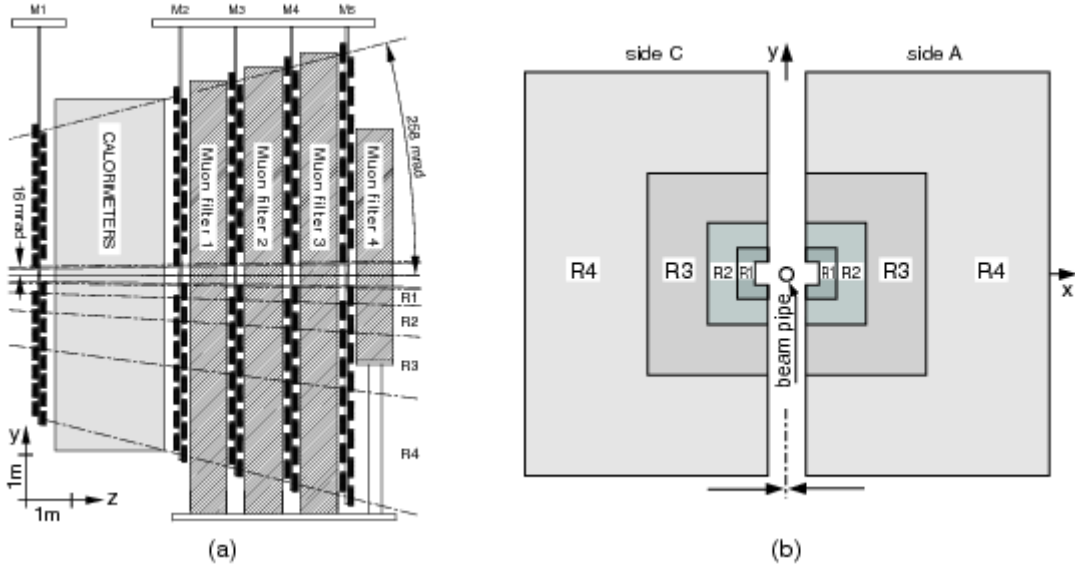


Figure 4.10: (a) Side view of the LHCb Muon Detector. (b) Station layout with the four regions R1-R4 [50].

### 867 4.2.5 Trigger

868 The LHCb trigger is one of the most important part of its infrastructure, as it allows for  
 869 a reduction of the crossing frequency with interactions visible by the spectrometer from  
 870 10MHz to about 2 - 5 kHz, at which rate the events are written to storage for further  
 871 offline analysis [49]. It is composed by two levels: Level-0 (L0) and the High Level Trigger  
 872 (HLT). Both parts are optimised to obtain the highest efficiency for the events selected  
 873 in the offline analysis, while avoiding storage of as much background events as possible.

#### 874 4.2.5.1 L0

875 The purpose of this first stage of the trigger is to reduce the LHC beam crossing rate  
 876 of 40 MHz to 1MHz, with which the entire detector can be read out [49]. This is done  
 877 reconstructing the highest  $E_T$  hadron, electron and photon clusters in the calorimeters,  
 878 together with the the two highest  $p_T$  muons in the muon chambers, as B meson decay  
 879 products are expected to have large  $p_T$  and  $E_T$ . A pile-up system in the VELO estimates  
 880 the number of primary pp interactions in each bunch crossing. The calorimeters calculate

881 the total observed energy and an estimate for the number of tracks, based on the number  
882 of hits in the SPD. With this, unwanted events are discarded.

883 It is composed by three parts, all connected to a different part of the LHCb, and all  
884 connected to the L0 DU (see 4.11):

- 885 1. The pile-up system: its purpose is distinguishing crossings with single and multiple  
886 visible interactions. For this, it uses four silicon sensors as the ones used in the  
887 VELO, that measure the radial position of the tracks. It consists of two silicon  
888 planes, situated upstream of the VELO and perpendicular to the beam-line, where  
889 the radii of track hits are measured. From this, the position of the track origin on  
890 the beam axis (the *vertex*) can be reconstructed.
- 891 2. The L0 calorimeter trigger: its goal is to look for high  $E_T$  electrons, photons, neutral  
892 pions or hadrons. This is done forming clusters by adding the transverse energy of  
893 2x2 cells and selecting the cluster with the highest  $E_T$ . This zone is large enough  
894 to contain most of the energy, while avoiding overlapping among different particles.  
895 Afterwards, such cluster is identified as one of the particle types using information  
896 from the SPD, PS, ECAL and HCAL subdetectors.
- 897 3. The L0 muon trigger: in the muon chambers muons are reconstructed with a resolution  
898 in  $p_T$  of  $\sim 20\%$ . The L0 muon trigger selects the two muons with the highest  $p_T$   
899 for each quadrant of the muon detector. The track finding is performed on the logical  
900 pads, searching for hits defining a straight line through the five muon stations  
901 and pointing towards the interaction point [49], also enabling the determination of  
902 the  $p_T$  of the track.

903 Multiplicities are measured by the SPD cells. charged track multiplicity

904 A L0 Decision Unit (DU) collects all the information and derives the final L0 trigger  
905 decision for each bunch crossing to the Readout Supervisor , allowing for overlapping of  
906 several trigger conditions, as well as for prescaling. The Readout Supervisor is in charge  
907 of the ultimate decision about whether to accept an event or not.

908 The L0 uses custom made electronics, fully synchronous with the 40 MHz bunch  
909 crossing signal of the LHC. All L0 electronics uses fully custom-designed boards that use  
910 parallelism and pipelining in order to speed up the process. The time passed between a  
911 pp interaction and the arrival of the L0 trigger decision is of  $4 \mu s$ , that leaves  $2 \mu s$  for data  
912 processing in the L0.

#### 913 4.2.5.2 HLT

914 The High Level Trigger (HLT) reduces the event rate from 1MHz down to 2 - 5 kHz,  
915 making use of the full event data. The HLT selected events are then saved on permanent  
916 storage. The algorithms that it uses refine candidates found by the L0 and divide them  
917 into independent alleys, selected from the L0 decision, requiring the candidate tracks to be  
918 reconstructed in the VELO and/or the T-tations. With this, the rate is reduced to about

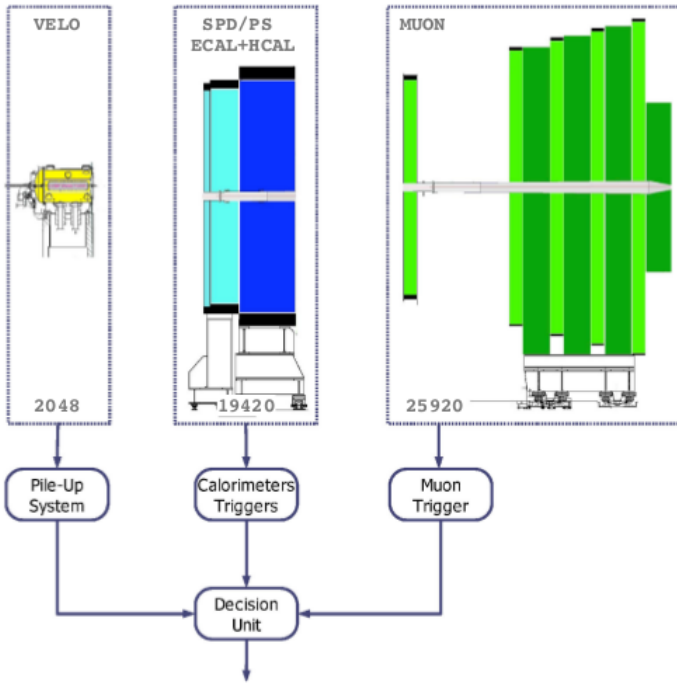


Figure 4.11: Overview of the L0 [49].

919 30kHz, where it becomes interesting to take into account both inclusive and exclusive  
920 criteria. It is further subdivided into HLT1 and HLT2, each with different purposes. The  
921 overall flow of all the trigger steps can be seen in 4.12.

922 It consists of a C++ application that runs on over 2000 computing nodes, the Event  
923 Filter Farm (EFF). Even though it can access all data in one event, the purpose is to  
924 discard uninteresting event using part of the full event data. The cuts applied at this stage  
925 are generally very loose compared to the offline analysis, so as to be able to study the  
926 sensitivity of the selections and to profit from refinements due to improved calibration  
927 constants. In order to compute systematic uncertainties and trigger efficiencies, both  
928 levels can be fully emulated on stored data.

929 Both HLT1 and HLT2 summaries, containing the information of all tracks and vertexes  
930 that triggered events, are stored. This allows the study of the trigger performance, as well  
931 as of the trigger source of each event. Furthermore, in order to ensure the traceability of  
932 the trigger conditions in the off-line analysis, the combination of trigger algorithms with  
933 their selection parameters are pre-loaded in the EFF before a fill in a Trigger Configuration  
934 Key (TCK).

#### 935 4.2.5.3 HLT1

936 The main goal of HLT1 is the so-called L0 confirmation, to reconstruct particle in the  
937 VELO and T-stations correspondence to the L0 objects, or for neutral particles to confirm

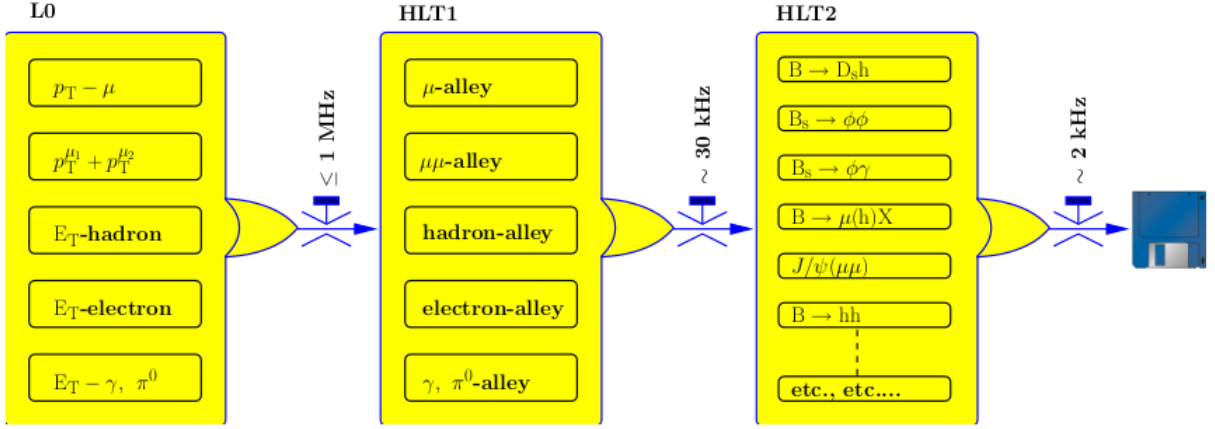


Figure 4.12: Flow-diagram of the different trigger sequences [49].

938 de absence of a charged particle that could be associated to these same objects. Different  
 939 reconstruction sequences (*alleys*) with different algorithms and selection cuts are applied  
 940 according to the L0 candidate type. The events can pass by more than one alley, provided  
 941 that they are selected by multiple triggers.

#### 942 4.2.5.4 HLT2

943 At this stage of the trigger, a set of tracks is selected with very broad cuts on their  
 944 momentum and impact parameter, and used to form composite particles. **These are then**  
 945 **used for all selections to avoid duplication in the creation of final states.** The selections  
 946 can be exclusive or inclusive, depending on whether the full final state is reconstructed  
 947 or not. The inclusive triggers are less dependent on the on-line reconstruction, while the  
 948 exclusive one produces a smaller rate, thus allowing for a more relaxed set of cuts.

#### 949 4.2.6 Tracking and Vertexing performance

950 In the track reconstruction software the hits in the VELO, the TT, the IT and the OT  
 951 detectors are combined to form particle trajectories from the VELO to the calorimeters,  
 952 with the purpose of finding all tracks in the event which leave sufficient detector hits.  
 953 Depending on the subdetectors used for the reconstruction, offline tracks are classified in  
 954 the following categories (see 4.13):

- 955 • **Long tracks:** those that traverse the VELO, the TT and the T-stations, hence  
       having the most precise momentum determination.
- 956 • **Upstream tracks:** those traversing only the VELO and TT stations. Generally,  
       they have lower momentum and are bent out of the detector acceptance by the mag-  
       netic field. Nevertheless, they pass through the RICH1 detector. Hence, they may

960 generate Cherenkov photons, and can be used to understand backgrounds. Besides,  
 961 they can also be used for flavour tagging, albeit their momentum resolution is poor.

- 962 • **Downstream tracks:** traversing only the TT and T stations. The most relevant  
 963 cases are the decay products of  $K_S^0$  and  $\Lambda$  that decay outside of the VELO accep-  
 964 tance.
- 965 • **VELO tracks:** measured in the VELO only and typically with large angle, or  
 966 backward tracks. They are useful for the primary vertex reconstruction.
- 967 • **T tracks:** the ones measured in the T stations, typically produced in secondary  
 968 interactions, but useful for the global pattern recognition in RICH2.

969 For  $K_S^0$  reconstruction, only long tracks and downstream tracks are used.

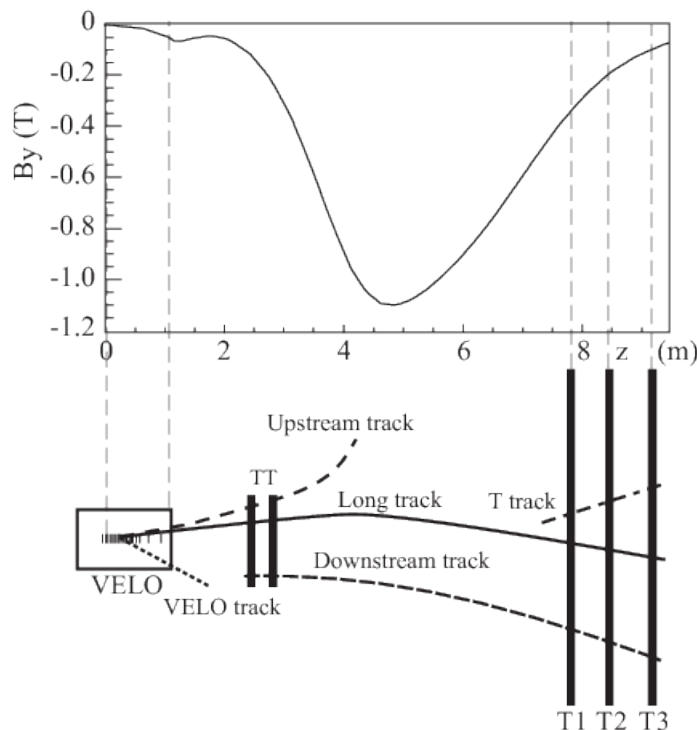


Figure 4.13: Schematic illustration of the various track types. For reference the main  $B$ -field component ( $B_y$ ) is plotted above as a function of the  $z$  coordinate [51].

970 For the track reconstruction algorithm, track *seeds* are used as starting points. These  
 971 are the initial track candidates in the VELO and T stations, where the magnetic field is  
 972 low. Their trajectories are refitted using the Kalman filter [ref](#), that accounts for multiple  
 973 scattering and energy loss. The quality of such fitting is monitored using the  $\chi^2$  of the fit  
 974 and the *pull* distribution for the different parameters.

975        The pattern recognition performance is evaluated in terms of efficiencies and ghost  
 976        rates. The efficiencies are the ratio of successfully reconstructed tracks over the total  
 977        amount of reconstructible tracks. A track is considered reconstructible if it has a minimum  
 978        number of hits in the relevant subdetector, and *successfully reconstructed* if at least 70%  
 979        of such hits originate from a single MonteCarlo (simulated) particle. Otherwise, it is  
 980        considered a *ghost track*.

981        Figure 4.14 shows this efficiency as a function of two kinetic variables, namely the  
 982        momentum,  $p$ , and the pseudorapidity,  $\eta$ , for 2011 and 2012. The performance in the  
 983        2012 data is slightly worse, which is partially due to the higher hit multiplicity at the  
 984        higher centre-of-mass energy [51]. The average efficiency is above 96% for  $5\text{GeV}/c < p <$   
 985         $200\text{GeV}/c$ ,  $2 < \eta < 2$ , thus covering the LHCb phase space.

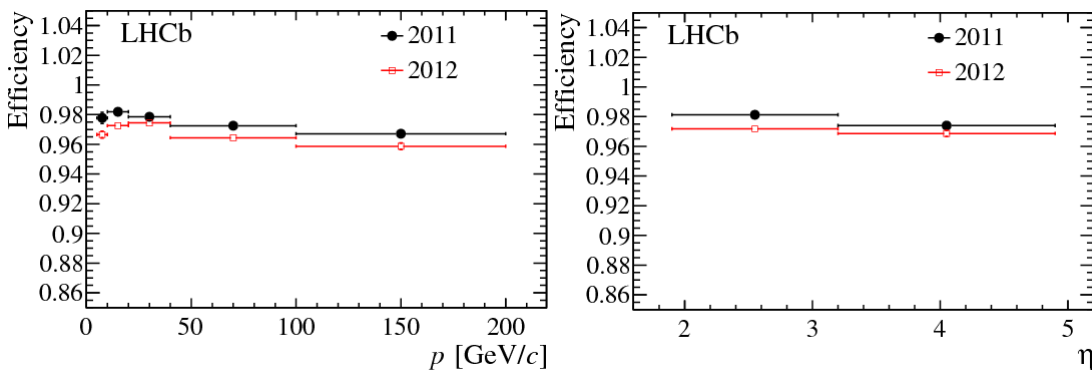


Figure 4.14: Tracking efficiency on muons from  $J/\psi$  as a function of momentum (left) and pseudorapidity (right). Black points correspond to 2011 data and red 2012 data [51].

986        As for the relative momentum resolution, as it is shown in 4.15 for two muons coming  
 987        from a  $J/\psi$ , it is better (about 5 per mille) for low-momentum than for high-momentum  
 988        (about 8 per mille) ranges. Hence, the best performances in terms of momentum resolution  
 989        are achieved for long tracks, as said before.

990        In order to assess the vertexing performance at LHCb, two main quantities are exam-  
 991        ined: the primary vertex (PV) resolution, and the impact parameter. The PV resolution  
 992        is measured by comparing two independent measurements of the vertex position in the  
 993        same event. This is achieved by randomly splitting the set of tracks in an event into two  
 994        and reconstructing the PVs in both sets.

995        The impact parameter (IP) of a track is defined as its distance from the primary vertex  
 996        at its point of closest approach to the primary vertex. Particles resulting from the decay  
 997        of long lived  $B$  or  $D$  mesons tend to have larger IP than those of particles produced at  
 998        the primary vertex. Selections on IP and the IP  $\chi^2$  are extensively used in LHCb analyses  
 999        to reduce the contamination from prompt backgrounds. Consequently, an optimal IP  
 1000        resolution and a good understanding of the effects contributing to the IP resolution are  
 1001        of prime importance to LHCb performance [51].

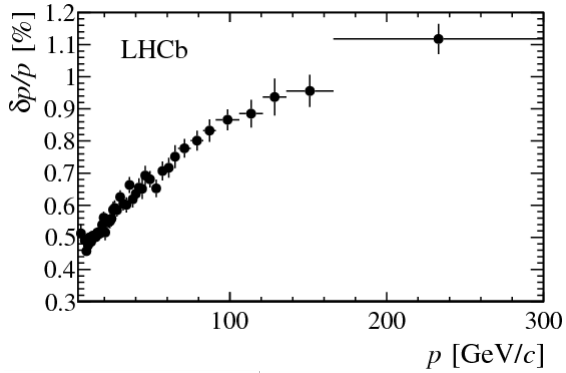


Figure 4.15: Relative momentum resolution versus momentum for long tracks in data obtained using  $J/\psi$  decays [51].

The IP resolution is governed by three main factors: multiple scattering of particles by the detector material; the resolution on the position of hits in the detector from which tracks are reconstructed; and the distance of extrapolation of a track between its first hit in the detector and the interaction point. The minimisation of these factors is achieved in the design of the VELO [51].

The left part of figure 4.16 shows the PV resolution in the  $x$  and  $y$  direction as a function of the number of tracks. It can be seen that in both cases it improves with the number of tracks. The right part shows the IP resolution in the  $x$  direction as a function of the inverse of the transverse momentum. Very good resolution is achieved in the VELO, thanks to the silicon strips.

### 4.2.7 PID performance

As explained in ??, particle identification at LHCb is performed in 4 different subdetectors. Each one of them gives a different performance that is then further combined into an overall PID performance.

For the calorimeters the main role is to distinguish photons, electrons and neutral pions. Electrons are differentiated from photons and  $\pi^0$  in the fact that they have a track associated before the energetic deposit in the calorimeter, as they are charged particles. Their associated likelihood is estimated using information from the ECAL, the PS and the HCAL. In order to separate photons from  $\pi^0$ , a neural network classifier is used, trained with pure samples. Non-converted photons are identified using a photon hypothesis likelihood, employing variables from the different subdetectors (PS and ECAL).

Both for photons and for electrons, the PID performance is assessed using the log-likelihood difference between the signal hypothesis (photon or electron) versus the background one (hadrons for electrons). In the case of the electrons, this log-likelihood is computed as the sum of log likelihoods:

$$\Delta \log \mathcal{L}^{\text{CALO}}(e - h) = \Delta \log \mathcal{L}^{\text{ECAL}}(e - h) + \Delta \log \mathcal{L}^{\text{HCAL}}(e - h) + \Delta \log \mathcal{L}^{\text{PS}}(e - h) \quad (4.1)$$

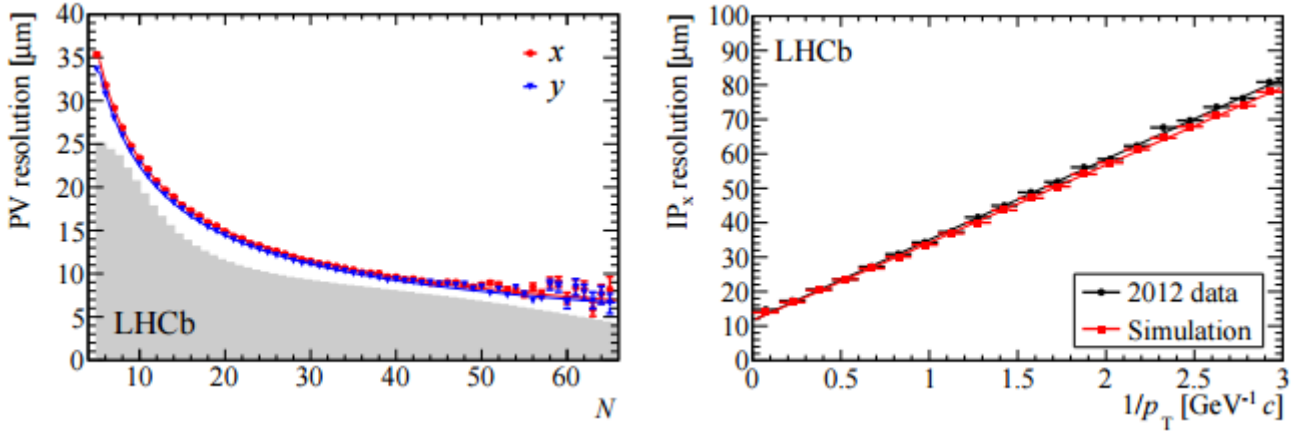
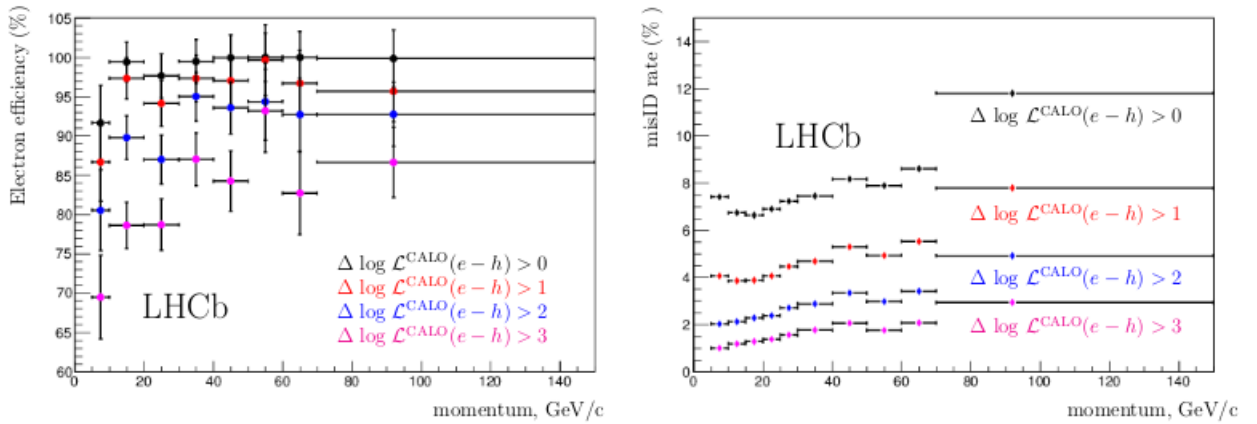


Figure 4.16: The primary vertex resolution (left), for events with one reconstructed primary vertex, as a function of track multiplicity. The  $x$  (red) and  $y$  (blue) resolutions are separately shown and the superimposed histogram shows the distribution of number of tracks per reconstructed primary vertex for all events that pass the high level trigger. The impact parameter in  $x$  resolution as a function of  $1/p_T$  (right). Both plots are made using data collected in 2012. [51].

1027 This is shown in 4.17, for different cuts. As expected, the higher momenta particles  
have higher misidentification rates.



1028 Figure 4.17: Electron identification performances for various  $\Delta \log \mathcal{L}^{\text{CALO}}(e - h)$  cut: elec-  
tron efficiency (left) and misidentification rate (right) as functions of the track momen-  
tum [51].

1029 As for the RICH, its mission is to distinguish charged hadrons ( $\pi, K, p$ ). The informa-  
1030 tion thus obtained is used at the final analysis level and as part of the software level of  
1031 the trigger. Complementary information on charged leptons can also be provided by the

1032 RICH. Its performance is evaluated using two variables:

- 1033 • The Cherenkov angle resolution,  $\theta(\sigma_C)$ , defined as the resolution of the Cherenkov  
1034 angle with which the emitted photons can be reconstructed.
- 1035 • The photoelectron yield, defined as the average number of detected photons for each  
1036 track traversing the Cherenkov radiator media.

1037 Because of the high average track multiplicity in LHCb events, a reconstructed  
1038 Cherenkov ring will generally overlap with several neighbouring rings. Figure 4.18 shows  
1039 the Cherenkov angle as a function of particle momentum using information from the ra-  
1040 ditor for isolated tracks selected in data. As expected, different bands represent different  
1041 masses, hence different particles.

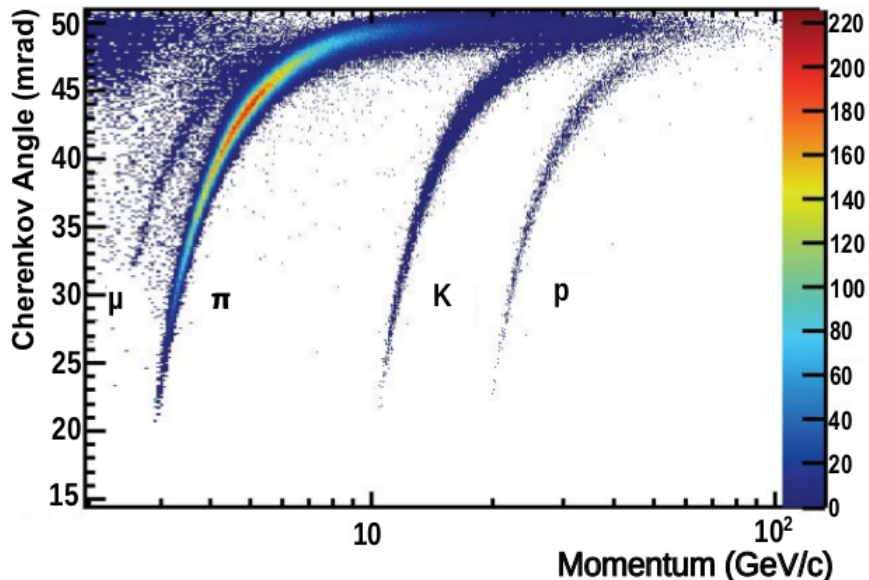


Figure 4.18: Reconstructed Cherenkov angle for *isolated* tracks, as a function of track momentum in the radiator. The Cherenkov bands for muons, pions, kaons and protons are clearly visible [51].

1042 Figure 4.19 shows the kaon efficiency (kaons identified as kaons) and pion misidentifi-  
1043 cation (pions misidentified as kaons) fraction achieved in LHCb data and simulation, as a  
1044 function of momentum. The results are shown both optimising efficiency and minimising  
1045 misidentification rate.

1046 Finally, muons are identified in the muon system. The algorithm is based on the  
1047 association of hits around its extrapolated trajectory. In this case, the logarithm of the  
1048 ratio between the muon and non-muon (protons, pions and kaons) hypothesis,  $\Delta \log \mathcal{L}(\mu)$   
1049 is used as discriminating variable. Figure 4.20 shows, as a function of the track momentum  
1050 and for different ranges of transverse momentum, the efficiency of the muon candidate

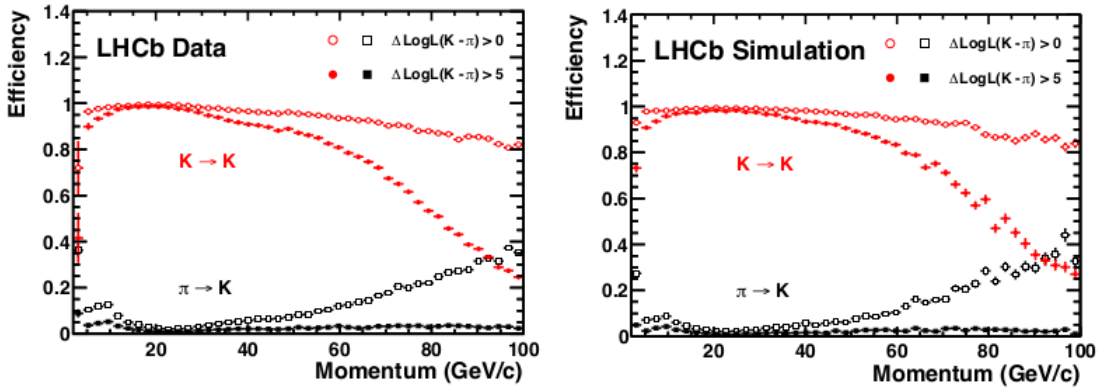


Figure 4.19: Kaon identification efficiency and pion misidentification rate as measured using data (left) and from simulation (right) as a function of track momentum [51]improve.

selection, and the probabilities of incorrect identification of protons, pions and kaons as muons.

The combined performance of the different PID subdetectors can be either be computed as a sum of the different likelihoods, or using multivariate techniques to get a single probability value for each particle hypothesis with different informations corresponding to each sub-system.

#### 4.2.8 Trigger performance

As discussed in 4.2.5, the LHCb trigger is composed of two parts, in order to reduce the input rate to an output rate of 2 -5 kHz. The performance of each part is assessed using a data-driven technique with representative samples, to account for inefficiencies due to the simplified reconstruction algorithm, possible misalignments and reduced resolution.

In the trigger system, an event is considered to be *Trigger on Signal (TOS)* if the trigger objects that are associated with the signal candidate are sufficient to trigger the event. On the contrary, if the event has been triggered by trigger objects not associated with the signal, it is considered *Trigger Independet of Signal (TIS)*. Notice that events can be both TIS and TOS. The TIS and TOS efficiencies are defined as follows:

$$\epsilon^{\text{TIS(TOS)}} = N^{\text{TIS&TOS}} / N^{\text{TOS(TIS)}} \quad (4.2)$$

##### 4.2.8.1 L0 hardware trigger

The L0 trigger consists of three independent nits:

- The L0-Calorimeter trigger, that uses information from the SPD, PS, ECAL and HCAL to compute  $E_T$  that particles deposit in clusters of 2x2 cells. From this, a candidate can be L0Hadron, LOPhoton or LOElectron.

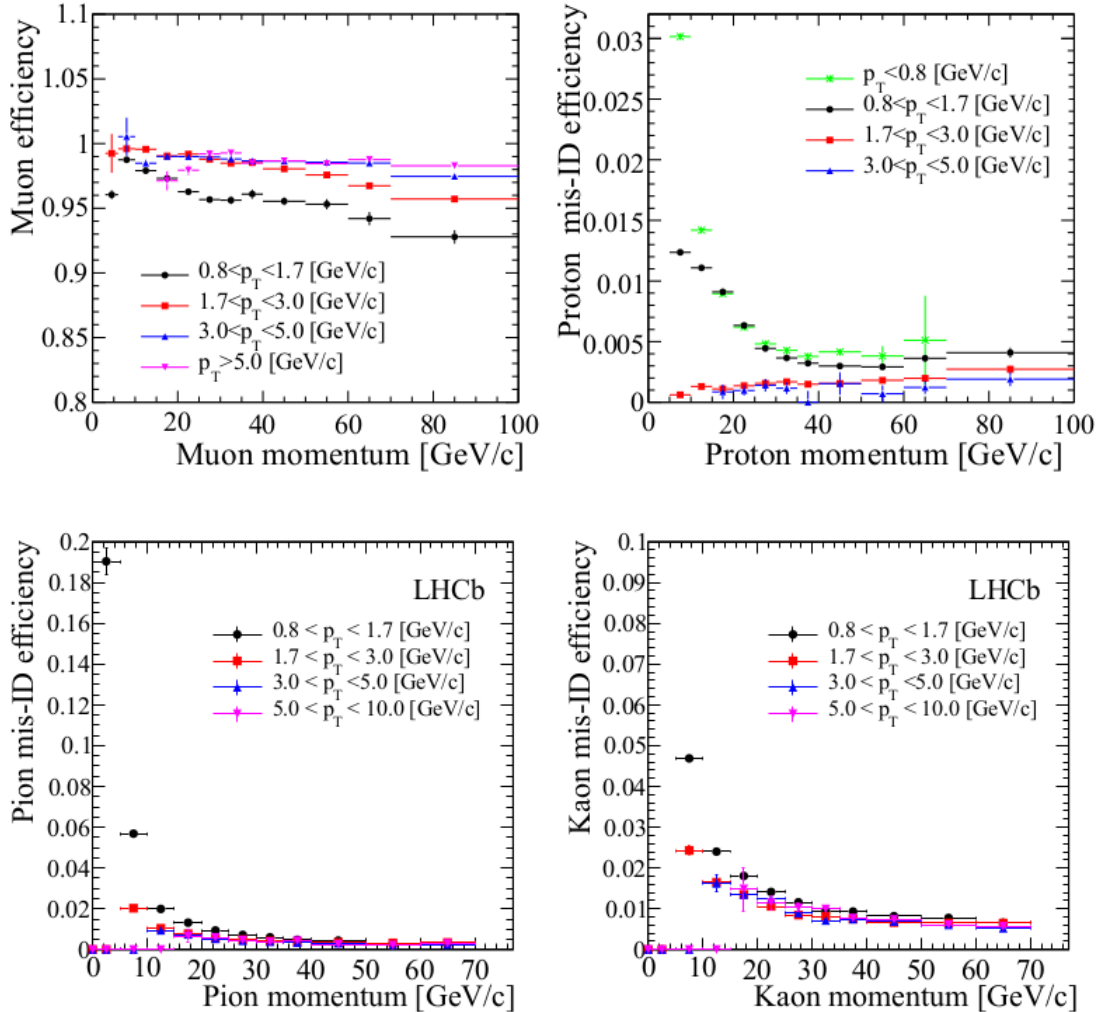


Figure 4.20: Top left: efficiency of the muon candidate selection based on the matching of hits in the muon system to track extrapolation, as a function of momentum for different  $p_T$  ranges. Other panels: misidentification probability of protons (top right), pions (bottom left), and kaons (bottom right) as muon candidate as a function of momentum, for different  $p_T$  ranges [51].

- 1072     • The L0-Muon trigger, that looks for the two highest  $p_T$  muon tracks in each quadrant,  
 1073       with thresholds on the  $p_T^{\text{largest}}$  and  $p_T^{\text{largest}} \times p_T^{\text{2ndlargest}}$ .
- 1074     • The L0-PileUp trigger, used for the computation of the luminosity.

1075     Figure 4.21 shows the L0 hadron efficiency for the representative channels. As expected,  
 1076     it increases with the transverse momentum.

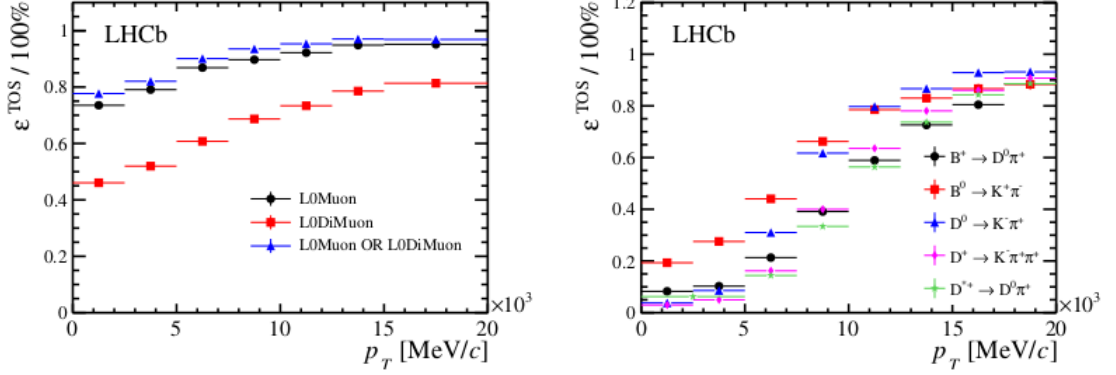


Figure 4.21: (left) L0 muon trigger performance: TOS trigger efficiency for selected  $B^+ \rightarrow J/\psi K^+$  candidates. (right) L0 hadron trigger performance: TOS trigger efficiency for different beauty and charm decay modes. [51].

#### 4.2.8.2 High Level Trigger

The HLT has a variety of so-called trigger "lines" that consist of selection parameters for specific classes of events. In HLT1, a partial event reconstruction is performed, while in HLT2 the complete event is reconstructed.

In the first level (HLT1), vertices are reconstructed from a minimum of five intersecting VELO tracks. Vertices within a radius of  $300 \mu\text{m}$  of the mean position of the pp-interaction envelope are considered to be primary vertices. During Run 1, the forward track search had a minimum momentum requirement that varied between 3 and 6 GeV/c. Dimuon candidates are either selected based on their mass without any displacement requirement, or based on their displacement without the mass restriction [ ]. The performance of HLT1 on muonic signatures as a function of  $p_T$  of the  $B^+$  parent is shown in 4.22.

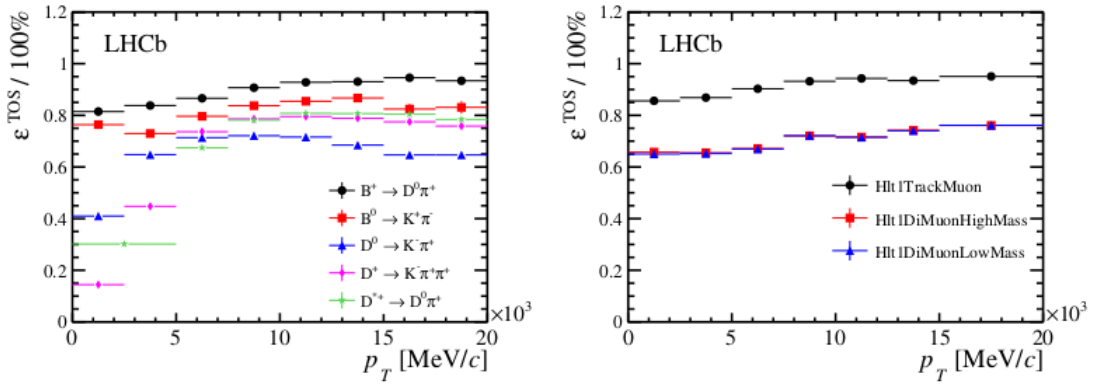


Figure 4.22: HLT1 inclusive track trigger performance: TOS efficiency for various channels as a function of  $B$  or  $D$   $p_T$  (left) . HLT1 muon trigger performance : TOS efficiency for  $B^+ \rightarrow J/\psi K^+$  [51].

1088 In the second level (HLT2), long tracks are searched based on VELO seeds, thus  
 1089 simplifying the offline tracking algorithm (because of CPU restrictions). There is a generic  
 1090 beauty trigger, for any partially reconstructed  $b$ -hadron decay, muon triggers, for decays  
 1091 with one or two muons, charm triggers and other exclusive and technical lines. Figure  
 1092 4.23 shows the performance of the  $J/\psi$  triggers.

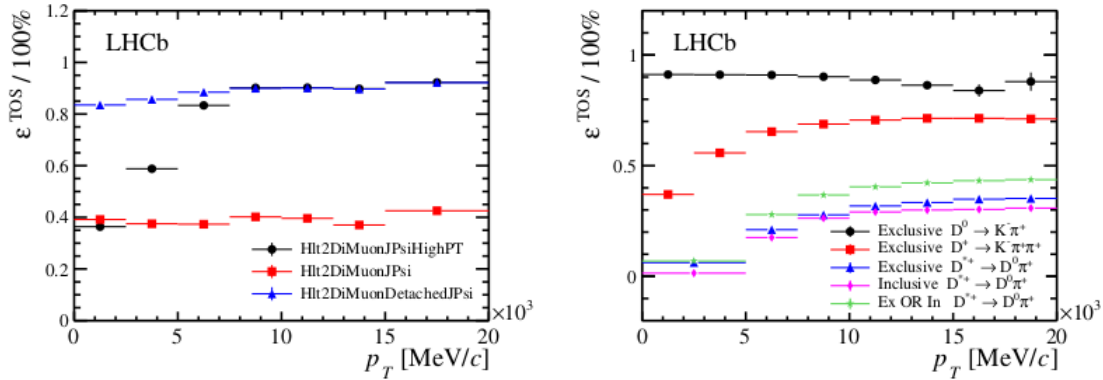


Figure 4.23: HLT2 muon trigger performance for the  $J/\psi$  trigger lines (left). HLT2 charm trigger performance for inclusive and exclusive selections (right). [51].

### 1093 4.2.9 The LHCb Upgrade

1094 The LHCb detector has proven to be an outstanding general-purpose detector in the for-  
 1095 ward pseudorapidity region. Nevertheless, some of the measurements are still statistically  
 1096 limited. Therefore, in order to fully exploit the potential of LHCb, an increase in the  
 1097 luminosity is required. This leads to the need of upgrading some of the subdetectors,  
 1098 since the upgraded detector is expected to collect  $50 \text{ fb}^{-1}$  during 5 years of data-taking,  
 1099 with a 40 MHz readout (Phase-I of the Upgrade).

1100 For the sake of this thesis, the changes made during the LHCb Upgrade will greatly  
 1101 benefit the sensitivity to rare strange decays, as the trigger limitation will disappear. Also,  
 1102 a significant improvement in the  $\phi_s$  measurement is expected. Prospects for the golden  
 1103 modes on these fields can be seen in 4.24.

#### 1104 4.2.9.1 Trigger Upgrade

1105 The main change that the LHCb trigger will undergo is the replacement of the L0 stage  
 1106 by a software one, the so-called *Low Level Trigger* (LLT), modified to run within the new  
 1107 readout architecture. It selects events containing clusters with high transverse energy in  
 1108 the calorimeters or tracks with high transverse momentum in the muon detector. A much  
 1109 larger LLT rate will be allowed, leading to a much larger rate to storage. Hence, the main  
 1110 limits will be processing power and bandwidth. The front-end electronics will be upgraded

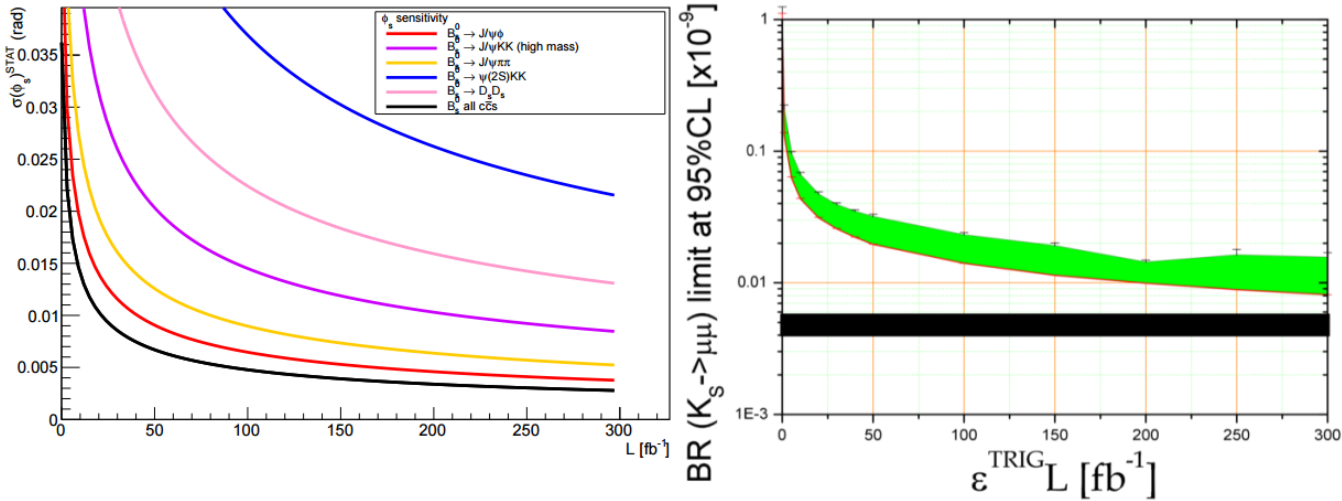


Figure 4.24: Left: expected sensitivity for  $\phi_s$  as a function of the luminosity. Right: Expected limit in  $\mathcal{B}(K_S^0 \rightarrow \mu^+ \mu^-)$  from LHCb and upgrades, as a function of integrated luminosity times trigger efficiency.

as well to allow reading events at the LHC clock rate. More details can be found in [REF](#).  
 hadronic final states? (nota de Lars)

#### 4.2.9.2 VELO Upgrade

The LHCb upgrade requires the VELO to have an excellent vertex resolution and two track separation, with fast pattern recognition capabilities. Moreover, because of the high luminosity, it has to have a sufficient radiation hardness to guarantee the performance throughout all the data-taking period. Besides, the upgraded trigger discussed before strongly relies on this subdetector.

In order to cope with these requirements, two alternatives were proposed:

- A fine-pitched silicon strip detector, similar to the current design, with improved cooling and a new ASIC.
- A hybrid pixel detector, called *VeloPix*, that uses the Timepix chip [ref](#).

Being the latter the one chosen for the Upgrade. The layout of the upgraded VELO can be seen in [4.25](#).

#### 4.2.9.3 PID Upgrade

As discussed before, the PID performance is crucial for the LHCb physics programme. Thus, its upgrade becomes of great importance.

The overall structure of the RICH will remain unchanged. In RICH1, the aerogel will be removed, as the efficiency gained by its removal outweighs the improvement on the PID

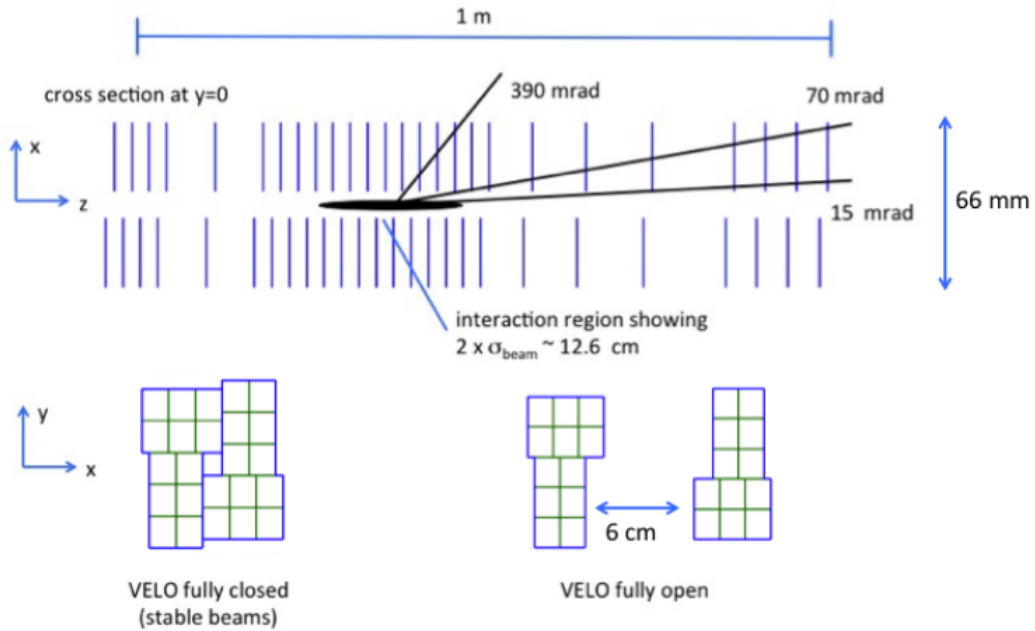


Figure 4.25: Schematic layout of the upgraded VELO.

provided by it. The HPDs will be replaced by commercial multianode photomultipliers (MaPMTs), with external readout electronics. Alternatively a lens system may be used there, to re-focus the Cherenkov images onto the 1-inch tubes and thus reduce the number of tubes required. A new subdetector, still under development, is being considered in order to recover the low momentum particle identification performance. It consists in a time-of-flight system, Time Of internally Reflected Cherenkov Light, TORCH.

As for the calorimeter, the electronics will be upgraded according to the new requirements. Also the PMTs gains will be reduced (and compensated by a gain increase in the electronics) to ensure a longer lifetime. Regarding the radiation hardness, studies have found the calorimeter resistant enough, even though some of the elements (such as the cells in the inner region of the ECAL) will need replacing in the long-term scale. Both the SOD and the PS will be removed, as they mainly contribute to the L0 trigger.

Finally, the muon system will have its first station removed, and additional shielding around the beam pipe in front of station M2. Similarly to the calorimeter, the electronics will be modified to comply with the new conditions.

**check**

#### 4.2.9.4 Tracking Upgrade

The TT stations will be replaced by a tracking detector composed of new, high-granularity silicon micro-strip planes with an improved coverage of the LHCb acceptance, the *Upstream Tracker* (UT). Behind the magnet, a *Scintillating Fibre Tracker* (SFT) will be

built, which is composed of 2.5m long fibres read out by silicon photomultipliers at the edge of the acceptance, replacing the current OT and IT stations. Both new subdetectors can be seen in 4.26.

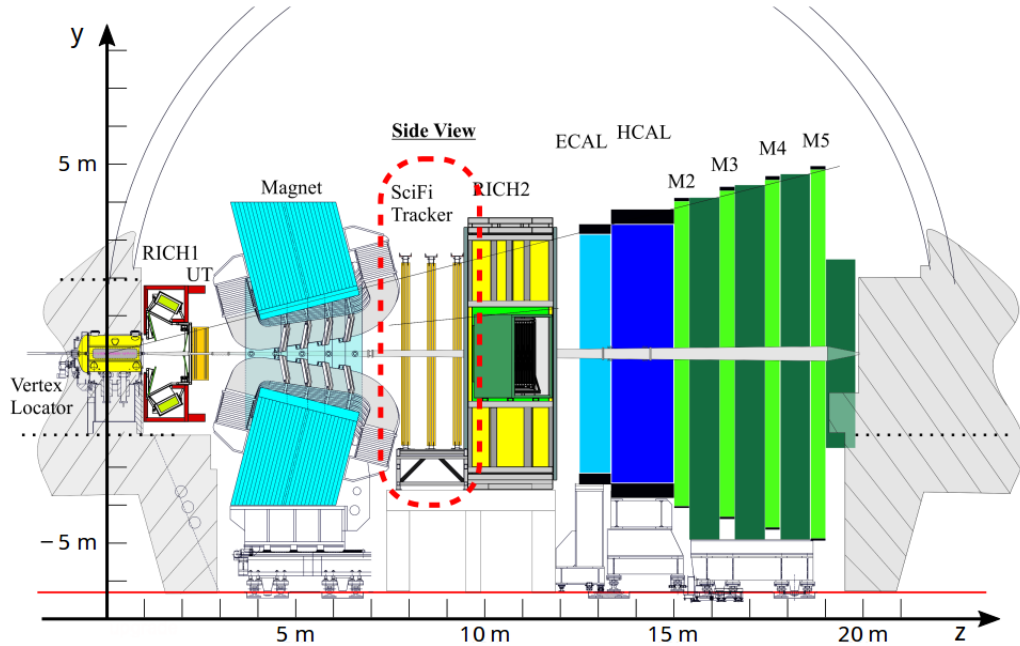


Figure 4.26: Side view of the upgraded LHCb.

### 4.2.10 Analysis workflow

Raw data from collisions is taken at LHCb at a rate of several million events per second. A fast, efficient treatment and distribution of such data is thus needed to perform an offline analysis of a given decay channel. For this, C++ tools and algorithms embedded inside the Gaudi [ref](#) project are used. The steps that are followed, together with their correspondance to the different projects inside such framework, are summarised below.

- As explained in 4.2.5, 4.2.8, a first loose selection is applied to the recorded data with the trigger. The trigger algorithms constitute what is known as the Moore project [ref](#).
- After data is recorded, it is necessary to convert the electronic signals to track and vertices. This was discussed in 4.2.3 and 4.2.6. Particle identification (4.2.4, 4.2.7) is also required to properly assign each of these variables to a given type of particle. This whole process is called *reconstruction*, and the group of C ++ LHCb libraries which contain the relevant tools, Brunel [ref](#). Proper knowledge alignment of each subdetector is also of great importance at this stage, for which tools under the Alignment project [ref](#) exist.

- 1169     3. Once all triggered events have been reconstructed, a process is necessary to properly  
 1170       separate them offline according to their physics content. Such process, called *stripping*,  
 1171       consists on a splitting procedure that selects the different decays according to  
 1172       their specific features (final state, PV, mother particle, etc.). Each of the selection  
 1173       criteria are contained in a *stripping line*. The LHCb libraries that take part of this  
 1174       stage are DaVinci [ref](#) and Erasmus [ref](#).
- 1175     4. In order to allow the access to the data, while keeping a backup of it, a distributed  
 1176       system, *Grid* [ref](#) is used by LHCb. Both stripped events and raw data are stored, so  
 1177       as to have the possibility of performing re-stripping and re-reconstruction if needed.  
 1178       Such system is of great computational power, and its spread in computing centers  
 1179       worldwide.
- 1180     5. Finally, to properly understand the effects from the detector and the steps before on  
 1181       data, simulation is used. Another important reason for which simulation is crucial  
 1182       is the need of training analysis tool on well-known states. Simulated Monte Carlo  
 1183       events (MC) are employed for this, mimicking as much as possible the data. The  
 1184       C++ libraries at LHCb dedicated to the MC production are contained in Gauss  
 1185       [ref](#), which is a collection of libraries for physics simulation based on Gaudi and with  
 1186       specialised algorithms and tools for generators (PYTHIA [ref](#), EvtGen [ref](#), ...) and  
 1187       detector simulation (Geant4 [ref](#)). The MC events can be further classified as follows:
- 1188       • Minimum Bias: keep all events generated by PYTHIA: elastic, diffractive,  
 1189           inelastic.
  - 1190       • Inclusive: extract events generated by PYTHIA with at least one  $b$  or  $c$  hadron  
 1191           in 400 mrad with respect to the LHCb  $z$  axis. If all of these hadrons have  
 1192            $p_z < 0$ , flip the whole event.
  - 1193       • Signal: extract events generated by PYTHIA containing at least one specific  
 1194           particle in 400 mrad. Again, if the candidate has  $p_z < 0$ , flip the whole event.  
 1195           In the case of  $b$  hadrons and to speed up the generation, if the interaction  
 1196           contains the  $b$ , repeat the hadronisation process of PYTHIA until the interaction  
 1197           contains the correct particle.

1198       [schematic view?](#)

# 1199 Chapter 5

## 1200 $\Delta F=2$

### 1201 5.1 Introduction

1202 The meson-antimeson oscillations are described by the mixing amplitudes [52]

$$M_{12}^{(M)} \equiv \langle M | \mathcal{H}_{\text{eff}}^{\Delta F=2} | \bar{M} \rangle \quad M = K^0, B_{d,s} \quad (5.1)$$

1203 Where  $\mathcal{H}_{\text{eff}}^{\Delta F=2}$  is the *effective* Jamiltonian. Within the MSSM, it has the form:

$$\mathcal{H}_{\text{eff}}^{\Delta F=2} = \sum_{i=1}^5 C_i Q_i + \sum_{i=1}^3 \tilde{C}_i \tilde{Q}_i + \text{h.c.} \quad (5.2)$$

1204 with the operators  $Q_i$  given, in the case of  $B_s$  mixing, by:

$$\begin{aligned} Q_1 &= (\bar{s}^\alpha \gamma_\mu P_L b^\alpha)(\bar{s}^\beta \gamma^\mu P_L b^\beta) \\ Q_2 &= (\bar{s}^\alpha P_L b^\alpha)(\bar{s}^\beta P_L b^\beta) \\ Q_3 &= (\bar{s}^\alpha P_L b^\beta)(\bar{s}^\beta P_L b^\alpha) \\ Q_4 &= (\bar{s}^\alpha P_L b^\alpha)(\bar{s}^\beta P_R b^\beta) \\ Q_5 &= (\bar{s}^\alpha P_L b^\beta)(\bar{s}^\beta P_R b^\alpha) \end{aligned} \quad (5.3)$$

1205 where  $P_{R,L} = \frac{1}{2}(1 \pm \gamma_5)$  and  $\alpha, \beta$  are colour indices. The operators  $\tilde{Q}_{1,2,3}$  are obtained from  
1206  $Q_{1,2,3}$  by the replacement  $L \leftrightarrow R$  [52]. In the case of  $B_d$ , the replacement  $s \rightarrow d$  needs to  
1207 be done in equation 5.3. Several representative observables can be extracted from these  
1208 amplitudes, such as the mixing phase and the oscillation frequency asl?:

$$\phi_s = \arg(M_{12}), \quad \Delta m_s = |M_{12}| \quad (5.4)$$

1209 Note that their value strongly depends on NP contributions:

$$M_{12} = M_{12}^{SM} + M_{12}^{NP} \quad (5.5)$$

1210 The experimental search of the weak mixing angle is discussed in detail in 5.2. Theoretical  
1211 interpretations of this result are reviewed in 5.3, and a MultiNest scan [53] is presented  
1212 in 5.4.

## 5.2 $\phi_s$ experimental

In the SM,  $CP$ -violation originates from a single-phase in the Cabibbo-Kobayashi-Maskawa (CKM) quark-mixing matrix [54], as explained in state? REF. There are 3 different kinds of  $CP$ -violation for neutral mesons, *e.g.*  $B_s^0$  and  $\bar{B}_s^0$ :

1. Direct  $CP$ -violation: originated by a difference in the amplitudes associated to the direct decay of the  $B_s^0$  and  $\bar{B}_s^0$  mesons into the same final state
2.  $CP$ -violation in the  $B_s^0 - \bar{B}_s^0$  oscillation, that arises when the oscillation from  $B_s^0$  to  $\bar{B}_s^0$  is different from the oscillation from  $\bar{B}_s^0$  to  $B_s^0$
3.  $CP$ -violation in the interference between the amplitudes associated to the direct decay of a  $B_s^0$  meson into a  $CP$ -eigenstate final state and those associated to the decay after  $B_s^0 - \bar{B}_s^0$  oscillation

This last type of  $CP$ -violation is characterized by the  $CP$ -violating phase,  $\phi_s$ , defined as:

$$\phi_s^f = -\arg(\lambda_f), \quad \lambda_f = \eta_f \frac{q}{p} \frac{\bar{\mathcal{A}}_f}{\mathcal{A}_f}, \quad (5.6)$$

where  $f$  is the final state,  $\eta_f$  is 1(-1) for CP-even(CP-odd) states,  $\left| \frac{q}{p} \right|$  determines the amount of  $CP$ -violation in mixing, and  $\mathcal{A}_f(\bar{\mathcal{A}}_f)$  is the amplitude of the  $B_s^0(\bar{B}_s^0)$  meson decaying into a given final state,  $f$ . Precision measurements of this phase are needed in order to properly disentangle SM and NP contributions.

In the SM, for  $b \rightarrow c\bar{c}s$  transitions and ignoring subleading penguin contributions, this phase is predicted to be  $-2\beta_s$ , where  $\beta_s = \arg[-(V_{ts}V_{tb}^*)/(V_{cs}V_{cb}^*)]$  and  $V_{ij}$  are elements of the CKM quark flavour mixing matrix [?]. The indirect determination via global fits to experimental data gives  $2\beta_s = 0.0364 \pm 0.0016$  rad ref. This precise indirect determination within the SM makes the measurement of  $\phi_s$  interesting since new physics (NP) processes could modify the phase if new particles were to contribute to the  $B_s^0 - \bar{B}_s^0$  box diagrams [?, ?].

The situation after including all Run 1 results from LHCb, and all results from ATLAS, CMS, CDF and D0 is shown in Figure 5.1. Current preliminary world averages (and their correlations) for the  $CP$  violating phase  $\phi_s$  and the decay width difference in the  $B_s^0$  system,  $\Delta\Gamma_s$ , are:

$$\begin{aligned} \phi_s &= -0.021 \pm 0.031 \text{ rad} \\ \Delta\Gamma_s &= 0.085 \pm 0.006 \text{ ps}^{-1} \\ \rho(\phi_s, \Delta\Gamma_s) &= -0.0095 \end{aligned}$$

The aim of this analysis is to perform the measurement of  $\phi_s$  in the  $B_s^0 \rightarrow J/\psi K^+ K^-$  channel by adding a further  $2\text{fb}^{-1}$  of integrated luminosity collected at 13 TeV in Run 2 of LHC in 2015 and 2016. In addition, updated measurements of the decay width difference of the light (L) and heavy (H)  $B_s^0$  mass eigenstates,  $\Delta\Gamma_s \equiv \Gamma_L - \Gamma_H$ , and the ratio between the average widths in the  $B_s^0$  and in the  $B_d^0$  systems,  $\Gamma_s/\Gamma_d$ .

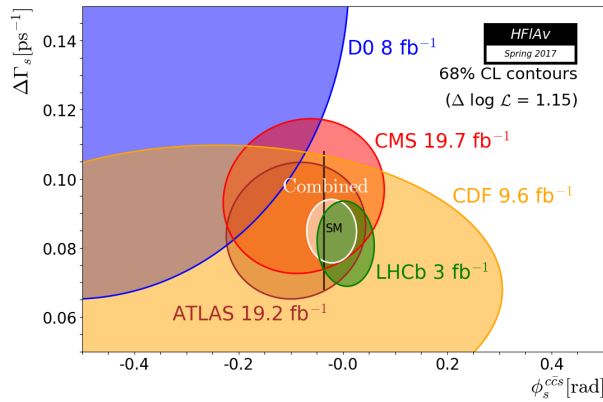


Figure 5.1: Individual 68% confidence-level contours of ATLAS, CMS, CDF, D0 and LHCb in the  $(\phi_s^{c\bar{c}s}, \Delta\Gamma_s)$ , their combined contour (solid line and shaded area), as well as the SM predictions (thick black rectangle) as performed by the HFLAV [?] averaging group.

### 5.2.1 Phenomenology

The baseline fit is obtained assuming that direct  $CP$  violation caused by penguin diagrams is the same for all polarization states, therefore  $\lambda_f$  is considered to be independent of the polarization state,  $f$ . Checks were made to check this ansatz.

The theoretical differential decay rate for an initial  $B_s^0$  as a function of decay time and angles using polarization dependent  $\lambda_f = |\lambda_f|e^{-i\phi_f} \equiv |\lambda_f|e^{-i\phi_f}$  ( $f = 0, ||, \perp, S$ ) is given as [?]

$$\frac{d^4\Gamma(t)}{dm_{KK}^2 d\cos\theta_K d\cos\theta_l d\phi} = \sum_{k=1}^{10} N_k h_k(t) f_k(\theta_K, \theta_l, \phi), \quad (5.7)$$

where the decay-time-dependent functions  $h_k(t)$  are given as

$$h_k(t) = \frac{3}{4\pi} e^{-\Gamma t} \left\{ a_k \cosh \frac{\Delta\Gamma t}{2} + b_k \sinh \frac{\Delta\Gamma t}{2} + c_k \cos(\Delta m t) + d_k \sin(\Delta m t) \right\}. \quad (5.8)$$

For an initial  $\bar{B}_s^0$  at production, the signs of  $c_k$  and  $d_k$  should be reversed. [appendix with coefficients?](#) For the purpose of reducing correlation between fit parameters, it can be chosen to fit for  $|\lambda_0|$ ,  $\phi_0$  and  $|\frac{\lambda_f}{\lambda_0}|$ ,  $\phi_f - \phi_0$ , for  $f \neq 0$ .

### 5.2.2 Samples and event selection

In this section, the data and simulated samples used in this analysis are introduced, together with the trigger, stripping and offline selections applied to these samples.

1251 **5.2.2.1 Data sample**

1252 The analysis presented in this report uses a data sample collected at the LHCb experiment  
 1253 at the LHC. The dataset corresponded to a total integrated luminosity  $\int \mathcal{L} 1.9 \text{fb}^{-1}$ . Of  
 1254 this,  $0.3 \text{fb}^{-1}$  were taken in 2015 at a centre-of-mass energy  $\sqrt{s} = 13 \text{TeV}$  and  $1.6 \text{fb}^{-1}$  were  
 1255 taken in 2016 at  $\sqrt{s} = 13 \text{TeV}$ .

1256 Stripping version 26 was used for 2016 data and stripping version 24 was used  
 1257 for 2015 data. All stripping versions use exactly the same selection, based on  
 1258 the `StrippingBetaSBs2JpsiPhiDetached` `StrippingBetaSBd2JpsiKstDetached` and  
 1259 `StrippingBetaSBu2JpsiKDetached` lines in the DIMUON stream. The data samples  
 1260 were processed using `DaVinci` version v42r1 and momentum scaling has been applied.

1261 **5.2.2.2 Simulation samples**

1262 In the LHCb simulation,  $pp$  collisions are generated using `Pythia` with a specific LHCb  
 1263 configuration [?, ?].

Table 5.1: MC samples used in the analysis. SX $X$  indicates the stripping version that  
 is used to flag the events. DecProdCut means that all the daughters are required to be  
 within LHCb acceptance.

| Event type      | Decay mode                             | Options                        | Year | Events |
|-----------------|--|--------------------------------|------|--------|
| Signal modes    |  |                                |      |        |
| 13144004        | $B_s^0 \rightarrow J/\psi \phi$        | Update2012,dG=0,DecProdCut,S26 | 2016 | 25M    |
| 13144011        | $B_s^0 \rightarrow J/\psi \phi$        | Update2016,DecProdCut,S26      | 2016 | 20M    |
| 13144011        | $B_s^0 \rightarrow J/\psi \phi$        | Update2012,DecProdCut,S28      | 2016 | 10M    |
| 13144011        | $B_s^0 \rightarrow J/\psi \phi$        | Update2016,DecProdCut,S24      | 2015 | XXM    |
| 13144041        | $B_s^0 \rightarrow J/\psi K^+ K^-$     | DecProdCut                     | 2016 | 7M     |
| Backgrounds     |  |                                |      |        |
| 15144001        | $\Lambda_b^0 \rightarrow J/\psi p K^-$ | PHSP, DecProdCut               | XXX  | XXM    |
| 24142001        | Inclusive Jpsi                         | JpsiInAcc                      | 2016 | 20M    |
| Control samples |  |                                |      |        |
| 11144001        | $B^0 \rightarrow J/\psi K^{*0}$        | Update2016,DecProdCut,S24      | 2015 | 10M    |
| 11144001        | $B^0 \rightarrow J/\psi K^{*0}$        | Update2016,DecProdCut,S26      | 2016 | 10M    |
| 12143001        | $B^+ \rightarrow J/\psi K^+$           | Update2016,DecProdCut,S24      | 2015 | 10M    |
| 12143001        | $B^+ \rightarrow J/\psi K^+$           | Update2016,DecProdCut,S26      | 2016 | 10M    |
| 24142001        | Inclusive Jpsi                         | JpsiInAcc                      | 2016 | 20M    |
| Generator Level |  |                                |      |        |

1264 Decays of hadronic particles are described by `EvtGen` [?], in which final state radia-  
 1265 tion is generated using `Photos` [?]. The `Geant4` toolkit simulates the interaction of the  
 1266 generated particles with the detector, and the detector response [?, ?]. Further details of  
 1267 the simulation process can be found in Ref. [?]. The simulated data is processed in a very

similar way to the real data, with the stripping run in flagging mode, with no prescales applied for the trigger. Sim09b was used for the simulated samples. The samples used are listed in Table 5.1.

Simulated signal samples are used to determine the angular acceptance. As will be discussed in Sec. ??, the samples are reweighted to match various distributions observed in data before obtaining the final acceptance. Similarly, the  $\Lambda_b^0$  and the  $B^0$  samples are used for background studies and decay time acceptance studies, respectively. This is discussed in Sec. ?? and Sec. ??, respectively. The  $B^+$  sample is used for tagging studies as described in Sec. ??.

The main physics parameters used in the main simulation used in this analysis, `Eventtype = 13144011, Bs_Jpsiphi,mm=CPV,update2016,DecProdCut`, are summarized in Table 5.2. For simulated samples a momentum smearing is applied in order to reproduce better the distributions in data.

Table 5.2: Decay model parameters for the Sim09b MC sample used in this analysis, `Eventtype = 13144011, Bs_Jpsiphi,mm=CPV,update2016,DecProdCut`.

| Parameter                       | Value             |
|---------------------------------|-------------------|
| $\Delta m_s$                    | $17.8 ps^{-1}$    |
| $\Delta \Gamma_s$               | $0.08543 ps^{-1}$ |
| $\Gamma_s$                      | $0.6614 ps^{-1}$  |
| $\phi_s$                        | $-0.03 rad$       |
| $ A_0(0) ^2$                    | 0.5242            |
| $ A_{\parallel}(0) ^2$          | 0.2256            |
| $ A_{\perp}(0) ^2$              | 0.2500            |
| $\delta_{\parallel} - \delta_0$ | $3.26 rad$        |
| $\delta_{\perp} - \delta_0$     | $3.08 rad$        |

### 5.2.2.3 Stripping selection

In order to select  $B_s^0 \rightarrow J/\psi \phi$  events, in data and MC we start from the stripping line `StrippingBetaSBs2JpsiPhiDetachedLine`, whose selection can be found in Table 5.3. We use Stripping version 26 or 28 for 2016 and Stripping version 24 for 2015. In both cases the selection is the same.

For time resolution studies we use the stripping line `BetaSBs2JpsiPhiPrescaledLine`, which has the same selection as shown in Table 5.3 apart from the cut on the decay time of the  $B_s^0$  candidate.

### 5.2.2.4 Trigger selection

The following trigger strategy has been identified in order to retain the largest number of signal events while keeping a small number of trigger lines.

Table 5.3: Selection criteria used to identify  $B_s^0 \rightarrow J/\psi\phi$  candidates.

|                                 | Variable                                 | Stripping                        |
|---------------------------------|--|----------------------------------|
| all tracks                      | $\chi_{\text{track}}^2/\text{nDoF}$      | < 3                              |
| $J/\psi \rightarrow \mu^+\mu^-$ | $\Delta\ln\mathcal{L}_{\mu\pi}(\mu^\pm)$ | > 0                              |
|                                 | $p_T(\mu^\pm)$                           | > 500 MeV/c                      |
|                                 | $\chi_{\text{DOCA}}^2$                   | < 20                             |
|                                 | $\chi_{\text{vtx}}^2/\text{nDoF}$        | < 16                             |
|                                 | $m(\mu^+\mu^-)$                          | $\in [3020, 3170]\text{MeV}/c^2$ |
| $\phi \rightarrow K^+K^-$       | $\chi_{\text{DOCA}}^2$                   | < 30                             |
|                                 | $p_T(\phi)$                              | > 500 MeV/c                      |
|                                 | $m(K^+K^-)$                              | $\in [980, 1050]\text{MeV}/c^2$  |
|                                 | $\chi_{\text{vtx}}^2/\text{nDoF}$        | < 25                             |
|                                 | $\Delta\ln\mathcal{L}_{K\pi}(K^+)$       | > 0                              |
| $B_s^0 \rightarrow J/\psi\phi$  | $m(J/\psi K^+K^-)$                       | $\in [5150, 5550]\text{MeV}/c^2$ |
|                                 | $\chi_{\text{vtx}}^2/\text{nDoF}$        | < 20                             |
|                                 | $t$                                      | > 0.2 ps                         |

- 1293 • No L0 requirements
- 1294 • HLT1 selection: `Jpsi_Hlt1DiMuonHighMassDecision_TOS` or  
1295    `B_Hlt1TrackMuonDecision_TOS` or `B_Hlt1TwoTrackMVADecision_TOS`
- 1296 • HLT2 selection: `Jpsi_Hlt2DiMuonDetachedJPsiDecision_TOS`

### 1297 5.2.2.5 Corrections

1298 Corrections are applied to the simulated samples to match the distributions obtained from  
1299 data:

- 1300 1. The stripped and triggered  $B_s^0 \rightarrow J/\psi K^+K^-$  candidates are taken, with the  $B_s^0$   
1301 decay time restricted to the range [0.3,15] ps.
- 1302 2. The data invariant mass distribution of stripped and triggered  $B_s^0 \rightarrow J/\psi K^+K^-$   
1303 candidates is fitted to obtain an sWeighted sample of data that is used in the  
1304 following steps.
- 1305 3. For MC, on top of the selection mentioned before only background categories 0  
1306 (signal) and 50 (radiative events) with true decay time different from 0 are included  
1307 [more details?](#).
- 1308 4. The simulation PID variable distributions are corrected using the `PIDCalib` package.

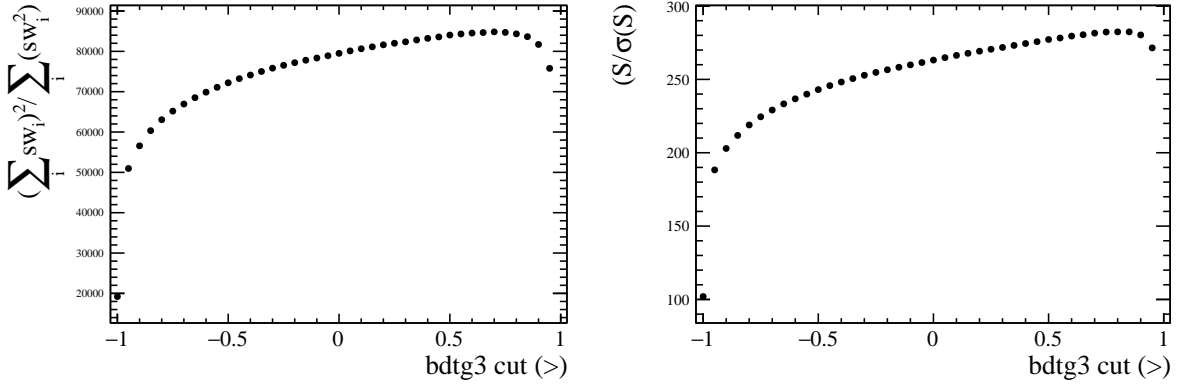


Figure 5.2: Distribution of the figure of merit used to optimise the cut on the BDT response (left) and distribution of signal yield divided by its uncertainty (right).

1309     5. Using the above data sample, the  $B_s^0$  production kinematics, nTracks distribution  
1310     and the muon/kaon track ghost probability variables are reweighted.

1311     A BDT is trained to further improve the signal to background ratio. It is trained  
1312     with 2016 samples. Namely, the 2016 corrected simulated sample for the signal sample  
1313     while 2016 data candidates with  $5450\text{MeV}/c^2 < m(J/\psi K^+ K^-) < 5550\text{MeV}/c^2$  are used  
1314     for the background sample. Special care was taken to avoid variables that could introduce  
1315     angular or decay time efficiencies, like impact parameter  $\chi^2$  of final state particles, the  
1316     direction angle of the  $B_s^0$  (DIRA) or transverse momentum of final state particles. The  
1317     figure of merit used to optimise the BDT response is given by

$$\text{FOM} = \frac{(\sum_i w_i)^2}{\sum_i w_i^2}, \quad (5.9)$$

1318     where the index  $i$  runs over all candidates in the sample and  $w_i$  are per-candidate weights  
1319     that are determined from the invariant mass fit that is performed at each point in the scan  
1320     over the BDT response. Figure 5.2 shows on the left how the figure of merit performs and  
1321     on the right the number of signal events divided by its uncertainty, both as a function  
1322     of the BDT response. A similar distribution is observed. The optimal value is found  
1323     to be at  $> 0.78$ . After the BDT requirement has been applied there are approximately  
1324     102 000 signal candidates and 26 000 background candidates in the mass window of the  
1325     fit,  $5320\text{MeV}/c^2 < m(J/\psi K^+ K^-) < 5420\text{MeV}/c^2$  in 2016. The signal to background ratio  
1326     is  $\sim 3.9$ . The mass fit used to determine sweights to statistically remove this background  
1327     and also the removal of peaking backgrounds for both 2015 and 2016 data samples is  
1328     described in detail in the next section.

### 1329     5.2.3 Mass fit and computation of signal sWeights

1330     The physics parameter of interest are extracted via a log-likelihood fit of the signal PDF  
1331     to the unbinned decay time and angular distributions. The events are first weighted

1332 to statistically subtract the background components using the *sPlot* method [?] with  
1333  $m(J/\psi K^+ K^-)$  as the discriminating variable.

1334 In order to have an improved resolution, the  $m(J/\psi K^+ K^-)$  is determined using both  
1335 the  $J/\psi$  mass and PV constraints. The combinatorial background is modelled with an  
1336 exponential function and the signal distribution with a double-sided *Crystal Ball* (CB)  
1337 function. The double-sided CB function uses the per-event mass error as conditional ob-  
1338 servable, so that the correlation between  $\cos \theta_\mu$  and mass resolution is taken into account.  
1339 The full *p.d.f* is the following:

1340

$$p = N_{sig} CB(x; \mu, \alpha_1, \alpha_2, n_1, n_2, s_1, s_2 | \sigma_i) \\ + N_{bkg}((1 - f_{B_d})e^{-\gamma_b x} + f_{B_d}Gauss(x; \mu_{B_d}, \sigma_{B_d}),$$

1341 where  $N_{sig}$  and  $N_{bkg}$  is a number of signal and background events correspondingly,  $\mu$  is the  
1342 mean of the distribution,  $s_1$  and  $s_2$  are the scale factors, which accounts for underestima-  
1343 tion of the per-event mass error,  $\alpha_1, \alpha_2, n_1, n_2$  are the tail parameters,  $\gamma_b$  is the coefficient  
1344 in the exponential to describe the background.

1345 The background sources that are considered **consist in**:

- 1346 •  $B^0 \rightarrow J/\psi K^{*0}$  peaking background, vetoed using PID cuts.
- 1347 •  $\Lambda_b^0 \rightarrow J/\psi p K^-$  peaking background, vetoed using PID cuts. The remaining events  
1348 are statistically subtracted by injecting simulated events into the data tuple with a  
1349 negative sum of weights equal to the expected number of events.
- 1350 •  $B^0 \rightarrow J/\psi K^+ K^-$  peaking background, modelled with a Gaussian in the nominal  
1351 mass fit.

1352 For the fit to the  $m(J/\psi K^+ K^-)$  distribution, the sample is divided into twenty-four  
1353 subsamples, each with an independent signal fraction and different signal mass shapes.  
1354 The subsamples correspond to six bins in the  $K^+ K^-$  mass, namely [990, 1008, 1016, 1020,  
1355 1024, 1032, 1050] MeV/ $c^2$ , two trigger categories:

- 1356 • “**Biased**”: `B_Hlt1TrackMuonDecision_TOS` or `B_Hlt1TwoTrackMVADecision_TOS`  
1357 and not `Jpsi_Hlt1DiMuonHighMassDecision_TOS`
- 1358 • “**Unbiased**”: `Jpsi_Hlt1DiMuonHighMassDecision_TOS`

1359 and two years of the data-taking (2015 and 2016). **plot?**

1360 The event multiplicity (ratio between the number of events containing more than one  
1361 candidate and the total number of events) is found to be 1.2% in the full  $B_s^0$  mass region,  
1362 but only 0.2% for candidates **in the signal region**. Most of these candidates are due to  
1363 cases where the  $J/\psi$  is shared and one or two different kaons are added, making these  
1364 events truly combinatorial in character. Given the low fraction of multiple events, it is  
1365 evaluated as a systematic contribution removed them randomly.

### 5.2.4 $C_{SP}$ factors

The relative change of the S-wave  $m_{KK}$  line shape with respect to that of the P wave has to be considered in the interference terms of the angular expressions, as we are performing the analysis in finite  $m_{KK}$  bins (see Ref. [?] for a detailed discussion). This is taken into account by adding a multiplicative correction factor,  $C_{SP}$ , to the signal PDF, namely to the S-P-wave interference terms with  $k = 8, 9, 10$  in Eq. (5.7), i.e.  $N_k \rightarrow C_{SP,i} N_k$ . There are in total six  $C_{SP}$  factors, one for each  $m_{KK}$  bin.

The line shapes of the P and S wave are denoted as  $p(m_{KK})$  and  $s(m_{KK})$ , respectively, where both are normalised to unity over a range  $[m_{KK}^L, m_{KK}^U]$ . Essentially, the issue is that  $\langle p \times s^* \rangle \neq \langle p \rangle \times \langle s^* \rangle$  in each  $m_{KK}$  bin. Therefore, the product  $p \times s^*$  is integrated, as it appears in the interference terms between the P and S wave. This yields

$$\frac{\int_{m_{KK}^L}^{m_{KK}^H} p \times s^* dm_{KK}}{\sqrt{\int_{m_{KK}^L}^{m_{KK}^H} |p|^2 dm_{KK} \int_{m_{KK}^L}^{m_{KK}^H} |s|^2 dm_{KK}}} = C_{SP} e^{-i\theta_{SP}}, \quad (5.10)$$

where  $C_{SP}$  is the correction factor and the phase  $\theta_{SP}$  is absorbed in the measurement of  $\delta_S - \delta_\perp$ . The shape of the P wave is a Breit-Wigner distribution, the same as in Eq.(4) of Ref. [?]. The S-wave line shape is an  $f_0$  with pole mass of  $0.9499 \text{ GeV}/c^2$  as measured in Ref. [?]. Both the  $f_0$  and  $\phi$  resonance distributions include a phase space factor  $\left(\sqrt{\frac{P_B}{m_B} \frac{P_R}{m_R} \frac{1}{\sqrt{s_{23}}}}\right)$ , two Blatt-Weisskopf factors for the  $B$  and the  $K^+K^-$  resonance, and birth and decay momenta of the  $f_0, \phi$  and  $B_s^0$ , where  $L_B = 1, L_R = 0$  for  $f_0$  and  $L_B = 0, L_R = 1$  for  $\phi$ . Note that the  $f_0$  mass is considered to be 949 MeV. This value, different from the PDG one ( $990 \pm 30$  MeV) [?], is taken from the  $B_s^0 \rightarrow J/\psi \pi^+ \pi^-$  measurement [?].

The detector resolution effect on the  $C_{SP}$  factors needs to be taken into account. While Eq.5.10 is defined in dependence on the true  $m_{KK}$ , the mass bins are defined in dependence on the measured  $m_{KK}$ . The resolution effect can be incorporated as an efficiency correction,  $\epsilon_i(m_{KK})$ , of the  $C_{SP}$  factors according to

$$C_{SP} e^{-i\theta_{SP}} = \frac{\int_{2m_K}^{m_{B_s^0}-m_{J/\psi}} p \times s^* \times \epsilon(m_{KK}) dm_{KK}}{\sqrt{\int_{2m_K}^{m_{B_s^0}-m_{J/\psi}} |p|^2 \times \epsilon(m_{KK}) dm_{KK} \int_{2m_K}^{m_{B_s^0}-m_{J/\psi}} |s|^2 \times \epsilon(m_{KK}) dm_{KK}}}, \quad (5.11)$$

where  $\epsilon(m_{KK})$  is

$$\epsilon(m_{KK}) = \begin{cases} 1, & \text{if } m_L < m_{KK} < m_H \\ 0 & \text{otherwise.} \end{cases}, \quad (5.12)$$

in the case where we bin in the true  $m_{KK}$  mass (or equivalently, have perfect resolution). In reality though, we cut on a measured mass that has a finite resolution, and hence  $\epsilon_i(m_{KK})$  will have a non-trivial structure. Note that in this definition we should consider events in the true  $m_{KK}$  spectrum up to  $2.27 \text{ GeV}/c^2$ , which is the value of  $m_{B_s^0} - m_{J/\psi}$ . However, the  $\phi$  contribution after a certain point in  $m_{KK}$  is too small to be modelled

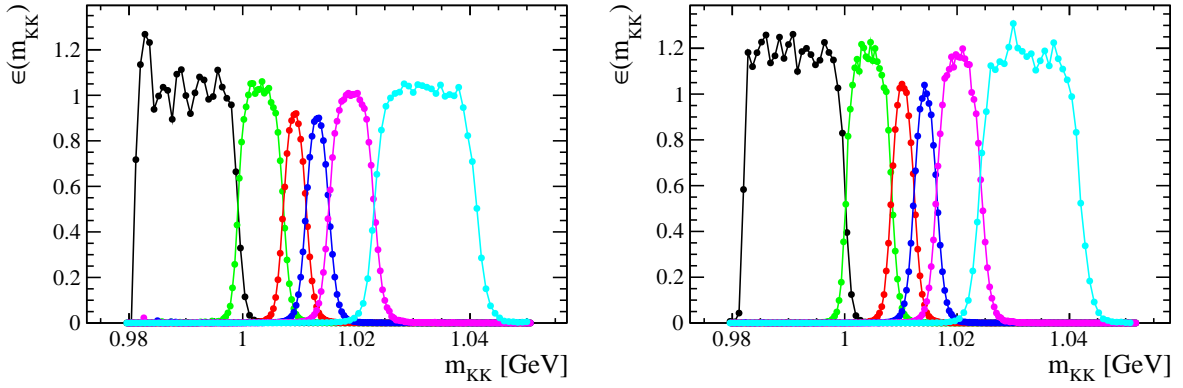


Figure 5.3: Efficiency of each  $m_{KK}$  bin selection as a function of MC true  $m_{KK}$  using MC without (left) and with (right) S wave.

well in MC, so we apply an upper limit cut at  $1.06 \text{ GeV}/c^2$ . We use simulated events from the 2016 MC sample with and without S wave (see Table 5.1) to determine  $\epsilon_i(m_{KK})$  by dividing the  $m_{KK}$  histogram before and after the selection of the events in each bin. Fig. 5.3 shows the corresponding distributions. We use the  $C_{SP}$  obtained from the MC without S wave with exception of the first bin, where the MC with S wave is used. The reason for this is that in the region of  $m_{KK}$ , the contribution of the S wave is the largest and the MC with S wave has more events. With this, we obtain the  $C_{SP}$  factors shown in Table 5.4.

Table 5.4:  $C_{SP}$  factors obtained using Eq. (5.11). The  $\phi$  resonance is parametrized with a relativistic Breit-Wigner.

| $m_{KK}$ bin | S-wave line shape |        |
|--------------|-------------------|--------|
|              |                   | $f_0$  |
| 1            |                   | 0.8569 |
| 2            |                   | 0.8768 |
| 3            |                   | 0.8478 |
| 4            |                   | 0.8821 |
| 5            |                   | 0.9406 |
| 6            |                   | 0.9711 |

### 1405 5.2.5 Decay time resolution

1406 An effective single-Gaussian model is used to parametrize the decay time resolution. This  
 1407 is sufficient to describe the damping effect of the time resolution. It is defined as follows,

$$\mathcal{P}(t) = \mathcal{R}(t) \otimes [f_{\text{prompt}}\delta(t) + f_{\text{ll}}(f_{\text{sl}}e^{-t/\tau_s} + (1-f_{\text{sl}})e^{-t/\tau_l})] + f_{\text{wpv}}W(t), \quad (5.13)$$

1408 Where  $t$  is the decay time,  $\delta_t$  the decay time uncertainty (both calculated from decay tree  
 1409 fit in which the PV position is constrained without constraining the  $J/\psi$  mass). This  
 1410 model is fitted to  $t$  in ten bins of  $\delta_t$ , with  $\mathcal{R}(t)$  being:

$$\mathcal{R}(t) \propto \sum_{i=1}^3 f_i \frac{1}{\sqrt{2\pi}\sigma_i} e^{-\frac{1}{2}\left(\frac{t-\mu}{\sigma_i}\right)^2}, \quad (5.14)$$

1411 where  $\sum_i f_i = 1$ . The three Gaussians have a common mean, different widths and two  
 1412 relative fractions, which are allowed to vary in the fit, as are the lifetime and relative  
 1413 fractions of the exponential functions. Another component corresponding to events with  
 1414 a wrongly-associated PV is added, the fraction of which is allowed to float in the fit. In  
 1415 each bin of  $\delta_t$ , the dilution of the triple Gaussian model is computed as,

$$D = \sum_{i=1}^3 f_i e^{-\sigma_i^2 \Delta m_s^2 / 2}, \quad (5.15)$$

1416 and the effective single Gaussian width as,

$$\sigma_{\text{eff}} = \sqrt{(-2/\Delta m_s^2) \ln D}, \quad (5.16)$$

1417 where  $\Delta m_s = 17.77\text{ps}^{-1}$ . This converts the resolution into a single-Gaussian function  
 1418 with an effective resolution that causes the same damping effect on the magnitude of the  
 1419  $B_s^0$  oscillation. A linear or quadratic calibration curve is then fitted to the variation of  
 1420 the effective resolution as a function of  $\langle\delta_t\rangle$  to determine the calibration parameters. For  
 1421 calibration, simulated  $B_s^0 \rightarrow J/\psi\phi$ , prompt  $J/\psi$  and inclusive  $J/\psi$  samples are used, as  
 1422 well as prompt  $J/\psi$  data. **check** The main source of systematic uncertainty in the calibra-  
 1423 tion of the decay time resolution model is the translation from the prompt background  
 1424 sample to the signal sample. In addition, there is a systematic arising from the choice to  
 1425 include or not the wrong-PV component.

### 1426 5.2.6 Angular acceptance

1427 The angular acceptance is modelled using *normalization weights*, **ref** obtained from fully  
 1428 simulated signal events from the Sim09b production. This simulation sample is iteratively  
 1429 weighted to match the distributions of final-state particle kinematics in the real data, as  
 1430 well as to match the physics parameters obtained from data, in order to correct for  
 1431 imperfections in the detector simulation. In order to do this, a GB reweighting is first  
 1432 applied in  $p(B_s^0)$ ,  $p_T(B_s^0)$  and  $m(K^+K^-)$ , together with a reweighting in  $p(K^\pm)$ ,  $p_T(K^\pm)$ .

1433 The angular normalizations are computed, and the process is repeated until convergence  
1434 is achieved (after 4 iterations).

1435 A total of 10 normalization weights are computed for each year and trigger category,  
1436 as indicated in table 5.5, where the combined weights are shown. The factorization of  
1437 angular acceptance and decay time acceptance is assumed. A systematic effect is assigned  
1438 to such assumption, comparing the final acceptance normalization weights obtained in six  
1439 equal populated decay time bins.

Table 5.5: Angular acceptance weights determined from all available Monte Carlo samples. The  $f_k$  are the normalizations of the angular functions (see Equation 5.7) including the acceptance. They are used in the normalization of the *p.d.f.*

| $k$                        | $f_k/f_1$              |                      |                        |                        |
|----------------------------|------------------------|----------------------|------------------------|------------------------|
|                            | 2015                   |                      | 2016                   |                        |
|                            | “Unbiased trigger”     | “Biased” trigger     | “Unbiased trigger”     | “Biased trigger”       |
| 1 (00)                     | $1 \pm 0$              | $1 \pm 0$            | $1 \pm 0$              | $1 \pm 0$              |
| 2 ( $\parallel\parallel$ ) | $1.0297 \pm 0.0019$    | $1.0278 \pm 0.0036$  | $1.02637 \pm 0.00079$  | $1.0181 \pm 0.0017$    |
| 3 ( $\perp\perp$ )         | $1.0299 \pm 0.0019$    | $1.0280 \pm 0.0035$  | $1.02590 \pm 0.00078$  | $1.0184 \pm 0.0017$    |
| 4 ( $\parallel\perp$ )     | $-0.0007 \pm 0.0015$   | $-0.0071 \pm 0.0030$ | $-0.00029 \pm 0.00063$ | $0.0017 \pm 0.0015$    |
| 5 ( $0\parallel$ )         | $-0.00013 \pm 0.00090$ | $0.0038 \pm 0.0017$  | $0.00115 \pm 0.00038$  | $0.00260 \pm 0.00080$  |
| 6 ( $0\perp$ )             | $0.00119 \pm 0.00089$  | $0.0026 \pm 0.0017$  | $-0.00010 \pm 0.00038$ | $-0.00091 \pm 0.00079$ |
| 7 (SS)                     | $1.0076 \pm 0.0013$    | $1.0123 \pm 0.0025$  | $1.00618 \pm 0.00054$  | $1.0112 \pm 0.0012$    |
| 8 (S $\parallel$ )         | $-0.0005 \pm 0.0012$   | $-0.0008 \pm 0.0023$ | $0.00045 \pm 0.00048$  | $-0.0003 \pm 0.0010$   |
| 9 (S $\perp$ )             | $-0.0008 \pm 0.0012$   | $0.0000 \pm 0.0023$  | $-0.00020 \pm 0.00049$ | $-0.0005 \pm 0.0010$   |
| 10 (S0)                    | $0.0013 \pm 0.0024$    | $-0.0047 \pm 0.0047$ | $-0.0008 \pm 0.0010$   | $-0.0059 \pm 0.0022$   |

1440 A cross-check has been performed using a sample of  $B^+ \rightarrow J/\psi K^+$  decays in 2016  
1441 data, **yielding a good consistency in the method.**

### 1442 5.2.7 Decay time acceptance

1443 The reconstruction efficiency is not constant as a function of the  $B_s^0$  decay time due to  
1444 displacement requirements made on signal tracks in the trigger and event selection and to  
1445 a decay-time-dependent efficiency to reconstruct the tracks in the VELO [?]. The overall  
1446 decay-time acceptance is determined using the control channel  $B^0 \rightarrow J/\psi K^*(892)^0$ , with  
1447  $K^*(892)^0 \rightarrow K^+\pi^-$ , which is kinematically very similar to the signal decay and it is  
1448 assumed to have a purely exponential decay-time distribution with a well-known lifetime  
1449 (i.e. the width difference  $\Delta\Gamma_d$  is ignored), namely  $1.518 \pm 0.004$  ps [?]. The strategy to  
1450 select  $B^0 \rightarrow J/\psi K^*(892)^0$  events and compute the sWeights is similar to the one used for  
1451  $B_s^0 \rightarrow J/\psi K^+K^-$  events. The  $K^+\pi^-$  system in the  $B^0 \rightarrow J/\psi K^+\pi^-$  decay can be in a  
1452 relative S-wave or P-wave configuration. A  $\sim 6\%$  presence of S-wave has been observed  
1453 in data, as described in [?]. However, the simulated  $B^0 \rightarrow J/\psi K^*(892)^0$  sample only  
1454 includes the P-wave component. To account for this, an iterative procedure similar to the

one described in 5.2.6 is applied, reweighting the simulation to match the  $B^0$   $p$  and  $p_T$ , as well as  $m(K^+\pi^-)$  distributions in data. [revisar](#)

The decay time acceptance is defined as

$$\varepsilon_{\text{data}}^{B_s^0}(t) = \varepsilon_{\text{data}}^{B^0}(t) \times \frac{\varepsilon_{\text{sim}}^{B_s^0}(t)}{\varepsilon_{\text{sim}}^{B^0}(t)}, \quad (5.17)$$

where  $\varepsilon_{\text{data}}^{B_s^0}(t)$  is the efficiency in data of the fully triggered, selected and weighted events in the  $B^0$  control channel and  $r(t) = \varepsilon_{\text{sim}}^{B_s^0}(t)/\varepsilon_{\text{sim}}^{B^0}(t)$  is the ratio of efficiencies of the simulated signal and control modes after the full trigger, selection and MC-data correction chain has been applied. This second term in the acceptance,  $r(t)$ , accounts for the small differences in the lifetime and kinematics between the signal and control modes. The MC events are reweighted to match the *p.d.f.* of the respective data. [more?](#)

To derive  $\varepsilon_{\text{data}}^{B_s^0}(t)$  a simultaneous fit is performed to both the simultaneous samples and the data control channel. This allows to have the overall uncertainties on the  $B_s^0$  data spline coefficients, thus providing an easier control on the associated systematic uncertainty. The decay time acceptance  $\varepsilon_{\text{data}}^{B_s^0}(t)$  is then used in the fit to the  $B_s^0$  data signal sample to determine the physics parameters.

For the  $B^0$  and  $B_s^0$  the model used for the fit is composed of the product of a single exponential, convoluted with a single Gaussian resolution, and the respective acceptance function. The latter is modelled using cubic splines with knots at [0.3, 0.58, 0.91, 1.35, 1.96, 3.01, 12.00]  $ps$  and the first coefficient is fixed to unity. The knot positions have been chosen according to an exponential distribution between [0.3, 15]  $ps$  in order to have six equally populated bins considering  $\Gamma = 0.66 ps$ . The last knot position is moved from 15  $ps$  to 12  $ps$  in order to have stable fits also for the trigger-year categories which have no decay candidates at these large decay times.

In order to obtain a single spline,  $s_{\text{data}}^{B_s^0}$ , that represents  $\varepsilon_{\text{data}}^{B_s^0}(t)$ , combinations of the following three splines are used to describe the acceptance of the three datasets:

- One spline representing the acceptance in  $B_s^0$  MC:  $s_{\text{sim}}^{B_s^0}$
- One spline representing the ratio of acceptances in  $B^0$  and  $B_s^0$  MC:  $s_{\text{sim}}^{B^0/B_s^0}$
- One spline representing the final acceptance in  $B_s^0$  data:  $s_{\text{data}}^{B_s^0}$

These splines are used in the following combinations to describe the acceptances for the three datasets:

- $B_s^0$  MC:  $s_{\text{sim}}^{B_s^0}$
- $B^0$  MC:  $s_{\text{sim}}^{B^0/B_s^0} \times s_{\text{sim}}^{B_s^0}$
- $B^0$  data:  $s_{\text{data}}^{B_s^0} \times s_{\text{sim}}^{B^0/B_s^0}$

1487 A single Gaussian models the resolution, and has a mean of 0ps and a width of  
 1488 42fs/39fs/42fs for  $B_s^0$  MC/ $B^0$  MC/ $B^0$  data, motivated by the studies in Section ?? and  
 1489 the difference of the resolution between  $B_s^0$  and  $B^0$  seen in truth matched MC. The lifetime  
 1490 in the fit is fixed to the World average value for data  $\tau_{B^0}^{\text{data}} = 1.518$  ps [?], and to the value  
 1491 used in the generation of the MC for the simulated samples, namely  $\tau_{B^0}^{\text{MC}} = 1.519$  ps and  
 1492  $\tau_{B_s^0}^{\text{MC}} = 1.512$  ps.

1493 The decay time acceptance is obtained separately for the data taking periods 2015  
 1494 and 2016 and two different trigger paths (“unbiased” and “exclusively biased”). [plots?](#)

1495 The lifetimes  $\tau(B^0)$  and  $\tau(B^+)$  in  $B^0 \rightarrow J/\psi K^{*0}$  and  $B^+ \rightarrow J/\psi K^+$  decays are  
 1496 measured as a crosscheck of the time acceptance procedure. 2016 data and simulation  
 1497 samples for both validation channels are used. The same procedure as for  $B_s^0 \rightarrow J/\psi\phi$  is  
 1498 used, including the spline knot positions and time resolution (see Sect. ??).

#### 1499 5.2.7.1 Measurement of $\tau(B^0)$

1500 The procedure to determine the decay time efficiency (Sect. ??) is validated by splitting  
 1501 the  $B^0 \rightarrow J/\psi K^{*0}$  control sample (both data and simulation) into two independent sets.  
 1502 One half of the sample is then used as a control while the other is used to measure  $\tau(B^0)$ .  
 1503 Three different criteria are considered for this, namely:

- 1504 • Splitting according to odd/even eventNumber in the original sample, where the  
 1505 sample that is used instead of  $B_s^0$  has a cut on  $\delta_t < 0.04$  ps.
- 1506 • Splitting according to odd/even eventNumber in the original sample, where the  
 1507 sample that is used for fitting has a cut on the opening angle between the kaon  
 1508 and the pion that come from the  $K^{*0}$ , angle  $< 0.025$  rad. The position of the cut  
 1509 is chosen such that the average of the opening angle distribution is close to the  
 1510 corresponding one for the  $B_s^0 \rightarrow J/\psi\phi$  sample.
- 1511 • Splitting on the  $K^{*0}$  mass: events with  $m(K^{*0}) < 890$  GeV/c<sup>2</sup> are used for fitting,  
 1512 events with  $m(K^{*0}) > 890$  GeV/c<sup>2</sup> are used as control sample.

1513 For the control samples, the  $B^0$  lifetime is fixed to its input for simulation (1.519 ps)  
 1514 and to the world average value for data (1.518 ps) [?]. We obtain the values listed in  
 1515 the first column of Table 5.6, where the deviation from the world average [?] is also  
 1516 shown. To further improve these results, we also try reweighting the simulated samples  
 1517 according such that the  $B^0$  meson  $p_T$  distribution matches that in data, as shown in  
 1518 Fig. 5.4. The corresponding values for the lifetime (second column of Table 5.6) show a  
 1519 better agreement with the PDG value. The fits to the decay time distribution with MC  
 1520 reweighting in  $p_T$  for the different splittings are shown in Fig. 5.5.

1521 Finally, a reweighting that takes into consideration the S-wave fraction present in data  
 1522 (in addition to the aforementioned MC reweighting in  $B^0 p_T$ ) is also considered, using the  
 1523 results from Section ???. The splitting that is applied is the one depending on the  $K^{*0}$   
 1524 mass. The corresponding fitted lifetime is found to be  $\tau(B^0) = 1.519 \pm 0.006$  ps,  $0.13\sigma$

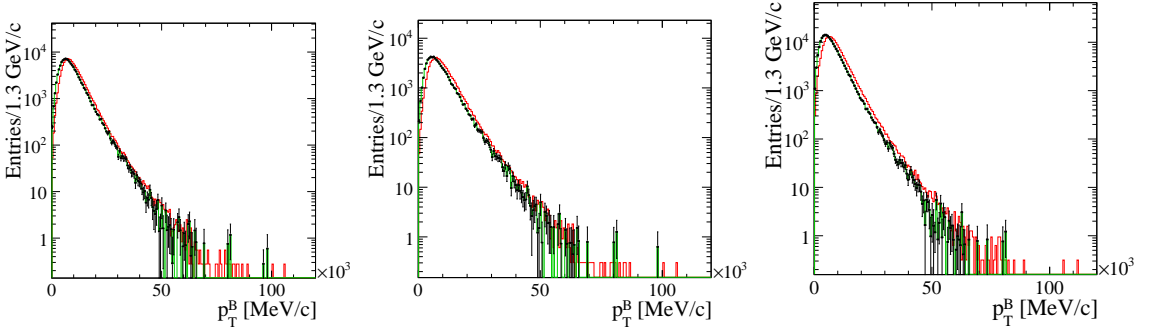


Figure 5.4: Distributions of  $p_T^B$  for  $B^0 \rightarrow J/\psi K^{*0}$  using splitting according to `eventNumber` with  $\sigma_t < 0.04$  (top left) and  $\text{angle} < 0.025$  (top right), and splitting according to  $m(K^{*0})$  (bottom). The black dots represent data and the red and green lines the MC before and after the reweighting, respectively.

1525 (0.05%) from the world average [?], thus showing a good agreement. The fitted decay  
 1526 time is shown in Fig. 5.5.

Table 5.6: Values of  $\tau(B^0)$  obtained for validation of the time acceptance method for the different considered splittings, with (first column) and without reweighting MC in  $p_T^B$ .

| Splitting                  | No $B^0 p_T$ reweighting                        | $B^0 p_T$ reweighting                           |
|----------------------------|---|---|
| $\delta_t < 0.04\text{ps}$ | $1.482 \pm 0.007\text{ps} (5.21\sigma, 2.35\%)$ | $1.518 \pm 0.007\text{ps} (0.05\sigma, 0.03\%)$ |
| angle $< 0.025\text{rad}$  | $1.522 \pm 0.008\text{ps} (0.52\sigma, 0.28\%)$ | $1.523 \pm 0.008\text{ps} (0.57\sigma, 0.31\%)$ |
| $m(K^{*0})$                | $1.518 \pm 0.006\text{ps} (0.02\sigma, 0.01\%)$ | $1.518 \pm 0.006\text{ps} (0.03\sigma, 0.01\%)$ |

1527 **uncertainties**

### 1528 5.2.8 Flavour tagging

1529 For time-dependent studies the ability of properly identifying the initial flavour of the  
 1530 meson (known as *flavour tagging*) is fundamental. To this end, two flavour tagging algo-  
 1531 rithms are used: the opposite-side (OS) taggers and the same-side kaon (SSK) taggers,  
 1532 which exploit specific features of the incoherent production of  $b\bar{b}$  quark pairs in  $pp$  colli-  
 1533 sions.

1534 Each tagging algorithm gives a tag decision and a mistag probability, the fraction of  
 1535 events with the wrong tag decision,  $\eta \in [0, 0.5]$ . The tag decision takes values +1, 1, or 0,  
 1536 if the signal meson is tagged as  $B_s^0$ ,  $\bar{B}_s^0$  or untagged, respectively. The fraction of events  
 1537 in the sample with a nonzero tagging decision gives the efficiency of the tagger,  $\varepsilon$ . The  
 1538 mistag probability is then calibrated to obtain the corrected per-event mistag probability,  
 1539  $\omega$ . This is used to determine the dilution factor,  $\mathcal{D} = (1 - 2\omega)$ , that rescales the efficiency  
 1540 of the tagger to quantify the fraction of the sample equivalent to perfectly tagged events.  
 1541 This effective efficiency is called tagging power, given by the product of the efficiency and  
 1542 the square dilution,  $\varepsilon\mathcal{D}^2$ .

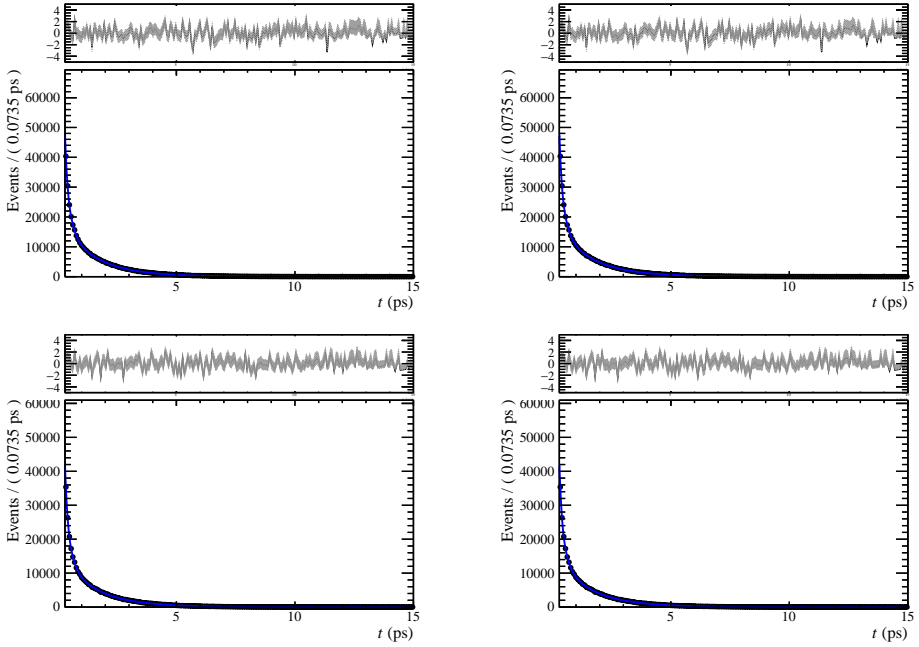


Figure 5.5: Decay time distribution of  $B^0 \rightarrow J/\psi K^{*0}$  decays and the corresponding likelihood fit result, splitting according to eventNumber with  $\sigma_t < 0.04$  (top left) and angle  $< 0.025$  (top right), and splitting according to  $m(K^{*0})$  without (bottom left) and with S-wave consideration.

1543 In this analysis the taggers have been optimised for Run 1 data but here their calibration  
 1544 is determined using Run 2 data. **update if necessary** A linear dependence of  $\omega$  with  
 1545  $\eta$  is assumed,

$$\omega = p_0 + p_1(\eta - \langle \eta \rangle) \quad (5.18)$$

1546 where  $p_0, p_1$  are calibration parameters and  $\langle \eta \rangle$  is the average predicted mistag probabilities  
 1547 for the calibration samples. When using OS and SSK algorithms, the calibration model become:  
 1548

1549

$$1550 \quad \omega^{\text{alg}} = (p_0^{\text{alg}} + \frac{\Delta p_0^{\text{alg}}}{2}) + (p_1^{\text{alg}} + \frac{\Delta p_1^{\text{alg}}}{2})(\eta^{\text{alg}} - \langle \eta^{\text{alg}} \rangle) \text{ for an initial } B_s^0 \text{ event}$$

$$1551 \quad \omega^{\text{alg}} = (p_0^{\text{alg}} - \frac{\Delta p_0^{\text{alg}}}{2}) + (p_1^{\text{alg}} - \frac{\Delta p_1^{\text{alg}}}{2})(\eta^{\text{alg}} - \langle \eta^{\text{alg}} \rangle) \text{ for an initial } \bar{B}_s^0 \text{ event}$$

1552 where  $r\text{malg} = \text{OS}, \text{SSK}$  and  $\Delta p_i^{\text{alg}}$  are mistag asymmetries.

1553 The calibration of the opposite-side tagger is made using  $B^+ \rightarrow J/\psi K^+$  decays,  
 1554 while for the same-side kaon tagger  $B_s^0 \rightarrow D_s^- \pi^+$  decays are used. The overall tagging performance is summarised in table 5.7.  
 1555

Table 5.7: Tagging performance

| Category | Fraction(%) | $\varepsilon(\%)$ | $\mathcal{D}^2$ | $\varepsilon\mathcal{D}^2(\%)$ |
|----------|-------------|-------------------|-----------------|--------------------------------|
| OS-only  | 14.44       | 10.26             | 0.087           | $0.90 \pm 0.03$                |
| SSK-only | 59.48       | 42.28             | 0.030           | $1.29 \pm 0.31$                |
| OS&SSK   | 26.09       | 18.54             | 0.099           | $1.84 \pm 0.12$                |
| Total    | 100         | 71.09             | 0.057           | $4.02 \pm 0.34$                |

### 1556 5.2.9 Data fitting

1557 The fitting procedure uses the sFit technique for background subtraction, as described  
 1558 in Section 5.2.3. The full PDF, based on Eq. (5.7) and taking into account all detector  
 1559 response effects, is given by

$$\begin{aligned} \mathcal{P}(t, \Omega | q^{\text{OS}}, q^{\text{SSK}}, \eta^{\text{OS}}, \eta^{\text{SSK}}, \sigma_t) &= \sum_{y=2015}^{2016} \sum_{g=b,ub} \sum_{i=1}^6 \sum_{k=1}^{10} \frac{1}{\mathcal{N}_{y,g}} \mathcal{P}_{i,k}(t, \Omega | q^{\text{OS}}, q^{\text{SSK}}, \eta^{\text{OS}}, \eta^{\text{SSK}}, \sigma_t) \\ &= \sum_{y=2015}^{2016} \sum_{g=b,ub} \sum_{i=1}^6 \sum_{k=1}^{10} \frac{1}{\mathcal{N}_{y,g}} \tilde{N}_{i,k} f_{g,y,k}(\Omega) \varepsilon_{g,y}(t) \\ &\quad \cdot \{ [(1 + q^{\text{OS}}(1 - 2\omega^{\text{OS}}(\eta^{\text{OS}}))) (1 + q^{\text{SSK}}(1 - 2\omega^{\text{SSK}}(\eta^{\text{SSK}}))) \\ &\quad \cdot h_k(t|B_s^0) \\ &\quad + (1 - q^{\text{OS}}(1 - 2\bar{\omega}^{\text{OS}}(\eta^{\text{OS}}))) (1 - q^{\text{SSK}}(1 - 2\bar{\omega}^{\text{SSK}}(\eta^{\text{SSK}}))) \\ &\quad \cdot h_k(t|\bar{B}_s^0)] \otimes G(t|\sigma_t) \}, \end{aligned} \quad (5.19)$$

1560 where  $i$  is the  $m_{KK}$  bin;  $y$  is the year of data taking;  $g$  is the trigger line (biased and unbiased);  
 1561  $q^{\text{OS}}$  and  $q^{\text{SSK}}$  are the OS and SSK tag decisions,  $\eta^{\text{OS}}$  and  $\eta^{\text{SSK}}$  the measured mistag probabilities,  
 1562  $\omega$  and  $\bar{\omega}$  the mistag probability calibration for  $B_s^0$  and  $\bar{B}_s^0$  (see Section ??);  $\varepsilon(t)$  is the decay time  
 1563 acceptance (see Section ??);  $G(t|\sigma_t)$  is the decay time resolution with decay time uncertainty  
 1564  $\sigma_t$  (see Section ??);  $\tilde{N}_{i,k} = N_k$  for  $k < 8$  and  $\tilde{N}_{i,k} = C_{\text{SP},i} N_k$  for  $k = 8, 9, 10$  (see Section 5.2.4);  
 1565  $\mathcal{N}_{y,g}$  is the normalisation given by

$$\mathcal{N}_{y,g}(t, \Omega | q^{\text{OS}}, q^{\text{SSK}}, \eta^{\text{OS}}, \eta^{\text{SSK}}, \sigma_t) = \int_{t=0.3\text{ps}}^{15\text{ps}} \int_{\Omega} \sum_{i=1}^6 \sum_{k=1}^{10} w_k \mathcal{P}_{i,k}(t, \Omega | q^{\text{OS}}, q^{\text{SSK}}, \eta^{\text{OS}}, \eta^{\text{SSK}}, \sigma_t) dt d\Omega, \quad (5.20)$$

1566 where  $w_k$  are the angular acceptance weights (see Section ??).

1567 The values of  $\phi_s$  and  $\Delta\Gamma_s$  were kept blinded during the full analysis.  
rephrase

### 1568 5.2.10 Baseline fit

1569  $\Delta\Lambda_d^s = \Lambda_s - \Lambda_d$  is fitted instead of  $\Lambda_s$ , given that it can be measured with a higher precision  
 1570 (independently of the value of  $\Lambda_d$  used in the determination of the time acceptance). Events

1571 with negative mistag probability are manually assigned  $\omega = 0$ . As said before,  $\lambda$  and  $\phi_s$  are  
 1572 assumed to be common to all polarisation states. Checks of this assumption are made, where  
 1573 polarisation dependence is instead considered. These are in agreement with the baseline fit.  
 1574 Several fitters were independently developed, including the baseline one, based on the usage of  
 1575 graphics processing units (GPUs). These are optimized for parallel calculations that allow a  
 1576 faster computation. A good agreement is found between the fit results provided by the different  
 1577 fitters.

1578 The fit result is given in Table ?? and the corresponding correlation matrix in Table ??.  
 1579 The statistical uncertainties reported are the symmetric uncertainties from Hesse<sup>ref</sup>. The  
 1580 background subtracted projection plots are shown in Figures ?? and ?? . One-dimensional  
 1581 likelihood profiles of the fit parameters are shown in Figures ??-?? . update A summary of the  
 1582 systematic uncertainties is shown in reference. ???

### 1583 5.2.11 Coverage of the uncertainty with the sFit

1584 To check the reliability of the uncertainties on the physics parameters in the data fit to the  
 1585 time and helicity angles, the method of bootstrapping is applied to both data and simulation.  
 1586 For this, a set of pseudo-samples is created by randomly selecting events from the simulation or  
 1587 data sample. The number of events in each pseudo-sample is the same as the number of events  
 1588 of the original one. After creating the samples, they are fitted, and the central value and pull  
 1589 distributions for each fit parameter are plotted (see figures in Appendix B). The correspond-  
 1590 ing bootstrapping uncertainty (and the uncertainty on the uncertainty) for each parameter is  
 1591 obtained from the RMS of the distribution of its central values.

#### 1592 5.2.11.1 Simulation

1593 The results for bootstrapping using simulation are shown in Table 5.8. For this study a simula-  
 1594 tion sample from 2016 has been used, with S26 applied. Good agreement is found between the  
 1595 errors provided by the fit and the ones computed using bootstrapping.

Table 5.8: Variation in the statistical uncertainties for the fit parameters using the errors provided by the fit and the ones obtained with bootstrapping for simulation.

| Parameter                        | Fit    | Bootstrapping             |
|----------------------------------|--------|---------------------------|
| $f_L$                            | 0.0006 | $0.0005819 \pm 0.000002$  |
| $f_\perp$                        | 0.0008 | $0.000796 \pm 0.0000126$  |
| $\phi_s$ [rad] *                 | 0.0016 | $0.0016091 \pm 0.0000256$ |
| $\delta_\perp$ [rad]             | 0.006  | $0.0063273 \pm 0.0001005$ |
| $\delta_\parallel$ [rad]         | 0.007  | $0.006711 \pm 0.0001066$  |
| $ \lambda $                      | 0.001  | $0.0010967 \pm 0.0000174$ |
| $\Delta\Gamma_d^s$ [ $ps^{-1}$ ] | 0.0005 | $0.00057 \pm 0.0000091$   |
| $\Delta\Gamma_s$ [ $ps^{-1}$ ] * | 0.0016 | $0.0015527 \pm 0.0000247$ |
| $\Delta ms$ [ $ps^{-1}$ ]        | 0.0021 | $0.0021915 \pm 0.0000348$ |

1596 **5.2.11.2 Signal and background simulation**

1597 A sample composed by signal and background is used for the bootstrapping studies. It is  
 1598 obtained using a S28, 2016 simulation sample, combined with background that is generated  
 1599 from 2016 data's sidebands. The preliminary results are shown in Table 5.9. Results for the  
 1600 nominal fit are shown in Table 5.10, together with the corresponding inputs used for MC. As  
 1601 for the test with pure signal MC (see Sec. 5.2.11.1), good agreement is found between the errors  
 1602 obtained using bootstrapping and the ones provided by the fit.

Table 5.9: Variation in the statistical uncertainties for the fit parameters using the errors provided by the fit and the ones obtained with bootstrapping for signal and background simulation.

| Parameter                        | Fit       | Bootstrapping             |
|----------------------------------|-----------|---------------------------|
| $f_L$                            | 0.0008834 | $0.0008598 \pm 0.0000118$ |
| $f_\perp$                        | 0.001239  | $0.0012018 \pm 0.0000165$ |
| $\phi_s$ [rad] *                 | 0.009296  | $0.0094382 \pm 0.0001296$ |
| $\delta_\perp$ [rad]             | 0.03491   | $0.036471 \pm 0.0005006$  |
| $\delta_\parallel$ [rad]         | 0.0289    | $0.0239876 \pm 0.0003292$ |
| $ \lambda $                      | 0.006291  | $0.0062407 \pm 0.0000857$ |
| $\Delta\Gamma_d^s$ [ $ps^{-1}$ ] | 0.0007465 | $0.0007257 \pm 0.000010$  |
| $\Delta\Gamma_s$ [ $ps^{-1}$ ] * | 0.002395  | $0.0022637 \pm 0.0000311$ |
| $\Delta m_s$ [ $ps^{-1}$ ]       | 0.01379   | $0.0144994 \pm 0.000199$  |

Table 5.10: Fit results for signal and background simulation

| Parameter                        | Fit                      | Input   |
|----------------------------------|--------------------------|---------|
| $f_L$                            | $0.5288 \pm 0.0008834$   | 0.5241  |
| $f_\perp$                        | $0.247 \pm 0.001239$     | 0.25    |
| $\phi_s$ [rad] *                 | $-0.04027 \pm 0.009296$  | -0.03   |
| $\delta_\perp$ [rad]             | $3.042 \pm 0.03491$      | 3.08    |
| $\delta_\parallel$ [rad]         | $3.23 \pm 0.0289$        | 3.26    |
| $ \lambda $                      | $0.9988 \pm 0.006291$    | 1.0     |
| $\Delta\Gamma_d^s$ [ $ps^{-1}$ ] | $0.005276 \pm 0.0007465$ | 0.00601 |
| $\Delta\Gamma_s$ [ $ps^{-1}$ ] * | $0.08673 \pm 0.002395$   | 0.0854  |
| $\Delta m_s$ [ $ps^{-1}$ ]       | $17.8 \pm 0.01379$       | 17.8    |

1603 **5.2.11.3 Data**

1604 The results for bootstrapping using 2016 data can be seen in Table 5.11. In this case, sWeighted  
 1605 2016 data has been used, with Stripping version 26. Contrary to simulation, discrepancies are  
 1606 found between bootstrapping and fit errors, especially in the strong phases and the S wave fit  
 1607 fractions. There could be a couple of possible explanations for this. First, the sWeights used for  
 1608 the fit are not recalculated for each randomly drawn sample, which can lead to differences in the  
 1609 uncertainties. However, this doesn't seem to affect the MC and so is probably only a secondary  
 1610 effect. Second, the bootstrapping test shows two minima for  $\delta_S^1 - \delta_\perp$ . A likelihood profile  
 1611 test on the data confirmed this. A reliable error estimation for the lower minimum is impossible  
 1612 because it merges with the higher minimum before the likelihood changes by a significance of  $1\sigma$ .  
 1613 Last but not least, the likelihoods of some parameters show an asymmetric and non-Gaussian  
 1614 behaviour. This is especially true for the S wave parameters, where the fit fractions are low and  
 1615 we lack the statistical power to determine their uncertainties. In these cases, the fit errors are  
 1616 not an apt estimate of the uncertainties. Instead, for the final result the uncertainties will be  
 1617 taken from the parameter likelihood profiles.

Table 5.11: Variation in the statistical uncertainties for the fit parameters using the errors provided by the fit and the ones obtained with bootstrapping for 2016 data.

| Parameter                       | Fit      | Bootstrapping             |
|---------------------------------|----------|---------------------------|
| $f_L$                           | 0.003124 | $0.0032169 \pm 0.0000474$ |
| $f_\perp$                       | 0.0043   | $0.0043788 \pm 0.0000645$ |
| $\phi_s$ [rad] *                | 0.04637  | $0.0474420 \pm 0.0006984$ |
| $\delta_\perp$ [rad]            | 0.1304   | $0.1492076 \pm 0.0021966$ |
| $\delta_\parallel$ [rad]        | 0.07729  | $0.0414571 \pm 0.0006103$ |
| $ \lambda $                     | 0.01579  | $0.0191426 \pm 0.0002818$ |
| $\Gamma_s$ [ $ps^{-1}$ ]        | 0.002529 | $0.0025023 \pm 0.0000368$ |
| $\Delta\Gamma_s$ [ $ps^{-1}$ ]* | 0.008355 | $0.0082595 \pm 0.0001216$ |
| $\Delta m_s$ [ $ps^{-1}$ ]      | 0.05667  | $0.0733526 \pm 0.0010799$ |
| $\delta_S^1 - \delta_\perp$     | 0.3492   | $0.6728437 \pm 0.0099055$ |
| $\delta_S^2 - \delta_\perp$     | 0.3653   | $0.3101728 \pm 0.0045663$ |
| $\delta_S^3 - \delta_\perp$     | 0.4979   | $0.4256790 \pm 0.0062668$ |
| $\delta_S^4 - \delta_\perp$     | 0.1823   | $1.6134152 \pm 0.0237524$ |
| $\delta_S^5 - \delta_\perp$     | 0.1006   | $0.4099490 \pm 0.0060352$ |
| $\delta_S^6 - \delta_\perp$     | 0.1935   | $0.2751857 \pm 0.0040512$ |
| $F_S^1$                         | 0.04565  | $0.0477817 \pm 0.0007034$ |
| $F_S^2$                         | 0.00963  | $0.0094324 \pm 0.0001389$ |
| $F_S^3$                         | 0.002055 | $0.0020870 \pm 0.0000307$ |
| $F_S^4$                         | 0.005845 | $0.0054945 \pm 0.0000809$ |
| $F_S^5$                         | 0.01386  | $0.0144309 \pm 0.0002124$ |
| $F_S^6$                         | 0.02029  | $0.0201681 \pm 0.0002969$ |

Table 5.12: Physics observables constraints imposed in this study.

| Observable  | Constraint  |
|---|---|
| $\Delta M_s^{\text{EXP/SM}}$  | $0.968 \pm 0.078$ <a href="#">TK: 0.887(59)[1712.06572]</a> |
| $\phi_s - \phi_s^{\text{SM}}$   | $0.0154 \pm 0.031$  |
| $\mathcal{B}(B_s^0 \rightarrow \mu^+ \mu^-)^{\text{EXP/SM}}$                              | $0.9 \pm 0.2(\text{EXP}) \pm 0.1(\text{TH})$                |
| $\mathcal{B}(B_d^0 \rightarrow \mu^+ \mu^-)^{\text{EXP/SM}}$                              | $4.0 \pm 2.0(\text{EXP}) \pm 0.4(\text{TH})$                |
| $\Delta m_s A_{SL} / \Delta \Gamma_s - (\Delta m_s A_{SL} / \Delta \Gamma_s)^{\text{SM}}$ | $-0.1258 \pm 0.5651$  |
| $\mathcal{B}(B^+ \rightarrow \tau^+ \nu_\tau)^{\text{EXP/SM}}$                            | $0.91 \pm 0.22$ [?]   |
| $\Delta C_7$  | $-0.02 \pm 0.02$ [?]  |
| $m_H$   | $125.09 \pm 20$ [GeV] <a href="#">[2016 PDG]</a>            |
| $\tan \beta$ : $M_A$ plane  | ATLAS limits for hMSSM scenario [?]                         |
| LSP   | Lightest neutralino   |

1618 combination with run 1?

## 1619 5.3 $\phi_s$ pheno

1620

1621 1. Introduction

1622 2. WCs

1623 3. Plots

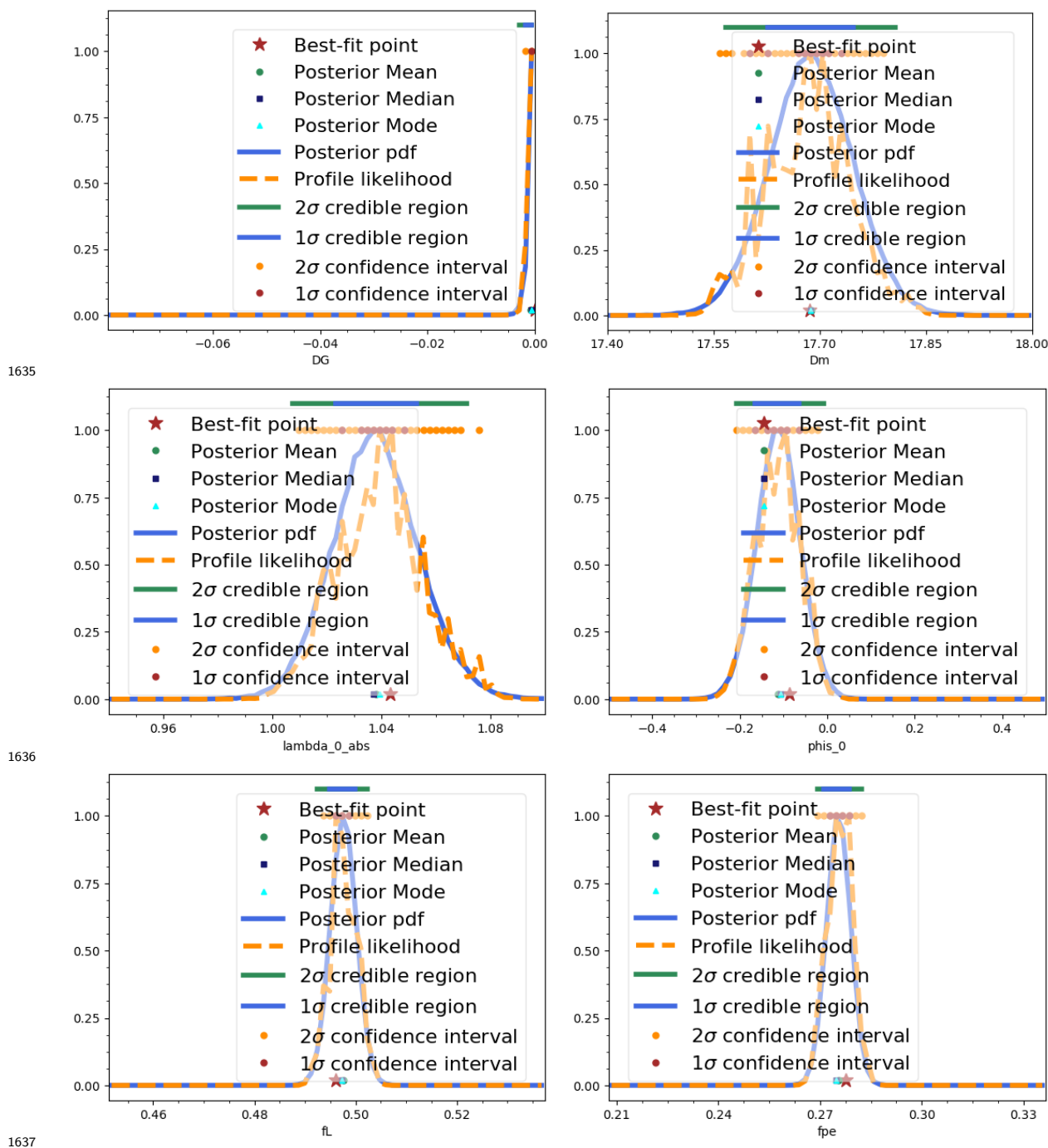
1624 4. Scan ranges

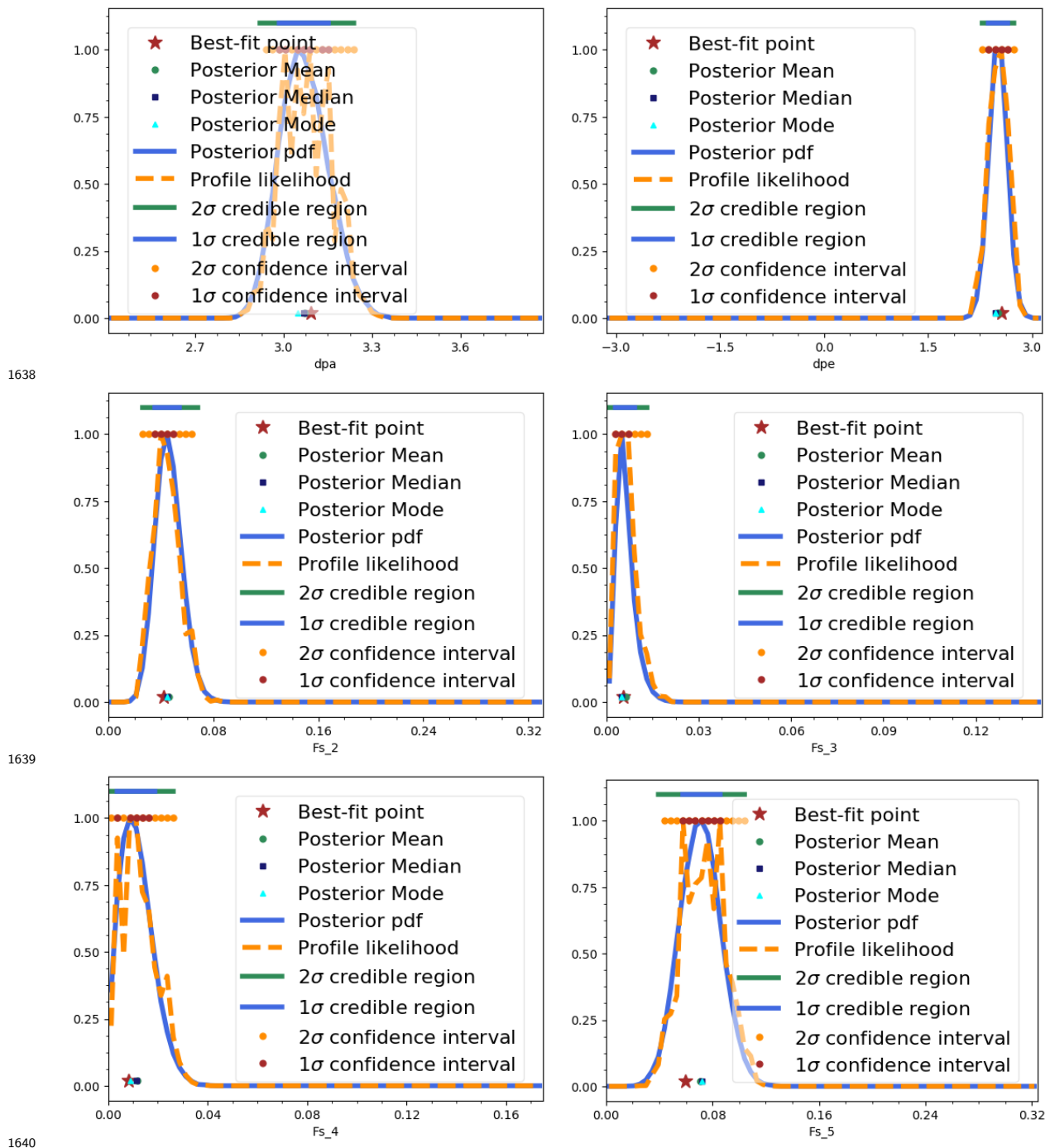
1625 5. Interpretation

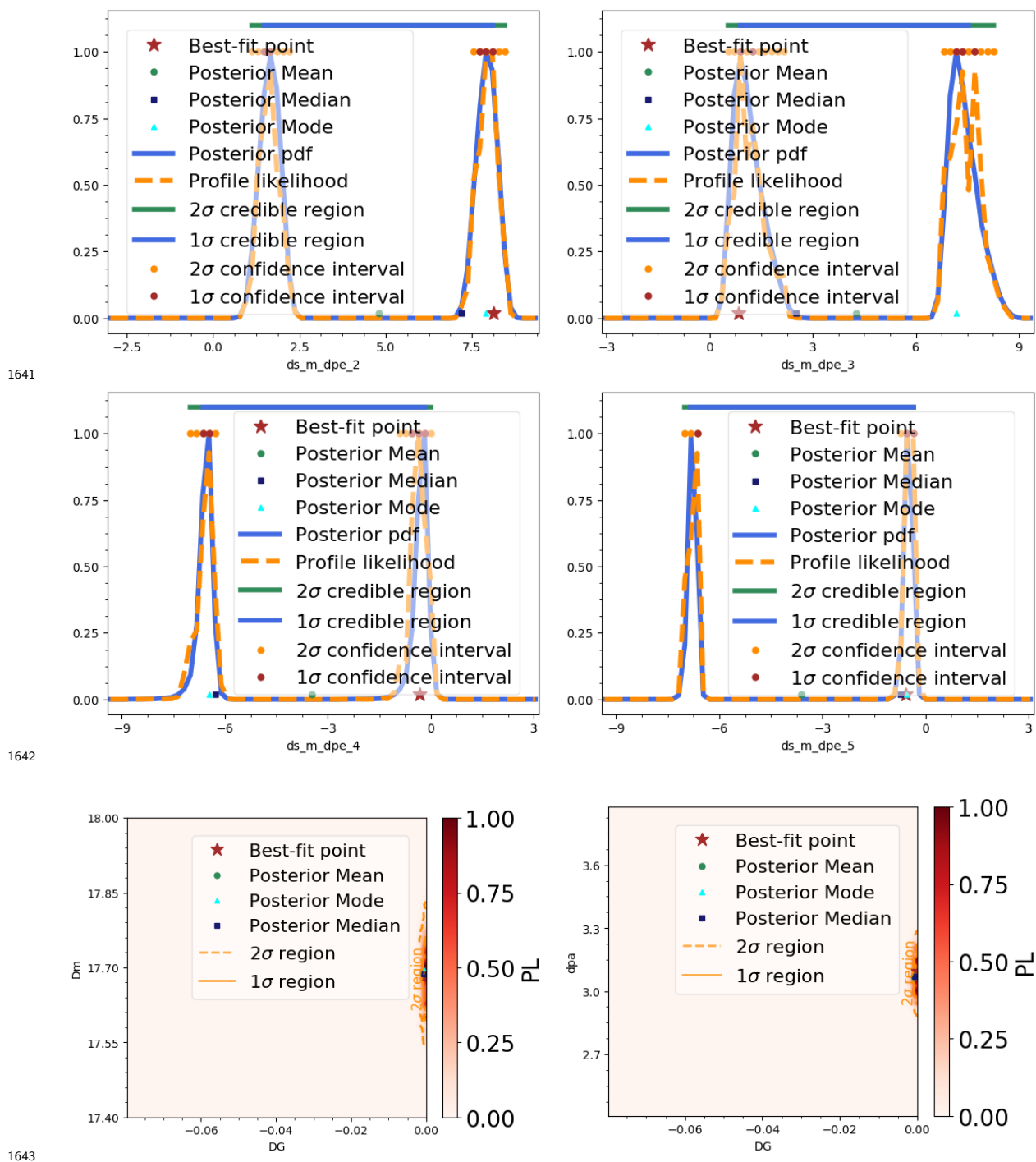
### 1626 5.3.1 Observables

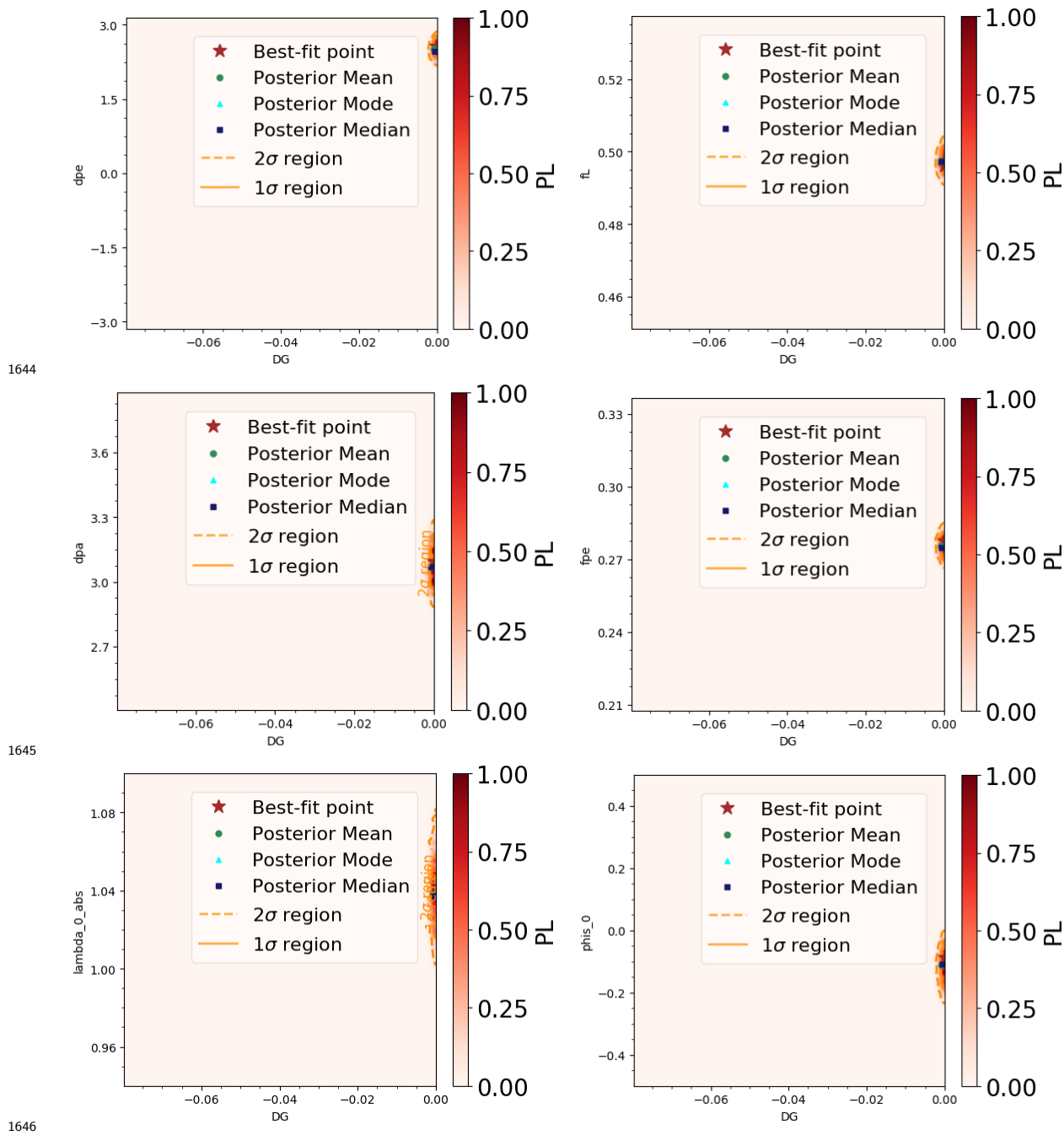
## 1627 5.4 $\phi_s$ MultiNest

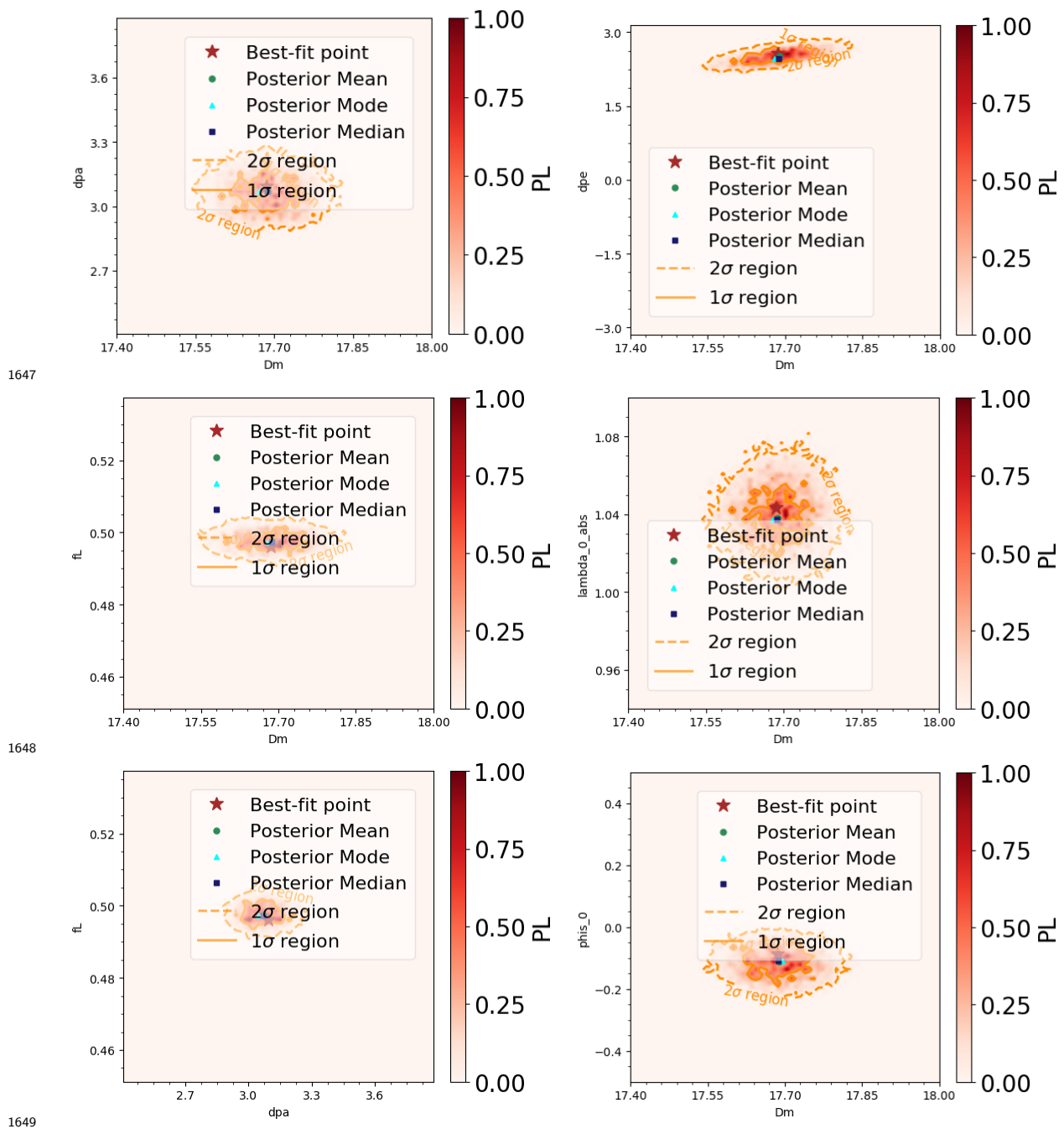
1628 A scan is performed using the `MultiNest` Bayesian inference tool [53], with [2016 LHCb data](#).  
1629 More details on the `MultiNest` algorithm are given in the following subsection. The lower and  
1630 upper bins are removed from the scan, as they represent a high computational cost and they  
1631 don't have much statistics. Therefore, only 4  $m_{KK}$  bins are used. To this same end,  $\Gamma_s - \Gamma_d$   
1632 is fixed to its [PDG value](#),  $-0.002678 \text{ ps}^{-1}$ . The results are shown in figures 5.4 and [5.4](#). As it  
1633 can be seen from these, the scan results are in agreement with the fit results. Moreover, two  
1634 minimas for positive and negative  $\Delta \Gamma_s$  are shown. ...

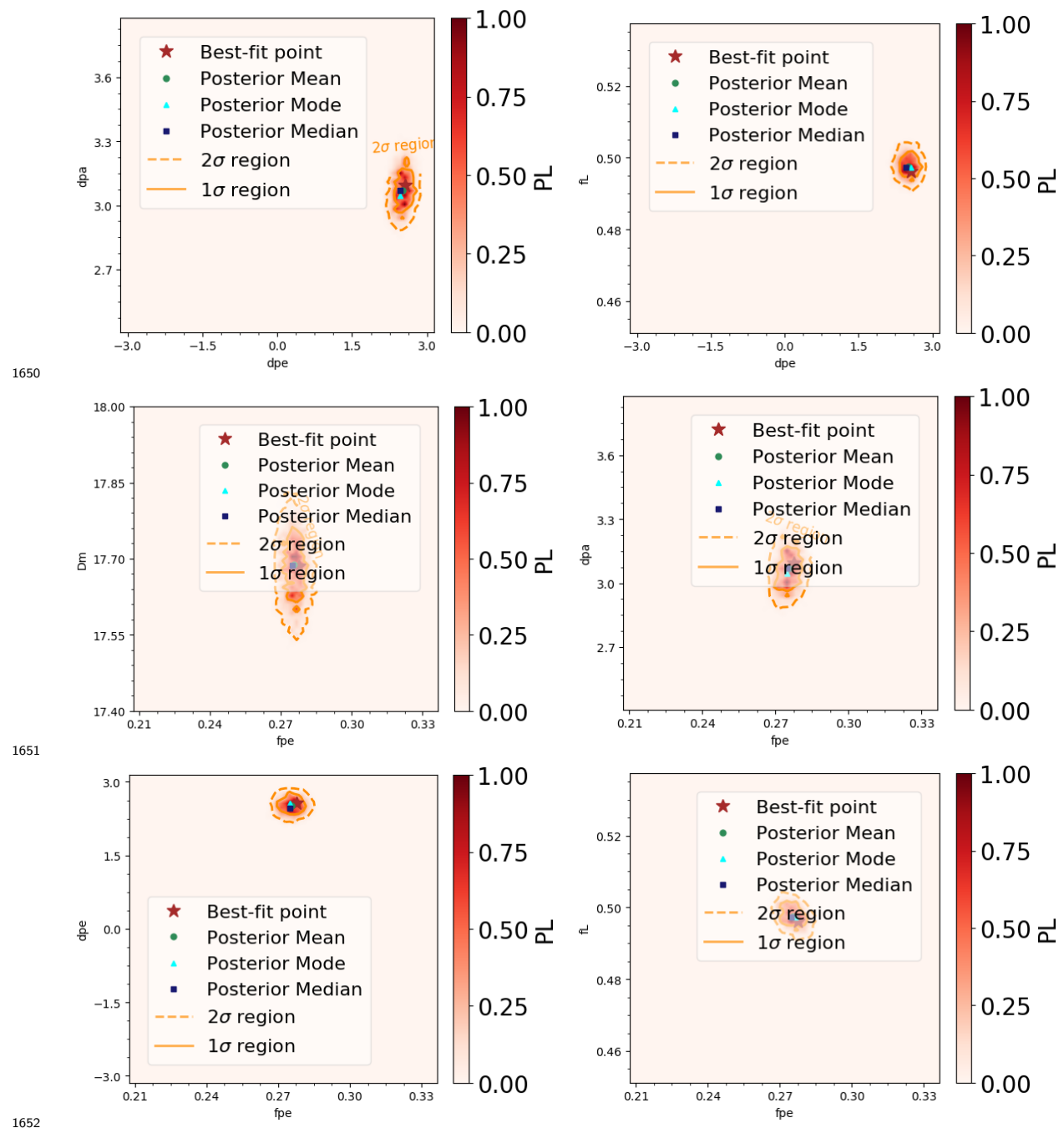


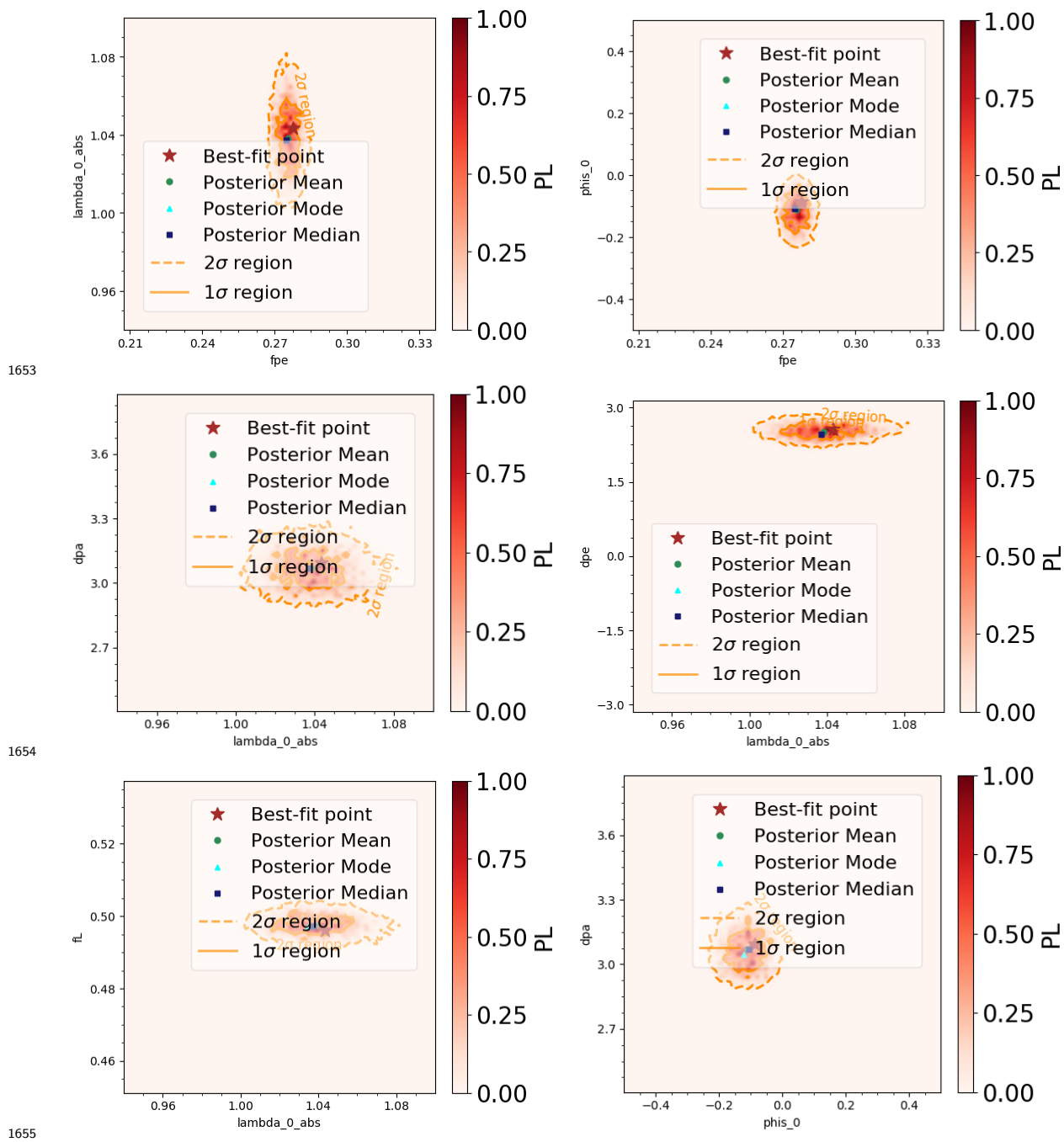


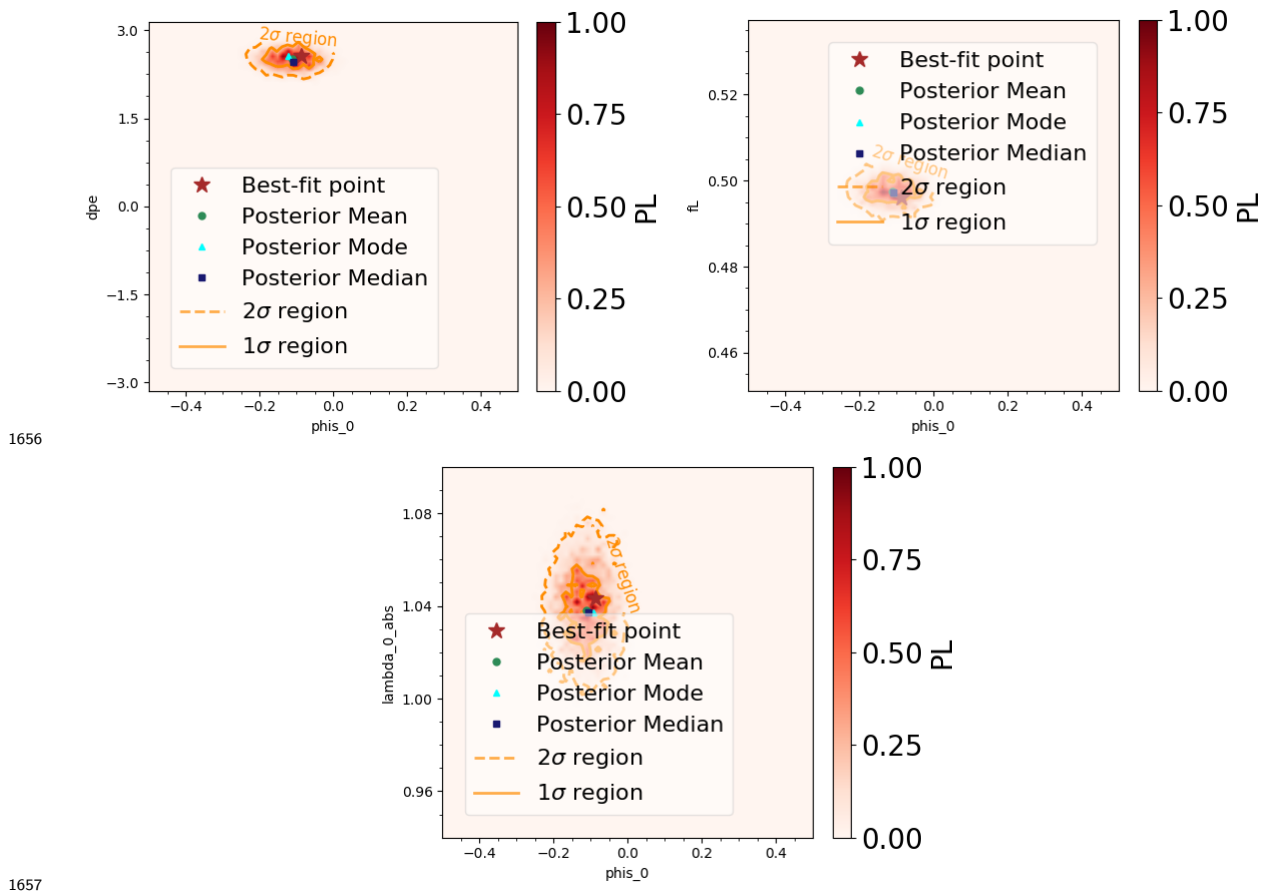












### 1659 1. Description of the tool

- 1660 2. Description of the plots + Methodology
- 1661 3. Conclusions from the plots

#### 1662 5.4.1 MultiNest

1663 ?? MultiNest is a multimodal, parallelizable nested sampling algorithm.

1664 It calculates the evidence, with an associated error estimate, and produces posterior samples  
 1665 from distributions that may contain multiple modes and/or pronounced (curving) degeneracies  
 1666 in high dimensions. The algorithm also naturally identifies individual modes of a distribution,  
 1667 allowing for the evaluation of the 'local' evidence and parameter constraints associated with  
 1668 each mode separately.

##### 1669 5.4.1.1 Bayesian inference

1670 Bayesian inference provides a consistent approach to the estimation of a set of parameters  $\Theta$  in  
 1671 a model or hypothesis  $H$ , for the data,  $D$ ,  $Pr(\Theta|D, H)$ , according to Bayes' theorem ref. The

1672 Bayesian evidence,  $Pr(D|H) \equiv \mathcal{Z}$ , usually ignored in parameter estimation problems, plays a  
 1673 central role in model selection. It is the factor required to normalize the posterior over  $\Theta$ .

$$\mathcal{Z} = \int \mathcal{L}(\Theta)\pi(\Theta)d^D\Theta \quad (5.21)$$

1674 Where D is the dimensionality of the parameter space. The evaluation of this integral is a  
 1675 challenging numerical task.

#### 1676 5.4.1.2 Nested sampling

1677 Nested sampling is a MC technique aimed at efficient evaluation of the Bayesian evidence, but  
 1678 also produces posterior inferences as a by-product. It exploits the relation between the likelihood  
 1679 and prior volumeeta ( $dX = \pi(\Theta)d^D\Theta$ ) to transform the multidimensional evidence integral into  
 1680 a one-dimensional integral:

$$\mathcal{Z} = \int_0^1 \mathcal{L}(X)dX \quad (5.22)$$

1681  $\mathcal{L}(X)$  is a monotonically decreasing function of X. Thus:

$$\mathcal{Z} = \sum_{i=1}^M \mathcal{L}_i w_i dX \quad (5.23)$$

1682 • i=0 and N 'active' or 'live' samples are drawn from the full prior  $\pi(\Theta)$ , so that the initial  
 1683 prior volume is  $X_0 = 1$ .

1684 • Samples are sorted in order of their likelihood and the smallest ( $\mathcal{L}_0$ ) is discarded, becoming  
 1685 'inactive', and replaced by a point drawn from the prior subject to the constraint  $\mathcal{L} > \mathcal{L}_0$ .  
 1686  $X_1 = t_1 X_0$ ,  $Pr(t) = Nt^{N-1}$

1687 • Repeat previous tep, until the entire prior volume has been traversed. The algorithm thus  
 1688 travels through nested shells of likelihood as the prior volume is reduced.

1689 •  $X_i = \exp(-i/N)$

1690 • Algorithm is terminated on determining the evidence to some specified precision:  $\Delta\mathcal{Z} =$   
 1691  $\sum_{i=1}^N \mathcal{L}_j w_{M+j}$ ,  $w_{M+j} = X_M/N$  where N are the active points.

1692 Once the evidence is found, posterior inferences can be easily generated using inactive and active  
 1693 points generated in the nested sampling process. Each point is assigned the weight:

$$p_j = \frac{\mathcal{L}_j w_j}{\mathcal{Z}} \quad (5.24)$$

1694 **5.4.1.3 Ellipsoidal nested sampling**

1695 The most challenging task in implementing the nested sampling algorithm is drawing samples  
1696 from the prior within the hard constraint  $\mathcal{L} > \mathcal{L}_i$  at each iteration  $i$ . Ellipsoidal nested sam-  
1697 ple tries to overcome this problem by approximating the iso-likelihood contour  $\mathcal{L} = \mathcal{L}_i$  by a  
1698 D-dimensional ellipsoid, determined from the covariance matrix of the current set of active  
1699 points. New points are selected from the prior within this ellipsoidal bound until one fulfills  
1700 the aforementioned condition. This method is not well suited to multimodal distribution. Its  
1701 efficiency is improved by identifying distinct *clusters* of active points that are well separated and  
1702 constructing an individual (enlarged) ellipsoid bound for each cluster.

1703 **5.4.1.4 The MultiNest algorithm**

1704 The clusters in which the set of active points are partitioned are then enclosed in ellipsoids and  
1705 a new point is drawn from the set of these 'overlapping' ellipsoids (properly taking into account  
1706 the overlaps. For highly multimodal problems, the nested sampling algorithm would require  
1707 a large number of active points to ensure that all the modes are detected, resulting in a slow  
1708 convergence.

1709 The MultiNest algorithm is controlled by two parameters:

- 1710 • The number of active points,  $N$ . It should be large enough that, in the initial sampling  
1711 from the full prior space, there is a high probability that at least one point lies in the  
1712 'basin of attraction' of each mode of the posterior. Also sufficiently large so that all the  
1713 regions of the parameter space are sampled adequately, bigger than the dimensionality of  
1714 the parameter space.
- 1715 • The maximum efficiency,  $e$ , that controls the sampling volume at each iteration, which is  
1716 equal to the sum of the volumes of the ellipsoids enclosing the active point set.

# <sup>1717</sup> Chapter 6

## <sup>1718</sup> Kaon Physics

### <sup>1719</sup> 6.1 Introduction

<sup>1720</sup> Kaons play a major role in particle physics, both for Standard Model (SM) and for New Physics  
<sup>1721</sup> (NP) searches. Their rare decays proceed mainly via flavour-changing neutral currents (FCNC),  
<sup>1722</sup> thus forbidden at loop level within the SM. This makes their branching fraction highly suppressed  
<sup>1723</sup> in the SM. Therefore, they constitute an excellent probe for New Physics manifesting in new  
<sup>1724</sup> particles entering the process.

<sup>1725</sup> Of all the possible kaon decays, the processes involving a  $s \rightarrow d$  transition (see Fig. 6.1) have  
<sup>1726</sup> the strongest CKM suppression factor ( $\propto V_{td}V_{ts} \sim 10^{-4}$ ). Hence, they are particularly sensitive  
<sup>1727</sup> to sources of flavour violation different from those of the Standard Model (SM). Indeed, flavour  
<sup>1728</sup> violation can induce detectable effects at accessible energy in flavour-changing processes even if  
<sup>1729</sup> the scale of the new dynamics is heavy and well above their direct production at accelerators.  
<sup>1730</sup> Among these transitions, the decay  $K_L^0 \rightarrow \pi^0\mu^+\mu^-$  has been shown to be sensitive to, for  
<sup>1731</sup> example, models with extra dimensions [?]. However, the potential for this decay to constrain  
<sup>1732</sup> scenarios beyond the Standard Model is limited by the large SM uncertainty on its branching  
<sup>1733</sup> fraction prediction [?],

$$\mathcal{B}(K_L^0 \rightarrow \pi^0\mu^+\mu^-)_{\text{SM}} = \{1.4 \pm 0.3; 0.9 \pm 0.2\} \times 10^{-11}. \quad (6.1)$$

<sup>1734</sup> The two numbers in the brackets correspond to two theoretical solutions, depending on whether  
<sup>1735</sup> constructive or destructive interference between the contributing waves is present. The reason  
<sup>1736</sup> for the large theoretical uncertainty on  $\mathcal{B}(K_L^0 \rightarrow \pi^0\mu^+\mu^-)_{\text{SM}}$  is the limited precision on the  
<sup>1737</sup> chiral-perturbation-theory parameter  $|a_S|$ . An improved measurement of  $\mathcal{B}(K_S^0 \rightarrow \pi^0\mu^+\mu^-)$  will  
<sup>1738</sup> reduce this uncertainty. The most precise measurement of  $\mathcal{B}(K_S^0 \rightarrow \pi^0\mu^+\mu^-)$  was performed by  
<sup>1739</sup> the NA48 experiment at CERN [?], which obtained

$$\mathcal{B}(K_S^0 \rightarrow \pi^0\mu^+\mu^-) = (2.9^{+1.5}_{-1.2}(\text{stat}) \pm 0.2(\text{syst})) \times 10^{-9}. \quad (6.2)$$

#### <sup>1740</sup> Missing connector

<sup>1741</sup> Leptonic decays of pseudoscalar mesons with down-type quarks are known to be very sensitive  
<sup>1742</sup> to the Higgs sector of the Minimal Supersymmetric Standard Model (MSSM), due to, among  
<sup>1743</sup> others, enhancement factors proportional to  $(\tan^6 \beta/M_A^4)$ .<sup>1</sup> This factor comes from the so-

---

<sup>1</sup>Note that this enhancement factor is not present in the up-type quark case.

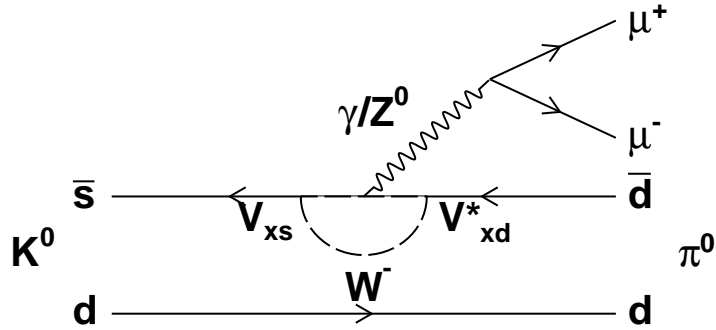


Figure 6.1: Feynman diagram of the process  $K^0 \rightarrow \pi^0 \mu^+ \mu^-$ .

1744 called non-holomorphic Yukawa terms at large  $\tan \beta$  [?, ?, ?, ?, ?, ?],<sup>2</sup> which are triggered by  
1745 the supersymmetric (SUSY)  $\mu$  term, and hence the non-SUSY two-Higgs-doublet model cannot  
1746 produce this enhancement [?]. The best known example is  $B_s^0 \rightarrow \mu^+ \mu^-$  [?, ?, ?, ?, ?, ?, ?, ?, ?, ?, ?, ?, ?, ?, ?, ?, ?, ?, ?].  
1747

1748 If Minimal Flavour Violation (MFV) is imposed, then  $B_s^0 \rightarrow \mu^+ \mu^-$  is the dominant constraint  
1749 in  $P \rightarrow \mu^+ \mu^-$  decays. This is due to the stronger Yukawa coupling of the  $b$ -quark compared to  
1750 the  $s$ -quark, and to the better experimental precision in  $B_s^0 \rightarrow \mu^+ \mu^-$  compared to  $B_d^0 \rightarrow \mu^+ \mu^-$ .  
1751 However, in the presence of new sources of flavour violation, the sensitivity of each mode depends  
1752 on the flavour and  $CP$  structures of the corresponding terms.

1753 Hence, a priori,  $B_s^0 \rightarrow \mu^+ \mu^-$ ,  $B_d^0 \rightarrow \mu^+ \mu^-$ ,  $K_S^0 \rightarrow \mu^+ \mu^-$ , and  $K_L^0 \rightarrow \mu^+ \mu^-$  are all separate  
1754 constraints that carry complementary information in the general MSSM. The observables related  
1755 to these decay modes are typically branching fractions and  $CP$  asymmetries. Even though  
1756 the muon polarization could carry interesting information, it cannot be observed by current  
1757 experiments.

1758 Even though the LHCb experiment ref was not initially designed to study these particles,  
1759 the large amount of kaons produced at LHCb ref makes them a rich area to study. moreIt  
1760 has demonstrated very good performance in the search for rare leptonic  $K_S^0$  decays [?]. In  
1761 the following sections, we evaluate the potential sensitivity of LHCb to  $\mathcal{B}(K_S^0 \rightarrow \pi^0 \mu^+ \mu^-)$   
1762 considering the data to be collected with the LHCb detector before and after its upgrade in  
1763 2018, as well as supersymmetric contributions to the decay  $K_S^0 \rightarrow \mu^+ \mu^-$  in light of current  
1764 experimental data.

## 1765 6.2 $K_S^0 \rightarrow \pi^0 \mu^+ \mu^-$ Sensitivity study

1766 ??

1767

---

<sup>2</sup> The higher-order contributions have been derived up to two-loop level in refs. [?, ?, ?].

### 1768 6.2.1 Analysis strategy

1769 Decays of the  $K_s^0$  in LHCb are characterized by decay vertices separated from the interaction  
 1770 point<sup>3</sup>, and with tracks having an average transverse momentum significantly lower than those  
 1771 from  $b$  and  $c$  decays. The transverse momentum range is similar to typical tracks generated in  
 1772 the proton-proton collision and hence has almost no discriminating power.

1773 Muon candidates are combined into  $\mu^+\mu^-$  pairs. Then a  $\pi^0$  can be added to the dimuon pair  
 1774 to make a fully reconstructed  $K_s^0$  decay. However, since the reconstruction efficiency of the  $\pi^0$   
 1775 is limited, events in which no  $\pi^0$  is found are also considered, based only on the dimuon informa-  
 1776 tion. This leads to two independent analyses: one for the events in which all decay products  
 1777 are considered (hereafter FULL) and one in which only the dimuon pair is used (hereafter PAR-  
 1778 TIAL). The reconstructed candidates are then passed through a selection algorithm followed by  
 1779 a *Boosted Decision Tree* (BDT) classification, to reduce the high level of background.

1780 The properties of the  $K_s^0 \rightarrow \pi^0\mu^+\mu^-$  decays are studied using simulated samples with a  
 1781 differential decay rate modeled according to Ref. [?]. The corresponding  $\mu\mu$  mass distribution,  
 1782  $m_{\mu\mu}$ , as well as the dependence of the (cosine of the) dimuon helicity angle,  $\cos\theta_\mu$  (see the angle  
 1783 definitions in Fig. 6.2), on  $m_{\mu\mu}$  are shown in Fig. 6.3.

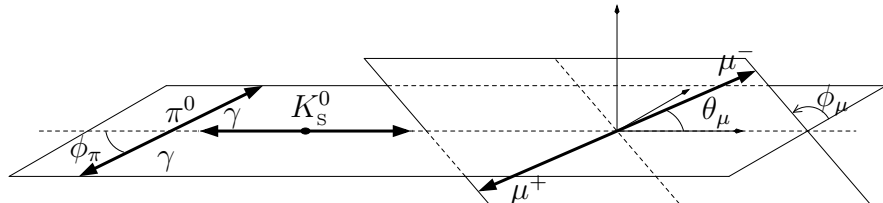


Figure 6.2: Definition of the helicity angles in the  $K_s^0$  rest frame.

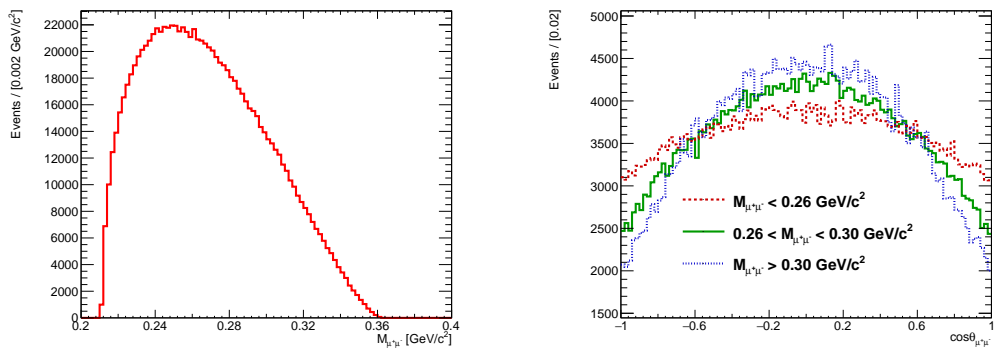


Figure 6.3:  $m_{\mu\mu}$  distribution (left), and the dimuon helicity angle depending on  $m_{\mu\mu}$  (right).

---

<sup>3</sup>The  $K_s^0$  at LHC typically decays after traversing tens of centimeters to even several meters.

1784        The BDT is trained with simulated signal events and combinatorial background events from  
 1785        the existing LHCb data. Since the main goal of this study is to evaluate the sensitivity for  
 1786        the LHCb upgrade, where the trigger efficiency is expected to be very high, trigger unbiased  
 1787        data samples are preferred. Therefore, the events are obtained from the *Trigger Independent of*  
 1788        *Signal* (TIS) [?] category of the LHCb trigger. This means that the tracks and clusters of the  
 1789        reconstructed candidate are not needed to fire the trigger at any level, because another object  
 1790        in the underlying event already fired it. This ensures an almost trigger unbiased data set, while  
 1791        still providing a sample much larger than random selection triggers.

1792        The expected signal yield is obtained assuming the NA48 central value for  $\mathcal{B}(K_s^0 \rightarrow \pi^0 \mu^+ \mu^-)$ ,  
 1793        normalizing the signal yield with respect to  $K_s^0 \rightarrow \pi^+ \pi^-$  as

$$\frac{N(K_s^0 \rightarrow \pi^0 \mu^+ \mu^-)}{N(K_s^0 \rightarrow \pi^+ \pi^-)} = \frac{\mathcal{B}(K_s^0 \rightarrow \pi^0 \mu^+ \mu^-) \epsilon_{K_s^0 \rightarrow \pi^0 \mu^+ \mu^-}}{\mathcal{B}(K_s^0 \rightarrow \pi^+ \pi^-) \epsilon_{K_s^0 \rightarrow \pi^+ \pi^-}}, \quad (6.3)$$

1794        where the observed  $K_s^0 \rightarrow \pi^+ \pi^-$  yield is extracted from data and the efficiency ratio,  $\frac{\epsilon_{K_s^0 \rightarrow \pi^0 \mu^+ \mu^-}}{\epsilon_{K_s^0 \rightarrow \pi^+ \pi^-}}$ ,  
 1795        is obtained from simulation.

1796        The  $\mathcal{B}(K_s^0 \rightarrow \pi^0 \mu^+ \mu^-)$  sensitivity is measured in a pseudo-experiment study. First, the  
 1797        signal and background yields are extrapolated for a desired expected luminosity and trigger effi-  
 1798        ciency, then pseudo-experiments are generated according to those yields. The  $\mathcal{B}(K_s^0 \rightarrow \pi^0 \mu^+ \mu^-)$   
 1799        uncertainty is obtained from a fit to the  $K_s^0$  mass distribution of the pseudo-experiments, using  
 1800        the signal and background models obtained from MC and the fit to the available LHCb data,  
 1801        respectively. The mass fit range is [420, 580] MeV/ $c^2$ .

## 1802        6.2.2 Reconstruction and selection

1803        Pairs of muon candidates are reconstructed combining opposite-charged tracks with hits in the  
 1804        vertex locator (VELO), trigger tracker, tracker stations, and muon chambers. In addition, the  
 1805        tracks are required to be separated by at least  $6\sigma$  from any  $p - p$  collision point in the event.  
 1806        Tracks with transverse momentum lower than 80 MeV/ $c$  are ignored. A dimuon candidate pair  
 1807        can be combined with a  $\pi^0$  candidate to build a  $K_s^0$  candidate. The events in which the entire  
 1808        decay chain is used are classified as FULL. When only the dimuon information is used, they are  
 1809        clasified as PARTIAL.

1810        Neutral pion candidates are reconstructed from  $\gamma$  candidate pairs that correspond to two  
 1811        independent clusters in the calorimeter. Each photon candidate is required to have a transverse  
 1812        momentum of at least 200 MeV/ $c$  and the pion candidate a mass within 30 MeV/ $c^2$  of the world  
 1813        average  $\pi^0$  mass. The mass resolution is then improved by constraining the  $\pi^0$  candidate mass  
 1814        to the world average  $\pi^0$  mass, and by constraining the three-momentum vector of the  $K_s^0$  to  
 1815        point back to the production vertex. For the PARTIAL candidates, a momentum vector with an  
 1816        absolute value of  $\approx 10$  GeV/ $c$  is used as a representative of the  $\pi^0$  momentum when calculating  
 1817        the invariant mass. As a consequence of these kinematic constraints, the  $K_s^0$  candidate mass  
 1818        resolution depends only weakly on the  $\pi^0$  momentum.

1819        Additional selection requirements are applied to reduce the amount of data to analyze, fulfil  
 1820        the rate requirements for LHCb offline processing and reduce the amount of background. These  
 1821        include a  $K_s^0$  candidate lifetime of at least 1 ps and removing events in the kinematic region of  
 1822         $\Lambda \rightarrow p\pi$  and  $K_s^0 \rightarrow \pi^+ \pi^-$  in the Armenteros-Podolski plane [?]. The total reconstruction and  
 1823        selection efficiency for the FULL channel is  $5.47 \times 10^{-4}$ .

Requiring a well-reconstructed  $\pi^0$  implies an inefficiency penalty of a factor ten. Thus, a complementary strategy for the PARTIAL candidates is also investigated. Indeed, the constraints on the  $\pi^0$  mass and the  $K_s^0$  momentum are sufficient to create a peaking distribution if there is an estimate of the typical value of the  $\pi^0$  momentum ( $\approx 10 \text{ GeV}/c$ ), as shown in Fig. 6.4. A comparison of the reconstructed mass resolution between FULL and PARTIAL is difficult due to the asymmetric and non-Gaussian distribution of the PARTIAL case. To get an estimate, the corresponding FWHM values are calculated. In the FULL case, it is  $23.3 \text{ MeV}/c^2$  and in the PARTIAL  $40.6 \text{ MeV}/c^2$ .

The PARTIAL selection does not require any information about a reconstructed  $\pi^0$ . Some requirements had to be tightened in order to keep the background at a manageable level. These include a lower distance of closest approach between the two muon tracks; a minimum requirement on the  $K_s^0$  vertex quality,  $\chi^2/ndof = 9$ ; a higher minimum requirement on the  $K_s^0$  vertex detachment from the interaction point; and minimum radial,  $z$ - and absolute distance requirements between the  $K_s^0$  vertex and the interaction point. The total reconstruction and selection efficiency for the PARTIAL analysis is  $3.0 \times 10^{-3}$ , well above that of the FULL, but at a cost of an increased background yield.

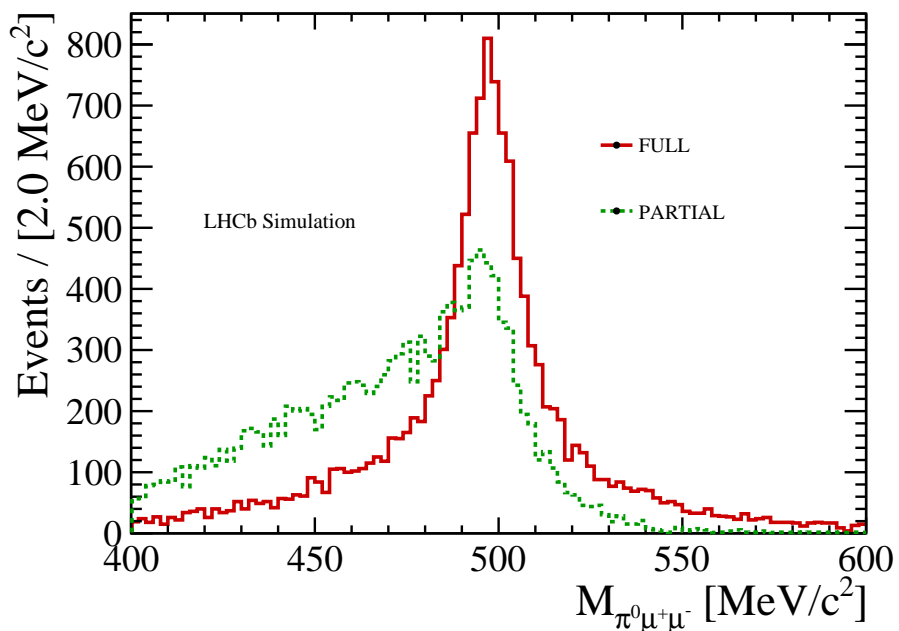


Figure 6.4: Comparison between the FULL (solid red) and PARTIAL (dashed green) kaon candidate mass distributions.

A BDT is used to separate signal from combinatorial background. It is trained with MC events (signal class) and a part of the data that is not used in the fit (combinatorial background class). The BDT uses information about the geometrical properties of the events, kinematics, track quality, and muon identification quality. The BDT response for signal and background for both FULL and PARTIAL is shown in Fig. 6.5.

The events are classified in four bins of the BDT response. The signal yields are obtained

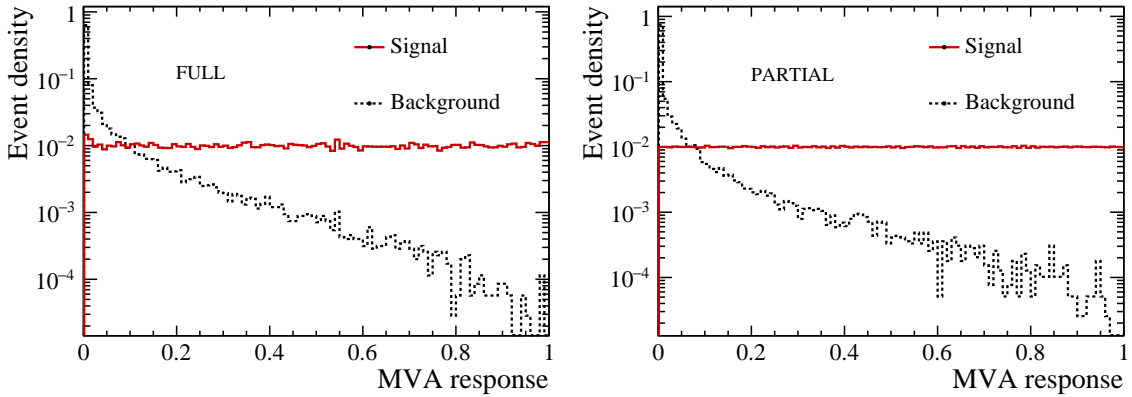


Figure 6.5: BDT response both for signal (solid red) and background (dashed black). Right: FULL channel. Left: PARTIAL channel. Signal and background are normalized to the same area.

1846 in a simultaneous fit of the mass distribution in each BDT bin, as described in the following  
1847 sections.

### 1848 6.2.3 Background sources

1849 Several sources of background are investigated to assess their relevance for a measurement of  
1850  $\mathcal{B}(K_s^0 \rightarrow \pi^0 \mu^+ \mu^-)$ :

1851 •  $K_s^0 \rightarrow \pi^+ \pi^-$  decays, where both pions are misidentified as muons, and in the case of  
1852 the FULL category, combined with a random  $\pi^0$  from the underlying event. These decays  
1853 have a mass larger than that of the  $K_s^0$  and do not enter the fit region, except for potential  
1854 residual tails that effectively add up to the combinatorial background. No evidence for  
1855  $K_s^0 \rightarrow \pi^+ \pi^-$  background is seen for the BDT region being fitted.

1856 •  $K^0 \rightarrow \mu^+ \mu^- \gamma\gamma$  decays. This background was considered in the NA48 analysis [?], How-  
1857 ever, its contribution at LHCb is found to be negligible: In the case of the  $K_L^0$  decay (with  
1858 a branching fraction of  $1.0_{-0.6}^{+0.8} \times 10^{-8}$  [1]) the upper decay time acceptance introduces  
1859 an effective  $10^{-3}$  reduction with respect to  $K_s^0$  and hence the effective  $\mathcal{B}(K_L^0 \rightarrow \mu^+ \mu^- \gamma\gamma)$   
1860 becomes as low as  $10^{-11}$ . There is no experimental measurement of  $\mathcal{B}(K_s^0 \rightarrow \mu^+ \mu^- \gamma\gamma)$ ,  
1861 however, since the process is dominated by the two-photon exchange<sup>4</sup>, it can be estimated  
1862 as:

$$\mathcal{B}(K_s^0 \rightarrow \mu^+ \mu^- \gamma\gamma) = \frac{\mathcal{B}(K_s^0 \rightarrow \gamma\gamma)}{\mathcal{B}(K_L^0 \rightarrow \gamma\gamma)} \mathcal{B}(K_L^0 \rightarrow \mu^+ \mu^- \gamma\gamma) \sim 4.8 \times 10^{-11} \quad (6.4)$$

1863 and is thus negligible.

1864 •  $K_L^0 \rightarrow \pi^0 \pi^+ \pi^-$  decays. The mass distribution of these decays is shown in Fig. 6.6 as  
1865 obtained in simulation. Since there is no evidence of this background in the data, it is

---

<sup>4</sup>Isidori and D'Ambrosio, private communication.

neglected. Including a  $K_L^0 \rightarrow \pi^0\pi^+\pi^-$  component to the observed background does not change significantly the sensitivity estimates. The  $K_S^0$  counterpart has a branching fraction of  $3.5 \times 10^{-7}$  and thus is about four orders of magnitude smaller than  $K_L^0 \rightarrow \pi^0\pi^+\pi^-$ . In general, no sign of a resonant structure in the  $\pi^+\pi^-\pi^0$  is seen on data.

- Combinatorial background. Combinatorial background is considered to be composed by random combination of tracks, including those generated by pseudo-random combinations of hits during the pattern recognition. It has a monotonic shape across the studied invariant mass range.

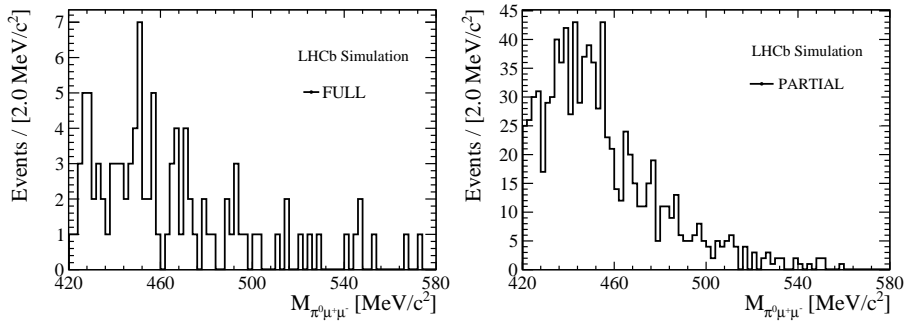


Figure 6.6: Invariant mass distribution of simulated  $K^0 \rightarrow \pi^+\pi^-\pi^0$  decays selected in the FULL (left) and PARTIAL (right) categories.

### 6.2.4 Fit model

Only events in the BDT range [0.6,1] are considered in the fit to the data. A simultaneous fit to the mass distribution across four equally-sized independent bins of the BDT response is performed. The combinatorial background is described with an exponential PDF for both FULL and PARTIAL analysis, with independent floating yields and decay constants in each BDT bin. The signal model is an Hypathia distribution [?] with different configurations for FULL and PARTIAL (see Fig. 6.7). The signal model parameters are independent in each BDT bin and are obtained from simulation. The fractions of signal events allotted to each BDT bin are also fixed from values obtained from simulation, with a total signal yield remaining as the sole free parameter describing signal in the simultaneous fit. The signal yield is floated in the fit to the data. It is measured to be compatible with zero within one to two sigma. The fit projections to the FULL and PARTIAL data are shown in Fig. 6.8.

### 6.2.5 Expected sensitivity

The expected statistical precision on  $\mathcal{B}(K_S^0 \rightarrow \pi^0\mu^+\mu^-)$  for multiple values of the integrated luminosity up to  $100 \text{ fb}^{-1}$  is estimated in this section. The TIS samples used are equivalent to a 100% trigger efficiency sample with an integrated luminosity of 4.9 and  $0.77 \text{ pb}^{-1}$  for the FULL and PARTIAL samples, respectively. The expected background yield is extrapolated from the

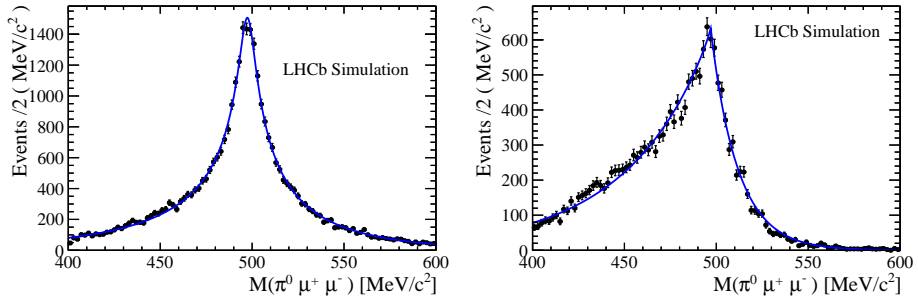


Figure 6.7: Signal fit using the Hypatia function for FULL (left) and PARTIAL (right) categories.

1891 current data fit result, where the signal yield is consistent with zero. The background yield is  
 1892 scaled linearly for larger integrated luminosities.

1893 For each integrated luminosity in the studied range, sets of pseudo-experiments are generated  
 1894 with the above background expectations, and with a signal yield expectation of

$$N_{sig} = \frac{\mathcal{B}(K_s^0 \rightarrow \pi^0 \mu^+ \mu^-)}{\mathcal{B}(K_s^0 \rightarrow \pi^+ \pi^-)} \frac{\epsilon_{K_s^0 \rightarrow \pi^0 \mu^+ \mu^-}}{\epsilon_{K_s^0 \rightarrow \pi^+ \pi^-}} N(K_s^0 \rightarrow \pi^+ \pi^-) \times \frac{L_{fut}}{L_{curr}}, \quad (6.5)$$

1895 where  $L_{fut}$  and  $L_{curr}$  are the future and current luminosities, respectively. The models de-  
 1896 scribed in Sect. 6.2.4 are fit to each pseudo-experiment with a floating  $\mathcal{B}(K_s^0 \rightarrow \pi^0 \mu^+ \mu^-)$ . The  
 1897 background model parameters used are the ones obtained from the fit to the data Sect. 6.2.4.  
 1898 The statistical uncertainties are obtained as the variations of  $\mathcal{B}(K_s^0 \rightarrow \pi^0 \mu^+ \mu^-)$  that deviate  
 1899 from the minimum of the log-likelihood profile by half a unit. Finally, the uncertainties are  
 1900 averaged across the set of pseudo-experiments for a given integrated luminosity. The uncer-  
 1901 tainties on the background extrapolation are large and translate into large uncertainties on the  
 1902 luminosity needed for achieving a given sensitivity. The resulting sensitivity curves are shown  
 1903 in Fig. 6.9. It can be seen that the analyses of both PARTIAL and FULL categories can lead  
 1904 to a precision better than NA48 for the LHCb upgrade if a trigger efficiency above  $\approx 50\%$  can  
 1905 be maintained. The  $K_s^0$  production cross-section increases by  $\approx 20\%$  at 14 TeV compared to 8  
 1906 TeV, but this increase is cancelled by a larger fraction of  $K_s^0$  decaying outside of the VELO vol-  
 1907 ume. For this reason, no energy correction has been applied to the sensitivity estimate. Studies  
 1908 of  $K_s^0 \rightarrow \pi^0 \mu^+ \mu^-$  and minimum bias samples simulated with the LHCb upgrade detector and  
 1909 conditions show that the High Level Trigger rate can be kept low enough for a 100 % efficiency.  
 1910 Further timing studies are currently ongoing.

## 1911 6.2.6 Conclusions

1912 A precise measurement of the  $K_s^0 \rightarrow \pi^0 \mu^+ \mu^-$  branching fraction is crucial for a precise  $\mathcal{B}(K_L^0 \rightarrow$   
 1913  $\pi^0 \mu^+ \mu^-)$  SM theoretical prediction and the search for physics beyond the SM in  $K_L^0 \rightarrow \pi^0 \mu^+ \mu^-$ .  
 1914 The sensitivity of the LHCb experiment to  $\mathcal{B}(K_s^0 \rightarrow \pi^0 \mu^+ \mu^-)$  was studied based on  $3 \text{ fb}^{-1}$  of data  
 1915 recorded at 7 and 8 TeV center-of-mass energy during 2011 and 2012, and on  $0.3 \text{ fb}^{-1}$  of data  
 1916 recorded at 13 TeV center-of-mass energy during 2016. Full and partial decay reconstruction

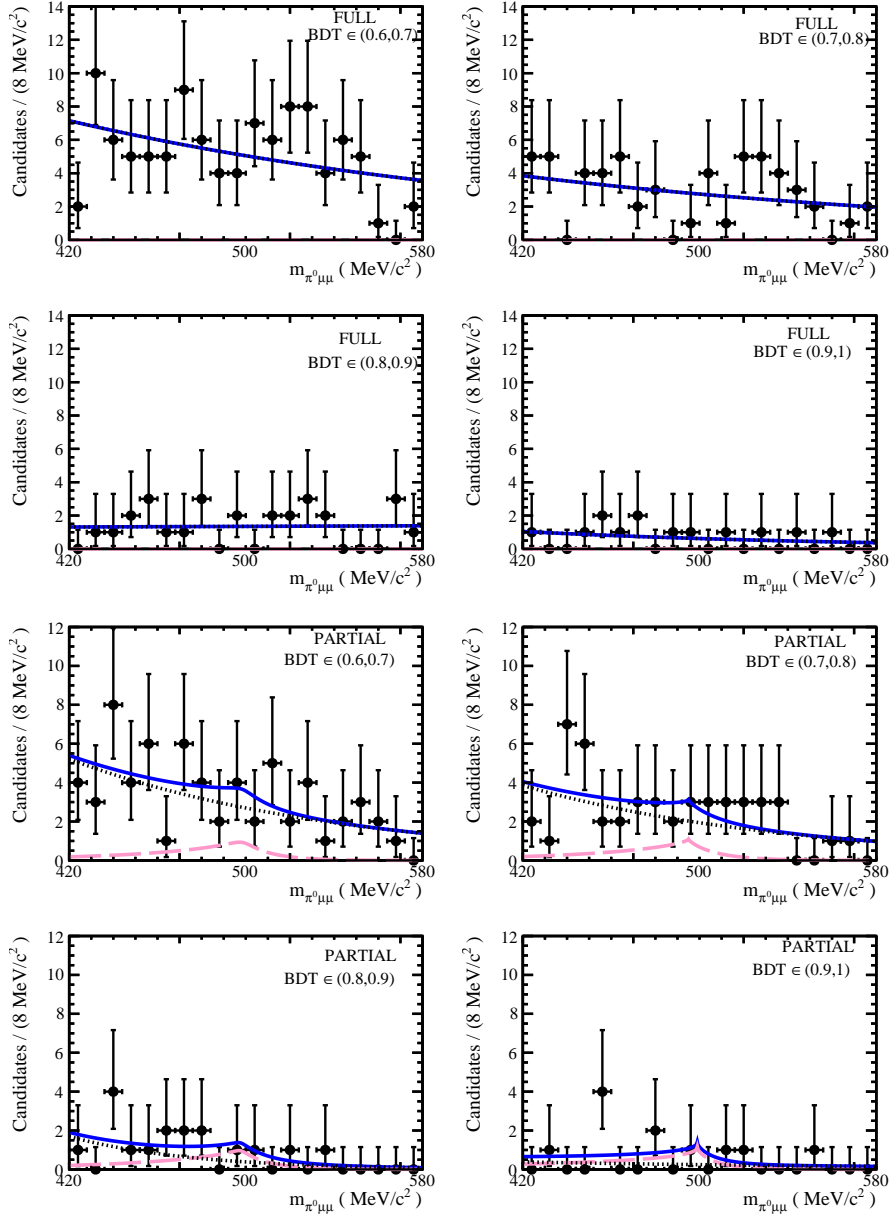


Figure 6.8: Fit to data for FULL (top) and PARTIAL (bottom) categories. The magenta dashed line shows the signal contribution, the dotted black line the background, and the solid blue line the prediction from the total fit model.

algorithms were considered, aiming at a high reconstruction efficiency. The sensitivity study was performed using pseudo-experiments by extrapolating signal yield results based on the currently available data to expected future integrated luminosities. If a trigger efficiency of at least 50% can be assured in the future, LHCb can determine  $\mathcal{B}(K_S^0 \rightarrow \pi^0 \mu^+ \mu^-)$  with a precision significantly better than that of NA48.

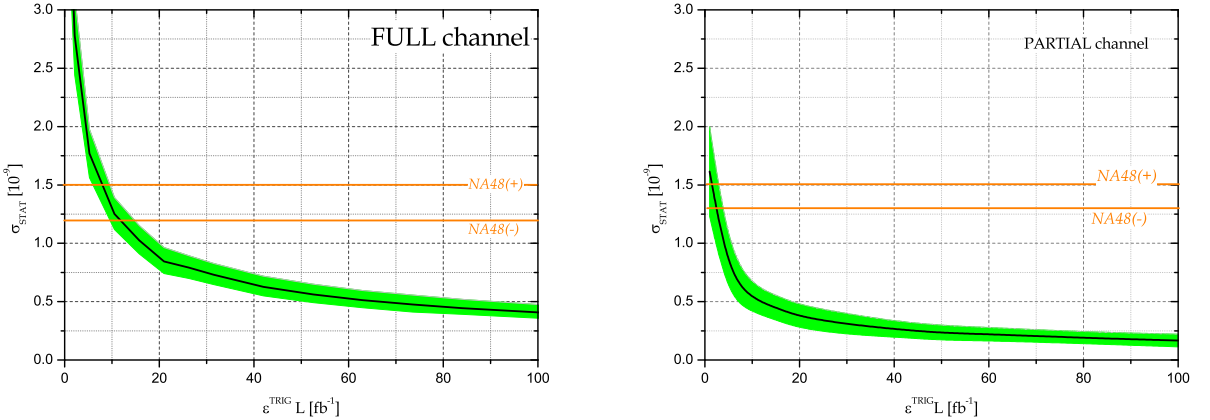


Figure 6.9: Expected precision on  $\mathcal{B}(K_s^0 \rightarrow \pi^0 \mu^+ \mu^-)$  for the FULL (top) and PARTIAL (bottom) channels, as a function of the integrated luminosity times trigger efficiency,  $L \times \varepsilon^{TRIG}/SEL$ .

### 1922 6.3 Probing SUSY effects in $K_s^0 \rightarrow \mu^+ \mu^-$

1923 In this section, the MSSM effects in the  $K_s^0 \rightarrow \mu^+ \mu^-$  decay are explored. The Standard Model  
 1924 (SM) expectation is  $(5.18 \pm 1.50_{LD} \pm 0.02_{SD}) \times 10^{-12}$  [?, ?, ?], where the first uncertainty comes  
 1925 from the long-distance (LD) contribution and the second one comes from the short-distance (SD)  
 1926 contribution. On the other hand, the current experimental upper bound is  $8 \times 10^{-10}$  at 90% C.L.,  
 1927 using  $3 \text{ fb}^{-1}$  of LHCb data [?]. The LHCb upgrade could reach sensitivities at the level of about  
 1928  $1 \times 10^{-11}$  or even below, approaching the SM prediction [?]. The branching ratio  $\mathcal{B}(K_s^0 \rightarrow \mu^+ \mu^-)$   
 1929 is predicted taking into account the relevant experimental constraints on the branching fractions  
 1930  $\mathcal{B}(K_L^0 \rightarrow \mu^+ \mu^-)$ ,  $\mathcal{B}(B^+ \rightarrow \tau^+ \nu_\tau)$  and  $\mathcal{B}(K^+ \rightarrow \mu^+ \nu_\mu)$ , the  $CP$  violation parameters  $\varepsilon'_K/\varepsilon_K$  and  
 1931  $\varepsilon_K$ , the  $K_L^0 - K_S^0$  mass difference,  $\Delta M_K \equiv M_{K_L^0} - M_{K_S^0} > 0$ , and the Wilson coefficient  $C_7$  from  
 1932  $b \rightarrow s\gamma$ . For this, the Mass Insertion Approximation (hereafter MIA) [?] is used, treating the  
 1933 corresponding terms as phenomenological parameters at the SUSY scale. The details of the  
 1934 formalism are given in subsection 6.3.1. The subsets of the MSSM parameter space are studied  
 1935 in scans performed on Graphics Processing Units (GPU), as detailed in section 6.3.2. The results  
 1936 are shown in section ?? and conclusions are drawn in section 6.2.6.

#### 1937 6.3.1 Formalism

1938 The followed notation is the one of refs. [?, 52]. The right-handed down and up squarks are  
 1939 denoted as  $D$  and  $U$ , respectively. Because of the  $SU(2)_L$  doublet, the two left-handed squarks  
 1940 are **degenerate**, and are denoted as  $Q$ . The average of the  $Q$ ,  $D$ , and  $U$ -squark masses squared  
 1941 are denoted by  $\tilde{m}_Q^2$ ,  $\tilde{m}_d^2$ ,  $\tilde{m}_u^2$ , respectively.

1942 The mass insertions (hereafter MIs) are defined as:

$$(\delta_d^{LL})_{ij} = \frac{[(\mathcal{M}_D^2)_{LL}]_{ij}}{\tilde{m}_Q^2} = \frac{(m_Q^2)_{ji}}{\tilde{m}_Q^2}, \quad (6.6)$$

$$(\delta_u^{LL})_{ij} = \frac{[(\mathcal{M}_U^2)_{LL}]_{ij}}{\tilde{m}_Q^2} = \frac{(Vm_Q^2 V^\dagger)_{ji}}{\tilde{m}_Q^2}, \quad (6.7)$$

$$(\delta_d^{RR})_{ij} = \frac{[(\mathcal{M}_D^2)_{RR}]_{ij}}{\tilde{m}_d^2} = \frac{(m_D^2)_{ij}}{\tilde{m}_d^2}, \quad (6.8)$$

1943 where  $V$  is the Cabibbo–Kobayashi–Maskawa (CKM) matrix and  $\mathcal{M}_{D,U}^2$  are the  $6 \times 6$  squark  
 1944 mass matrices. Note that the indices  $ij$  are inverted for  $LL$ . Comparison with the SUSY Les  
 1945 Houches Accord 2 convention [?] is given in the appendix of ref. [52].

1946 The running coupling constants  $\alpha_1$ ,  $\alpha_2$ , and  $\alpha_3$  are defined as

$$\alpha_1 = \frac{g_1^2}{4\pi} = \frac{5}{3} \frac{g'^2}{4\pi}, \quad (6.9)$$

$$\alpha_2 = \frac{g_2^2}{4\pi} = \frac{g^2}{4\pi}, \quad (6.10)$$

$$\alpha_3 = \frac{g_3^2}{4\pi} = \frac{g_s^2}{4\pi}, \quad (6.11)$$

1947 where  $g'$ ,  $g$ , and  $g_s$  are the  $U(1)_Y$ ,  $SU(2)_L$ , and  $SU(3)_C$  group coupling constants, respectively.  
 1948 In the following, these couplings are evaluated at the  $\mu^{\text{SUSY}}$  scale, defined as  $\mu^{\text{SUSY}} = \sqrt{\tilde{m}_Q M_3}$ .

### 1949 6.3.1.1 Observables

1950 As will be shown in the next subsections, the main MSSM contribution to  $\mathcal{B}(K_S^0 \rightarrow \mu^+ \mu^-)$  is  
 1951 proportional to  $\left[ (\delta_d^{LL(RR)})_{12} \mu \tan^3 \beta M_3 / M_A^2 \right]^2$ . In order to constrain those parameters, the  
 1952 following observables are calculated in addition to  $\mathcal{B}(K_S^0 \rightarrow \mu^+ \mu^-)$ :

- 1953 • Observables sensitive, among others, to the off-diagonal mass insertion terms  $(\delta_d^{LL(RR)})_{12}$ :  
 1954  $\mathcal{B}(K_L^0 \rightarrow \mu^+ \mu^-)$ ,  $\varepsilon'_K / \varepsilon_K$ ,  $\varepsilon_K$ , and  $\Delta M_K$ .<sup>5</sup>
- 1955 • Observables sensitive to  $\tan \beta$  and the heavy Higgs mass:  $\mathcal{B}(B^+ \rightarrow \tau^+ \nu_\tau)$ ,  $\mathcal{B}(K^+ \rightarrow \mu^+ \nu_\mu)$ ,  
 1956  $\Delta C_7$ .

1957 The definitions of  $\mathcal{B}(B^+ \rightarrow \tau^+ \nu_\tau)$ ,  $\mathcal{B}(K^+ \rightarrow \mu^+ \nu_\mu)$ , and  $C_7$  are given in ref. [52] and  
 1958 the remaining observables are defined in the following subsections. The CKM matrix is fitted  
 1959 excluding measurements with potential sensitivity to MSSM contributions.

1960 The constraints that are imposed on physics observables sensitive to the MSSM same pa-  
 1961 rameters as  $\mathcal{B}(K_S^0 \rightarrow \mu^+ \mu^-)$  are listed in table 6.1, where the EXP/SM represents the measured  
 1962 value over the SM prediction with their uncertainties. Due to the poor theoretical knowledge  
 1963 of  $\Delta M_K$ , it is assigned a 100% theoretical uncertainty; thus, the constraint imposed on this

---

<sup>5</sup> The contributions to  $\mathcal{B}(K \rightarrow \pi \nu \bar{\nu})$  are controlled by an additional free parameter, the slepton mass, and  $\mathcal{O}(1)$  effects are possible in this scenario [?].

Table 6.1: Physics observables constraints imposed in this study. The two different constraints on  $\mathcal{B}(K_L^0 \rightarrow \mu^+ \mu^-)^{\text{EXP/SM}}$  arise from an unknown sign of  $A_{L\gamma\gamma}^\mu$  in eq. (6.21) (see refs. [?, ?]).

| Observable   | Constraint   |
|--|--|
| $\mathcal{B}(K_S^0 \rightarrow \mu^+ \mu^-)^{\text{EXP/SM}}$   | unconstrained  |
| $\mathcal{B}(K_L^0 \rightarrow \mu^+ \mu^-)^{\text{EXP/SM}}$   | $1.00 \pm 0.12 (+) [?, ?, ?]$<br>$0.84 \pm 0.16 (-) [?, ?, ?]$         |
| $\Delta M_K^{\text{EXP/SM}}$                                   | $1 \pm 1$  |
| $\varepsilon_K^{\text{EXP/SM}}$                                | $1.05 \pm 0.10 [?, ?, ?]$  |
| $\Delta(\varepsilon'_K/\varepsilon_K)^{\text{EXP-SM}}$         | $[15.5 \pm 2.3(\text{EXP}) \pm 5.07(\text{TH})] \times 10^{-4} [?, ?]$ |
| $\mathcal{B}(B^+ \rightarrow \tau^+ \nu_\tau)^{\text{EXP/SM}}$ | $0.91 \pm 0.22 [?]$  |
| $\mathcal{B}(K^+ \rightarrow \mu^+ \nu_\mu)^{\text{EXP/SM}}$   | $1.0004 \pm 0.0095 [?]$  |
| $\Delta C_7$   | $-0.02 \pm 0.02 [?]$   |
| $\tan \beta : M_A$ plane                                       | ATLAS limits for hMSSM scenario [?]                                    |
| LSP  | Lightest neutralino  |
| $B_G$  | $1 \pm 3(\text{TH}) [?, ?]$  |

observable penalizes only  $\mathcal{O}(1)$  effects. It is not counted as a degree of freedom in the  $\chi^2$  tests, so that the  $\Delta M_K$  constraint can only make the bounds tighter, but never looser.

Remaining constraints can in principle be satisfied by adjusting the other parameters of the model. In particular,  $B$  physics constraints not included in the list can be satisfied by parameters unspecified in the scan (e.g. setting  $\delta_{13} \approx \delta_{23} \approx 0$  and small  $A_t$ ). The relation of eq. (6.7) may induce non-zero up-type MIIs in the  $B$  sector and hence modify  $B_{s(d)}^0 \rightarrow \mu^+ \mu^-$ . These effects were checked and found to be negligible in the considered scenarios. The large SUSY masses in our scan are typically beyond the reach of LHC.

The lattice values for  $(\varepsilon'_K/\varepsilon_K)^{\text{SM}}$  used are from refs. [?, ?, ?, ?], although the conclusions extracted from this study remain largely unchanged if the  $\chi_{PT}$  value from refs. [?, ?, ?] is used instead. Both  $\varepsilon_K^{\text{EXP/SM}}$  and  $\Delta(\varepsilon'_K/\varepsilon_K)^{\text{EXP-SM}}$  are discussed in more detail in the following subsections.

### 6.3.1.2 $K_s^0 \rightarrow \mu^+ \mu^-$

The  $|\Delta S| = 1$  effective Hamiltonian relevant for the  $K^0 \rightarrow \ell\bar{\ell}$  transition at the  $Z$  boson mass scale is

$$\mathcal{H}_{\text{eff}} = -C_A Q_A - \tilde{C}_A \tilde{Q}_A - C_S Q_S - \tilde{C}_S \tilde{Q}_S - C_P Q_P - \tilde{C}_P \tilde{Q}_P + \text{H.c.}, \quad (6.12)$$

where  $C_A$ ,  $C_S$  and  $C_P$  are the axial, scalar and pseudoscalar Wilson coefficients. The right-handed and left-handed axial ( $\tilde{Q}_A$ ,  $Q_A$ ), scalar ( $Q_S$ ,  $\tilde{Q}_S$ ) and pseudoscalar ( $Q_P$ ,  $\tilde{Q}_P$ ) operators

1981 are given by:

$$\begin{aligned} Q_A &= (\bar{s}\gamma^\mu P_L d)(\bar{\ell}\gamma_\mu\gamma_5\ell), & \tilde{Q}_A &= (\bar{s}\gamma^\mu P_R d)(\bar{\ell}\gamma_\mu\gamma_5\ell), \\ Q_S &= m_s(\bar{s}P_R d)(\bar{\ell}\ell), & \tilde{Q}_S &= m_s(\bar{s}P_L d)(\bar{\ell}\ell), \\ Q_P &= m_s(\bar{s}P_R d)(\bar{\ell}\gamma_5\ell), & \tilde{Q}_P &= m_s(\bar{s}P_L d)(\bar{\ell}\gamma_5\ell), \end{aligned} \quad (6.13)$$

1982 where  $P_{L,R}$  are the left and right-handed projection operators. For  $\mathcal{B}(K_{S,L}^0 \rightarrow \mu^+\mu^-)$ <sup>6</sup>, there  
1983 are two contributions from S-wave ( $A_{S,L}$ ) and P-wave transitions ( $B_{S,L}$ ), resulting in:<sup>7</sup>

$$\mathcal{B}(K_{S,L}^0 \rightarrow \mu^+\mu^-) = \tau_{S,L}\Gamma(K_{S,L}^0 \rightarrow \mu^+\mu^-) = \tau_{S,L} \frac{f_K^2 M_K^3 \beta_\mu}{16\pi} (|A_{S,L}|^2 + \beta_\mu^2 |B_{S,L}|^2), \quad (6.14)$$

1984 with

$$A_S = \frac{m_s M_K}{m_s + m_d} \text{Im}(C_P - \tilde{C}_P) + \frac{2m_\mu}{M_K} \text{Im}(C_A - \tilde{C}_A), \quad (6.15)$$

$$B_S = \frac{2G_F^2 M_W^2 m_\mu}{\pi^2 M_K} B_{S\gamma\gamma}^\mu - \frac{m_s M_K}{m_s + m_d} \text{Re}(C_S - \tilde{C}_S), \quad (6.16)$$

1985 and

$$A_L = \frac{2G_F^2 M_W^2 m_\mu}{\pi^2 M_K} A_{L\gamma\gamma}^\mu - \frac{m_s M_K}{m_s + m_d} \text{Re}(C_P - \tilde{C}_P) - \frac{2m_\mu}{M_K} \text{Re}(C_A - \tilde{C}_A), \quad (6.17)$$

$$B_L = \frac{m_s M_K}{m_s + m_d} \text{Im}(C_S - \tilde{C}_S), \quad (6.18)$$

1986 where

$$\beta_\mu = \sqrt{1 - \frac{4m_\mu^2}{M_K^2}}. \quad (6.19)$$

1987 The long-distance contributions are [?, ?, ?, ?]:

$$\frac{2G_F^2 M_W^2 m_\mu}{\pi^2 M_K} B_{S\gamma\gamma}^\mu = (-2.65 + 1.14i) \times 10^{-11} (\text{GeV})^{-2}, \quad (6.20)$$

$$\frac{2G_F^2 M_W^2 m_\mu}{\pi^2 M_K} A_{L\gamma\gamma}^\mu = \pm(0.54 - 3.96i) \times 10^{-11} (\text{GeV})^{-2}, \quad (6.21)$$

1988 with<sup>8</sup>

$$B_{S\gamma\gamma}^\mu = \frac{\pi\alpha_0}{G_F^2 M_W^2 f_K M_K |H(0)|} \mathcal{I}\left(\frac{m_\mu^2}{M_K^2}, \frac{m_{\pi^\pm}^2}{M_K^2}\right) \sqrt{\frac{2\pi}{M_K} \frac{\mathcal{B}(K_S^0 \rightarrow \gamma\gamma)^{\text{EXP}}}{\tau_S}}, \quad (6.22)$$

$$A_{L\gamma\gamma}^\mu = \frac{\pm 2\pi\alpha_0}{G_F^2 M_W^2 f_K M_K} \mathcal{A}(M_K^2) \sqrt{\frac{2\pi}{M_K} \frac{\mathcal{B}(K_L^0 \rightarrow \gamma\gamma)^{\text{EXP}}}{\tau_L}}, \quad (6.23)$$

---

<sup>6</sup> The electron modes are suppressed by  $m_e^2/m_\mu^2$ , and we do not consider them in this paper.

<sup>7</sup> Our result agrees with refs. [?, ?, ?, ?]. However, it disagrees with notable literature [?, 52] after discarding the long-distance contributions. We found that  $C_{10}^{\text{SM}}$  should be  $-C_{10}^{\text{SM}}$  in eq. (3.45) of ref. [52], and  $(C_P - C'_P)$  should be  $(C'_P - C_P)$  in eq. (2.4) of ref. [?].

<sup>8</sup> Note that  $B_{S\gamma\gamma}^\mu$  is denoted by  $A_{S\gamma\gamma}^\mu$  in refs. [?, ?].

where a two-loop function  $\mathcal{I}(a, b)$  from the  $2\pi^\pm 2\gamma$  intermediate state is given in refs. [?, ?], a pion one-loop contribution with two external on-shell photons is represented as  $H(0) = 0.331 + i0.583$  [?], and a one-loop function  $\mathcal{A}(s)$  from the  $2\gamma$  intermediate state is given in refs. [?, ?].

Here,  $\alpha_0 = 1/137.04$ ,  $f_K = (155.9 \pm 0.4)$  MeV [?], and  $\tau_{S,L}$  are the  $K_{S,L}^0$  lifetimes. Note that there is a theoretically and experimentally unknown sign in  $A_{L\gamma\gamma}^\mu$ , which is determined by higher chiral orders than  $\mathcal{O}(p^4)$  contributions [?, ?], and they provide two different constraints on  $\mathcal{B}(K_L^0 \rightarrow \mu^+ \mu^-)^{\text{EXP/SM}}$  in table 6.1. This sign can be determined by a precise measurement of the interference between  $K_L^0 \rightarrow \mu^+ \mu^-$  and  $K_S^0 \rightarrow \mu^+ \mu^-$  [?]. In addition, in the MSSM, the correlation between  $\mathcal{B}(K_S^0 \rightarrow \mu^+ \mu^-)$  and  $\mathcal{B}(K_L^0 \rightarrow \mu^+ \mu^-)$  depends on the unknown sign of  $A_{L\gamma\gamma}^\mu$ .

In the case in which new physics enters only in  $\tilde{C}_S$  and  $\tilde{C}_P = \tilde{C}_S$  (pure left-handed MSSM scenario), the following relations between the branching fractions of  $K_S^0$  and  $K_L^0$  decaying into  $\mu^+ \mu^-$  can be established:

$$\begin{aligned} \mathcal{B}(K_S^0 \rightarrow \mu^+ \mu^-) &\propto \beta_\mu^2 |N_S^{\text{LD}}|^2 + (A_{S,\text{SM}}^{\text{SD}})^2 - 2M_K \left[ A_{S,\text{SM}}^{\text{SD}} \text{Im}(\tilde{C}_S) - \beta_\mu^2 \text{Re}(N_S^{\text{LD}}) \text{Re}(\tilde{C}_S) \right] \\ &\quad + M_K^2 \left\{ [\text{Im}(\tilde{C}_S)]^2 + \beta_\mu^2 [\text{Re}(\tilde{C}_S)]^2 \right\}, \end{aligned} \quad (6.24)$$

$$\begin{aligned} \mathcal{B}(K_L^0 \rightarrow \mu^+ \mu^-) &\propto |N_L^{\text{LD}}|^2 + (A_{L,\text{SM}}^{\text{SD}})^2 - 2M_K \text{Re}(\tilde{C}_S) [A_{L,\text{SM}}^{\text{SD}} - \text{Re}(N_L^{\text{LD}})] \\ &\quad + M_K^2 \left\{ [\text{Re}(\tilde{C}_S)]^2 + \beta_\mu^2 [\text{Im}(\tilde{C}_S)]^2 \right\} - 2A_{L,\text{SM}}^{\text{SD}} \text{Re}(N_L^{\text{LD}}), \end{aligned} \quad (6.25)$$

with

$$A_{S,\text{SM}}^{\text{SD}} = \frac{2m_\mu}{M_K} \text{Im}(C_{A,\text{SM}}), \quad A_{L,\text{SM}}^{\text{SD}} = \frac{2m_\mu}{M_K} \text{Re}(C_{A,\text{SM}}), \quad (6.26)$$

and

$$N_S^{\text{LD}} = \frac{2G_F^2 M_W^2 m_\mu}{\pi^2 M_K} B_{S\gamma\gamma}^\mu, \quad N_L^{\text{LD}} = \frac{2G_F^2 M_W^2 m_\mu}{\pi^2 M_K} A_{L\gamma\gamma}^\mu, \quad (6.27)$$

where  $m_d$  terms are discarded for simplicity.

The long-distance term  $\text{Re}(N_L^{\text{LD}})$  holds the unknown sign from  $A_{L\gamma\gamma}^\mu$ , which changes the correlation significantly, as will be shown.

On the other hand, if new physics produces only  $C_S$  and  $C_P = -C_S$  (pure right-handed MSSM), the two branching fractions are

$$\begin{aligned} \mathcal{B}(K_S^0 \rightarrow \mu^+ \mu^-) &\propto \beta_\mu^2 |N_S^{\text{LD}}|^2 + (A_{S,\text{SM}}^{\text{SD}})^2 - 2M_K \left[ A_{S,\text{SM}}^{\text{SD}} \text{Im}(C_S) + \beta_\mu^2 \text{Re}(N_S^{\text{LD}}) \text{Re}(C_S) \right] \\ &\quad + M_K^2 \left\{ [\text{Im}(C_S)]^2 + \beta_\mu^2 [\text{Re}(C_S)]^2 \right\}, \end{aligned} \quad (6.28)$$

$$\begin{aligned} \mathcal{B}(K_L^0 \rightarrow \mu^+ \mu^-) &\propto |N_L^{\text{LD}}|^2 + (A_{L,\text{SM}}^{\text{SD}})^2 - 2M_K \text{Re}(C_S) [A_{L,\text{SM}}^{\text{SD}} - \text{Re}(N_L^{\text{LD}})] \\ &\quad + M_K^2 \left\{ [\text{Re}(C_S)]^2 + \beta_\mu^2 [\text{Im}(C_S)]^2 \right\} - 2A_{L,\text{SM}}^{\text{SD}} \text{Re}(N_L^{\text{LD}}). \end{aligned} \quad (6.29)$$

It is shown that  $\mathcal{B}(K_L^0 \rightarrow \mu^+ \mu^-)$  is the same as the pure left-handed one by a replacement of  $C_S \rightarrow \tilde{C}_S$ , while  $\mathcal{B}(K_S^0 \rightarrow \mu^+ \mu^-)$  is not; the final terms of the first line have opposite sign. Hence, the relations between the two branching fractions are different for left-handed and right-handed new physics scenarios.

For those cases, the experimental measurement of  $\mathcal{B}(K_L^0 \rightarrow \mu^+ \mu^-)$  [?],

$$\mathcal{B}(K_L^0 \rightarrow \mu^+ \mu^-)^{\text{EXP}} = (6.84 \pm 0.11) \times 10^{-9}, \quad (6.30)$$

imposes an upper bound on  $\mathcal{B}(K_S^0 \rightarrow \mu^+ \mu^-)$ . This bound can be alleviated if  $|C_S| \neq |C_P|$  or if new physics is present simultaneously in the left-handed and right-handed Wilson coefficients.

Experimentally, an *effective* branching ratio of  $K_S^0 \rightarrow \mu^+ \mu^-$  [?] can also be accessed. This includes an interference contribution with  $K_L^0 \rightarrow \mu^+ \mu^-$  in the neutral kaon sample,

$$\begin{aligned} \mathcal{B}(K_S^0 \rightarrow \mu^+ \mu^-)_{\text{eff}} &= \tau_S \left( \int_{t_{\min}}^{t_{\max}} dt e^{-\Gamma_S t} \varepsilon(t) \right)^{-1} \left[ \int_{t_{\min}}^{t_{\max}} dt \left\{ \Gamma(K_S^0 \rightarrow \mu^+ \mu^-) e^{-\Gamma_S t} \right. \right. \\ &\quad \left. \left. + \frac{D f_K^2 M_K^3 \beta_\mu}{8\pi} \text{Re} [i (A_S A_L - \beta_\mu^2 B_S^* B_L) e^{-i\Delta M_K t}] e^{-\frac{\Gamma_S + \Gamma_L}{2} t} \right\} \varepsilon(t) \right], \end{aligned} \quad (6.31)$$

where the dilution factor  $D$  is a measure of the initial ( $t = 0$ )  $K^0 - \bar{K}^0$  asymmetry,

$$D = \frac{K^0 - \bar{K}^0}{K^0 + \bar{K}^0}, \quad (6.32)$$

and  $\varepsilon(t)$  is the decay-time acceptance of the detector. The second line of eq. (6.31) corresponds to an interference effect between  $K_L^0$  and  $K_S^0$ , and for  $D = 0$ ,  $\mathcal{B}(K_S^0 \rightarrow \mu^+ \mu^-)_{\text{eff}}$  corresponds to  $\mathcal{B}(K_S^0 \rightarrow \mu^+ \mu^-)$ . The current experimental bound [?],

$$\mathcal{B}(K_S^0 \rightarrow \mu^+ \mu^-)^{\text{EXP}} < 8 \times 10^{-10} \text{ [90% C.L.],} \quad (6.33)$$

uses untagged  $K^0$  and  $\bar{K}^0$  mesons produced in almost equal amounts, and hence  $D = 0$  is assumed. A pure  $K_L^0 \rightarrow \mu^+ \mu^-$  background can be subtracted by a combination of **simultaneous measurement of  $K_S^0 \rightarrow \pi^+ \pi^-$  events** and knowledge of the observed value of  $\mathcal{B}(K_L^0 \rightarrow \mu^+ \mu^-)$  in eq. (6.30) [?]. The decay-time acceptance of the LHCb detector is parametrized by  $\varepsilon(t) = \exp(-\beta t)$  with  $\beta \simeq 86 \text{ ns}^{-1}$ , and the range of the detector for selecting  $K^0 \rightarrow \mu^+ \mu^-$  is  $t_{\min} = 8.95 \text{ ps} = 0.1\tau_S$  and  $t_{\max} = 130 \text{ ps} = 1.45\tau_S$ .

Given the potential measurement of an effective branching ratio by different dilution factors  $D > 0$  and  $D' < 0$  using  $K^-$  tagging and  $K^+$  tagging [?], respectively, the direct  $CP$  asymmetry can be measured using the difference  $\mathcal{B}(K_S^0 \rightarrow \mu^+ \mu^-)_{\text{eff}}(D) - \mathcal{B}(K_S^0 \rightarrow \mu^+ \mu^-)_{\text{eff}}(D')$ , which is a theoretically clean quantity that emerges from a genuine direct  $CP$  violation. Here, the charged kaon is accompanied by the neutral kaon beam as, for instance,  $pp \rightarrow K^0 K^- X$  or  $pp \rightarrow \bar{K}^0 K^+ X$ . Note that a definition of  $D'$  is the same as  $D$  in eq. (6.32) but charged kaons of opposite sign are required in the event selection. Therefore, following direct  $CP$  asymmetry in  $K_S^0 \rightarrow \mu^+ \mu^-$  can be defined:

$$A_{CP}(K_S^0 \rightarrow \mu^+ \mu^-)_{D,D'} = \frac{\mathcal{B}(K_S^0 \rightarrow \mu^+ \mu^-)_{\text{eff}}(D) - \mathcal{B}(K_S^0 \rightarrow \mu^+ \mu^-)_{\text{eff}}(D')}{\mathcal{B}(K_S^0 \rightarrow \mu^+ \mu^-)_{\text{eff}}(D) + \mathcal{B}(K_S^0 \rightarrow \mu^+ \mu^-)_{\text{eff}}(D')} \quad (6.34)$$

The indirect  $CP$ -violating contributions, numerically negligible when compared to the  $CP$ -conserving and the direct  $CP$ -violating contributions [?], were discarded. Within the SM, the Wilson coefficients are,

$$C_{A,\text{SM}} = -\frac{[\alpha_2(M_Z)]^2}{2M_W^2} (V_{ts}^* V_{td} Y_t + V_{cs}^* V_{cd} Y_c), \quad (6.35)$$

$$\tilde{C}_{A,\text{SM}} = C_{S,\text{SM}} = \tilde{C}_{S,\text{SM}} = C_{P,\text{SM}} = \tilde{C}_{P,\text{SM}} \simeq 0, \quad (6.36)$$

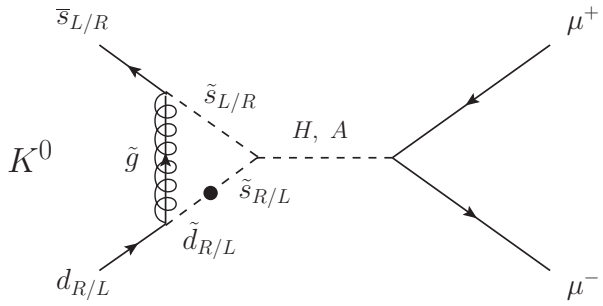


Figure 6.10: Feynman diagram of the leading (pseudo-)scalar MSSM contributions to  $K_S^0 \rightarrow \mu^+ \mu^-$  and  $K_L^0 \rightarrow \mu^+ \mu^-$ , which include a gluino and a heavy Higgs boson. The black dot is the corresponding mass insertion term.

where  $Y_t = 0.950 \pm 0.049$  and  $Y_c = (2.95 \pm 0.46) \times 10^{-4}$  [?]. Using the CKM matrix tailored for probing the MSSM contributions, we obtain the SM prediction of  $A_{CP}$ ,

$$A_{CP}(K_S^0 \rightarrow \mu^+ \mu^-)_{D,D'}^{\text{SM}} = \begin{cases} -\frac{3.71(D-D')}{(10.53 \pm 3.01) - 3.71(D+D')}, & (+) \\ \frac{3.98(D-D')}{(10.53 \pm 3.01) + 3.98(D+D')}, & (-) \end{cases} \quad (6.37)$$

where (+) and (-) correspond to the unknown sign of  $A_{L\gamma\gamma}^\mu$  in eq. (6.21). The uncertainty is totally dominated by  $B_{S\gamma\gamma}^\mu$  [?] and it will be sharpened by the dispersive treatment of  $K_S^0 \rightarrow \gamma^{(*)}\gamma^{(*)}$  [?].

In the case where  $D' = -D$ , achieved by the accompanying opposite-charged-kaon tagging, the SM prediction of  $A_{CP}$  is simplified:

$$A_{CP}(K_S^0 \rightarrow \mu^+ \mu^-)_{D,-D}^{\text{SM}} = \begin{cases} (-0.704_{-0.281}^{+0.156}) \times D, & (+) \\ (+0.756_{-0.168}^{+0.302}) \times D. & (-) \end{cases} \quad (6.38)$$

In the MSSM, the leading contribution to  $C_A$ , induced by terms of second order in the expansion of the squark mass matrix of the chargino  $Z$ -penguin, is [?, ?],

$$C_A = -\frac{(\alpha_2)^2}{16M_W^2} \frac{[(\mathcal{M}_U^2)_{LR}]_{23}^* [(\mathcal{M}_U^2)_{LR}]_{13}}{M_2^4} l(x_2^Q, x_2^u), \quad (6.39)$$

$$\tilde{C}_A = 0, \quad (6.40)$$

where  $x_2^Q = \tilde{m}_Q^2/M_2^2$  and  $x_2^u = \tilde{m}_u^2/M_2^2$ . The loop function  $l(x, y)$  [?] is defined in appendix ???. Here, contributions from the Wino-Higgsino mixing are omitted. Setting  $\tilde{m}_Q^2 = \tilde{m}_u^2$  gives the MIA result of refs. [?, ?].

The leading MSSM contributions to  $C_{S(P)}$  and  $\tilde{C}_{S(P)}$  in  $K_S^0 \rightarrow \mu^+ \mu^-$  and  $K_L^0 \rightarrow \mu^+ \mu^-$  are

2052 shown in figure 6.10. For  $C_S$  and  $\tilde{C}_S$ , it is obtained

$$C_S = -\frac{2}{3} \frac{\alpha_s \alpha_2 m_\mu}{M_W^2} \frac{\mu M_3}{M_A^2 \tilde{m}_d^2} (\delta_d^{RR})_{12} \frac{\tan^3 \beta}{(1 + \epsilon_g \tan \beta)^2 (1 + \epsilon_\ell \tan \beta)} G(x_d^3, x_d^Q) \\ -\frac{2}{3} \frac{\alpha_s \alpha_2 m_\mu}{M_W^2} \frac{m_b}{m_s} \frac{\mu M_3 \tilde{m}_Q^2}{M_A^2 \tilde{m}_d^4} (\delta_d^{RR})_{13} (\delta_d^{LL})_{32} \\ \times \frac{\tan^3 \beta}{(1 + \epsilon_g \tan \beta)[1 + (\epsilon_g + \epsilon_Y y_t^2) \tan \beta](1 + \epsilon_\ell \tan \beta)} H(x_d^3, x_d^Q), \quad (6.41)$$

$$\tilde{C}_S = -\frac{2}{3} \frac{\alpha_s \alpha_2 m_\mu}{M_W^2} \frac{\mu M_3}{M_A^2 \tilde{m}_Q^2} (\delta_d^{LL})_{12} \frac{\tan^3 \beta}{(1 + \epsilon_g \tan \beta)^2 (1 + \epsilon_\ell \tan \beta)} G(x_Q^3, x_Q^d) \\ -\frac{2}{3} \frac{\alpha_s \alpha_2 m_\mu}{M_W^2} \frac{m_b}{m_s} \frac{\mu M_3 \tilde{m}_d^2}{M_A^2 \tilde{m}_Q^4} (\delta_d^{LL})_{13} (\delta_d^{RR})_{32} \\ \times \frac{\tan^3 \beta}{(1 + \epsilon_g \tan \beta)[1 + (\epsilon_g + \epsilon_Y y_t^2) \tan \beta](1 + \epsilon_\ell \tan \beta)} H(x_Q^3, x_Q^d) \\ + \frac{(\alpha_2)^2 m_\mu m_t^2}{8 M_W^4} \frac{\mu A_t}{M_A^2 \tilde{m}_Q^2} V_{ts}^* V_{td} \frac{\tan^3 \beta [1 + (\epsilon_g + \epsilon_Y y_t^2) \tan \beta]^2}{(1 + \epsilon_g \tan \beta)^4 (1 + \epsilon_\ell \tan \beta)} F(x_Q^\mu, x_Q^u) \\ + \frac{(\alpha_2)^2 m_\mu}{4 M_W^2} \frac{\mu M_2}{M_A^2 \tilde{m}_Q^2} (\delta_u^{LL})_{12} \frac{\tan^3 \beta}{(1 + \epsilon_g \tan \beta)^2 (1 + \epsilon_\ell \tan \beta)} G(x_Q^2, x_Q^\mu), \quad (6.42)$$

2053 with

$$\epsilon_g = \frac{2 \alpha_s}{3 \pi} \frac{\mu M_3}{\tilde{m}_Q^2} F(x_Q^3, x_Q^d), \quad (6.43)$$

$$\epsilon_Y = \frac{1}{16 \pi} \frac{\mu A_t}{\tilde{m}_Q^2} F(x_Q^\mu, x_Q^u), \quad (6.44)$$

$$\epsilon_\ell \simeq -\frac{3 \alpha_2}{16 \pi}, \quad (6.45)$$

2054 where  $x_d^3 = M_3^2 / \tilde{m}_d^2$ ,  $x_d^Q = \tilde{m}_Q^2 / \tilde{m}_d^2$ ,  $x_Q^3 = M_3^2 / \tilde{m}_Q^2$ ,  $x_Q^d = \tilde{m}_d^2 / \tilde{m}_Q^2$ ,  $x_Q^\mu = \mu^2 / \tilde{m}_Q^2$ ,  $x_Q^u = \tilde{m}_u^2 / \tilde{m}_Q^2$ ,  
2055  $x_Q^2 = M_2^2 / \tilde{m}_Q^2$ , and  $x_Q^\mu = \mu^2 / \tilde{m}_Q^2$ . The loop functions  $F(x, y)$ ,  $G(x, y)$ , and  $H(x, y)$  are defined  
2056 in appendix ???. These results are consistent with ref. [52] in the universal squark mass limit  
2057 after changing the flavour and its chirality for  $B_s^0$  decay. Here, the following approximation is  
2058 used

$$\alpha \simeq \beta - \frac{\pi}{2}, \quad M_H \simeq M_A, \quad (6.46)$$

2059 where  $\alpha$  is an angle of the orthogonal rotation matrix for the  $CP$ -even Higgs mass, and  $M_H$   
2060 ( $M_A$ ) is a  $CP$ -even (odd) heavy Higgs mass. On the other hand, the contributions to  $C_P$  and  
2061  $\tilde{C}_P$  are

$$C_P = -C_S, \quad \tilde{C}_P = \tilde{C}_S. \quad (6.47)$$

2062 Note that the Wilson coefficients in the MSSM are given at the  $\mu^{\text{SUSY}}$  scale, and there is no  
2063 QCD correction from the renormalization-group (RG) evolution at the leading order.

2064 **6.3.1.3  $\varepsilon'_K/\varepsilon_K$**

2065 New physics models affecting  $\varepsilon'_K/\varepsilon_K$  have recently attracted some attention, since lattice results  
 2066 from the RBC and UKQCD collaborations [?, ?, ?, ?] have been reporting 2–3 $\sigma$  below [?, ?] the  
 2067 experimental world average of  $\text{Re}(\varepsilon'_K/\varepsilon_K)$  [?]. This is consistent with the recent calculations in  
 2068 the large- $N_c$  analyses [?, ?]. Although the lattice simulation [?] includes final-state interactions  
 2069 partially along the line of ref. [?], final-state interactions have to be still fully included in the  
 2070 calculations in light of a discrepancy of a strong phase shift  $\delta_0$  [?, ?, ?]. Conversely, combining  
 2071 large- $N_c$  methods with chiral loop corrections can bring the value of  $\varepsilon'_K/\varepsilon_K$  in agreement with  
 2072 the experiment [?, ?, ?].

2073 The hadronic matrix elements used in this paper come from lattice simulations. For the  $\chi^2$   
 2074 test, the following constraint is used,

$$\Delta \left( \frac{\varepsilon'_K}{\varepsilon_K} \right)^{\text{EXP-SM}} \equiv \text{Re} \left( \frac{\varepsilon'_K}{\varepsilon_K} \right)^{\text{EXP}} - \left( \frac{\varepsilon'_K}{\varepsilon_K} \right)^{\text{SM}} = [15.5 \pm 2.3(\text{EXP}) \pm 5.07(\text{TH})] \times 10^{-4}, \quad (6.48)$$

2075 with

$$\left( \frac{\varepsilon'_K}{\varepsilon_K} \right)^{\text{SM}} \rightarrow \left( \frac{\varepsilon'_K}{\varepsilon_K} \right)^{\text{SM}} + \left( \frac{\varepsilon'_K}{\varepsilon_K} \right)^{\text{SUSY}}, \quad (6.49)$$

2076 where the SM prediction at the next-to-leading order in ref. [?] is used. The experimental value  
 2077 of  $\varepsilon_K$  is used in the calculation of the ratio.

2078 Within the MSSM, the SUSY contributions to  $\varepsilon'_K/\varepsilon_K$  are dominated by gluino box, chargino-  
 2079 mediated  $Z$ -penguin, and chromomagnetic dipole contributions. The first two contributions are  
 2080 represented by the same  $|\Delta S| = 1$  four-quark effective Hamiltonian at the  $\mu^{\text{SUSY}}$  scale, which  
 2081 is:

$$\mathcal{H}_{\text{eff}} = \frac{G_F}{\sqrt{2}} \sum_q \sum_{i=1}^4 \left[ C_i^q Q_i^q + \tilde{C}_i^q \tilde{Q}_i^q \right] + \text{H.c.}, \quad (6.50)$$

2082 with

$$\begin{aligned} Q_1^q &= (\bar{s}d)_{V-A} (\bar{q}q)_{V+A}, & \tilde{Q}_1^q &= (\bar{s}d)_{V+A} (\bar{q}q)_{V-A}, \\ Q_2^q &= (\bar{s}_\alpha d_\beta)_{V-A} (\bar{q}_\beta q_\alpha)_{V+A}, & \tilde{Q}_2^q &= (\bar{s}_\alpha d_\beta)_{V+A} (\bar{q}_\beta q_\alpha)_{V-A}, \\ Q_3^q &= (\bar{s}d)_{V-A} (\bar{q}q)_{V-A}, & \tilde{Q}_3^q &= (\bar{s}d)_{V+A} (\bar{q}q)_{V+A}, \\ Q_4^q &= (\bar{s}_\alpha d_\beta)_{V-A} (\bar{q}_\beta q_\alpha)_{V-A}, & \tilde{Q}_4^q &= (\bar{s}_\alpha d_\beta)_{V+A} (\bar{q}_\beta q_\alpha)_{V+A}, \end{aligned} \quad (6.51)$$

2083 where  $(V \mp A)$  refers to  $\gamma_\mu(1 \mp \gamma_5)$ , and  $\alpha$  and  $\beta$  are color indices.

2084 The Wilson coefficients from the gluino box contributions are leading contributions when  
 2085 the mass difference between right-handed squarks exists [?, ?]. They are shown in appendix ??  
 2086 with their corresponding loop functions defined in appendix ???. Here,  $(\delta_d)_{13}(\delta_d)_{32}$  terms are  
 2087 discarded for simplicity.

2088 The Wilson coefficients of the chargino-mediated  $Z$ -penguin are induced by terms of second  
 2089 order in the expansion of MIA. These ones are shown in appendix ??, where the loop function  
 2090  $l(x, y)$  is given by eq. (??).

2091 The matching conditions to the standard four-quark Wilson coefficients [?] are

$$\begin{aligned}
s_1 &= 0, & s_2 &= 0, \\
s_3 &= \frac{1}{3} (C_3^u + 2C_3^d), & s_4 &= \frac{1}{3} (C_4^u + 2C_4^d), \\
s_5 &= \frac{1}{3} (C_1^u + 2C_1^d), & s_6 &= \frac{1}{3} (C_2^u + 2C_2^d), \\
s_7 &= \frac{2}{3} (C_1^u - C_1^d), & s_8 &= \frac{2}{3} (C_2^u - C_2^d), \\
s_9 &= \frac{2}{3} (C_3^u - C_3^d), & s_{10} &= \frac{2}{3} (C_4^u - C_4^d).
\end{aligned} \tag{6.52}$$

2093 The coefficients for the opposite-chirality operators,  $\tilde{s}_{1,\dots,10}$ , are trivially found from the previous  
2094 ones by replacing  $C_{1,2,3,4}^q \rightarrow \tilde{C}_{1,2,3,4}^q$ . Using the Wilson coefficients  $\vec{s} = (s_1, s_2, \dots, s_{10})^T$  and  
2095  $\tilde{\vec{s}} = (\tilde{s}_1, \tilde{s}_2, \dots, \tilde{s}_{10})^T$  at the  $\mu^{\text{SUSY}}$  scale, the dominant box and penguin contributions to  $\varepsilon'_K/\varepsilon_K$   
2096 are given by [?]

$$\left. \frac{\varepsilon'_K}{\varepsilon_K} \right|_{\text{box+pen}} = \frac{G_F \omega_+}{2|\varepsilon_K^{\text{EXP}}| \text{Re} A_0^{\text{EXP}}} \langle \vec{Q}_{\varepsilon'}(\mu)^T \hat{U}(\mu, \mu^{\text{SUSY}}) \text{Im} [\vec{s} - \tilde{\vec{s}}] \rangle, \tag{6.53}$$

2097 with

$$\omega_+ = (4.53 \pm 0.02) \times 10^{-2}, \tag{6.54}$$

$$|\varepsilon_K^{\text{EXP}}| = (2.228 \pm 0.011) \times 10^{-3}, \tag{6.55}$$

$$\text{Re} A_0^{\text{EXP}} = (3.3201 \pm 0.0018) \times 10^{-7} \text{ GeV}. \tag{6.56}$$

2098 The hadronic matrix elements at  $\mu = 1.3$  GeV, including  $I = 0$  and  $I = 2$  parts, are [?]

$$\langle \vec{Q}_{\varepsilon'}(\mu)^T \rangle = \left( 0.345, 0.133, 0.034, -0.179, 0.152, 0.288, 2.653, 17.305, 0.526, 0.281 \right) (\text{GeV})^3, \tag{6.57}$$

2099 and the approximate function of the RG evolution matrix  $\hat{U}(\mu, \mu^{\text{SUSY}})$  is given in ref. [?].

2100 Next, the  $|\Delta S| = 1$  chromomagnetic-dipole operator that contributes to  $\varepsilon'_K/\varepsilon_K$  is

$$\mathcal{H}_{\text{eff}} = C_g^- Q_g^- + \text{H.c.}, \tag{6.58}$$

2101 with

$$Q_g^- = -\frac{g_s}{(4\pi)^2} (\bar{s} \sigma^{\mu\nu} T^A \gamma_5 d) G_{\mu\nu}^A. \tag{6.59}$$

2102 The complete expression for the Wilson coefficient  $C_g^-$  at the  $\mu^{\text{SUSY}}$  scale is shown in ap-  
2103 pendix ??, where  $(\delta_d)_{13}(\delta_d)_{32}$  terms are discarded for simplicity. The corresponding loop func-  
2104 tions  $I(x, y)$ ,  $J(x, y)$ ,  $K(x, y)$ ,  $L(x, y)$ ,  $M_3(x)$ , and  $M_4(x)$  are defined in appendix ??.

2105 The chromomagnetic-dipole contribution to  $\varepsilon'_K/\varepsilon_K$  is [?]

$$\left. \frac{\varepsilon'_K}{\varepsilon_K} \right|_{\text{chromo}} = \frac{\omega_+}{|\varepsilon_K^{\text{EXP}}| \text{Re} A_0^{\text{EXP}}} \left( 1 - \hat{\Omega}_{\text{eff}} \right) \frac{11\sqrt{3}}{64\pi^2} \frac{M_\pi^2 M_K^2}{f_\pi(m_s + m_d)} \eta_s B_G \text{Im} C_g^-, \tag{6.60}$$

2106 where  $f_\pi = (130.2 \pm 1.7)$  MeV [?], and [?, ?, ?]

$$\hat{\Omega}_{\text{eff}} = 0.148 \pm 0.080, \quad (6.61)$$

$$\eta_s = \left[ \frac{\alpha_s(m_b)}{\alpha_s(1.3 \text{ GeV})} \right]^{\frac{2}{25}} \left[ \frac{\alpha_s(m_t)}{\alpha_s(m_b)} \right]^{\frac{2}{23}} \left[ \frac{\alpha_s(\mu^{\text{SUSY}})}{\alpha_s(m_t)} \right]^{\frac{2}{21}}. \quad (6.62)$$

2107 According to refs. [?, ?], the hadronic matrix element for the chromomagnetic-dipole operator  
2108 into two pions,  $B_G$ , is enhanced by  $1/N_c \cdot M_K^2/M_\pi^2$  from the large next-to-leading-order corrections  
2109 that it receives. Therefore, the leading order in the chiral quark model,  $B_G = 1$ , is implausible.  
2110 In the following analyses, it is considered  $B_G = 1 \pm 3$ .

2111 The other contributions are negligible [?]. Note that the sub-leading contributions which  
2112 come from the gluino-mediated photon-penguin and the chargino-mediated  $Z$ -penguins induced  
2113 by terms of first order in the expansion of the squark mass matrix, have opposite sign and  
2114 practically cancel each other [?].

2115 Finally, the SUSY contributions to  $\varepsilon'_K/\varepsilon_K$  are given as

$$\left( \frac{\varepsilon'_K}{\varepsilon_K} \right)^{\text{SUSY}} \simeq \left. \frac{\varepsilon'_K}{\varepsilon_K} \right|_{\text{box+pen}} + \left. \frac{\varepsilon'_K}{\varepsilon_K} \right|_{\text{chromo}}. \quad (6.63)$$

2116 Note that the contributions to  $\varepsilon'_K/\varepsilon_K$  from the heavy Higgs exchanges were discarded, although  
2117 they give the strong isospin-violating contribution naturally: the contribution is enhanced by  
2118  $\tan^3 \beta$  for only down-type four-fermion scalar operators. These contributions must be propor-  
2119 tional to  $m_d m_s$  which cannot be compensated by  $\tan^3 \beta$ , so that they should be the higher-order  
2120 contributions for  $\varepsilon'_K/\varepsilon_K$ .

### 2121 6.3.1.4 $\varepsilon_K$ and $\Delta M_K$

2122 Although  $\varepsilon_K$  is one of the most sensitive quantities to new physics, the SM prediction is still  
2123 controversial. Especially, the leading short-distance contribution to  $\varepsilon_K$  in the SM is proportional  
2124 to  $|V_{cb}|^4$  (cf., ref. [?]), whose measured values from inclusive semileptonic  $B$  decays ( $\bar{B} \rightarrow X_c \ell^- \bar{\nu}$ )  
2125 and from exclusive decays ( $\bar{B} \rightarrow D^{(*)} \ell^- \bar{\nu}$  and  $\Lambda_b \rightarrow \Lambda_c \ell^- \bar{\nu}$ ) are inconsistent at a  $4.1\sigma$  level [?, ?].  
2126 A recent discussion about the exclusive  $|V_{cb}|$  is given in refs. [?, ?, ?].

2127 In this paper, for the SM prediction, we use [?]

$$\varepsilon_K^{\text{SM}} = (2.12 \pm 0.18) \times 10^{-3}, \quad (6.64)$$

2128 with

$$\varepsilon_K = e^{i\varphi_\varepsilon} \varepsilon_K^{\text{SM}}, \quad (6.65)$$

2129 where  $\varphi_\varepsilon = \tan^{-1}(2\Delta M_K/\Delta\Gamma_K) = (43.51 \pm 0.05)^\circ$  [?]. This value and the uncertainty are based  
2130 on the inclusive  $|V_{cb}|$  [?], the Wolfenstein parameters in the angle-only-fit method [?], and the  
2131 long-distance contribution obtained by the lattice simulation [?]. Combining the measured value  
2132 in eq. (6.55)

$$\varepsilon_K^{\text{EXP/SM}} = 1.05 \pm 0.10(\text{TH}), \quad (6.66)$$

2133 on the  $\chi^2$  test, with

$$\varepsilon_K^{\text{SM}} \rightarrow \varepsilon_K^{\text{SM}} + \varepsilon_K^{\text{SUSY}}. \quad (6.67)$$

2134 Note that it is also imposed that  $\text{Re}(\varepsilon_K) > 0$  from  $\text{Re}(\varepsilon_K) = (1.596 \pm 0.013) \times 10^{-3}$  [?].

2135 Within the MSSM, the SUSY contributions to  $\varepsilon_K$  are dominated by gluino box diagrams. In  
2136 this paper, however, we will focus on their suppressed region. The crossed and uncrossed gluino-  
2137 box diagrams give opposite sign contributions and there is a certain cancellation region [?, ?],  
2138 and/or simultaneous mixings of  $(\delta_d^{LL})$  and  $(\delta_d^{RR})$  can also produce the cancellation. Therefore,  
2139 we also consider the sub-dominant contributions which come from Wino and Higgsino boxes.  
2140 The  $|\Delta S| = 2$  four-quark effective Hamiltonian at the  $\mu^{\text{SUSY}}$  scale is [?]

$$\mathcal{H}_{\text{eff}} = \sum_{i=1}^5 C_i Q_i + \sum_{i=1}^3 \tilde{C}_i \tilde{Q}_i + \text{H.c.}, \quad (6.68)$$

2141 with

$$\begin{aligned} Q_1 &= (\bar{d}\gamma_\mu P_L s) (\bar{d}\gamma^\mu P_L s), & Q_2 &= (\bar{d}P_L s) (\bar{d}P_L s), & Q_3 &= (\bar{d}_\alpha P_L s_\beta) (\bar{d}_\beta P_L s_\alpha), \\ Q_4 &= (\bar{d}P_L s) (\bar{d}P_R s), & Q_5 &= (\bar{d}_\alpha P_L s_\beta) (\bar{d}_\beta P_R s_\alpha), \\ \tilde{Q}_1 &= (\bar{d}\gamma_\mu P_R s) (\bar{d}\gamma^\mu P_R s), & \tilde{Q}_2 &= (\bar{d}P_R s) (\bar{d}P_R s), & \tilde{Q}_3 &= (\bar{d}_\alpha P_R s_\beta) (\bar{d}_\beta P_R s_\alpha). \end{aligned} \quad (6.69)$$

2142 The kaon mixing amplitude  $M_{12}^{(K)}$ ,  $\Delta M_K$  and  $\varepsilon_K$  are given by

$$M_{12}^{(K)} = \frac{\langle K^0 | \mathcal{H}_{\text{eff}} | \bar{K}^0 \rangle}{2M_K}, \quad (6.70)$$

$$\Delta M_K = 2\text{Re}[M_{12}^{(K)}], \quad (6.71)$$

$$\varepsilon_K = \kappa_\varepsilon \frac{e^{i\varphi_\varepsilon}}{\sqrt{2}} \frac{\text{Im}[M_{12}^{(K)}]}{\Delta M_K^{\text{EXP}}} = e^{i\varphi_\varepsilon} \varepsilon_K^{\text{SUSY}}, \quad (6.72)$$

2143 where  $\kappa_\varepsilon = 0.94 \pm 0.02$  [?]. Using the latest lattice result [?], for the hadronic matrix elements

$$\langle K^0 | \vec{Q}(\mu) | \bar{K}^0 \rangle = (0.00211, -0.04231, 0.01288, 0.09571, 0.02452) \text{ (GeV)}^4, \quad (6.73)$$

2144 with  $\langle K^0 | \tilde{Q}_{1,2,3}(\mu) | \bar{K}^0 \rangle = \langle K^0 | Q_{1,2,3}(\mu) | \bar{K}^0 \rangle$ , where  $\mu = 3$  GeV and it was used  $m_s(\mu) =$   
2145  $(81.64 \pm 1.17)$  MeV and  $m_d(\mu) = (2.997 \pm 0.049)$  MeV [?].

2146 The leading-order QCD RG corrections are given by [?]

$$C_1(\mu) = \eta_1^K C_1(\mu^{\text{SUSY}}), \quad (6.74)$$

$$\begin{pmatrix} C_2(\mu) \\ C_3(\mu) \end{pmatrix} = X_{23} \eta_{23}^K X_{23}^{-1} \begin{pmatrix} C_2(\mu^{\text{SUSY}}) \\ C_3(\mu^{\text{SUSY}}) \end{pmatrix}, \quad (6.75)$$

$$\begin{pmatrix} C_4(\mu) \\ C_5(\mu) \end{pmatrix} = \begin{pmatrix} (\eta_1^K)^{-4} & \frac{1}{3} \left[ (\eta_1^K)^{-4} - (\eta_1^K)^{\frac{1}{2}} \right] \\ 0 & (\eta_1^K)^{\frac{1}{2}} \end{pmatrix} \begin{pmatrix} C_4(\mu^{\text{SUSY}}) \\ C_5(\mu^{\text{SUSY}}) \end{pmatrix}, \quad (6.76)$$

2147 with

$$\eta_1^K = \left[ \frac{\alpha_s(m_b)}{\alpha_s(\mu)} \right]^{\frac{6}{25}} \left[ \frac{\alpha_s(m_t)}{\alpha_s(m_b)} \right]^{\frac{6}{23}} \left[ \frac{\alpha_s(\mu^{\text{SUSY}})}{\alpha_s(m_t)} \right]^{\frac{6}{21}}, \quad (6.77)$$

$$\eta_{23}^K = \begin{pmatrix} (\eta_1^K)^{\frac{1}{6}(1-\sqrt{241})} & 0 \\ 0 & (\eta_1^K)^{\frac{1}{6}(1+\sqrt{241})} \end{pmatrix}, \quad (6.78)$$

$$X_{23} = \begin{pmatrix} \frac{1}{2}(-15 - \sqrt{241}) & \frac{1}{2}(-15 + \sqrt{241}) \\ 1 & 1 \end{pmatrix}. \quad (6.79)$$

2148 The QCD corrections to  $\tilde{C}_{1,2,3}$  are the same as  $C_{1,2,3}$ .

2149 The Wilson coefficients from the  $|\Delta S| = 2$  gluino boxes are shown in appendix ?? with their  
2150 corresponding loop functions defined in appendix ???. In the universal squark mass limit, these  
2151 results are consistent with ref. [52]. Here, the terms proportional to  $[(\mathcal{M}_D^2)_{LR}]_{12}$  or  $(\delta_d)_{13}(\delta_d)_{32}$   
2152 are discarded for simplicity.

2153 The Wilson coefficients and their corresponding loop functions for the sub-leading contribu-  
2154 tions to  $\varepsilon_K$  are given in appendix ?? and ??, respectively.

### 2155 6.3.2 Parameter scan

2156 The MSSM parameter scan is performed with the framework **Ipanema- $\beta$**  [?] using a GPU of the  
2157 model GeForce GTX 1080. The samples are a combination of flat scans plus scans based on  
2158 genetic algorithms [?]. The cost function used by the genetic algorithm is the likelihood function  
2159 with the observable constrains. In addition, aiming to get a dense population in regions with  
2160  $\mathcal{B}(K_S^0 \rightarrow \mu^+ \mu^-)$  significantly different from the SM prediction, specific penalty contributions are  
2161 added to the total cost function. Specific scans at  $\tan \beta \approx 50$  and  $M_A \approx 1.6$  TeV are performed,  
2162 as for those values the chances to get sizable MSSM effects are larger. Three different scenarios  
2163 are studied (for the ranges of the scanned parameters see table 6.2):

- 2164 • **Scenario A:** A generic scan with universal gaugino masses. No constraint on the Dark  
2165 Matter relic density is applied in this case, other than the requirement of neutralino  
2166 Lightest Supersymmetric Particle (LSP). The LSP is Bino-like in most cases, although  
2167 some points with Higgsino LSP are also found.
- 2168 • **Scenario B:** A scan motivated by scenarios with Higgsino Dark Matter. In this scenario,  
2169 the relic density is mostly function of the LSP mass, which fulfills the measured density [?]  
2170 at  $m_{\chi_1^0} \approx 1$  TeV [?, 30, 40, 41]. Thus, a scan is performed with  $|\mu| = 1$  TeV  $< M_1$ . **Universal**  
2171 **gaugino masses** are assumed in this scenario, which then implies that  $M_3 > 4.5$  TeV.
- 2172 • **Scenario C:** A scan motivated by scenarios with Wino Dark Matter, which is possible  
2173 in mAMSB or pMSSM, although it is under pressure by  $\gamma$ -rays and antiprotons data [?].  
2174 In those scenarios, the relic density is mostly function of the LSP mass, which fulfills the  
2175 experimental value [?] at  $m_{\chi_1^0} \approx 3$  TeV [?, 30]. Thus, a scan is made with  $M_2 = 3$  TeV  
2176  $< |\mu|, M_{1,3}$ . The Bino mass  $M_1$  is set to 5 TeV for simplicity. Since it is only necessary  
2177 in order to ensure that the LSP is Wino-like, any other value above 3 TeV (such as,  
2178 e.g., an mAMSB-like relation  $M_1 \approx 9.7$  TeV) could also be used without changing the  
2179 obtained results. The lightest neutralino and the lightest chargino are nearly degenerate,

Table 6.2: Scan ranges for scenario A, B (motivated by Higgsino Dark Matter) and C (motivated by Wino Dark Matter). All masses are in TeV. The nuisance parameter  $B_G$  appears in the chromomagnetic-dipole contribution to  $\varepsilon'_K/\varepsilon_K$ .

| Parameter   | Scenario A  | Scenario B  | Scenario C  |
|---|---|---|-------------|
| $\tilde{m}_Q$                                       | [2, 10]   | [2, 10]   | [4, 10]     |
| $\tilde{m}_Q^2/\tilde{m}_d^2$                       | [0.25, 4]   | [0.25, 4]   | [0.25, 4]   |
| $M_3$   | [2, 10]   | [4.5, 15]   | [4, 15]     |
| $\tan \beta$  | [10, 50]  | [10, 50]  | [10, 50]    |
| $M_A$   | [1, 2]  | [1, 2]  | [1, 2]      |
| $ \mu $   | [1, 10]   | 1   | [5, 20]     |
| $M_1$   | $\frac{\alpha_1(\mu^{SUSY})}{\alpha_3(\mu^{SUSY})} M_3$ | $\frac{\alpha_1(\mu^{SUSY})}{\alpha_3(\mu^{SUSY})} M_3$ | 5           |
| $M_2$   | $\frac{\alpha_2(\mu^{SUSY})}{\alpha_3(\mu^{SUSY})} M_3$ | $\frac{\alpha_2(\mu^{SUSY})}{\alpha_3(\mu^{SUSY})} M_3$ | 3           |
| $B_G$   | [-2, 4]   | [-2, 4]   | [-2, 4]     |
| $\text{Re} \left[ (\delta_d^{LL(RR)})_{12} \right]$ | [-0.2, 0.2]   | [-0.2, 0.2]   | [-0.2, 0.2] |
| $\text{Im} \left[ (\delta_d^{LL(RR)})_{12} \right]$ | [-0.2, 0.2]   | [-0.2, 0.2]   | [-0.2, 0.2] |

and radiative corrections are expected to bring the chargino mass to be  $\approx 160$  MeV heavier than the lightest neutralino [?].

For simplicity, in all cases the trilinear couplings and the mass insertions (other than  $(\delta_d^{LL(RR)})_{12}$  and  $(\delta_u^{LL})_{12}$ ) are set to zero, and  $\mu$  is treated as a real parameter, with both signs allowed a priori.

Further studies were also performed at the MFV limit, using RG equations induced MIs in CMSSM. As expected, no significant effect is found in this case.

For the squark masses, it is considered that  $\tilde{m}_Q = \tilde{m}_u \neq \tilde{m}_d$ . This set up is motivated by the SUSY SU(5) grand unified theory, where  $Q$  and  $U$ -squark are contained in **10** representation matter multiplet while  $D$ -squark is in **5** representation one. In general, their soft-SUSY breaking masses are different and depend on couplings between the matter multiplets and the SUSY breaking spurion field.

### 6.3.3 Results

In this subsection, the main results of the performed scans are showed. The points with  $\chi^2 < 12.5$ , corresponding to 95% C.L. for six degrees of freedom, are considered experimentally viable. The number of degrees of freedom has been calculated as the number of observables, not counting the nuisance parameter  $B_G$ , the rigid bound on the  $\tan \beta : M_A$  plane, and  $\Delta M_K$ , which are not Gaussian distributed. Therefore, the  $\chi^2$  requirement corresponds to a 95% C.L. or tighter.

Similar plots are obtained applying a looser bound on the absolute  $\chi^2$  accompanied with a  $\Delta \chi^2 < 5.99$  across the plane being plotted. Due to the large theory uncertainty,  $\mathcal{B}(K_L^0 \rightarrow \mu^+ \mu^-)$  can go up to  $\approx 1 \times 10^{-8}$  at  $2\sigma$  level. Values slightly above that limit can still be allowed if they reduce the  $\chi^2$  contribution in other observables. The allowed regions are separated by the sign

of  $A_{L\gamma\gamma}^\mu$  in eq. (6.21). Results for  $A_{CP}$  are also shown, which could be experimentally accessed by means of a tagged analysis.

### 6.3.3.1 Effects from $(\delta_d^{LL(RR)})_{12}$ separately

The effects of pure left-handed(right-handed) MIs are studied separately, to determine the regions of the MSSM parameter space in which either *LL* MIs or *RR* MIs dominate<sup>9</sup>. The obtained scatter plots for  $\mathcal{B}(K_L^0 \rightarrow \mu^+ \mu^-)$  vs  $\mathcal{B}(K_S^0 \rightarrow \mu^+ \mu^-)$  and  $\mathcal{B}(K_S^0 \rightarrow \mu^+ \mu^-)$  vs  $\varepsilon'_K/\varepsilon_K$  are shown in figure 6.11 and figure 6.12 for Scenario A, figure 6.13 and figure 6.14 for Scenario B, and figure 6.15 and figure 6.16 for Scenario C. The points in the planes correspond to predictions from different values of the input parameters. It should be noted that in such cases, the SUSY contributions to  $\varepsilon_K$  can be suppressed naturally in a heavy gluino region ( $M_3 \gtrsim 1.5\tilde{m}_Q$ ) [?, ?].

In Scenario A (see figure 6.11) and Scenario C (see figure 6.15), we can see that the 95% C.L. allowed regions for  $\mathcal{B}(K_S^0 \rightarrow \mu^+ \mu^-)$  in light of the constraints listed in table 6.1 are approximately  $[0.78, 14] \times 10^{-12}$  for *LL*-only contributions, and  $[1.5, 35] \times 10^{-12}$  for *RR*-only contributions, without any need of fine-tuning the parameters to avoid constraints from  $\mathcal{B}(K_L^0 \rightarrow \mu^+ \mu^-)$ . The MSSM contributions are similar for *RR* and *LL*, and the differences on the allowed ranges for  $\mathcal{B}(K_S^0 \rightarrow \mu^+ \mu^-)$  arise from the interference with the SM amplitudes in  $K_{S(L)}^0 \rightarrow \mu^+ \mu^-$ , which are shown in section ??.

The allowed regions for scenarios A and C are very similar to each other, although marginally larger on A. It can also be seen that, in Scenario B (see figure 6.13) the maximum departure of  $\mathcal{B}(K_S^0 \rightarrow \mu^+ \mu^-)$  from the SM is smaller than in the other scenarios, since  $C_{S,P} \propto \mu$  and  $\mu$  is small relative to squark and gluino masses. In the contributions to  $(\varepsilon'_K/\varepsilon_K)^{\text{SUSY}}$ , the chromomagnetic-dipole contribution can be significant in both *LL*-only and *RR*-only cases when  $\mu \tan \beta$  and  $B_G$  have large values, while the box contributions can be significant only via *LL* MIs [?]. Note that the penguin contributions to  $(\varepsilon'_K/\varepsilon_K)^{\text{SUSY}}$  are neglected in the parameter scan.

The effective branching fraction and *CP* asymmetry are shown in figure 6.17 for Scenario A. Note that the negative value of  $\mathcal{B}(K_S^0 \rightarrow \mu^+ \mu^-)_{\text{eff}}$  is compensated in data by inclusion of the background events from  $K_L^0 \rightarrow \mu^+ \mu^-$ , so that the overall  $K^0 \rightarrow \mu^+ \mu^-$  is always positive. Correlation patterns of  $A_{CP}$  with other observables can be seen in figure 6.18, where  $D' = -D$  and  $D = 0.5$  are chosen for simplicity. It is found that *CP* asymmetries can be up to  $\approx 6$  (at  $D = 1$ ), approximately eight times bigger than in the SM. The largest effects are found in left-handed scenarios.

### 6.3.3.2 Floating *LL* and *RR* MIs simultaneously

A priori, one possibility to avoid the constraint from  $\mathcal{B}(K_L^0 \rightarrow \mu^+ \mu^-)$  is to allow simultaneously for non-zero *LL* and *RR* mass insertions. This way both  $C_{S(P)}$  and  $\tilde{C}_{S(P)}$  are non zero and eqs. (6.24)–(6.29) do not hold. Tuning the values of the MIs, regions in which the MSSM contributions to  $\mathcal{B}(K_S^0 \rightarrow \mu^+ \mu^-)$  do not alter  $\mathcal{B}(K_L^0 \rightarrow \mu^+ \mu^-)$  significantly (thus satisfying the experimental bound) can be found. Choosing for example

$$\text{Re} [(\delta_d^{LL})_{12}] = -\text{Re} [(\delta_d^{RR})_{12}], \quad \text{Im} [(\delta_d^{LL})_{12}] = \text{Im} [(\delta_d^{RR})_{12}], \quad (6.80)$$

---

<sup>9</sup>As an example, MFV models the *LL* MIs can become non-zero after RGE, which does not happen for *RR* MIs.

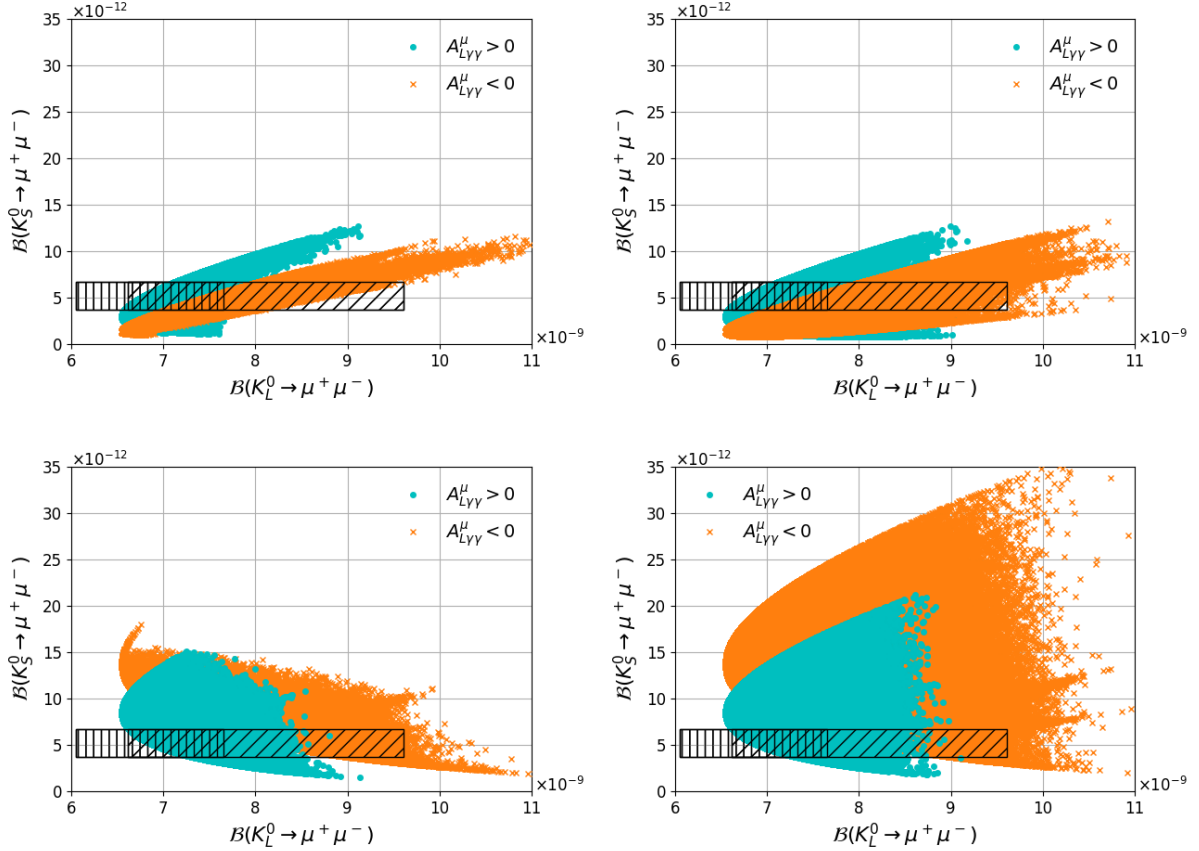


Figure 6.11: Scenario A  $\mathcal{B}(K_S^0 \rightarrow \mu^+\mu^-)$  vs  $\mathcal{B}(K_L^0 \rightarrow \mu^+\mu^-)$  for  $(\delta_d^{LL})_{12} \neq 0$  and  $(M_3 \cdot \mu) > 0$  (upper left),  $(\delta_d^{LL})_{12} \neq 0$  and  $(M_3 \cdot \mu) < 0$  (upper right),  $(\delta_d^{RR})_{12} \neq 0$  and  $(M_3 \cdot \mu) > 0$  (lower left), and  $(\delta_d^{RR})_{12} \neq 0$  and  $(M_3 \cdot \mu) < 0$  (lower right). The cyan dots correspond to  $A_{L\gamma\gamma}^\mu > 0$  and the orange crosses to  $A_{L\gamma\gamma}^\mu < 0$ . The vertically hatched area corresponds to the SM prediction for  $A_{L\gamma\gamma}^\mu > 0$  and the inclined hatched area corresponds to the SM prediction for  $A_{L\gamma\gamma}^\mu < 0$ .

then the SUSY contributions to  $\mathcal{B}(K_L^0 \rightarrow \mu^+\mu^-)$  are canceled, while the SUSY contributions to  $\mathcal{B}(K_S^0 \rightarrow \mu^+\mu^-)$  are maximized (see eqs. (6.14)–(6.18)). However, it is known that in those cases the bounds from  $\Delta M_K$  and  $\varepsilon_K$  are very stringent. Fine-tuned regions with  $\mathcal{B}(K_S^0 \rightarrow \mu^+\mu^-) > 10^{-10}$ , or even at the level of the current experimental bound of  $8 \times 10^{-10}$  at 90% C.L. [?] (consistent with all the listed constraints ref?) while targetting large values of  $\mathcal{B}(K_S^0 \rightarrow \mu^+\mu^-)$ , can be found using genetic algorithms with cost functions.

These points are located along very narrow strips in the  $(\delta_d^{LL})_{12}$  vs  $(\delta_d^{RR})_{12}$  planes, as shown in figure 6.19. The figure corresponds to Scenario C as it is the one with higher density of points at large values of  $\mathcal{B}(K_S^0 \rightarrow \mu^+\mu^-)$  and the pattern observed in Scenario A is nearly identical. A particularly favorable region corresponds to  $|(\delta_d^{LL})_{12}| \approx 2|(\delta_d^{RR})_{12}| \sim 0.03$  and  $\arg[(\delta_d^{LL})_{12}] \approx -\arg[(\delta_d^{RR})_{12}] + \pi$ , which is in the vicinity of eq. (6.80), and with  $\delta_u^{LL}$  given by the symmetry relation of eq. (6.7). They also favor narrow regions in the squark vs gluino

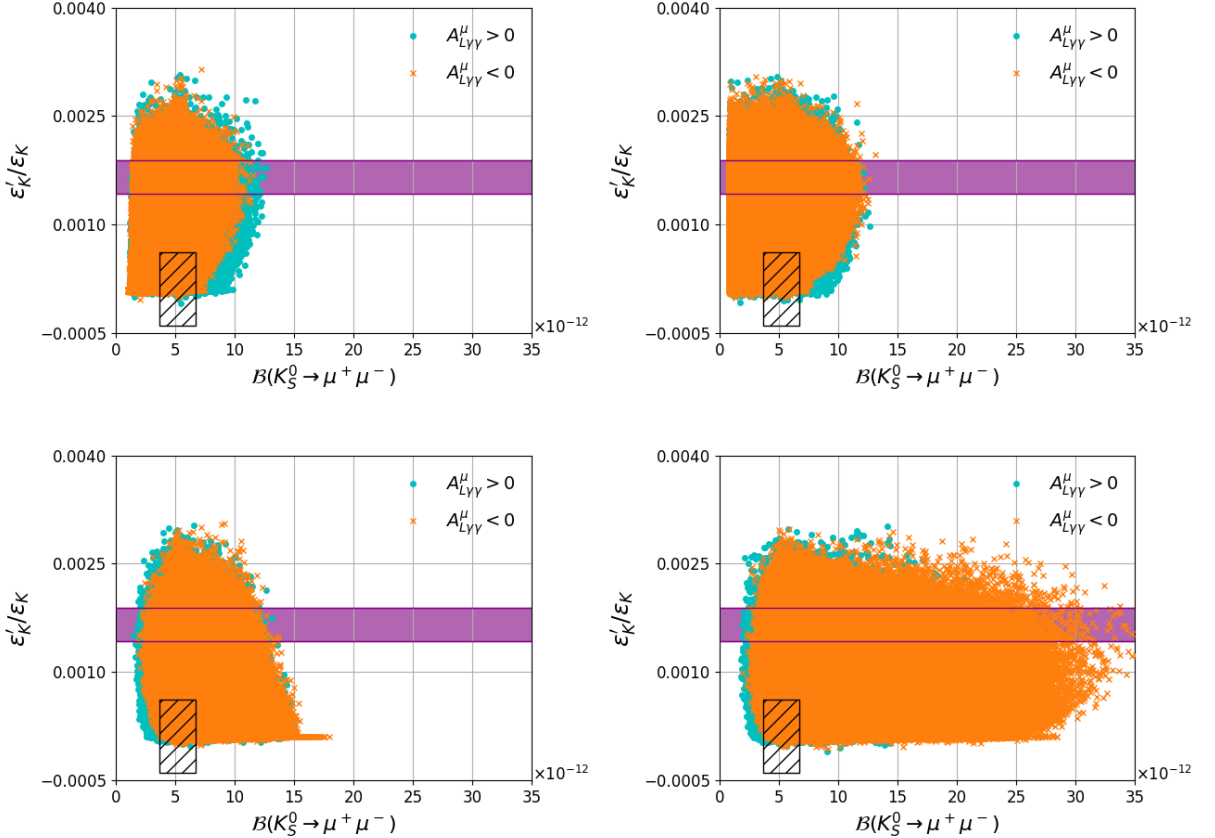


Figure 6.12: Scenario A  $\frac{\varepsilon'_K}{\varepsilon_K}$  vs  $\mathcal{B}(K_S^0 \rightarrow \mu^+ \mu^-)$  for  $(\delta_d^{LL})_{12} \neq 0$  and  $(M_3 \cdot \mu) > 0$  (upper left),  $(\delta_d^{LL})_{12} \neq 0$  and  $(M_3 \cdot \mu) < 0$  (upper right),  $(\delta_d^{RR})_{12} \neq 0$  and  $(M_3 \cdot \mu) > 0$  (lower left), and  $(\delta_d^{RR})_{12} \neq 0$  and  $(M_3 \cdot \mu) < 0$  (lower right). The cyan dots correspond to  $A_{L\gamma\gamma}^\mu > 0$  and the orange crosses to  $A_{L\gamma\gamma}^\mu < 0$ . The deep purple band corresponds to the experimental results and the hatched area to the SM prediction.

masses planes as shown in figure 6.20. The values close to the experimental upper bound can still be obtained even if the constraint on  $\Delta M_K$  is significantly tightened.

Using the SM prediction for  $\varepsilon_K$  provided in ref. [?]:

$$\varepsilon_K^{\text{EXP/SM}} = 1.41 \pm 0.16(\text{TH}), \quad (6.81)$$

It is found that it is easier to accommodate *LL* and *RR* MIs of similar sizes, and fine-tuned regions with  $\mathcal{B}(K_S^0 \rightarrow \mu^+ \mu^-) > 10^{-10}$  are found with higher chances. The shapes of the strips in the mass insertion planes do not change substantially. Notice however that this prediction, that is obtained using  $|V_{cb}|$  from exclusive decays, is less consistent with data than the one that was used previously.

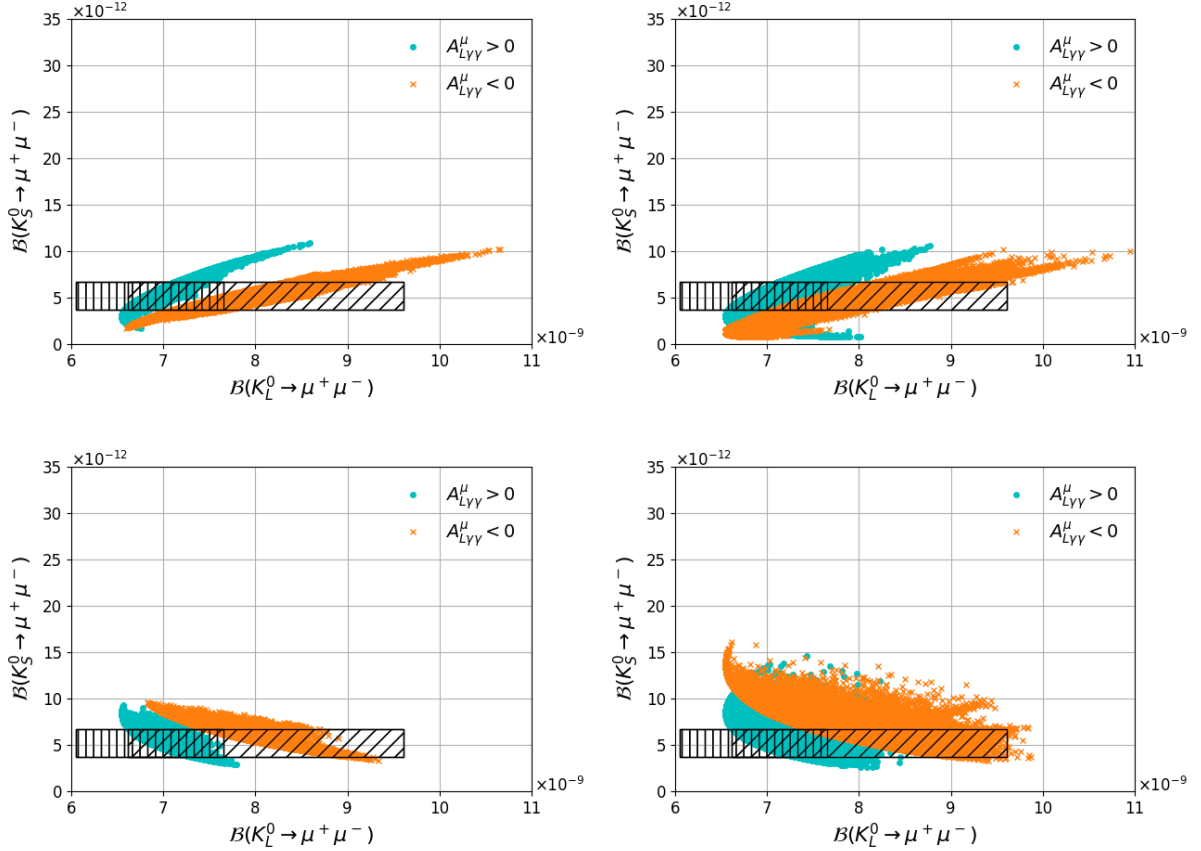


Figure 6.13: Scenario B, motivated by Higgsino Dark Matter with universal gaugino masses,  $\mathcal{B}(K_S^0 \rightarrow \mu^+ \mu^-)$  vs  $\mathcal{B}(K_L^0 \rightarrow \mu^+ \mu^-)$  for  $(\delta_d^{LL})_{12} \neq 0$  and  $(M_3 \cdot \mu) > 0$  (upper left),  $(\delta_d^{LL})_{12} \neq 0$  and  $(M_3 \cdot \mu) < 0$  (upper right),  $(\delta_d^{RR})_{12} \neq 0$  and  $(M_3 \cdot \mu) > 0$  (lower left), and  $(\delta_d^{RR})_{12} \neq 0$  and  $(M_3 \cdot \mu) < 0$  (lower right). The cyan dots correspond to  $A_{L\gamma\gamma}^\mu > 0$  and the orange crosses to  $A_{L\gamma\gamma}^\mu < 0$ . The vertically hatched area corresponds to the SM prediction for  $A_{L\gamma\gamma}^\mu > 0$  and the inclined hatched area corresponds to the SM prediction for  $A_{L\gamma\gamma}^\mu < 0$ .

### 2259 6.3.3.3 Non degenerate Higgs masses

2260 The results so far have been obtained in the MSSM framework, in which  $|C_S| \approx |C_P|$ , due to the  
 2261 mass degeneracy  $M_H \approx M_A$ . In models in which such degeneracy can be broken, the constraint  
 2262 that  $\mathcal{B}(K_L^0 \rightarrow \mu^+ \mu^-)$  imposes to  $\mathcal{B}(K_S^0 \rightarrow \mu^+ \mu^-)$  becomes looser the more those two masses  
 2263 differ. This happens for example at low values of  $M_A$  in the MSSM, and requiring  $\tan \beta$  to be  
 2264 small to avoid constraints from  $\tan \beta : M_A$  planes from LHC. Those regions are more difficult to  
 2265 study, since it would require a detailed specification of the MSSM and test it against bounds of  
 2266 the Higgs sector. The mass degeneracy is also broken in extensions such as NMSSM. According  
 2267 to the scans performed, on those cases values of  $\mathcal{B}(K_S^0 \rightarrow \mu^+ \mu^-) > 10^{-10}$  could be reached for  
 2268 mass differences of  $\mathcal{O}(33\%)$  or larger without fine-tuning the MIs.

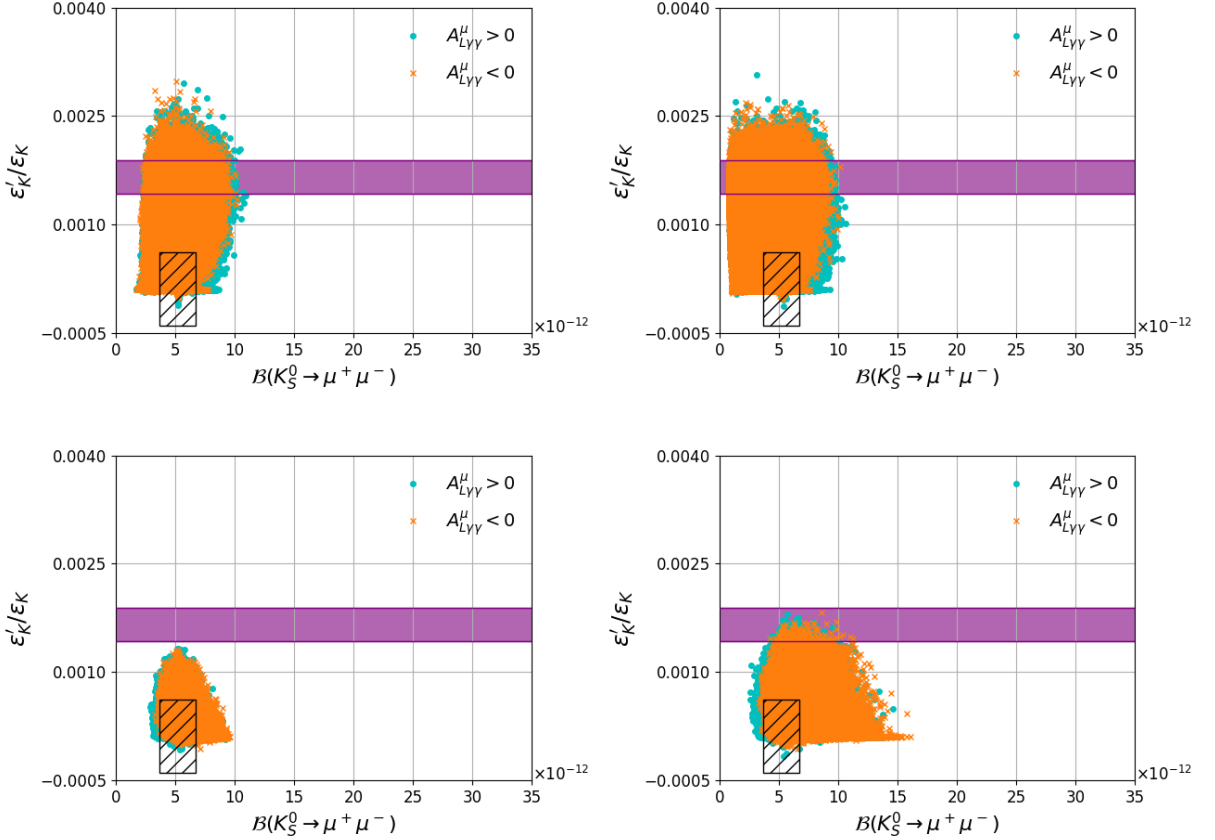


Figure 6.14: Scenario B, motivated by Higgsino Dark Matter and universal gaugino masses,  $\frac{\varepsilon'_K}{\varepsilon_K}$  vs  $\mathcal{B}(K_S^0 \rightarrow \mu^+\mu^-)$  for  $(\delta_d^{LL})_{12} \neq 0$  and  $(M_3 \cdot \mu) > 0$  (upper left),  $(\delta_d^{LL})_{12} \neq 0$  and  $(M_3 \cdot \mu) < 0$  (upper right),  $(\delta_d^{RR})_{12} \neq 0$  and  $(M_3 \cdot \mu) > 0$  (lower left), and  $(\delta_d^{RR})_{12} \neq 0$  and  $(M_3 \cdot \mu) < 0$  (lower right). The cyan dots correspond to  $A_{L\gamma\gamma}^\mu < 0$  and the orange crosses to  $A_{L\gamma\gamma}^\mu > 0$ . The deep purple band corresponds to the experimental results and the hatched area to the SM prediction.

### 2269 6.3.4 Conclusions

2270 The MSSM contribution to  $\mathcal{B}(K_S^0 \rightarrow \mu^+\mu^-)$  for non-zero  $(\delta_d^{LL})_{12}$  and  $(\delta_d^{RR})_{12}$  mass insertions  
 2271 has been studied, motivated by the experimental value of  $\varepsilon'_K/\varepsilon_K$ , and in the large  $\tan\beta$  regime.  
 2272 It is found that MSSM contributions to  $\mathcal{B}(K_S^0 \rightarrow \mu^+\mu^-)$  can surpass the SM contributions  
 2273 [ $\mathcal{B}(K_S^0 \rightarrow \mu^+\mu^-)^{\text{SM}} = 5.18 \times 10^{-12}$ ] by up to a factor of seven (see figure 6.11), reaching the  
 2274 level of  $3.5 \times 10^{-11}$  even for large SUSY masses, with no conflict with existing experimental  
 2275 data, and are detectable by LHCb. This is also the case even if  $\varepsilon'_K/\varepsilon_K$  turns out to be SM-  
 2276 like as predicted by refs. [?, ?, ?]. Figures of correlations between  $\mathcal{B}(K_S^0 \rightarrow \mu^+\mu^-)$  and other  
 2277 observables have been provided for different regions of the MSSM parameter space, and can be  
 2278 used to understand which scenarios are more or less favoured, depending on the experimental  
 2279 outcomes. The  $3.5 \times 10^{-11}$  bound is due to the combined effect of  $\Delta M_K, \varepsilon_K$ , and  $K_L^0 \rightarrow \mu^+\mu^-$

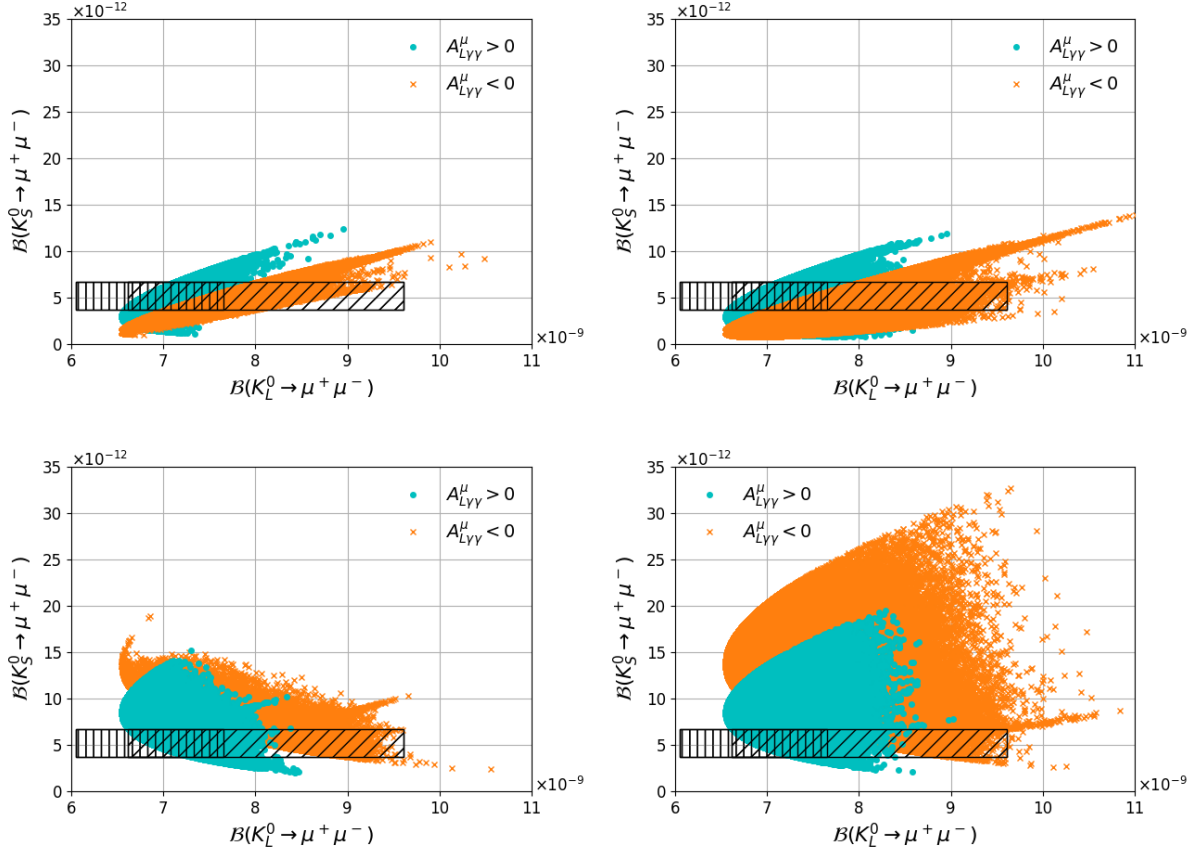


Figure 6.15: Scenario C (motivated by Wino Dark Matter)  $\mathcal{B}(K_S^0 \rightarrow \mu^+ \mu^-)$  vs  $\mathcal{B}(K_L^0 \rightarrow \mu^+ \mu^-)$  for  $(\delta_d^{LL})_{12} \neq 0$  and  $(M_3 \cdot \mu) > 0$  (upper left),  $(\delta_d^{LL})_{12} \neq 0$  and  $(M_3 \cdot \mu) < 0$  (upper right),  $(\delta_d^{RR})_{12} \neq 0$  and  $(M_3 \cdot \mu) > 0$  (lower left), and  $(\delta_d^{RR})_{12} \neq 0$  and  $(M_3 \cdot \mu) < 0$  (lower right). The cyan dots correspond to  $A_{L\gamma\gamma}^\mu > 0$  and the orange crosses to  $A_{L\gamma\gamma}^\mu < 0$ . The vertically hatched area corresponds to the SM prediction for  $A_{L\gamma\gamma}^\mu > 0$  and the inclined hatched area corresponds to the SM prediction for  $A_{L\gamma\gamma}^\mu < 0$ .

constraints. Such bound is not rigid, and fine-tuned regions can bring the branching fraction above the  $10^{-10}$  level, even up to the current experimental bound; the largest deviations from SM are found at  $|(\delta_d^{LL})_{12}| \approx 2|(\delta_d^{RR})_{12}| \sim 0.03$  and  $\arg[(\delta_d^{LL})_{12}] \approx -\arg[(\delta_d^{RR})_{12}] + \pi$  for large squark and gluino masses. The the  $CP$  asymmetry of  $K^0 \rightarrow \mu^+ \mu^-$  can be significantly modified by MSSM contributions, being up to eight times bigger than the SM prediction in the pure LL case. It should be noted that, for simplicity, only the main contributions in the large  $\tan \beta$  regime have been considered. Discarded terms could, in principle, provide even more flexibility to the allowed regions.

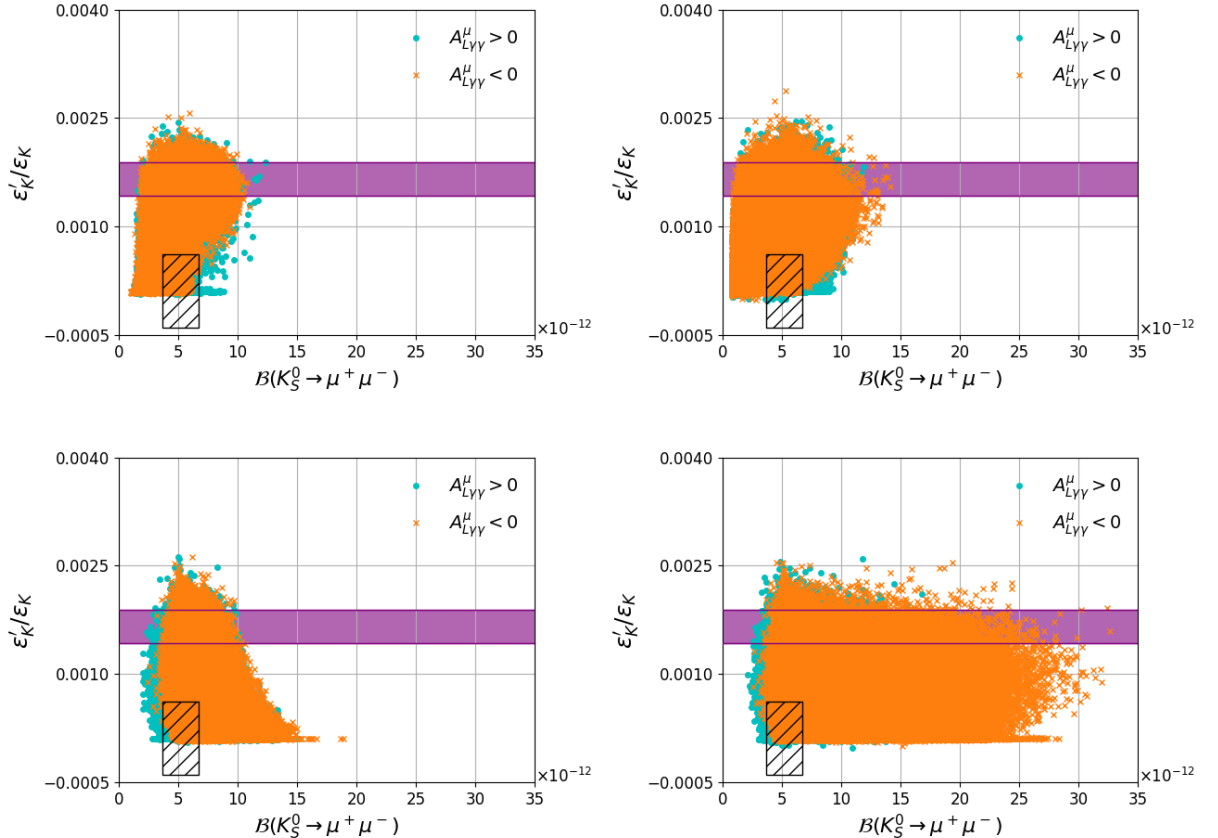


Figure 6.16: Scenario C, motivated by Wino Dark Matter,  $\frac{\varepsilon'_K}{\varepsilon_K}$  vs  $\mathcal{B}(K_S^0 \rightarrow \mu^+ \mu^-)$  for  $(\delta_d^{LL})_{12} \neq 0$  and  $(M_3 \cdot \mu) > 0$  (upper left),  $(\delta_d^{LL})_{12} \neq 0$  and  $(M_3 \cdot \mu) < 0$  (upper right),  $(\delta_d^{RR})_{12} \neq 0$  and  $(M_3 \cdot \mu) > 0$  (lower left), and  $(\delta_d^{RR})_{12} \neq 0$  and  $(M_3 \cdot \mu) < 0$  (lower right). The cyan dots correspond to  $A_{L\gamma\gamma}^\mu > 0$  and the orange crosses to  $A_{L\gamma\gamma}^\mu < 0$ . The deep purple band corresponds to the experimental results and the hatched area to the SM prediction.

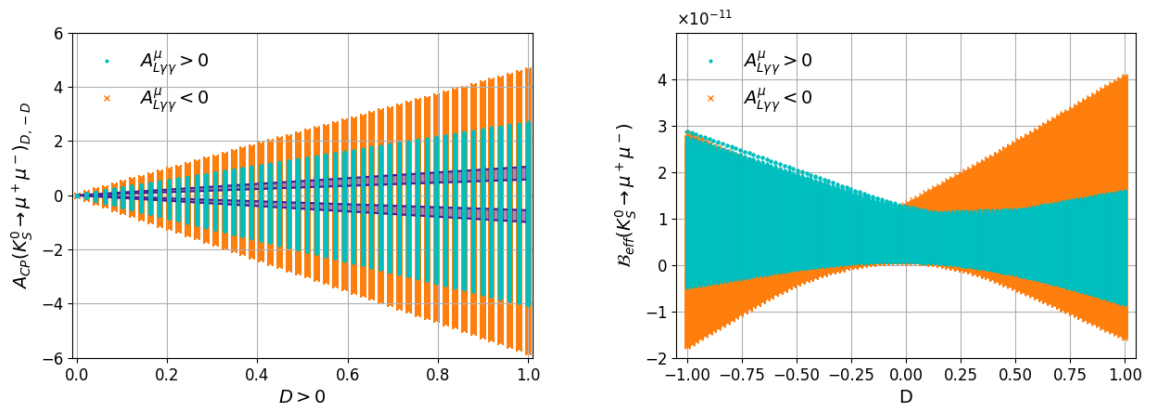


Figure 6.17: Scenario A,  $(\delta_d^{LL})_{12} \neq 0$  and  $(M_3 \cdot \mu) < 0$ . Plots of  $A_{CP}(K_S^0 \rightarrow \mu^+ \mu^-)$  vs  $D$  (left) for the case  $D = -D'$  ( $D > 0$ ) where the cyan dots correspond to  $A_{L\gamma\gamma}^\mu > 0$ , the orange crosses to  $A_{L\gamma\gamma}^\mu < 0$ , and the deep purple bands correspond to the SM predictions in eq. (6.38).  $\mathcal{B}(K_S^0 \rightarrow \mu^+ \mu^-)_{\text{eff}}$  vs  $D$  (right).

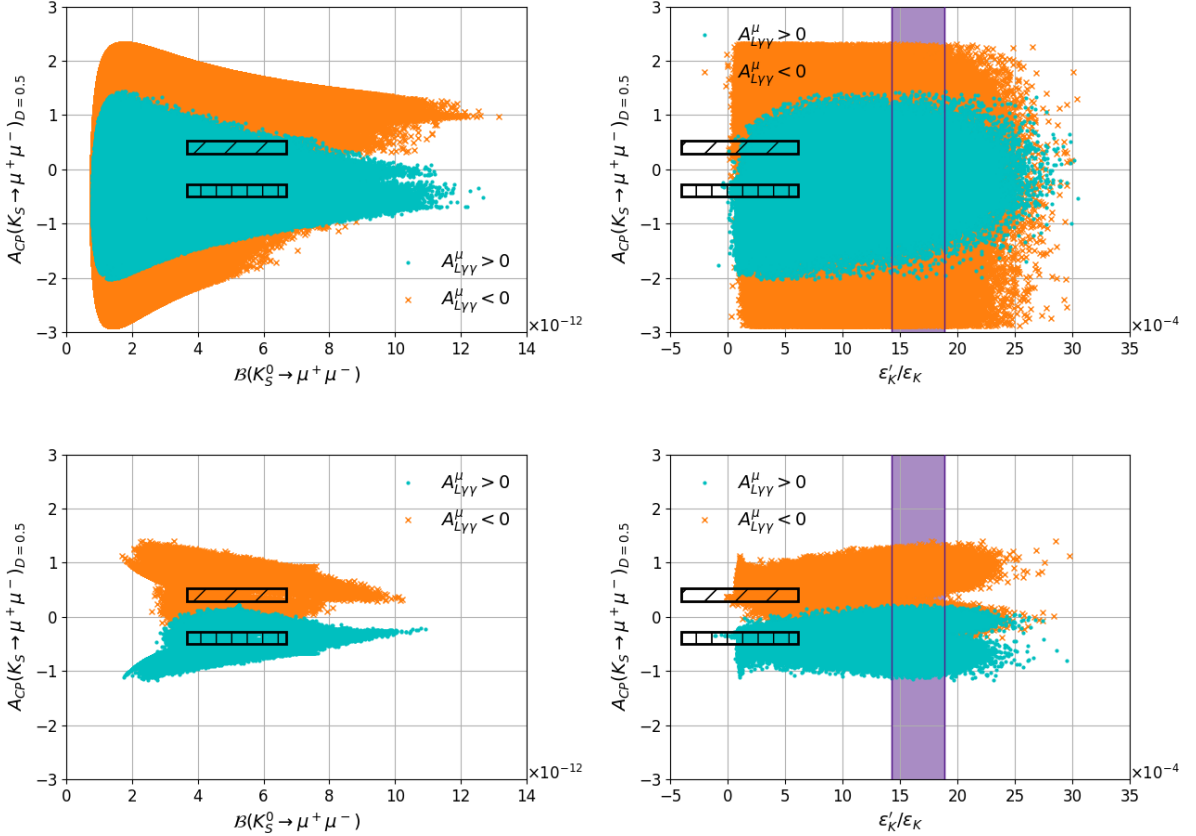


Figure 6.18:  $A_{CP}$  vs  $\mathcal{B}(K_S^0 \rightarrow \mu^+ \mu^-)$  (left) and vs  $\varepsilon'_K / \varepsilon_K$  (right). The top panels correspond to Scenario A,  $(\delta_d^{LL})_{12} \neq 0$  and  $(M_3 \cdot \mu) < 0$ . The bottom panels correspond to Scenario B,  $(\delta_d^{LL})_{12} \neq 0$  and  $(M_3 \cdot \mu) > 0$ . The plots are done for  $D = -D' = 0.5$ . The cyan dots correspond to  $A_{L\gamma\gamma}^\mu > 0$  and the orange crosses to  $A_{L\gamma\gamma}^\mu < 0$ . The deep purple bands correspond to the experimental value of  $\varepsilon'_K / \varepsilon_K$ , the vertically hatched areas correspond to the SM prediction for  $A_{L\gamma\gamma}^\mu > 0$  and the inclined hatched areas to the SM prediction for  $A_{L\gamma\gamma}^\mu < 0$ .

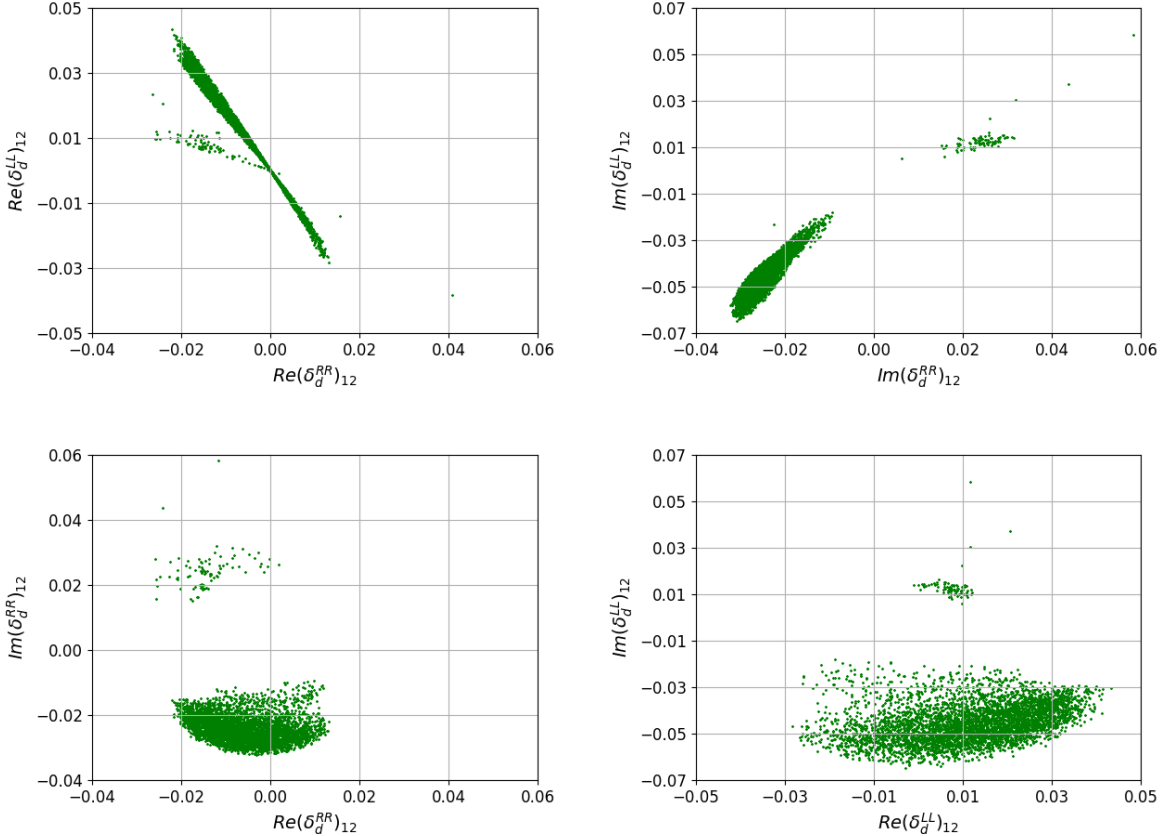


Figure 6.19: Scatter plots of the real (upper left) and the imaginary (upper right) parts of the mass insertions  $(\delta_d^{RR})_{12}$  and  $(\delta_d^{LL})_{12}$  for  $\mathcal{B}(K_S^0 \rightarrow \mu^+ \mu^-) > 2 \times 10^{-10}$ , of the real vs imaginary  $(\delta_d^{RR})_{12}$  (lower left) and of the real vs imaginary  $(\delta_d^{LL})_{12}$  (lower right). All points in the plane pass the experimental constraints defined in section ???. The up-type MI  $(\delta_u^{LL})_{12}$  is given by eq. (6.7). The plots correspond to Scenario C, with a sample of 4378 points with  $\mathcal{B}(K_S^0 \rightarrow \mu^+ \mu^-) > 2 \times 10^{-10}$  and  $\chi^2 < 12.5$ , produced after 6M generations of  $200k$  points each. The pattern observed in Scenario A is very similar.

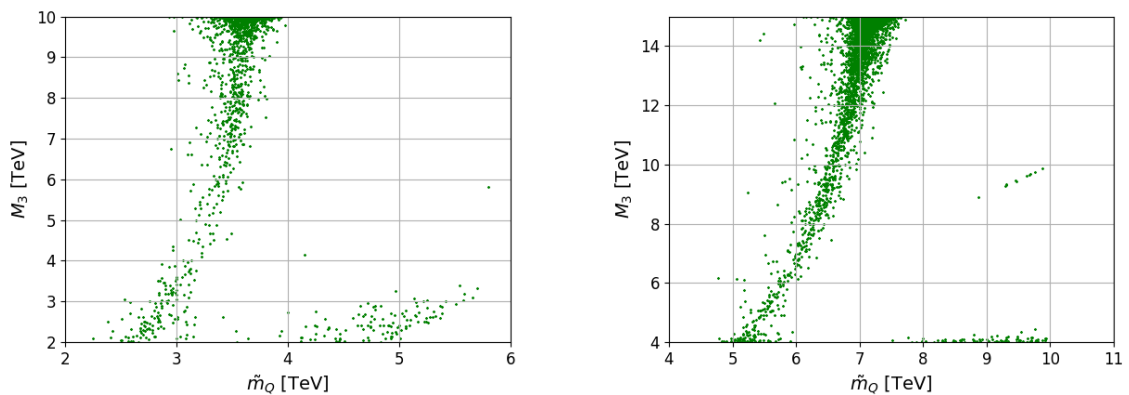


Figure 6.20: Scatter plot of the squark and gluino masses for  $\mathcal{B}(K_S^0 \rightarrow \mu^+ \mu^-) > 2 \times 10^{-10}$  taking into account the constraints defined in section ???. Left: Scenario A, Right: Scenario C. The  $\chi^2$  cut in Scenario A has been relaxed to 14 to increase the density of points.

2288 **Chapter 7**

2289 **CMSSM**

2290 **7.1 MasterCode framework**

2291 The `MasterCode` framework performs global fits following a frequentist approach. Its core con-  
2292 sists of tools to compute the different the SUSY observables, tools to calculate the  $\chi^2$  (that  
2293 will be discussed in more details in [ref](#)) and the interface to an appropriate sampling algorithm,  
2294 `MultiNest` [ref](#). So as to compute the SUSY observables, the full MSSM spectrum for [electroweak](#)  
2295 [observables](#) (including masses, mixing matrices and couplings) is computed by `SoftSUSY 3.7.2`.  
2296 The Higgs sector of this spectrum is further refined using calculations from `FeynHiggs 2.10.0`.  
2297 This spectrum (in a format compliant with SUSY Les Houches Accord [ref](#)) is then used as input  
2298 for other codes to compute more observables and constraints, summarised in [7.1](#). From this,  
2299 a global likelihood function is constructed, including contributions from electroweak precision  
2300 observables, flavour measurements, the cosmological dark matter density and direct searches for  
2301 dark matter, as well as the LHC Higgs mass measurement and  $E_T$  searches.

Table 7.1: Codes used to calculate SUSY observables in the `MasterCode` framework.

| Code  | Reference   | Observables  |
|---|---|--|
| <code>SoftSUSY 3.7.2</code>   | <a href="#">ref</a>   | SUSY spectrum  |
| <code>FeynHiggs-2.10.0</code>   | <a href="#">ref</a>   | Higgs sector, $(g - 2)_\mu$  |
| <code>micrOMEGAs-3.2</code><br>SSARD  | <a href="#">ref</a><br><a href="#">ref</a>                        | $\Omega_{\text{CDM}} h^2$<br>$\sigma_p^{\text{SI}}, \Delta\sigma_p^{\text{SI}}$                        |
| <code>SuFla, SuperIso v3.5</code><br><code>FeynWZ</code>                                      | <a href="#">ref</a><br><a href="#">ref</a>                        | Flavour physics<br>$M_W, Z$ -pole  |
| <code>HiggsSignals-1.3.1</code><br><code>HiggsBounds-4.2.0</code><br><code>SDECAY-1.3b</code> | <a href="#">ref</a><br><a href="#">ref</a><br><a href="#">ref</a> | Constraints Higgs signal-strengths<br>Constraints $H/A \rightarrow \tau^+\tau^-$ decay<br>Decay tables |

## 2302 7.2 Sampling algorithm

2303 The main goal of the `MasterCode` framework is establishing confidence intervals for parameters  
2304 and observables. In order to do this, the desired region is sampled and the likelihood function is  
2305 inspected by means of the `MultiNest` algorithm ref. Even though it was designed as a Bayesian  
2306 inference tool, it has proven to be very sucessful in computing profile likelihood functions ref.

2307 The likelihood is computed iteratively based on the so-called ellipsoidal neted sample. In  
2308 this mechanism, ellipsoidal bounds are constructed in the unit cube based on clustering of N  
2309 active points. For each iteration, the point with the lowest likelihood amongst a set of points  
2310 (*live* or active) is discarded, and another one with higher likelihood is searched. When found, it  
2311 replaces the former, that turns into an *inactive* point. This is done until the Bayesian evidence  
2312 has reaches a value controled by the *tolerance*.

2313 Apart from its robustness and efficiency, this algorithm was specifically designed to deal  
2314 with multiple local maxima and elongated curving degeneracies, thus fulfilling `MasterCode`'s  
2315 requirements. A special feature of `MultiNest` is that once a point becomes active, it forms a  
2316 basin of attraction, so that proximal points will be sampled. This ensures the coverage of small  
2317 volumes, provided one of their points becomes active.

2318 In order to ensure a good coverage of the parameter space, this is divided into segments.  
2319 The "cross-product" of these segments constitute *boxes*. For each of these boxes, the number  
2320 of active points is  $N = 1000$ . Priors are defined in order to convert the input parameters into  
2321 physical quantities computable by the likelihood. Usually soft flat priors are used (an example of  
2322 this distribution can be seen in 7.1). With this, 80% of the distribution lies within the nominal  
2323 segment range, with the rest 20 % lies outside these bounds. This allows for some overlap  
2324 between boxes, hence avoiding edge effects between neighbouring parameter segments.

## 2325 7.3 Scan Ranges

2326 The scan ranges are chosen such that they include a full coverage of parameter space, paying  
2327 spacial attention to the mass scales relevant for LHC, while maintaining the Yukawa couplings  
2328 perturbatively small (hence  $1.2 \leq \tan \beta \geq 65$ ). The input parameters and the nuisance param-  
2329 eters are sampled using soft flat and Gaussian priors, respectively. The ranges, the number of  
2330 segments and the resulting number of boxes that are used in the scan are given in 7.2.

Table 7.2: Sampling ranges and segment definitions in the MODEL.

| Parameter | Range   | # Segments |
|-----------|---------|------------|
| MISSING   | MISSING | MISSING    |

## 2331 7.4 Method

2332 So as to explore the different models within the `MasterCode` framework, frequentist confidence  
2333 intervals and regins for the model parameters and corresponding predictions for physical ob-

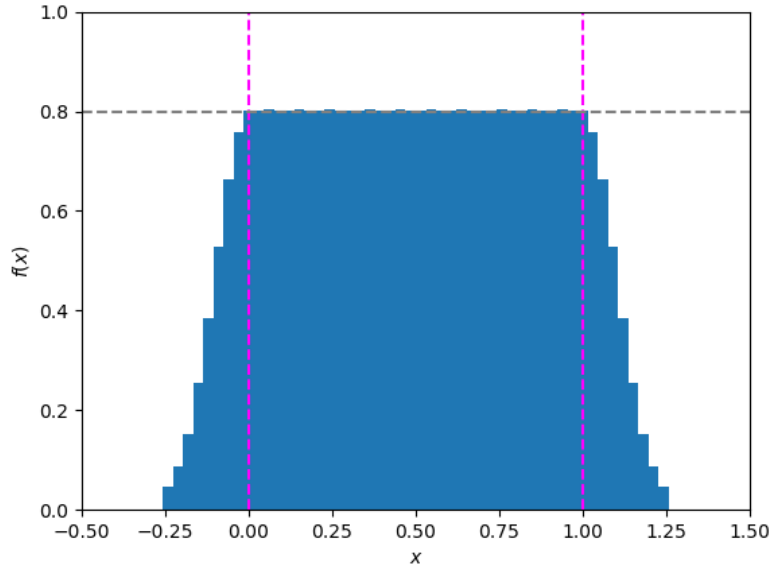


Figure 7.1: Illustration of soft flat prior, for which 80% is flat and lies within the nominal range of the segment ( $[0,1]$ ]), while 20% of the distribution lies outside the nominal range, and is normally distributed.

2334 servables are established. In order to do this, a  $\chi^2$  function is constructed from the likelihood  
 2335 function using Wilks' theorem,  $\chi^2 \approx -2 \ln(\theta) + \text{const.}$ , being this normalisation constant irrelevant.  
 2336 For the sake of this study. The  $\chi^2$  function is given by

$$\chi^2(\theta) \equiv \sum_i \left( \frac{O_{i,\text{meas.}} - O_{i,\text{pred.}}}{\sigma(O_i)} \right)^2 + \sum_j \left( \frac{\theta_{j,\text{meas.}}^{\text{SM}} - \theta_{j,\text{nuis.}}^{\text{SM}}}{\sigma(\theta_{j,\text{meas.}}^{\text{SM}})} \right)^2 + \sum_k \chi_{k,\text{non-Gaussian}}^2 \quad (7.1)$$

2337 where  $O_{i,\text{pred.}}(\theta)$  ( $O_{i,\text{meas.}}(\theta)$ ) are the predicted (measured) values for the observables,  $\theta(O_i)$  is the  
 2338 total uncertainty, obtained adding the experimental and theoretical uncertainties in quadrature,  
 2339 and  $\theta_{k,\text{nuis.}}$  are the SM nuisance parameters  $m_t$ ,  $\Delta\alpha_{\text{had}}^{(5)}(M_Z)$ ,  $M_Z$  that are allowed to vary in  
 2340 the fit while being constrained according to their measured values and uncertainties. The first  
 2341 two terms in 7.1 correspond to a normal distribution of the likelihood, thus being "Gaussian"  
 2342 constraints, while the third term is "non-Gaussian" and a more refined treatment is needed.  
 2343 The confidence intervals for  $n$  parameters and/or physical observables of interest at a confidence  
 2344 level  $\alpha$  are thus given by the condition  $\Delta\chi^2 \leq \Delta\chi^2(\alpha, n)$ . Some typical values are given in 7.3.

2345 Therefore, 68% CL intervals (regions) correspond to  $\Delta\chi^2 < 1$  ( $\Delta\chi^2 < 2.30$ ), while 95%  
 2346 CL intervals (regions) correspond to  $\Delta\chi^2 < 4$  ( $\Delta\chi^2 < 5.99$ ) for one- (two-)dimensional profile  
 2347 likelihood functions.

#### 2348 7.4.1 Gaussian Constraints

2349 The following Gaussian Constraints are used in the study:

Table 7.3: Sampling ranges and segment definitions in the MODEL.

| $\alpha(\%)$ | $\Delta\chi^2(\alpha, 1)$ | $\Delta\chi^2(\alpha, 2)$ |
|--------------|---------------------------|---------------------------|
| 68           | 0.99                      | 2.27                      |
| 68.3         | 1                         | 2.30                      |
| 95           | 3.84                      | 5.99                      |
| 95.4         | 4                         | 6.18                      |
| 99           | 6.63                      | 9.21                      |
| 99.7         | 9                         | 11.82                     |

- 95% CL lower limits on the masses of SUSY particles from ALEPH, DELPHI, L3, OPAL experiments [ref](#).
- Top Mass,  $m_t = 173.34 \pm 0.76$ GeV[ref](#), treated as a nuisance parameter.
- Light Higgs Boson, with a measured mass[ref](#) of  $M_h = 125.09 \pm 0.24_{\text{EXP}} \pm 1.5_{\text{SUSY}}$ GeV. The assumed theoretical uncertainty for the lightest Higgs mass within MSSM (computed using **FeynHiggs-2.10.0**) is a conservative but accurate estimate of the point-by-point uncertainty that can be calculated with such [code](#). Further constraints on the Higgs decays are incorporated using **HiggsSignals-1.3.1**.
- Dark Matter Relic Density, determined from anisotropies in the Cosmic Microwave Background and satellite measurements,  $\Omega_{\text{CDM}}h^2 = 0.1186 \pm 0.0022_{\text{EXP}} \pm 0.012_{\text{TH}}$ , from [ref](#). The SUSY prediction is taken from **micrOMEGAs-3.2**. Given the high sensitivity of such prediction to the given spectrum, a theoretical uncertainty of  $\sim 10\%$  is assumed.
- The Anomalous Dipole Moment of the Muon,  $(g - 2)_\mu^{\text{EXP}} - (g - 2)_\mu^{\text{SM}} = (30.2 \pm 5.4_{\text{stat}} \pm 3.3_{\text{sys}} \pm 6.1_{\text{SM}} \pm 2.0_{\text{SUSY}}) \times 10^{-10}$ , from [refs](#). The anomalous dipole moment is computed within MSSM using **FeynHiggs-2.10.0**.
- Electroweak Precision Observables,  $M_W$  and the  $Z$ -pole observables. These are computed using **FeynWZ**. Its inputs,  $\Delta\alpha_{\text{had}}^{(5)}(M_Z)$  and  $M_Z$ , are treated as nuisance parameters in the fit.
- Flavour Physics Observables, such as branching fractions from rare  $B$  decays, rare  $K$  decays,  $B - \bar{B}$  mixing and  $\epsilon_K$ . The SUSY predictions for flavour physics observables are calculated using **SuFla** [update](#).

## 7.4.2 Non-Gaussian Constraints

Contributions from non-Gaussian constraints include:

- Searches for Squarks and Gluinos by ATLAS and CMS [ref](#), that strongly constraint the parameter space of the models. A  $\chi^2$  is extrapolated from the provided contour plots. [ref 38 en Higgs](#)

- 2376     • Production of heavy neutral Higgs bosons decaying into taus,  $H/A \rightarrow \tau^+\tau^-$ . As before,  
2377        a  $\chi^2$  is constructed from the exclusion contours from ATLAS [ref](#) and CMS [ref](#) using  
2378        [HiggsBounds-4.2.0](#).
- 2379     • Spin-independent cross-section of neutralino-nucleus elastic scattering, taking into account  
2380        results from LUX, XENON and PICO [check](#), [refs](#) and theor experimental uncertainties in  
2381        the theoretical calculation [ref 79](#) Kees.
- 2382     • [reinterpretation of searches?](#)

# Appendices



# Appendix A

## MasterCode observables

### A.1 Mass Spectrum

The electroweak symmetry breaking of the MSSM leads to 4 physical Higgs particles: a  $CP$ -odd scalar ( $A$ ), two  $CP$ -even neutral scalars ( $h^0$  and  $H^0$ ) and two charged scalars ( $H^\pm$ ), with masses given by

$$\begin{aligned} M_A^2 &= |\mu|^2 + m_{H_u}^2 + m_{H_d}^2 \\ M_{h^0, H^0}^2 &= \frac{1}{2} \left[ M_A^2 + M_Z^2 \mp \sqrt{(M_A^2 + M_Z^2)^2 - 4M_Z^2 M_A^2 \cos 2\beta^2} \right] \\ M_{H^\pm}^2 &= M_A^2 + M_W^2 \end{aligned} \quad (\text{A.1})$$

As for the neutralinos, its mass matrix is given by

$$\mathbf{Y} = \begin{pmatrix} M_1 & 0 & -c_\beta s_W M_Z & s_\beta s_W M_Z \\ 0 & M_2 & c_\beta c_W M_Z & -s_\beta c_W M_Z \\ -c_\beta s_W M_Z & c_\beta c_W M_Z & 0 & -\mu \\ s_\beta s_W M_Z & -s_\beta c_W M_Z & -\mu & 0 \end{pmatrix} \quad (\text{A.2})$$

where  $s_\beta = \sin \beta$ ,  $c_\beta = \cos \beta$ ,  $c_W = \cos W$ ,  $s_W = \sin W$ . The four neutralino masses are obtained diagonalising [A.2](#),  $\mathbf{N} \mathbf{Y} \mathbf{N}^{-1} = \text{diag}(m_{\tilde{\chi}_1^0}, m_{\tilde{\chi}_2^0}, m_{\tilde{\chi}_3^0}, m_{\tilde{\chi}_4^0})$ , where  $m_{\tilde{\chi}_1^0} < m_{\tilde{\chi}_2^0} < m_{\tilde{\chi}_3^0} < m_{\tilde{\chi}_4^0}$ .

In the case of the charginos, its mass matrix is:

$$\mathbf{X} = \begin{pmatrix} M_2 & \sqrt{2}s_\beta M_W \\ \sqrt{2}c_\beta M_W & \mu \end{pmatrix} \quad (\text{A.3})$$

It is diagonalised by two unitary matrices,  $\mathbf{U}$ ,  $\mathbf{V}$  as  $\mathbf{U}^* \mathbf{X} \mathbf{V}^{-1} = \text{diag}(m_{\tilde{\chi}_1^\pm}, m_{\tilde{\chi}_2^\pm})$ , where

$$m_{\tilde{\chi}_1^\pm}^2, m_{\tilde{\chi}_2^\pm}^2 = \frac{1}{2} \left\{ |M_2|^2 + |\mu|^2 + M_W^2 \mp \sqrt{(|M_2|^2 + |\mu|^2 + 2M_W^2)^2 - 4|\mu M_2 - M_W \sin 2\beta|^2} \right\} \quad (\text{A.4})$$

For the sfermion, the mass terms are given in the MSSM Lagrangian by <https://arxiv.org/pdf/hep-ph/0604147.pdf>:

$$\mathcal{L} = -\frac{1}{2}(\tilde{f}_L^\dagger, \tilde{f}_R^\dagger) \begin{pmatrix} M_L^2 + m_f^2 & m_f X_f^* \\ m_f X_f & M_R^2 + m_f^2 \end{pmatrix} \begin{pmatrix} \tilde{f}_L \\ \tilde{f}_R \end{pmatrix} \quad (\text{A.5})$$

2397 where

$$\begin{aligned} M_L^2 &= M_{\tilde{F}}^2 + M_Z^2 \cos 2\beta (I_3^f - Q_f s_W^2), \\ M_R^2 &= M_{\tilde{F}'}^2 + M_Z^2 \cos 2\beta Q_f s_W^2, \\ X_f &= A_f - \mu * \cot \beta, \tan \beta \end{aligned} \quad (\text{A.6})$$

2398  $\cot \beta$  and  $I_3^f = \frac{1}{2}$  ( $\tan \beta$  and  $I_3^f = -\frac{1}{2}$ ) correspond to up-type squarks (down-type squarks  
2399 and sleptons) and  $M_{\tilde{F}, \tilde{F}'}$  denote the left-handed and right-handed soft SUSY breaking mass  
2400 parameters respecitvely, and  $Q_f$  is the electromagnetic charge. The sfermion mass eigenstate  
2401 can be obtained with unitary matrix,  $\mathbf{U}_{\tilde{\mathbf{f}}}$ , giving the eigenvalues:

$$m_{\tilde{f}_{1,2}}^2 = m_f^2 + \frac{1}{2} [(M_L^2 - M_R^2)^2 + 4m_f^2 |X_f|^2] \quad (\text{A.7})$$

2402 **sneutrino masses?**

## 2403 A.2 Dark Matter Relic Density

2404 The cosmological dark matter density is one of two most important dark matter constraints. Its  
2405 value is measured by Planck to be  $\Omega_{\text{CDM}} h^2 = 0.1186 \pm 0.0020_{\text{EXP}} \pm 0.0024_{\text{TH}}$  ref, where  $h$  is  
2406 the reduced Hubble constant. Assuming the neutralino to be the supersymmetric DM candidate  
2407 and the only responsible for the DM relic density, different (co)annihilation mechanisms are  
2408 suggested to bring the obtained density into the observed range. Some of these mechanisms  
2409 (hereafter, DM mechanisms) are:

- 2410 1. Bulk region: in the case where the neutralino is mostly Bino-like and at least one of the  
2411 sfermions is not too heavy, the neutralino annihilates to a pair of SM particles (e.g., a pair  
2412 of fermions) via t-channel exchange of a sfermion. [plot?](#)
- 2413 2. Sfermion coannihilation: it takes place when sfermions have nearly degenerate masses and  
2414 the LSP is mostly Bino-like. The condition for stau and stop coannihilation ( $\tilde{f}$ ) is:

$$\left( \frac{m_{\tilde{f}}}{m_{\tilde{\chi}_1^0}} - 1 \right) < 0.15 \quad (\text{A.8})$$

- 2415 3.  $A/H$ ,  $h$  and  $Z$  Funnels: in this mechanism, the neutralino is mostly Bino-like and  
2416  $\left| \frac{M_{A,H,h}}{m_{\tilde{\chi}_1^0}} - 2 \right| < 0.1$
- 2417 4. *Hybrid* regions: where more than one of the aforementioned DM mechanism dominate.  
2418 [more?](#)
- 2419 5. Chargino coannihilation: fulfilled when the lightest chargino and neutralino are nearly  
2420 degenerate:  $\left( \frac{m_{\tilde{\chi}_1^\pm}}{m_{\tilde{\chi}_1^0}} - 2 \right) < 0.25$ , being the LSP either Higgsino-like (with very heavy  
2421 neutralinos) or Bino-like.

2422     6. Focus-point region: fulfilled when the LSP has an enhanced Higgsino component as a  
 2423       result of a near-degeneracy in the neutralino mass matrix,  $\left(\frac{\mu}{m_{\tilde{\chi}_1^0}} - 1 < 0.3\right)$

2424     7. Your model here

## 2425   A.3 Neutralino Scattering off Nuclei

2426   One of the most powerful ways in which to search for DM is to look for its scattering on nuclei  
 2427   in low-background underground experiments ref, both in direct (**XENON1T**, **LUX**, **PandaX-II**  
 2428   ...) and indirect (**IceCube**, **PICO**) dark matter detection experiments, that include searches  
 2429   for  **$\gamma$ -rays**, **neutrinos**, **positrons or antiprotons** from DM annihilations near the Galactic Center,  
 2430   Galactic Halo and in dwarf galaxies, and for highly energetic neutrinos produced by the annihi-  
 2431   lations of DM particles inside the Sun ref or Earth ref. In both cases, the signals are proportional  
 2432   to the local density of dark matter and the  $\chi$ -nucleon cross-section. Within MSSM, four ob-  
 2433   servables can contribute to this scattering: the spin-independent and dependent cross sections  
 2434   of neutralinos on protons and nucleons. These contributions appear in non velocity dependent  
 2435   part of the MSSM Lagrangian that addresses the  $\chi$ -nucleon scattering:

$$\mathcal{L} = \alpha_{2i} \bar{\chi} \gamma^\mu \gamma^5 \bar{q}_i \gamma_\mu \gamma^5 q_i + \alpha_{3i} \bar{\chi} \chi \bar{q}_i q_i \quad (\text{A.9})$$

2436   where the coefficients sum over the quark generations, denoting  $i$  up-type ( $i = 1$ ) and down-type  
 2437   ( $i = 2$ ) quarks. The first term is spin-dependent, while the second part is spin-dependent. The  
 2438   cross-sections for these two parts are obtained from  $\alpha_{3i}$  and  $\alpha_{2i}$ , respectively.

### 2439   A.3.1 Spin-Independent Term

2440   The scalar or spin-independent (SI) part of the cross-section can be written in the zero-  
 2441   momentum-transfer limit as

$$\sigma_{\text{SI}} = \frac{4m_r^2}{\pi} [Z f_p + (A - Z) f_n]^2 \quad (\text{A.10})$$

2442   where  $m_r$  is the  $\chi$ -nuclear reduced mass,  $Z$  the atomic number,  $A$  the atomic weight, and for  
 2443    $N = n$  or  $p$

$$\frac{f_N}{m_N} = \sum_{q=u,d,s} f_{T_q}^{(N)} \frac{\alpha_{3q}}{m_q} + \frac{2}{27} f_{TG}^{(N)} \sum_{q=c,b,t} \frac{\alpha_{3q}}{m_q} \quad (\text{A.11})$$

2444   and

$$m_N f_{T_q}^{(N)} \equiv \langle N | m_q \bar{q} q \rangle \equiv m_q B_q^{(N)}, \quad f_{TG}^{(N)} = 1 - \sum_{q=u,d,s} f_{T_q}^{(N)} \quad (\text{A.12})$$

2445   The  $\pi$ -nucleon sigma term,  $\Sigma_{\pi n}$ , may be written as

$$\Sigma_{\pi n} \equiv \frac{1}{2} (m_u + m_d) \times (B_u^{(N)} + B_d^{(N)}) \quad (\text{A.13})$$

2446   It is related to the strange scalar density in the nucleon,  $y$ , by

$$y = 1 - \sigma_0 / \Sigma_{\pi N} \quad (\text{A.14})$$

### 2447 A.3.2 Spin-Dependent Term

2448 The scalar or spin-dependent (SD) part of the cross-section can be written in the zero-  
 2449 momentum-transfer limit as

$$\sigma_{\text{SD}} = \frac{32}{\pi} G_F^2 m_r^2 \Lambda^2 J(J+1) \quad (\text{A.15})$$

2450 where  $J$  is the spin of the nucleus and

$$\Lambda \equiv \frac{1}{J} (a_p \langle S_p \rangle + a_n \langle S_n \rangle) \quad (\text{A.16})$$

2451 and

$$a_p = \sum_q \frac{\alpha_{2q}}{\sqrt{2}G_f} \Delta_q^{(p)}, \quad a_n = \sum_i \frac{\alpha_{2q}}{\sqrt{2}G_f} \Delta_q^{(n)} \quad (\text{A.17})$$

2452 The factors  $\Delta_q^{(N)}$  parametrize the quark spin content of the nucleon and are only significant  
 2453 for the light (u,d,s) quarks.

2454 The biggest uncertainty in spin-independent scattering is due to the poor knowledge of the  
 2455  $\langle N|q\bar{q}|N\rangle$  matrix elements linked to the  $\pi$ -nucleon  $\sigma$  term,  $\Sigma_{\pi N}$ , followed by uncertainties in  
 2456 the SU(3) octet symmetry-breaking contribution to the nucleon mass,  $\sigma_0$ . The treatment of  
 2457 the spin-independent nuclear scattering matrix element within `MasterCode` is performed with  
 2458 `SSARD`.

2459 Given the expressions in A.10 and A.15, experiments with heavy elements such as Ge and  
 2460 Xe are more sensitive to  $\sigma_{\text{SI}}$  (proportional to  $Z^2$ ) than to  $\sigma_{\text{SD}}$ . The SD cross sections are on the  
 2461 other hand nearly independent on the quark masses ref.

## 2462 A.4 Anomalous Magnetic Moment of the Muon

2463 The magnetic moment for a given lepton,  $l$ , is related to its intrinsic spin,  $\vec{S}$ , through the Dirac  
 2464 equation:

$$\vec{M} = g_l \frac{e}{2m_l} \vec{S} \quad (\text{A.18})$$

2465 Where  $m_l$  is the lepton mass and  $g_l$  is the gyromagnetic ratio. Quantum loop effects to the  
 2466 Dirac prediction are parameterized by the anomalous magnetic moment

$$a_l \equiv \frac{g_l - 2}{2} \quad (\text{A.19})$$

2467 While for the electron this quantity is the most precisely measured ref and calculated ref quantity  
 2468 in Nature, this is not the case for the muon. For this particle,  $g_\mu = 2$ , while

$$a_\mu^{\text{SM}} = a_\mu^{\text{QED}} + a_\mu^{\text{EW}} + a_\mu^{\text{Had}} \quad (\text{A.20})$$

2469 where photonic and leptonic contributions are embedded inside  $a_\mu^{\text{QED}}$ ,  $W^\pm$ ,  $Z$  or Higgs loops are  
 2470 accounted for in  $a_\mu^{\text{EW}}$  and  $a_\mu^{\text{Had}}$  contain hadronic (quark and gluon) loop contributions:

$$a_\mu^{\text{QED}} = 116584718.95(0.08) \times 10^{-11} \quad (\text{A.21})$$

2471 where the main contribution to the uncertainty comes from the fine structure constant,  $\alpha$  ref

$$a_\mu^{\text{EW}} = a_\mu^{\text{EW}}[1 - \text{loop}] + a_\mu^{\text{EW}}[2 - \text{loop}] = 153.6(1.0) \times 10^{-11} \quad (\text{A.22})$$

2472 and

$$a_\mu^{\text{Had}}[\text{LO}] = 6931(33)(7) \times 10^{-11}, \quad a_\mu^{\text{Had}}[\text{N(N)LO}] = 19(26) \times 10^{-11} \quad (\text{A.23})$$

2473 where the error is dominated by systematic uncertainties and perturbative QCD for Lead-  
2474 ing Order (LO), and by hadronic light-by-light uncertainty in (Next-to-)Next-Leading Order  
2475 (N(N)NLO). Summing all these contributions give rise to the SM prediction:

$$a_\mu^{\text{SM}} = 116591823(1)(34)(26) \times 10^{-11} \quad (\text{A.24})$$

2476 being the errors due to the electroweak, lowest-order hadronic and higher-order hadronic contrib-  
2477 utions, respectively. As it can be seen, the hadronic contribution to the anomalous magnetic  
2478 moment dominates the uncertainty. The most precise measurement of this quantity has been  
2479 made studying the precession of  $\mu^+$  and  $\mu^-$  in a constant external magnetic field inside a con-  
2480 fining storage ring by the E821 experiment at Brookhaven National Lab (BNL), yielding:

$$a_\mu^{\text{exp}} = 11659209.1(5.4)(3.3) \times 10^{-10} \quad (\text{A.25})$$

2481 where the first error is statistic and the second systematic. Therefore

$$\Delta a_\mu = a_\mu^{\text{exp}} - a_\mu^{\text{SM}} = 268(63)(43) \times 10^{-11} \quad (\text{A.26})$$

2482 where the first error is experimental and the second theoretical. Hence, there is a  $3.5\sigma$  discrep-  
2483 ency between the experimental and SM results. Possible explanations for such difference arise  
2484 in a Supersymmetric scenario, where there is an additional contribution:

$$a_\mu^{\text{SUSY}} \simeq \pm 130 \times 10^{-11} \left( \frac{100 \text{GeV}}{m_\Lambda} \right)^2 \tan \beta \quad (\text{A.27})$$

2485 An alternative scenario that can give explanation to this disagreement is that with a *dark photon*,  
2486 a relatively light vector boson from the dark matter sector that couples to the SM sector through  
2487 mixing with the ordinary photon. refs

## 2488 A.5 Electroweak Precision Observables

2489 Electroweak precision observables (henceforth, EWPO), are known with high accuracy. There-  
2490 fore, they serve as useful constraints in NP models. The EWPO that are used within the  
2491 **MasterCode** framework are the following: **Inclusive Quantities: Cross-Sections and Par-**  
2492 **tial Widths:**

- 2493 •  $Z$  mass,  $M_Z$
- 2494 • Total decay width,  $\Gamma_Z$
- 2495 • Hadronic pole cross-section  $\sigma_{\text{had}}^0 \equiv \frac{12\pi}{M_Z^2} \frac{\Gamma_{ee}\Gamma_{\text{had}}}{\Gamma_Z^2}$

- 2496     • Ratio of hadronic to leptonic decay  $R_l^0 \equiv \Gamma_{\text{had}}/\Gamma_{ll}$   
 2497     • Ratio of partial decay width into  $q\bar{q}$  ( $q = b, c$ ) to the total hadronic width  $R_q^0 = \Gamma_{q\bar{q}}/\Gamma_{rmhad}$

2498   **Asymmetries and Effective Fermionic Weak Mixing Angle:**

- 2499     • Asymmetry parameters,  $\mathcal{A}_f \equiv 2 \frac{\text{Re}(g_{Vf} g_{Af})}{1 + \text{Re}(g_{Vf}/g_{Af})^2}$ , where  $g_{Vf}$  and  $g_{Af}$  are the effective vector  
 2500       and axial couplings  
 2501     • Forward backward asymmetries,  $A_{FB}^{0,f} = \frac{3}{4} \mathcal{A}_e \mathcal{A}_f$   
 2502     • Effective fermionic weak mixing angle,  $\sin \theta_{\text{eff}}^f$

2503   Observables with the superscript 0 are *pseudo-observables*, derived from measured quantities to  
 2504   facilitate the theoretical interpretation.

2505   **A.6 Flavour Physics Observables**

2506   Flavour Physics Observables (hereafter, FPO) are also included within the `MasterCode` frame-  
 2507   work, as their observables are also affected by NP. The  $B$ -meson decays  $B_{s,d} \rightarrow \mu^+ \mu^-$ ,  $B \rightarrow X_s \gamma$ ,  
 2508    $B \rightarrow \tau \nu$ ,  $B \rightarrow X_s ll$ , the  $K$ -mesond decays  $K \rightarrow \mu \nu$ ,  $K \rightarrow \pi \nu \bar{\nu}$ , observables related to  $B - \bar{B}$   
 2509   mixing  $\Delta M_{B_s}$ ,  $\frac{\Delta M_{B_s}^{\text{EXP/SM}}}{\Delta M_{B_d}^{\text{EXP/SM}}}$  and  $\Delta \epsilon_K$  are included. [ref](#)

2510 **Appendix B**

2511 **Coverage of the uncertainty with the  
2512 sFit**

2513 Figures below show the distributions of the parameters from the fit, together with their cor-  
2514 responding pull distributions, obtained when performing the bootstrapping test, for both sim-  
2515 ulation (Fig. B.2 and Fig. B.1), data (Fig. B.4 and Fig. B.3), and simulation of signal and  
2516 background (Fig. B.6 and Fig. B.5).

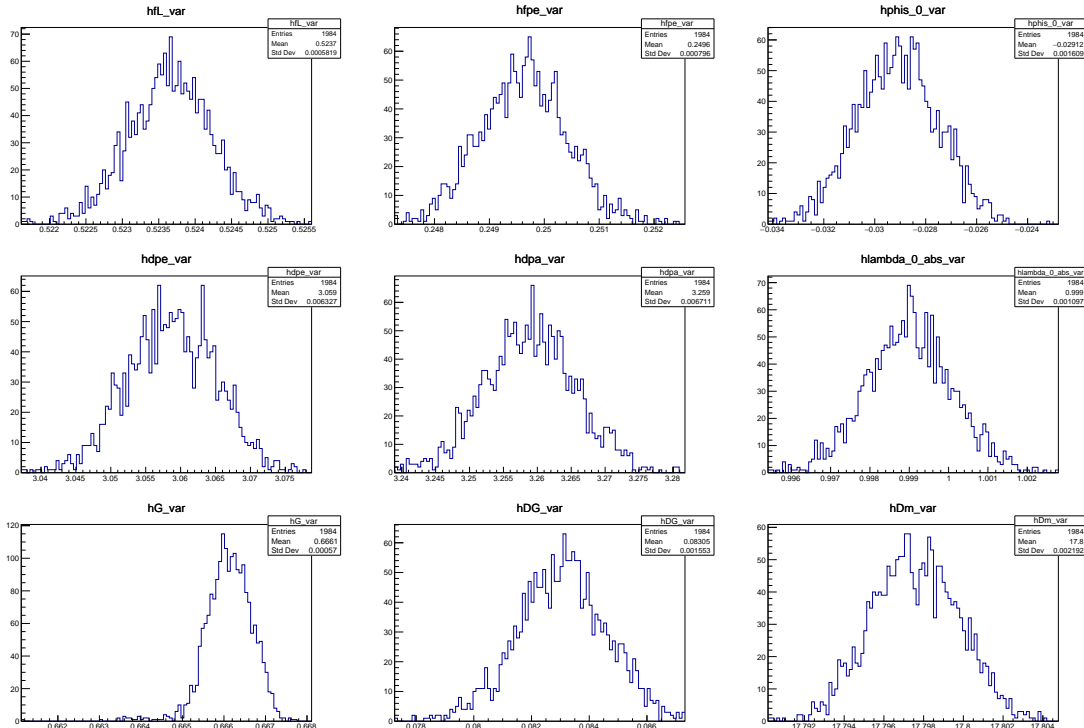


Figure B.1: Distributions of the fit parameters using bootstrapping (MC).

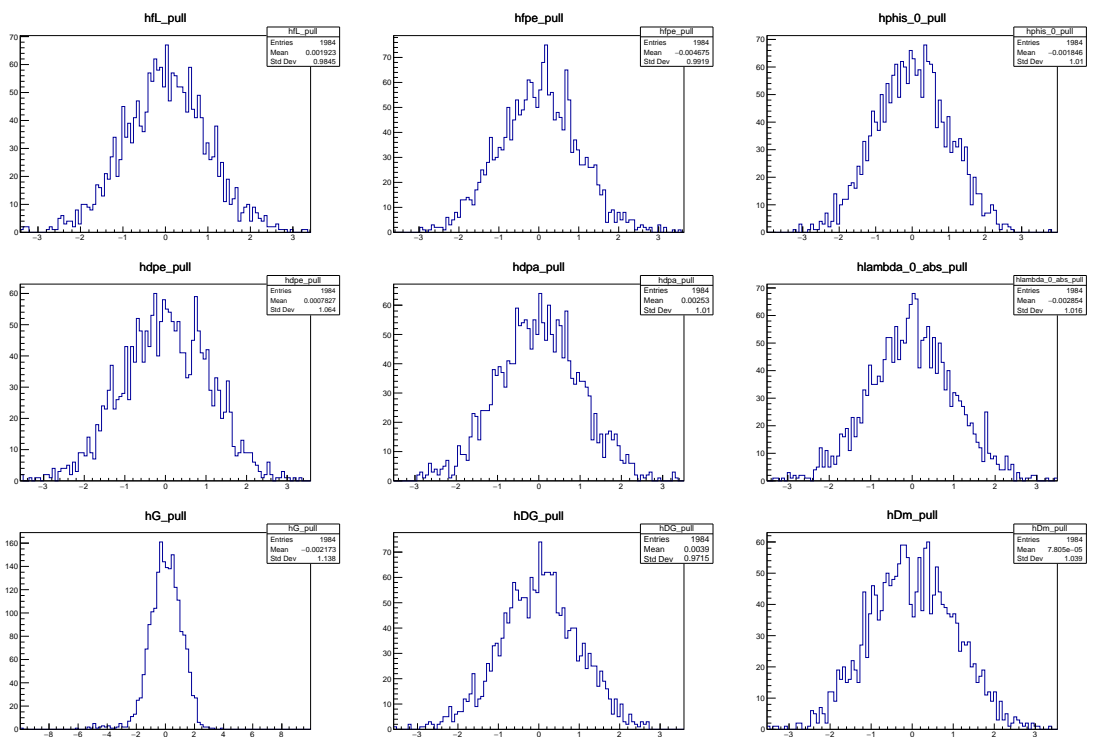


Figure B.2: Pull distributions of the fit parameters using bootstrapping (MC). Pulls are computed relative to MC generation values.

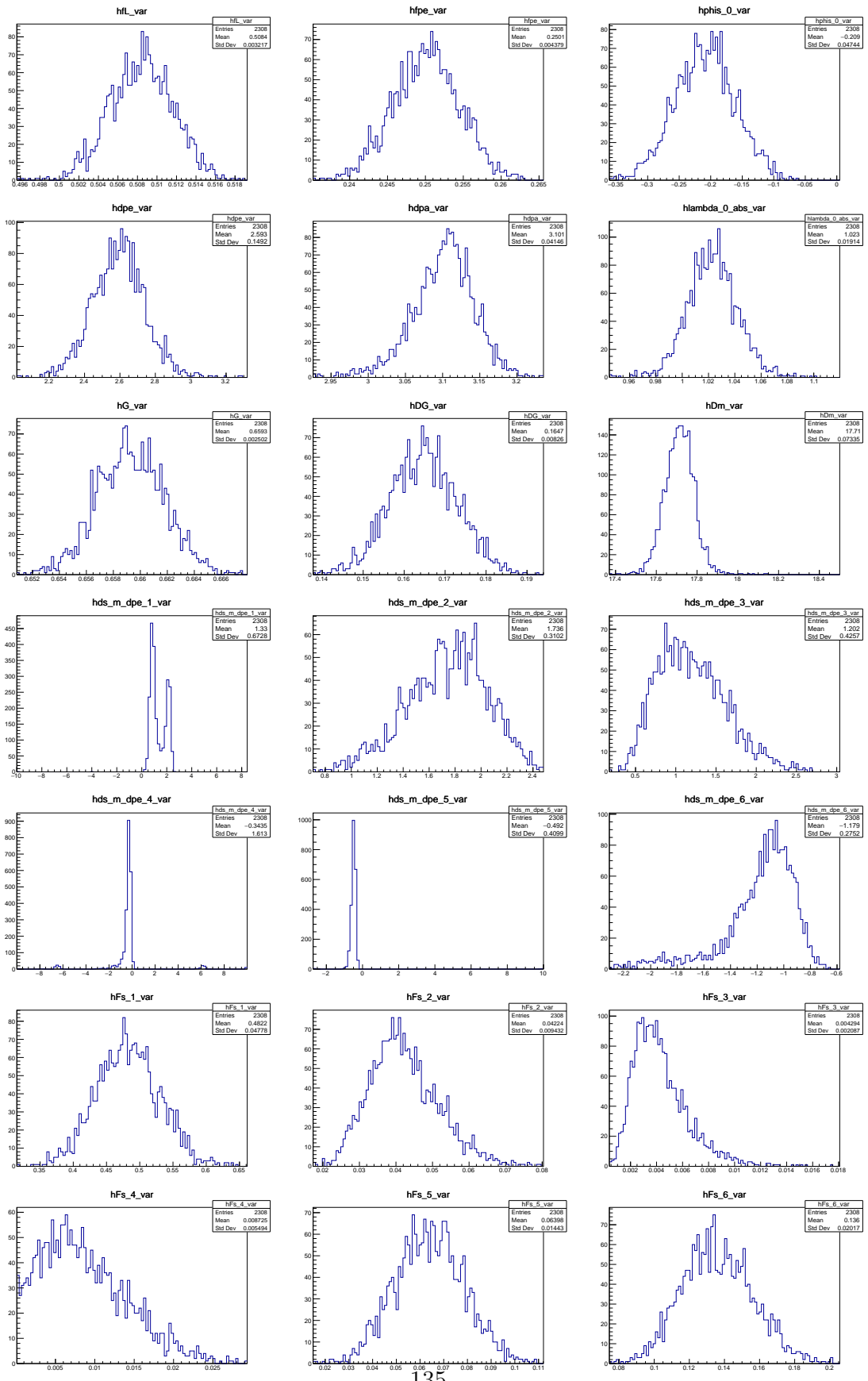


Figure B.3: Distributions of the fit parameters using bootstrapping (data).

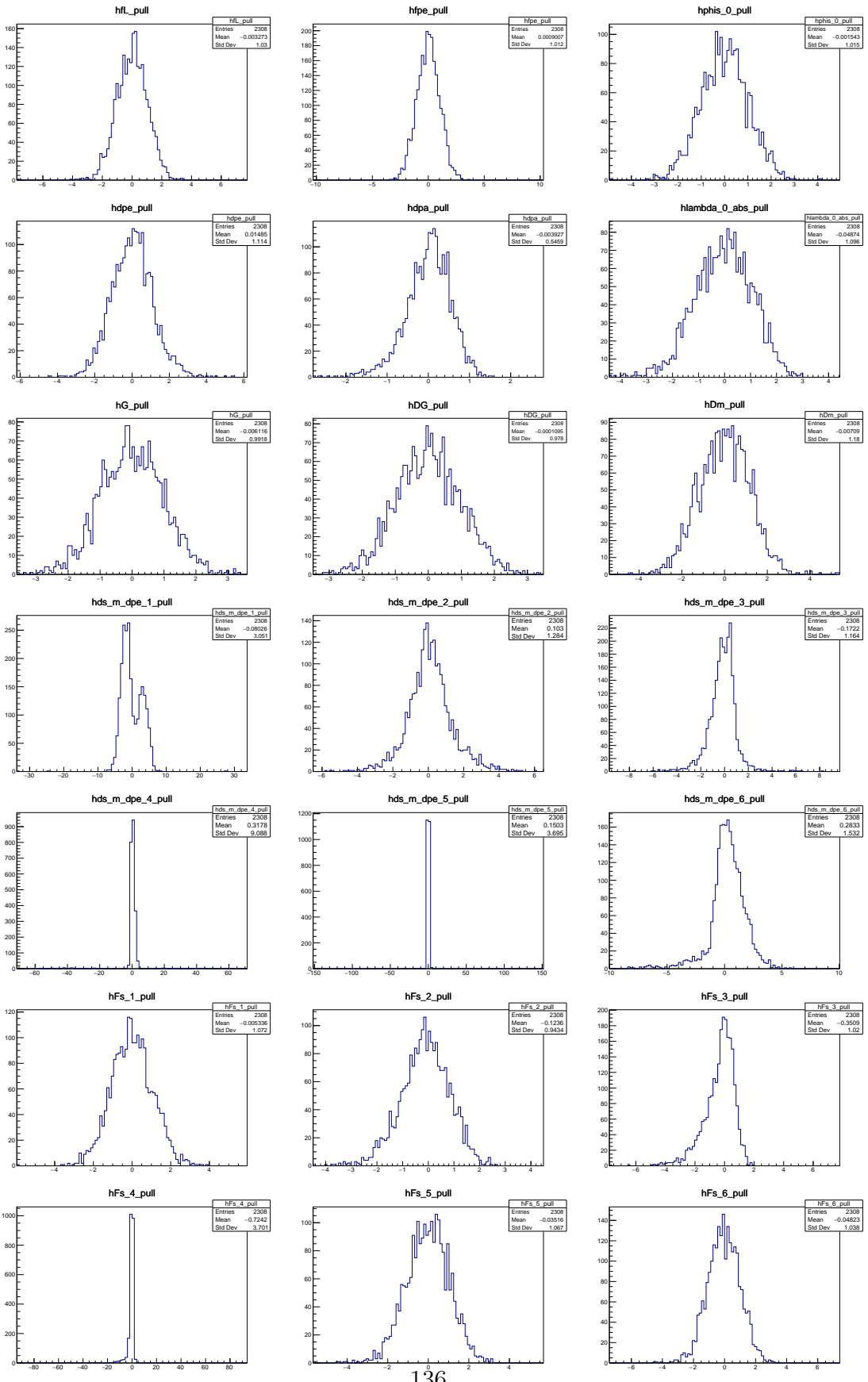


Figure B.4: Pull distributions of the fit parameters using bootstrapping (data). Pulls are computed relative to data central values.

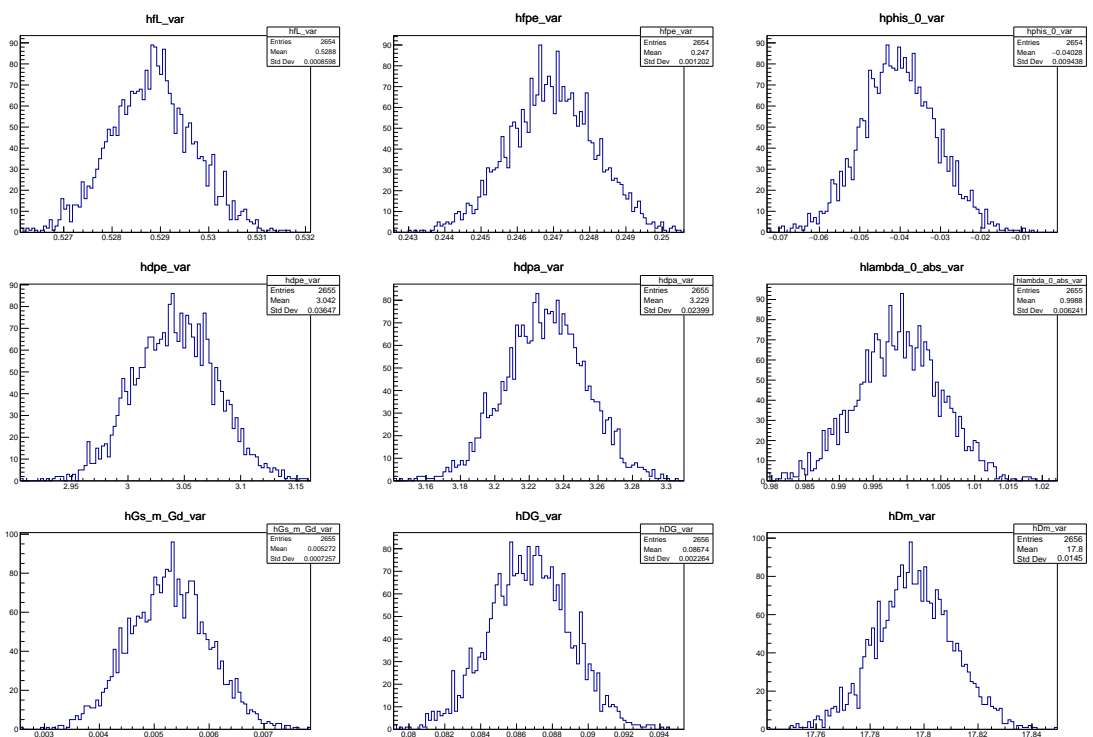


Figure B.5: Distributions of the fit parameters using bootstrapping (simulation and background simulation).

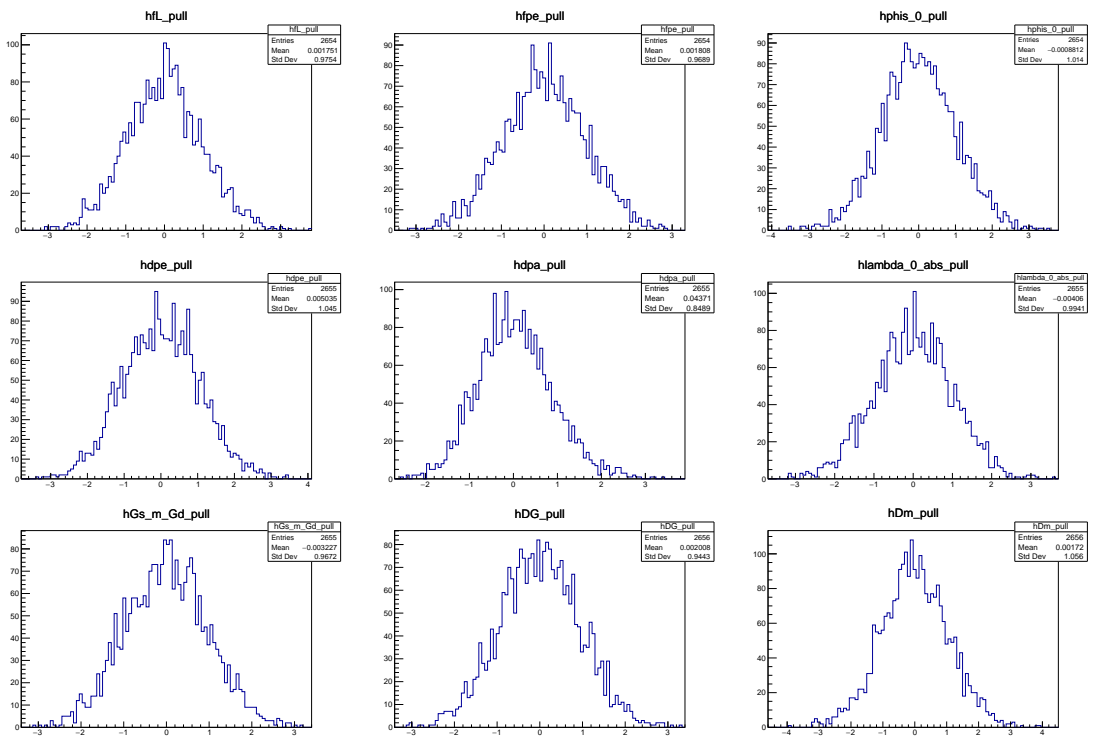


Figure B.6: Pull distributions of the fit parameters using bootstrapping (signal and background simulation).



2517

# Bibliography

- 2518 [1] Particle Data Group, C. Patrignani *et al.*, *Review of Particle Physics*, Chin. Phys. **C40**  
2519 (2016), no. 10 100001.
- 2520 [2] P. W. Higgs, *Broken symmetries and the masses of gauge bosons*, Phys. Rev. Lett. **13** (1964)  
2521 508.
- 2522 [3] ATLAS, G. Aad *et al.*, *Observation of a new particle in the search for the Standard  
2523 Model Higgs boson with the ATLAS detector at the LHC*, Phys. Lett. **B716** (2012) 1,  
2524 [arXiv:1207.7214](https://arxiv.org/abs/1207.7214).
- 2525 [4] CMS, S. Chatrchyan *et al.*, *Observation of a new boson at a mass of 125 GeV with the  
2526 CMS experiment at the LHC*, Phys. Lett. **B716** (2012) 30, [arXiv:1207.7235](https://arxiv.org/abs/1207.7235).
- 2527 [5] M. Maltoni, T. Schwetz, M. A. Tortola, and J. W. F. Valle, *Status of global fits to neutrino  
2528 oscillations*, New J. Phys. **6** (2004) 122, [arXiv:hep-ph/0405172](https://arxiv.org/abs/hep-ph/0405172).
- 2529 [6] M. Drewes, *The Phenomenology of Right Handed Neutrinos*, Int. J. Mod. Phys. **E22** (2013)  
2530 1330019, [arXiv:1303.6912](https://arxiv.org/abs/1303.6912).
- 2531 [7] P. Kooijman and N. Tuning, *Lectures on CP Violation*, 2015.
- 2532 [8] J. M. Cline, *Baryogenesis*, in *Les Houches Summer School - Session 86: Particle Physics  
2533 and Cosmology: The Fabric of Spacetime Les Houches, France, July 31-August 25, 2006*,  
2534 2006. [arXiv:hep-ph/0609145](https://arxiv.org/abs/hep-ph/0609145).
- 2535 [9] N. P. Vogt, M. P. Haynes, T. Herter, and R. Giovanelli, *M/L, H-alpha rotation curves, and  
2536 HI measurements for 329 nearby cluster and field spirals. 1. Data*, Astron. J. **127** (2004)  
2537 3273, [arXiv:astro-ph/0402649](https://arxiv.org/abs/astro-ph/0402649).
- 2538 [10] R. Massey, T. Kitching, and J. Richard, *The dark matter of gravitational lensing*, Rept.  
2539 Prog. Phys. **73** (2010) 086901, [arXiv:1001.1739](https://arxiv.org/abs/1001.1739).
- 2540 [11] R. D. Peccei and H. R. Quinn, *Constraints imposed by CP conservation in the presence of  
2541 pseudoparticles*, Phys. Rev. D **16** (1977) 1791.
- 2542 [12] S. Weinberg, *A new light boson?*, Phys. Rev. Lett. **40** (1978) 223.
- 2543 [13] F. Wilczek, *Problem of strong p and t invariance in the presence of instantons*, Phys. Rev.  
2544 Lett. **40** (1978) 279.
- 2545 [14] <http://www.theo-physik.uni-kiel.de/~bonitz/public/nobel04/public.html>.

- 2546 [15] J. R. Ellis, J. Hisano, M. Raidal, and Y. Shimizu, *A New parametrization of the seesaw*  
 2547 *mechanism and applications in supersymmetric models*, Phys. Rev. **D66** (2002) 115013,  
 2548 [arXiv:hep-ph/0206110](https://arxiv.org/abs/hep-ph/0206110).
- 2549 [16] F. Jegerlehner and A. Nyffeler, *The Muon g-2*, Phys. Rept. **477** (2009) 1, [arXiv:0902.3360](https://arxiv.org/abs/0902.3360).
- 2550 [17] KamLAND-Zen, A. Gando *et al.*, *Search for Majorana Neutrinos near the Inverted Mass*  
 2551 *Hierarchy Region with KamLAND-Zen*, Phys. Rev. Lett. **117** (2016), no. 8 082503,  
 2552 [arXiv:1605.02889](https://arxiv.org/abs/1605.02889), [Addendum: Phys. Rev. Lett.117,no.10,109903(2016)].
- 2553 [18] GERDA, M. Agostini *et al.*, *Improved Limit on Neutrinoless Double- $\beta$  Decay of  $^{76}\text{Ge}$  from*  
 2554 *GERDA Phase II*, Phys. Rev. Lett. **120** (2018), no. 13 132503, [arXiv:1803.11100](https://arxiv.org/abs/1803.11100).
- 2555 [19] R. D. Peccei, *The Strong CP problem and axions*, Lect. Notes Phys. **741** (2008) 3,  
 2556 [arXiv:hep-ph/0607268](https://arxiv.org/abs/hep-ph/0607268), [3(2006)].
- 2557 [20] T. Kaluza, *On the Unification Problem in Physics*, Sitzungsber. Preuss. Akad. Wiss. Berlin  
 2558 (Math. Phys. ) **1921** (1921) 966, [arXiv:1803.08616](https://arxiv.org/abs/1803.08616).
- 2559 [21] O. Klein, *Quantentheorie und fünfdimensionale relativitätstheorie*, Zeitschrift für Physik **37**  
 2560 (1926) 895.
- 2561 [22] L. Randall and R. Sundrum, *Large mass hierarchy from a small extra dimension*, Phys.  
 2562 Rev. Lett. **83** (1999) 3370.
- 2563 [23] A. Lenz, *Constraints on a fourth generation of fermions from Higgs Boson searches*, Adv.  
 2564 High Energy Phys. **2013** (2013) 910275.
- 2565 [24] V. Sanz and J. Setford, *Composite Higgs Models after Run 2*, Adv. High Energy Phys.  
 2566 **2018** (2018) 7168480, [arXiv:1703.10190](https://arxiv.org/abs/1703.10190).
- 2567 [25] S. Coleman and J. Mandula, *All possible symmetries of the s matrix*, Phys. Rev. **159** (1967)  
 2568 1251.
- 2569 [26] S. S. AbdusSalam *et al.*, *Benchmark Models, Planes, Lines and Points for Future SUSY*  
 2570 *Searches at the LHC*, Eur. Phys. J. **C71** (2011) 1835, [arXiv:1109.3859](https://arxiv.org/abs/1109.3859).
- 2571 [27] D. Z. Freedman, P. van Nieuwenhuizen, and S. Ferrara, *Progress Toward a Theory of Su-*  
 2572 *pergravity*, Phys. Rev. **D13** (1976) 3214.
- 2573 [28] J. R. Ellis, K. A. Olive, and Y. Santoso, *The MSSM parameter space with nonuniversal*  
 2574 *Higgs masses*, Phys. Lett. **B539** (2002) 107, [arXiv:hep-ph/0204192](https://arxiv.org/abs/hep-ph/0204192).
- 2575 [29] A. Datta, A. Kundu, and A. Samanta, *New bounds on slepton and Wino masses*  
 2576 *in anomaly mediated supersymmetry breaking models*, Phys. Rev. **D64** (2001) 095016,  
 2577 [arXiv:hep-ph/0101034](https://arxiv.org/abs/hep-ph/0101034).
- 2578 [30] E. Bagnaschi *et al.*, *Likelihood Analysis of the Minimal AMSB Model*, Eur. Phys. J. **C77**  
 2579 (2017), no. 4 268, [arXiv:1612.05210](https://arxiv.org/abs/1612.05210).
- 2580 [31] S. P. Martin, *A Supersymmetry primer*, [arXiv:hep-ph/9709356](https://arxiv.org/abs/hep-ph/9709356), [Adv. Ser. Direct. High  
 2581 Energy Phys.18,1(1998)].

- 2582 [32] Super-Kamiokande, H. Nishino *et al.*, *Search for Proton Decay via  $p \rightarrow e^+ \pi^0$  and  $p \rightarrow \mu^+ \pi^0$  in a Large Water Cherenkov Detector*, *Phys. Rev. Lett.* **102** (2009) 141801, [arXiv:0903.0676](#).
- 2585 [33] A. Masiero and J. W. F. Valle, *A model for spontaneous r parity breaking*, *Physics Letters B* **251** (1990), no. 2 273 .
- 2587 [34] J. C. Romão, C. A. Santos, and J. W. F. Valle, *How to spontaneously break r parity*, *Physics Letters B* **288** (1992), no. 3 311 .
- 2589 [35] D. K. Ghosh, G. Senjanovic, and Y. Zhang, *Naturally Light Sterile Neutrinos from Theory of R-parity*, *Phys. Lett. B* **698** (2011) 420, [arXiv:1010.3968](#).
- 2591 [36] GAMBIT, P. Athron *et al.*, *Combined collider constraints on neutralinos and charginos*, [arXiv:1809.02097](#).
- 2593 [37] GAMBIT, P. Athron *et al.*, *A global fit of the MSSM with GAMBIT*, *Eur. Phys. J. C* **77** (2017), no. 12 879, [arXiv:1705.07917](#).
- 2595 [38] GAMBIT, P. Athron *et al.*, *Global fits of GUT-scale SUSY models with GAMBIT*, *Eur. Phys. J. C* **77** (2017), no. 12 824, [arXiv:1705.07935](#).
- 2597 [39] E. Bagnaschi *et al.*, *Likelihood Analysis of Supersymmetric SU(5) GUTs*, *Eur. Phys. J. C* **77** (2017), no. 2 104, [arXiv:1610.10084](#).
- 2599 [40] E. Bagnaschi *et al.*, *Likelihood Analysis of the pMSSM11 in Light of LHC 13-TeV Data*, *Eur. Phys. J. C* **78** (2018), no. 3 256, [arXiv:1710.11091](#).
- 2601 [41] J. C. Costa *et al.*, *Likelihood Analysis of the Sub-GUT MSSM in Light of LHC 13-TeV Data*, *Eur. Phys. J. C* **78** (2018), no. 2 158, [arXiv:1711.00458](#).
- 2603 [42] P. Paradisi and D. M. Straub, *The SUSY CP Problem and the MFV Principle*, *Phys. Lett. B* **684** (2010) 147, [arXiv:0906.4551](#).
- 2605 [43] W. Altmannshofer, A. J. Buras, and D. Guadagnoli, *The MFV limit of the MSSM for low  $\tan(\beta)$ : Meson mixings revisited*, *JHEP* **11** (2007) 065, [arXiv:hep-ph/0703200](#).
- 2607 [44] G. D'Ambrosio, G. F. Giudice, G. Isidori, and A. Strumia, *Minimal flavor violation: An Effective field theory approach*, *Nucl. Phys. B* **645** (2002) 155, [arXiv:hep-ph/0207036](#).
- 2609 [45] C. Csaki, Y. Grossman, and B. Heidenreich, *MFV SUSY: A Natural Theory for R-Parity Violation*, *Phys. Rev. D* **85** (2012) 095009, [arXiv:1111.1239](#).
- 2611 [46] D. M. Straub, *MFV and the SUSY CP Problem*, *AIP Conf. Proc.* **1200** (2010) 904, [arXiv:0909.3296](#).
- 2613 [47] A. J. Buras *et al.*, *Universal unitarity triangle and physics beyond the standard model*, *Phys. Lett. B* **500** (2001) 161, [arXiv:hep-ph/0007085](#).
- 2615 [48] CKMfitter Group, J. Charles *et al.*, *CP violation and the CKM matrix: Assessing the impact of the asymmetric B factories*, *Eur. Phys. J. C* **41** (2005), no. 1 1, [arXiv:hep-ph/0406184](#).

- 2617 [49] LHCb collaboration, A. A. Alves Jr. *et al.*, *The LHCb detector at the LHC*, JINST **3** (2008)  
2618 S08005.
- 2619 [50] A. A. Alves, Jr. *et al.*, *Performance of the LHCb muon system*, JINST **8** (2013) P02022,  
2620 arXiv:1211.1346.
- 2621 [51] LHCb, R. Aaij *et al.*, *LHCb Detector Performance*, Int. J. Mod. Phys. **A30** (2015), no. 07  
2622 1530022, arXiv:1412.6352.
- 2623 [52] W. Altmannshofer *et al.*, *Anatomy and Phenomenology of FCNC and CPV Effects in SUSY*  
2624 *Theories*, Nucl. Phys. **B830** (2010) 17, arXiv:0909.1333.
- 2625 [53] F. Feroz, M. P. Hobson, and M. Bridges, *MultiNest: an efficient and robust Bayesian*  
2626 *inference tool for cosmology and particle physics*, Mon. Not. Roy. Astron. Soc. **398** (2009)  
2627 1601, arXiv:0809.3437.
- 2628 [54] J. Charles *et al.*, *Predictions of selected flavour observables within the Standard Model*,  
2629 Phys. Rev. **D84** (2011) 033005, arXiv:1106.4041.